

ÉCOLE DOCTORALE *Physique et Chimie-Physique*

Institut franco-allemand de recherches de Saint-Louis, laboratoire NS3E –
ISL/CNRS/UNISTRA UMR 3208

THÈSE

 présentée par :

Pierre FEHLEN

Soutenue le : **23 octobre 2023**

Pour obtenir le grade de : **Docteur de l'université de Strasbourg**

Discipline/ Spécialité : **Physique et Chimie-Physique**

**Détection sensible et sélective de composés
organophosphorés par spectroscopie infrarouge
exaltée par effet de surface**

THÈSE dirigée par :

M. SPITZER Denis
M. TALIERCIO Thierry

Directeur de recherches
Professeur des universités
Institut de Saint-Louis
Université de Montpellier

THÈSE co-encadrée par :

M. THOMAS Guillaume
M. GONZALEZ-POSADA Fernando

Chargé de recherches
Maître de conférences
Institut de Saint-Louis
Université de Montpellier

RAPPORTEURS :

Mme VERRIER Isabelle
M. MOREAU Antoine

Chargé de recherches
Maître de conférences
Université Saint-Étienne
Université Clermont Auvergne

AUTRES MEMBRES DU JURY :

M. BOUHELIER Alexandre
M. MASENELLI Bruno

Directeur de recherches
Professeur des universités
Université de Bourgogne
INSA Lyon

Contents

General introduction	1
1 State of the art	5
Introduction	5
1.1 Part one: Chemical warfare agents	5
1.1.1 Organophosphorous compounds	5
1.1.2 CWAs detection: state of the art	9
1.2 Part two: Plasmonics fundamentals	18
1.2.1 Fundamentals	18
1.2.2 Surface-enhanced infrared absorption	28
1.3 Part three: ϵ -near-zero media	33
1.3.1 Origins	33
1.3.2 Principles	34
1.3.3 ENZ-supporting materials	35
1.3.4 ENZ-associated phenomena	35
Conclusion	38
2 Conception, fabrication and characterisations	41
Introduction	41
2.1 Conception	41
2.1.1 The plasmonic structure	41
2.1.2 Electromagnetic simulations	43
2.2 Samples growth	45
2.2.1 Molecular-beam epitaxy	45
2.2.2 Growth characterisations	47
2.3 Fabrication	50
2.3.1 The nano-patterning process: step-by-step	50
2.3.2 Fabrication characterisations	53
2.4 Optical characterisations	54
2.4.1 Fourier-transform infrared spectroscopy	54
2.4.2 Validation of the plasmonic samples	56
Conclusion	58

3 Study of plasmonic ϵ-near-zero effects in the infrared with III-V semi-	59
conductors	59
Introduction	59
3.1 Presentation of the samples	60
3.2 Optical characterisation	62
3.2.1 Bulk material characterisation	62
3.2.2 Processed samples characterisation	63
3.3 The plasmonic resonance pinning phenomenon	65
3.3.1 Experimental results	65
3.3.2 Theoretical results	68
3.4 The dispersive behaviour associated to ENZ media	74
3.4.1 The effective index theory	74
3.4.2 The near-constant phase	74
3.4.3 The enhanced electromagnetic field	76
Conclusion	77
4 Gas sensing of organophosphorous compounds	79
Introduction	79
4.1 Experiment prerequisites	79
4.1.1 Experimental setup	79
4.1.2 The plasmonic sample	81
4.2 Experimental results	83
4.2.1 Optical characterisations	83
4.2.2 Sensitivity study	85
4.2.3 Selectivity study	90
4.3 Oxide-DMMP interactions	95
4.3.1 Infrared spectroscopy	96
4.3.2 Raman spectroscopy	97
4.3.3 X-ray photoelectron spectroscopy	98
4.3.4 Surface chemistry discussion	99
4.4 Numerical simulation results	101
4.4.1 Kramers-Kronig relations	101
4.4.2 FDTD simulations	102
4.4.3 RCWA simulations	103
Conclusion	104
General conclusion and perspectives	107
Annexes	111
A. Brewster experiments	111
B. Dispersion relation calculi	112
C. Gas sensing simulations	114

List of Figures

1.1	Classification of weapons of mass destruction.	6
1.2	Schematic diagram of a neuromuscular junction in absence and in presence of the sarin nerve agent.	7
1.3	CWAs commercial methods of detection.	10
1.4	Evolution of the literature for different keywords.	15
1.5	Schematic diagram representing SPPs propagating along the metal/dielectric interface.	20
1.6	Dispersion relations of a perfect metal/insulator interface and a real doped semiconductor/insulator interface.	21
1.7	Diagram of the operating frequency of various plasmonic materials as a function of the electromagnetic spectrum.	23
1.8	Three different light-plasma coupling techniques.	25
1.9	Microscopy images of different plasmonic antennas from the literature: a review.	25
1.10	Influence of the plasmonic antenna size and shape over its optical response.	27
1.11	Infrared absorption spectra of sarin and DMMP.	29
1.12	SPR and SEIRA effects.	31
1.13	Review of ENZ materials.	36
2.1	Schematic diagram of the metal-insulator-metal structure.	42
2.2	Reflectance simulations performed by RCWA.	44
2.3	Normalised electric and magnetic fields of plasmonic nanoribbons by RCWA simulation.	45
2.4	Photograph of the molecular beam epitaxy system.	46
2.5	Atomic force microscopy images of InAsSb:Si digital alloy grown on GaSb and GaSb grown on GaAs.	47
2.6	High resolution X-ray diffraction spectra of a slightly mismatched InAsSb on GaSb, a perfectly matched InAsSb on GaSb and InAsSb on GaAs.	48
2.7	Experimental Brewster measurement and associated simulation.	49
2.8	Photographs of photolithography and EBL systems.	51
2.9	Scheme of the fabrication process in three main steps.	53

2.10 Fabrication characterisations: SEM image of nanoribbon shape plasmonic antennas, optical microscopy image of the processed sample, and 3D reconstruction image obtained by AFM.]	54
2.11 Photograph of the Hyperion 3000 FTIR.]	56
2.12 Single spectrum of the reflected light by a surface of nanoribbons plasmonic antennas.]	57
2.13 Reflectance spectrum from $\sim 1 \mu\text{m}$ wide nanoribbons plasmonic antennas.]	58
3.1 Schematic diagrams of the three studied MIM ENZ samples.]	60
3.2 Real part of the permittivity ϵ_r]	61
3.3 Optical microscopy images of ENZ samples.]	62
3.4 Brewster mode measurements of ENZ samples.]	62
3.5 Reflectance measurements obtained by FTIR spectroscopy of the ENZ samples.]	65
3.6 Reflectance spectra of 500 nm width nanoantennas for all three samples, illustrating the influence of the spacer doping level over the optical response.]	66
3.7 Experimental reflectance spectra with increasing nanoantennas widths of ENZ samples highlighting the red-shift.]	67
3.8 LSPR frequencies function of the nanoantennas width of ENZ samples.]	68
3.9 3D and 2D representations of dispersion relation equation for a three layers photonic structure (air/InAsSb:Si (n++)/InAsSb:Si (n+)]	70
3.10 Screenshot from FDTD Lumerical software of the bandstructure calculator model.]	71
3.11 Dispersion relations of the ENZ samples]	72
3.12 Normalized electric and magnetic field maps of nanoribbon plasmonic antennas by RCWA.]	73
3.13 Effective refractive index n_{eff} of the ENZ samples]	75
3.14 Calculated modal reflection phase ϕ_r of the ENZ samples.]	75
3.15 Enhanced electromagnetic $ E_x/E_0 ^2$ field a standard MIM structure, and an M-ENZ-M structure.]	77
4.1 Experimental setup for detection of DMMP in gas phase.]	80
4.2 Sample S structure: the plasmonic-based MIM sensor.]	81
4.3 Sample S characterisations: optical, SEM, and AFM.]	82
4.4 Infrared reflectance spectra translating the absorption from DMMP and environmental interferences.]	83
4.5 Sample S plasmonic response in the MIR.]	84
4.6 Reflectance of DMMP in the MIR as a function of the water bath temperature.]	85
4.7 Intensity of DMMP main absorption line at 1050 cm^{-1} over time.]	86
4.8 210 ppm DMMP reflectance measurements for three antenna widths.]	87
4.9 210 ppm DMMP differential reflectance for three antenna widths.]	88

4.10 Sensing of 100, 210, 320, and 500 ppm of DMMP.]	89
4.11 Histogram summing up the average DMMP sensing results of the three plasmonic regions studied.]	90
4.12 Selectivity test with 200 ppm of benzene.]	91
4.13 Selectivity test with 50000 ppm of methane.]	92
4.14 Experimental setup for detection of DMMP in gas phase, adapted to in- troduce humidity.]	92
4.15 Sensing of 100 ppm of DMMP with 50% relative humidity.]	93
4.16 Histogram summing up selectivity and sensitivity results of the plasmonic sensor.]	94
4.17 Schematic representation of the adsorption process between DMMP and InAsSb native oxide, resulting in a 5 Å DMMP monolayer.]	95
4.18 Absorption coefficients κ of pure DMMP and dried DMMP on InAsSb:Si under N ₂ flux.]	97
4.19 Raman spectra of the liquid DMMP, and dried DMMP, on the InAsSb:Si surface.]	98
4.20 XPS spectra of InAsSb:Si surface and dried DMMP on the surface.]	99
4.21 Proposed schemes of DMMP adsorbed onto InAsSb surfaces.]	101
4.22 Refractive index n and absorption coefficient κ of DMMP in pure phase and dried on InAsSb:Si, calculated from Kramers-Kronig relations.]	102
4.23 FDTD simulation software Lumerical for the simulation of a 5 Å thick monolayer of DMMP adsorbed at the surface of the plasmonic sensor.] . . .	103
4.24 Differential reflectances: experimental measurements, FDTD simulations and RCWA-corrected simulations.]	104

List of Tables

1.1	AEGLs in ppb of sarin.	8
1.2	Chemical properties: a comparison between sarin and DMMP.	9
1.3	Summarising table of commercial CWAs detection methods.	13
1.4	Limit of detection of various chemical threats for different plasmonic-based systems.	16
1.5	Overview of the different plasmons.	19
1.6	Review of gas sensing performed by SEIRA-based sensors.	32
3.1	Materials parameters of the ENZ samples.	63
3.2	Measured geometrical parameters of ENZ samples.	63
4.1	Main peaks data of DMMP from this work and literature in IR and Raman spectroscopies.	98

Abbreviations list:

ACh: acetylcholine	InAsSb:Si: silicon doped indium arsenide antimony
AChE: acetylcholinesterase	IPA: isopropanol
AEGL: acute exposure guideline level	IR: infrared
AFM: atomic force microscopy	LOD: limit of detection
AlSb: aluminum antimony	LSP: localised surface plasmon-polaritons
AZO: aluminum [doped] zinc oxide	LSPR: localised surface plasmon resonance
CWA: chemical warfare agent	MBE: molecular beam epitaxy
CWC: chemical weapons convention	MCT: mercury cadmium telluride
DI: deionised [water]	MIM: metal-insulator-metal
DMMP: dimethyl methylphosphonate	MIP: molecular imprinted polymer
DTGS: deuterated triglycide sulfate	MIR: mid infrared
EBL: electron beam lithography	MOF: metal-organic framework
EELS: electron energy loss spectroscopy	nid: non-intentionally doped
EM: electromagnetic	NIR: near infrared
FCO: fluorine [doped] cadmium oxide	OP: organophosphorous [compound]
FDTD: finite difference time domain	ppb: parts-per-billion
FEM: finite element method	ppm: parts-per-million
FPD: flame photometry detector	ppt: parts-per-trillion
FT: Fourier transform	RCWA: rigorous coupled-wave analysis
FTIR: Fourier transform infrared [spectroscopy]	RIE: reactive ion etching
FWHM: full-width at half-maximum	SAM: self-assembled monolayer
GaAs: gallium arsenide	SAW: surface acoustic wave
GaSb: gallium antimony	SC: semiconductor
GB: sarin	SEIRA: surface-enhanced infrared absorption
GZO: gallium [doped] zinc oxide	SEM: scanning electron microscopy
HF: hydrofluoric [acid]	SNR: signal to noise ratio
HRXRD: high-resolution X-ray diffraction	SP: surface plasmon
ICO: indium [doped] cadmium oxide	SPP: surface plasmon-polaritons
ICP: induced coupled plasma	SPR: surface plasmon resonance
IMS: ion mobility spectrometry	TCO: transparent conducting oxide
InAs: indium arsenide	TE: transverse electric
	THz: terahertz
	TM: transverse magnetic

General introduction

Chemical weapons remain an extremely dangerous threat despite the 1997 Chemical Weapons Convention (CWC) resulting from international consensus that strictly prohibits their use, development, production and stockpiling by countries who have acceded to it. The CWC stems from the Geneva Protocol of 1925 following the trauma caused by the large-scale use of tear gas, chlorine, and mustard gas by France and the German Empire during the World War 1. The CWC represents the extended international response against chemical weapons used in the 1995 Tokyo terrorist attack and by Iraq in the 1980s in the war against Iran. Still, their usage persists in wars and assassinations. Nerve agent sarin (GB) and chlorine were used by the Syrian government during the civil war, and the Islamic State used mustard gas in northern Iraq from 2015 up to 2016. Recently, modern Novichok and V class nerve agents have been employed for the assassination of political figures including Kim Jong Nam, Sergei Skripal, and Alexei Navalny. For these reasons, it is manifest that chemical weapons subsist as a menace towards military, civil population, and public figures. The development of sensors is a necessary countermeasure against such hazardous chemicals.

The immense lethal potency of chemical warfare agents (CWA), including organophosphorous compounds (OP), even at extremely low concentrations, combined with odourless, invisibility, and persistency features, make this category of molecules particularly dangerous as they elude our natural senses. Upon inhalation, nerve agents lethal effects appear for concentrations as low as few $\text{mg}\cdot\text{m}^{-3}$, corresponding to few molecules per billions. Additionally, these molecules are composed of commonly found elements, *e.g.*, carbon, nitrogen, oxygen, fluorine, and phosphorus, with a light molecular weight around $100\text{ g}\cdot\text{mol}^{-1}$. Both of these characteristics represent major challenges in terms of sensitivity, selectivity, and response time of a sensor. Commercially available techniques are mostly represented by devices that suffer from significant drawbacks such as bulkiness (gas chromatography), selectivity (gravimetric sensors), sensitivity (ion mobility spectrometry), or response time (colorimetric paper). As a result, there has been a growing interest in developing innovative techniques that overcome the disadvantages of aforementioned methods. We notice that the growth of modern sensing devices is intimately related to the research for new physico-chemically reactive surfaces and materials in order to improve interactions between the molecules and the sensor. In a way, the transducer and the enhancing medium

(either physical or chemical) are the two modern faces of the sensing coin.

In this framework, plasmonics appears to be an underestimated, yet promising, mean for the detection of chemical warfare agents. Plasmonics studies and exploits free carrier oscillations of matter, which may improve the sensitivity of a sensing device. In particular, since the Physical Review Letters paper published in 1980, entitled ‘Enhancement of the infrared absorption from molecular monolayers with thin metal overlayers’ by Hartstein *et al.*, it has been shown that the absorption of molecules can be ameliorated by exploiting surface plasmon modes arising from metallic particles. The absorption of molecules is especially interesting in the infrared, the spectral region where molecules display characteristic resonances known as vibrational modes. Ultimately, numerous studies have successfully demonstrated the use of plasmon-based devices for the sensing of molecules by surface-enhanced infrared absorption (SEIRA). However, only a handful of articles have addressed the problematic of gas sensing using this technique.

On the other hand, modern sensing platforms are further improved by surface chemistry, or functionalisation. A variety of different technologies has been developed in that regard, including polymers, self-assembled monolayers, metal-organic frameworks, oxides, and even nanoparticles with plasmonic properties. While these are interesting in terms of sensitivity and selectivity, as they improve molecule-sensor interactions, they have a number of practical limitations such as reusability and stability (temporal, thermal, etc.). A second approach to improve a sensor performance is to employ a medium that enhances the response of the transducer. In that respect, epsilon-near-zero (ENZ) media have emerged as an exciting mean to improve light-matter interactions when the permittivity of the medium reaches zero. In the mid-2000s, this novel class of materials gathered enormous interest in the electromagnetic community due to the peculiar effects the low permittivity index is associated with. Nonetheless, their application to sensing remains marginal compared to waveguiding and metamaterial design.

In this thesis work, we develop a plasmonic-based device for the detection of CWAs, and more particularly for the detection of sarin. The plasmonic behaviour is obtained using highly-doped III-V semiconductors (InAsSb and GaSb) such that a plasmonic resonance occurs in the mid-infrared. Plasmon-molecule coupling is attained upon spectral and spatial overlap. The spectral overlap implies that the plasmonic resonance and the vibrational modes of the molecule are at the same frequency. The spatial overlap refers to the proximity between molecules and the enhanced electromagnetic field, associated with free carrier oscillations, at plasmonic resonance frequency. The structure of the sample is based on a metal-ENZ-metal structure designed to improve light-matter interactions and enhance the infrared absorption from the CWA molecules. We successfully demonstrate the applicability of III-V semiconductor plasmonics for sensing applications in the in-

frared and for the engineering of metamaterials with improved control over the plasmonic response by the use of an ENZ medium.

The project brought together two research teams: the laboratory Nanomaterials for systems under extreme stress (NS3E) part of the French-German Research Institute of Saint-Louis (ISL), and the nanoMIR group of the Institute of Electronics and Systems (IES), respectively from the University of Strasbourg and the University of Montpellier. The former instigated the project since the development of innovative solutions for the detection of dangerous molecules has been one of their main axis of research for years. On the other hand, the nanoMIR group is a renowned team for its expertise in the growth of III-Sb materials and their applications in plasmonic devices, photodetectors, and lasers. The pooling of their respective expertise in dangerous molecules detection and semiconductor devices such as sensors, combined with the financial support of the Directorate General of Armament (Direction Générale de l'Armement (DGA), project supervised by 'Agence de l'Innovation de Défense' (AID)), provides an unique collaboration to address the serious danger that chemical weapons represent for civilian and military populations.

We hereby outline the content of the thesis manuscript. The first chapter introduces the reader to fundamental notions, both theory and state of the art, essential for understanding the following chapters. It is divided into three parts: Part 1 talks about the state of the art of organophosphorous compounds sensing, Part 2 introduces the basics of plasmonics and its use in sensing, including SEIRA, and Part 3 addresses the origins, principles, applications and phenomena of ENZ media.

The second chapter deals with the design, fabrication, and characterisations of plasmonic samples. We describe the entire process: simulation, growth, fabrication, and characterisations, resulting in plasmonic samples that will be used for the study of ENZ phenomena and sensing applications.

The third chapter focuses on the study of plasmonic ENZ effects using III-V semiconductors. Particular interest is given to understanding the optical response of ENZ samples and the dispersion relation they are associated with. First, we study the influence of the ENZ layer doping level within a metal-insulator-metal structure. Second, we discuss how the plasmonic antenna length impacts the optical response of the structure, depending on the ENZ optical nature. Then, electromagnetic simulations are performed to obtain the dispersion relation and we discuss the various phenomena encountered such as antenna geometry independence, near-constant phase, enhanced electromagnetic field, and the dispersive behaviour of this novel metal-ENZ-metal architecture.

Finally, the fourth chapter concerns the gas sensing of organophosphorous compounds, using samples fabricated (as described in chapter 2), following the study of ENZ-plasmon samples (addressed in chapter 3). We discuss the experimental setup, experimental results, interactions that occur between the organophosphorous molecules and the sensor surface, and lastly numerical simulations. Various experiments are presented in two different studies about the selectivity and the sensitivity of the designed sensor. A special concern is given to understand the chemical reactions that occur between organophosphorous molecules and the sensor surface, through its native oxide, by performing infrared, Raman, and X-ray photoelectron spectroscopies. The experimental results are then cross-confirmed by numerical simulations, demonstrating the successful development of a novel plasmonic-based sensor of organophosphorous compounds. We finalise the thesis with a general conclusion and perspectives.

Chapter 1

State of the art

Introduction

This introductory chapter develops the theory, state of the art and concepts of organophosphorous compounds, plasmonics and ϵ -near-zero media. In this first part, organophosphorous compounds, their effects on the human body, their simulants and how to detect them will be presented. A brief overview of commercially available methods and modern experimental developments will be introduced before comparing them to the plasmonic sensor we aim to develop. The second part presents plasmonics, its theory and applications such as surface-enhanced infrared absorption (SEIRA). Finally, ϵ -near-zero media are discussed in the third part of this chapter. We demonstrate why this emerging class of materials may further benefits to a plasmonic-based sensor, through its peculiar effects.

1.1 Part one: Chemical warfare agents

1.1.1 Organophosphorous compounds

Generalities

OPs are a class of chemicals containing phosphorus ^{15}P . This class includes pesticides^[1] and nerve agents. Nerve agents are a class of chemical warfare agents (CWAs) known for their action on the neuromuscular system and their acute toxicity. They are used as weapons of mass destruction which are intended to harm a large number of people. They are classified as lethal chemical weapons. Nerve agents are often liquid at 20 °C, atmospheric pressure and are highly volatile. They generally are odourless (or may have a slight odour) and colorless, making them particularly dangerous as they elude our senses.

While the use of chemical warfare agents, such as the infamous mustard gas and phosgene, during World War 1 is well-known [1], the discovery of nerve agents occurred in the 1930's decade in Germany [2]. Since then, their usage has been increasingly prohibited

¹A chemical used for killing pests, especially insects.

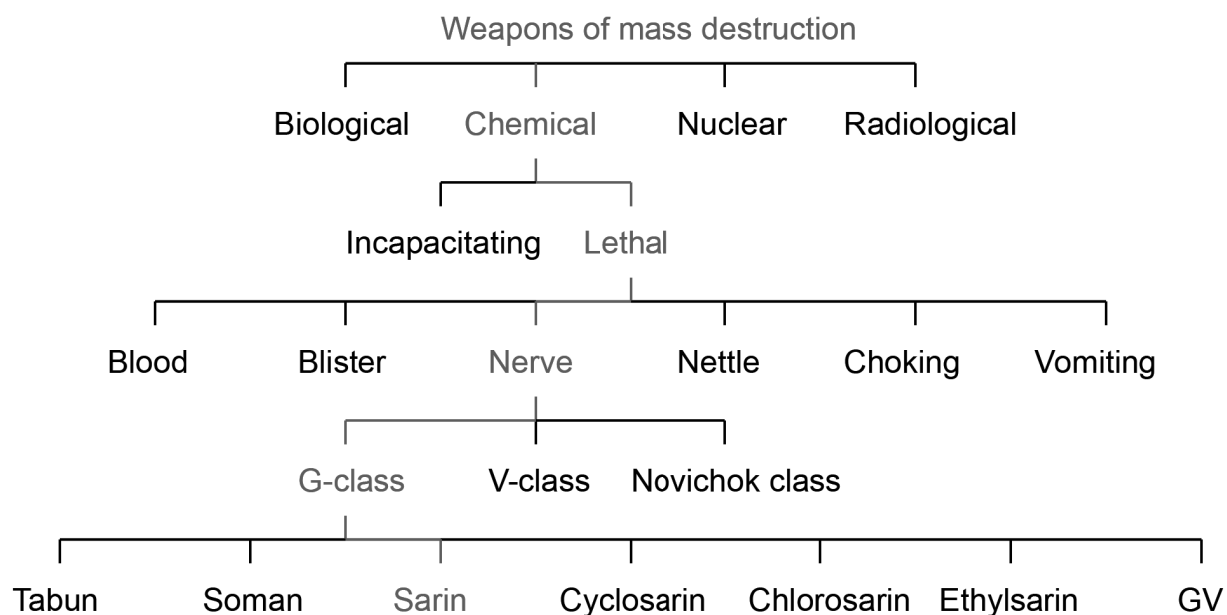


Figure 1.1: Classification of weapons of mass destruction. The red track highlights the sarin classification.

with the milestone date of 1997, where the Chemical Weapons Convention (CWC) was established, the world’s first multilateral disarmament agreement to provide for the elimination of an entire category of weapons of mass destruction within a fixed time frame [3]. Recently, in 2019, it has been decided that annexes should be updated to include newly developed chemical weapons, such as the Novichok class [4]. Nowadays, nerve agents are classified into three types: ‘G’ (standing for German agents), mostly represented by tabun, sarin, cyclosarin, chlorosarin, ethylsarin and soman, ‘V’ agents (standing for venomous), and Novichok, as represented in Figure 1.1. Sarin, compared to other nerve agents is characterised by a high vapor pressure and a persistency of up to 24 hours [5].

Still, CWAs, and in particular sarin, have been repeatedly used. For example, during the first Persian Gulf War, specifically during the Iran-Iraq War and against Kurdish rebels [6]. As well as, in 1995, terrorist attacks in Tokyo, Japan, were perpetrated using Sarin, resulting in 12 casualties and more than 5,000 victims [7]. More recently in Syria, from 2013 to 2018, both chlorine and sarin have been used [8], despite Syria having acceded to the CWC. Given the repeated use of sarin, it has become necessary to develop a system to detect and counter this ever-present threat to military and civilian populations. This is why this research work focuses on the detection of sarin gas, part of the nerve agents G-class, highlighted in red in Figure 1.1.

Pathophysiology

Nerve agents are cholinesterase inhibitors. Cholinesterases are enzymes that catalyse the hydrolysis of choline-based esters, of which neurotransmitters² found in the human body, are made of. Two cholinesterases exist, namely, butyrylcholinesterase and acetylcholinesterase (AChE). AChE is responsible for the breakdown of the neurotransmitters such as acetylcholine (ACh), into choline and acetic acid. An important fact to know is that AChE has a high catalytic activity with a turnover number (limiting number of chemical conversions per second) $> 10^4 \text{ s}^{-1}$, one of the highest among enzyme catalysis [9], highlighting why its blockade could lead to a knock-on effect on the nervous system. This neurotransmitter operates within cholinergic systems, *e.g.*, muscarinic and nicotinic synapses³, which are responsible for the proper functioning of the nervous system. Because AChE acts as the turnoff switch of the cholinergic signal transmission, preventing it from getting out of control, the blockade of AChE will immediately cause overstimulation of the neurotransmitter receptors [10].

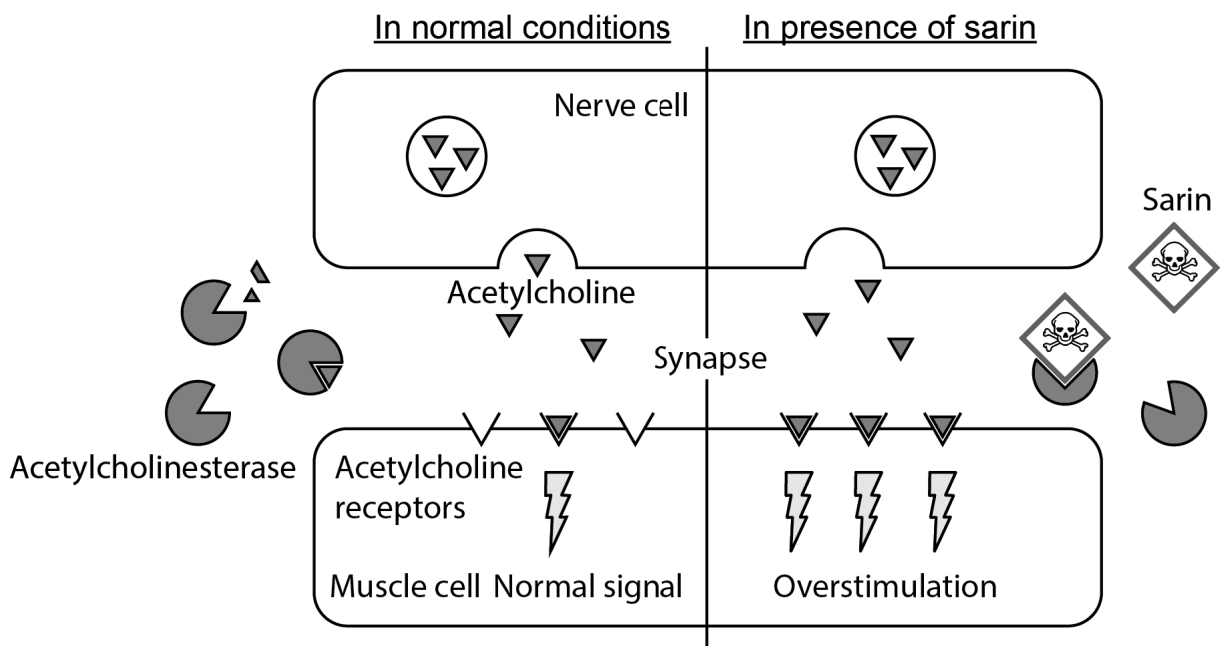


Figure 1.2: Schematic diagram of a neuromuscular junction in absence and in presence of the sarin nerve agent.

Figure 1.2 represents how a neuromuscular junction works in normal conditions and under exposure to a nerve agent, *e.g.*, sarin. First, in normal conditions, the nerve cell releases ACh in the space separating the nerve cell from the muscle cell (or any other cells having ACh receptors), which is called the synapse. Upon binding to the specific receptors of the target cell, an electrical signal is released. The AChE acts in order to

²A chemical that carries messages from nerve cells to other nerve cells or muscles.

³A connection between two nerve cells.

prevent overstimulation, and by doing so, controls the biological system it is responsible of. Second, when exposed to sarin gas, the latter binds to the only active site of AChE, irreversibly inhibiting it from regulating the ACh-induced stimuli, resulting in an overstimulation [10]. This overstimulation leads to various clinical effects: 1) muscarinic effects include miosis, hypersecretion from bronchial glands, vomiting, incontinence and bradycardia; 2) nicotinic effects include fasciculations, muscle twitching and flaccid paralysis. Death usually occurs by respiratory failure from depression of the respiratory centre, paralysis of the respiratory muscles, and bronchoconstriction [5].

According to the level of concentration and the exposure time, physiological effects are different. Acute Exposure Guideline Levels (AEGLs) are values that describe the expected effects on human health after exposure to CWAs from a given concentration. Table 1.1 presents the AEGLs values of sarin in parts-per-billion (ppb) [11]. These values are also goals for sensors in terms of limit of detection (LOD) according to a response time.

Classification	10 min	30 min	1 h	4 h	8 h
AEGL-1	1.2	0.68	0.48	0.24	0.17
AEGL-2	15	8.5	6.0	2.9	2.2
AEGL-3	64	32	22	12	8.7

Table 1.1: AEGLs in ppb of sarin. AEGL-1, -2 and -3, respectively mean nondisabling, disabling and lethal.

From the table, we first understand how dangerous sarin, and nerve agents overall, are, as an exposure of 64 ppb is sufficient to kill within minutes, compared to 1700 parts-per-million (ppm) for carbon monoxide. Second, we conclude that a sarin sensor must detect at least 64 ppb and at best 170 parts-per-trillion (ppt) to operate in field conditions, which may differ from laboratory conditions in terms of temperature, humidity, dust and weather conditions.

Working with CWAs

Due to its extreme toxicity, working with sarin is highly dangerous and only dedicated laboratories are authorised to work on it. Consequently, research on nerve agents often use simulants for experiments in order to achieve a proof of concept. The ideal simulant is a molecule that would mimic every property of a CWA (chemical, physical and biological), except for its toxicity. Yet this cannot be achieved, therefore, a simulant must be adequate to the method of detection for which it acts as a calibration vector [12]. Depending on the detection method, the choice of a simulant is based on its chemical structure, its spectral response, its chemical reactivity, or its physical properties. The most commonly used simulant of sarin for optical detection is the dimethyl methylphosphonate (DMMP), due to its low toxicity compared to sarin, low cost, high vapor pressure, similar chemi-

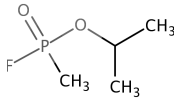
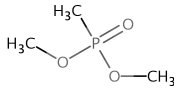
Specifications	Sarin	DMMP
Chemical formula	$C_4H_{10}FO_2P$	$C_3H_9O_3P$
Chemical structure		
Molar mass	140 g.mol ⁻¹	124 g.mol ⁻¹
Vapor pressure (P_{atm})	2.9 mmHg @20 °C	2.4 mmHg @25 °C
Melting point	-56 °C	-50 °C
Boiling point	158 °C	181 °C
Solubility in water	Miscible	Slowly hydrolyses
Appearance and odor	Clear colourless liquid and odorless	Colourless liquid and sweet odour
Risks	Toxic	Harmful and health hazardous
LD ₅₀ (rat)	39 µg.kg ⁻¹ intravenous	8 g.kg ⁻¹ oral

Table 1.2: Chemical properties: a comparison between sarin and DMMP.

cal structure and infrared absorption spectrum [13]. This is why, in this research work DMMP has been selected.

In table [1.2], the chemical structure along with various chemical parameters of sarin and DMMP are represented. Both molecules have similar structures, sharing a central phosphorus atom double-bonded to an oxygen atom $P=O$, and bonded to a methyl group CH_3 , as well as to an oxygen atom, itself bonded to a methyl group. The main difference between the two molecules is the single bond between phosphorus and fluorine atoms. This bond is one of the causes responsible for sarin potency, as well as, soman, cyclosarin, ethylsarin and GV.

1.1.2 CWAs detection: state of the art

In this section, different methods of detection, first commercially available, and second, experimental methods reported in the literature will be presented. When addressing detection, it is important to keep in mind numerous detector requirements, with various degree of importance depending on the application. These requirements include selectivity, sensitivity, response time, compactness and portability, set-up, warm up and recovery time, calibration, ease of use, training requirements and power consumption.

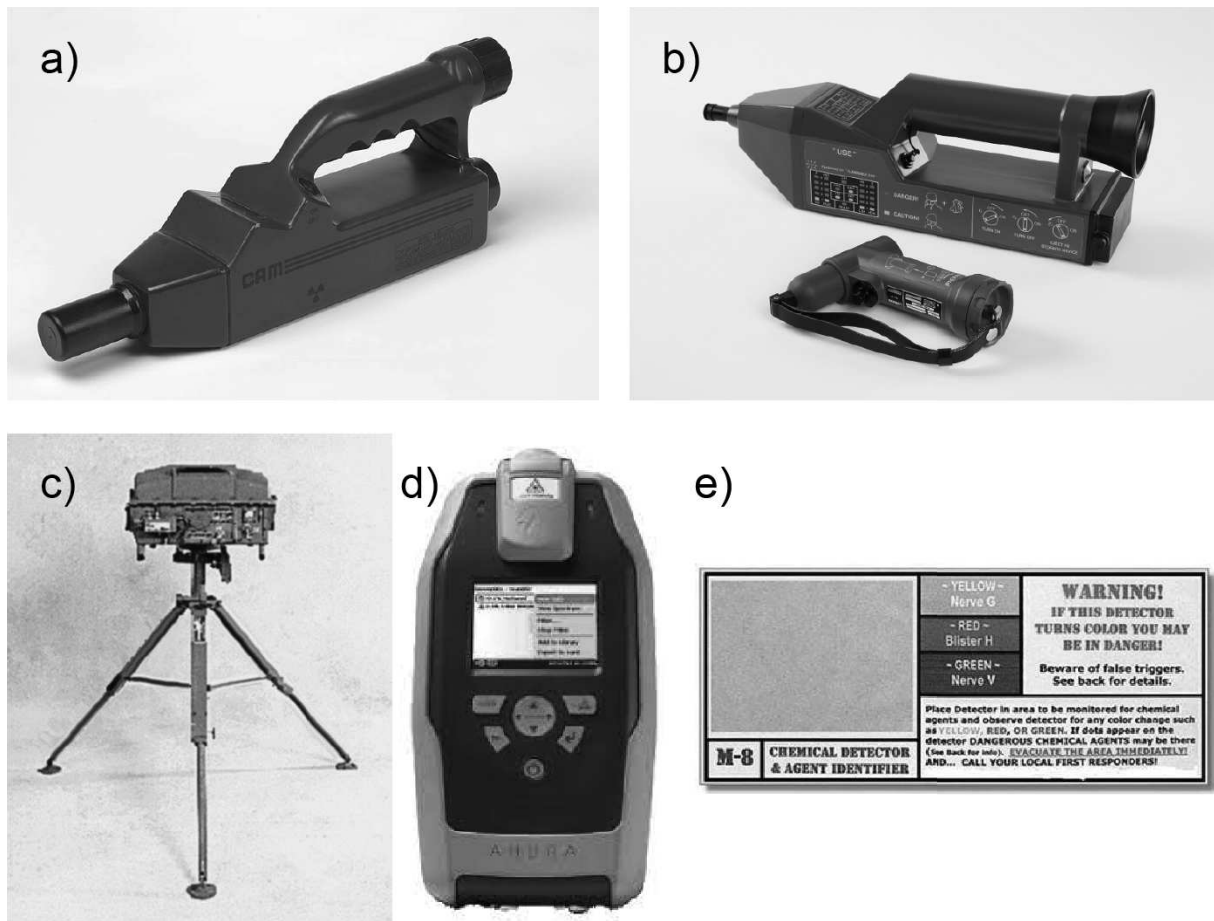


Figure 1.3: CWAs commercial methods of detection: a) IMS Chemical Agent Monitor, b) FPD Proengin SA AP2C, c) IR detector M21 Remote Sensing Chemical Agent Alarm, d) Raman detector Ahura FirstDefender and e) M8 detection colorimetric paper [14].

Commercial detection methods

Commercial detection methods of CWAs include infrared (IR) spectroscopy, Raman spectroscopy, colorimetry, ion mobility spectrometry (IMS), flame photometry (FPD), surface acoustic wave (SAW) devices, photo-ionisation detection and flame ionisation detection. For each of these detection techniques, several equipments have been developed and commercialised, thus, for the sake of conciseness, the most commonly employed devices are described in a non-exhaustive way [14, 2]. Figure 1.3 shows the most employed equipments for on-field detection of CWAs. These devices are, for the most part, hand-held and easy to operate.

IMS-based detectors are the most commonly deployed detectors for the monitoring of chemical substances by the military. Additionally, they are widely employed in airports for the screening of luggage to detect the presence of explosives and drugs. The Chemical Agent Monitor was the first mass produced, hand-held instrument for the detection of nerve and blister agents (figure 1.3(a)). The reason for its success is based on its ease of use, its portability, its price and it can detect nerve agents below AEGL-2 levels (< 5 ppb)

with a rapid response on the order of few seconds. Few disadvantages include poor selectivity and subject to interferences, both sources of false positive alarms, plus it is prone to saturation which leads to signal saturation, contamination and long clearance time [15]. Environmental conditions may have significant impact on the performance of IMS-based detectors [16].

FPDs are mostly found in laboratories coupled to gas chromatography (GC). GC-FPD is used to determine CWAs concentrations in samples for confirmatory analysis [17]. The most notable on-field and hand-held FPD is the Proengin SA AP2C (figure 1.3(b)). It is simultaneously sensitive to both phosphorus and sulfur containing compounds, with a fast response time and a limit of detection (LOD) on the order of ppb. It recovers after chemical exposure and is reliable under extreme environmental conditions (temperature and humidity). The main drawback of this equipment is that it only detects compounds containing phosphorus and/or sulfur [18]. In addition, because of this characteristic, it is difficult to discriminate between molecules like soman and sarin for example, which is an important criterion to apply a dedicated treatment strategy to the patient suffering from OP poisoning.

Raman spectroscopy is based on the Raman inelastic scattering of molecules under monochromatic light. This technique is non-destructive, and benefits from high specificity by detecting molecule fundamental vibrations with great signal-to-noise ratio and a fast response time. The main disadvantage of this technique is that it suffers from interferences from other analytes, typically because of fluorescence. The Ahura FirstDefender (figure 1.3(d)) is one of the few Raman-based detectors for field applications and it has been tested under 88 different cases of exposure with a success rate of $\sim 89\%$, failing in case of fluorescence, exhibited from cyclosarin and mustard gases [2].

Just as Raman spectroscopy, SAW detectors are relatively new as commercial products. They are a class of microelectromechanical systems, commonly known as MEMS. They are inexpensive, which would make a popular choice for civilian applications. This technology can be viewed as a very sensitive balance, that can be miniaturized and have fast response time. Still, it is not intrinsically selective, therefore this technique requires a coating in the form of polymers or surface chemistry to capture and adsorb analytes on the surface. This comes with many drawbacks in terms of selectivity, reproducibility and sensitivity under environmental conditions, affecting the detector performance. Few SAW-based commercial products were independently evaluated (for example, HAZMAT-CAD) and those who were are still far from standards for on-field applications, yet, this is a promising technology and it is highly studied in laboratories.

IR spectroscopy is a well-known technique for its ability to identify with precision the molecular structure of a compound, through excitation of its vibrational modes. The result is a spectrum relative to the molecule absorption according to its fingerprint. It is an intrinsically highly selective technique, as one can directly target characteristic chemical bonds of nerve agents, *e.g.*, phosphorus-oxygen (P-O, P=O), phosphorus-fluorine (P-F), and phosphorus-sulfur (P-S). Also, this technology is based on optics, which benefits greatly the response time and is non-destructive with minimal, if any, sample preparation. Still, this technology suffers from several disadvantages: cost, complexity, training, bulkiness and it is sensitive to environmental conditions like vibrations, snow, rain and dust. An example of this kind of technology and based on passive IR detection is presented in figure [1.3\(c\)](#): the M21 Remote Sensing Chemical Agent Alarm. Others IR detectors technologies include photoacoustics, filter, and differential [\[17\]](#). This equipment is also interesting compared to the rest as it can detect clouds of CWAs up to 5 km, along a 60° arc, and it has the ability to automatically scan and monitor a surrounding area. Still, its sensitivity lacks compared to other technologies, with a LOD of 10 ppm.

The last commercial method presented is the colorimetry, coming in the form of detection tubes or papers, they are by far the fastest, cheapest, lightest and easiest type of detector to use on-field. The main disadvantage is that the detection relies on the user colour perception, which may be affected or different for each user. The M8 detection paper is a commercial example of this technology figure [1.3\(e\)](#). It is widely used because of the mentioned pros. This type of paper works like well-known pH indicator papers, but it suffers from a lack of specificity and false positives. The performance of the presented techniques are summarised in table [1.3](#).

CAM	FPD AP2C	IR M21	Raman First-Defender	SAW HAZ-MATCAD	Colorimetry M8 paper
, blis- chocking erve	Nerve	Nerve and mustard	CWAs	CWAs	G, H and VX
D re- nents	~ ppb	10 ppm	N/A	IDLH levels ^[4]	100 µL drops
	< 2 s	line of sight-dependent	15 s	20-120 s	30 s
held < 2	Handheld < 2.5 kg	Vehicule mountable ~ 20 kg	Handheld < 1.5 kg	< 1 kg	Handheld

ve summarising table of commercial CWAs detection methods. N/A stands for not available.

th limits: concentration of a chemical in the air to which healthy adult workers could be exposed (if their respirators fail) aining health effects.

Despite the diversity of detectors commercially available, research is still abundantly produced to further improve the state of the art and develop novel technologies and strategies to compensate for the disadvantages of commercial techniques. The most encountered drawbacks are a lack of selectivity and sensitivity, respectively leading to false positives and false negatives.

IR spectroscopy is a technique that is intrinsically selective as it probes the fingerprint of multiple molecules in a complex environment, plus it is quite sensitive as shown by the previously presented equipment. Plus, having the ability to improve this technique sensitivity will equally ameliorate its selectivity. This research work focuses on such challenge, while addressing other sensor problematics that include miniaturisation, a fast response time and reproducibility. In the next section, we introduce the different techniques actively studied as promising technologies beside the one developed in this work.

Experimental methods of detection

Recent developments reported in the literature for the detection of CWAs and their simulants, both in terms of techniques and strategies employed to improve them, are hereby introduced. The figure [1.4\(a\)](#) represents some of the most employed technologies in the literature for the sensing of CWAs over the past 5 years. This graph highlights how plasmonics may be underappreciated as a mean to detect CWAs, over traditionally used techniques such as Raman spectroscopy, GC-MS and colorimetry. Still, we observe that sensors, based on fluorescence, luminescence and novel optical probe techniques, dominates the field. Plasmonics presents numerous advantages compared to other techniques as, first it can drastically improve the optical response of a sensor, second it paves the way to miniaturisation and, finally, coupled to IR spectroscopy, it further contributes to ameliorate the selectivity.

One of the main challenges to improve the sensitivity of sensors is that it relies on efficient and selective interactions between the target molecules and the sensor itself. For example, an optical transducer⁵ is limited by light-matter interactions, which may be intrinsically selective but their sensitivity is related to the path length within which interactions take place. Strategies employed to improve the sensing abilities of techniques, such as surface chemistry (*i.e.*, functionalisation) are as important as the techniques themselves. Those include: metal-organic frameworks (MOFs) [19, 4], molecular imprinted polymers (MIPs) [20], cavitands [21], self-assembled monolayers (SAMs) [22, 23], nanoparticles [24, 25], metal oxides [26], zeolites [27], porous materials [28], carbon nanotubes [29] and hydrogel films [30]. These materials, coming in the form of coating, have

⁵A device for producing an electrical signal from another form of energy such as pressure, temperature, optics, etc.

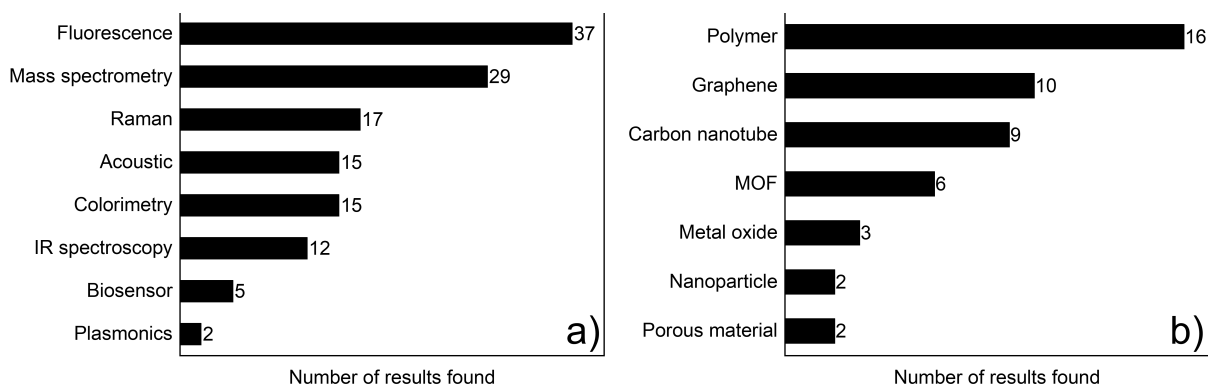


Figure 1.4: Number of results obtained from the website Web of Science, as of July 2023, over the past 5 years, a) with the keywords ‘sensing’ or ‘detection’ in the title, ‘chemical warfare agents’ in the abstract and the mentioned sensing techniques in the text, and b) with the keywords ‘sensing’ or ‘detection’ in the title, ‘chemical warfare agents’ and the mentioned surface chemistry in the abstract.

the ability to bind, host, or interact selectively with CWAs and adsorb them at the surface of the detector in order to improve the interactions between the detector and molecules by increasing the amount of CWA molecules over time in the vicinity. Figure 1.4(b) sums up some of the most mentioned surface chemistry strategies in the literature. It is important to note that most of these strategies have already been combined with plasmonics to further ameliorate a detector’s response towards CWAs [20].

The ramping number of references with great diversity of surface chemistries illustrates the increasing interest for sensor-matter interactions enhancing strategies. Still, each of these chemistries has pros and cons. For example, MOFs and cavitands are difficult to synthesize, stabilize and despite the fact that they can be engineered toward a targeted molecule, they still act as sponge and environmental water remains a problem [31]. Metal oxides constitute a large class of materials that have been reported to interact with CWAs and their simulant, yet it is not clear which mechanisms are at play on the molecular level at the surface, making it difficult to design layers reacting with specific molecules [32]. Concerning SAMs, they are one of the most promising approaches. These molecules, characterized by anchor and terminal functions, are stable over time and tunable in terms of length, anchor and terminal functions. Still, they suffer from difficulties such as the complexity to confirm the layer grafting, and additionally they may also have ‘over-grafting’ issues ending up in stacking rather than the desired monolayer. Porous silicon and zeolites are emerging and therefore lack understanding and hindsight [32].

Focusing more on optical transducers, a second strategy to improve a sensor’s performance is to employ cavities. A cavity is a system within which the interaction taking place is multiplied. Hence, an optical cavity can be considered as (i) a system within which light travels back and forth, artificially increasing the path length according to the

number of round trips; or as (ii) any system within which the interaction is concentrated and enhanced [33]. About the latter, cavities are often found in the form of resonators, *i.e.*, a system that displays a resonance which is exploited to increase the detector response. Their use increased over the last years with the development of multiple different resonators including photo-acoustic resonators, plasmonic particles, or any shape structured in a way to obtain a resonance that can interact with light and/or molecules [34]. We will discuss in further details such systems in the next part of the first chapter. In this context, plasmonics stands as a promising solutions as it can act both as a transducer and a cavity resonator that would benefit sensitivity and selectivity when coupled to infrared or Raman spectroscopies.

Plasmonics has been exploited for the detection of numerous chemical threats [35, 20], such as the detection of atrazine [36], mercury [37], heavy metal ions [38], 1, 4-dioxane [39], diethanolamine [39], sulfur mustard (HD) [40], 2-chloroethyl ethyl sulfide [19], and OPs such as methylphosphonothioic acid (VX) [40], DMMP [41, 19, 21], paraoxon [25], chlorpyrifos [42], and 4-methylumbelliferyl phosphate [30]. It is important to note that, besides the fact that these reported sensing results are based on plasmonic effects, they differ in their practical application as well as in terms of ‘plasmonics’, meaning that they bring into play different ways of taking advantage of plasmonic effects. This can be appreciated by the different units reported as LOD. Indeed, a SPR-based sensor typically uses RIU⁻¹ unit because this type of sensor is based on the sensing of refractive index variations, as opposed to SERS methods that quantify their results in absolute and relative concentrations. These results are summarised in Table 1.4.

Targeted chemical	LOD
Atrazine	10 ⁻¹² g.mL ⁻¹
Mercury	58 pM
Heavy metal ions	~ μM
1,4-dioxane and diethanolamine	50,000 nm.RIU ⁻¹
VX	2.5 × 10 ⁻³ μg.mL ⁻¹
Mustard gas	1.8 × 10 ⁻³ μg.mL ⁻¹
DMMP	16 ppb [21], 130 ppb [41] and 2.5 ppm [19]
Paraoxon	80 μM
Chlorpyrifos	55 ng.L ⁻¹
2-choloroethyl ethyl sulfide	76 ppb
4-methylumbelliferyl phosphate	1 mM

Table 1.4: Limit of detection of various chemical threats for different plasmonic-based systems.

In conclusion, OPs are extremely toxic molecules which can be used on civilian territory or warzone. It is crucial to develop dedicated sensors to detect them with high selectivity and sensitivity in order to anticipate their use and protect civilians and mil-

itary forces. Commercially available methods, covering a wide range of techniques, give us a grasp of a detector requirements for on-field applications. Experimental methods developed these past few years show that a sensor's performance are not only governed by the sensor's intrinsic sensitivity anymore, but are also strongly dependent on strategies employed to ameliorate important features, especially sensitivity, selectivity and response time. Finally, we report numerous studies attesting that plasmonics is a relatively recent and promising way to design a sensor for CWAs detection, either as a transducer or as a strategy to improve the sensor's response through enhancing effects.

On these bases, we know that the development of a new plasmonic device must fulfill specific requirements in terms of sensitivity, selectivity and response time, and how it should compare to existing methods in terms of price, portability and reuse. This is of particular importance for military applications as the developed sensor must selectively detect ppb-level traces of OPs, handheld and easy to use. The next two sections will respectively address plasmonic theory and the strategy to improve its response, namely the epsilon (ϵ)-near-zero (ENZ) medium.

1.2 Part two: Plasmonics fundamentals

1.2.1 Fundamentals

Basics of electromagnetics

Before diving into the heart of plasmonics, we introduce in this brief section the fundamental laws of electromagnetism and relations required to understand the following sections. First, the plasma model which describes the optical properties of metals, considering their free electrons density as an electron gas or a plasma^[6], is introduced. The starting point equation is the equation of motion x , for an electron of charge e and mass m , of the plasma under an external electric field E , defined by equation [1.1] with γ the damping rate taking into account plasma losses from the free electrons collisions.

$$m\ddot{x} + m\gamma\dot{x} = -eE \quad (1.1)$$

Assuming a harmonic time dependence of the driving field, it can be shown that the free electrons density governs the optical properties of metals such that we obtain the dielectric function, as follows by equation [1.2].

$$\epsilon(\omega) = \epsilon_\infty \left(1 - \frac{\omega_p^2}{\omega^2 + i\gamma\omega} \right) \quad (1.2)$$

With ϵ the permittivity, which describes the polarisability of the material under an external electric field, such as light, of frequency ω . ϵ_∞ characterises the deformation of the lattice ion cores, resulting in a residual polarisation. The screened plasma frequency ω_p is defined in equation [1.3] as the natural oscillation frequency of the free electrons constituting the plasma. In the rest of the manuscript, we refer the screened plasma frequency simply as the plasma frequency.

$$\omega_p = \sqrt{\frac{Ne^2}{\epsilon_\infty\epsilon_0m^*}} \quad (1.3)$$

With N the free electrons density, ϵ_0 the vacuum permittivity and m^* the effective mass of the electrons. The derivation of the electron motion up to the dielectric function is known as the Lorentz-Drude model.

Overview of plasmons

Plasmonics is the field that studies the interactions between electromagnetic waves and free carriers within matter. Free carriers most of the time refer to unbounded electrons that are found often in metals, hence plasmonics is intimately linked to metals as they are, historically and practically, the most common media encountered in the literature.

⁶A free charge carrier gas.

Upon excitation by light, the free electrons which form a plasma can be excited and, in result, will oscillate. Plasma oscillations carry a surface wave propagating along a metal/dielectric interface, known as surface plasmon-polaritons (SPP). To clarify, plasmons are plasma oscillation quanta while polaritons are photons coupled to matter, *i.e.*, dipole excitation or charge density wave. This description informs about, first the considered elementary excitation in solid matter: plasmon, phonon, exciton⁷, polaron⁸, etc., and second, the mean of excitation considered: polariton (light), phonon, but they could also be excited electrically or using an electron beam.

We herein discuss the different kind of plasmons, summarised in table [1.5](#). First, plasmons are either ‘pure’, meaning only the collective charge oscillations are considered, but they are not of interest as, being longitudinal electric waves, they cannot couple to transverse waves (light). Either, plasmon-polaritons are mixed plasmon-photon excitations and they are electromagnetic modes that can be considered either within the bulk or at the surface of the free carriers-containing material. Therefore, it comes to light why the term surface is of importance, as SPPs would not exist without the metal/dielectric interface and their properties depend on the optical properties, *i.e.*, the dielectric function [1.2](#), of both materials.

	Pure plasmon	Plasmon-polaritons
Bulk modes	Pure bulk plasmon: a collective oscillations of the plasma charge density that occurs at the plasma frequency.	Bulk plasmon-polaritons can be viewed as photons whose properties are modified by the interactions with the electrons of the metal.
Surface modes	Pure surface plasmon is a mathematical approximation given that the light contribution is negligible.	Surface plasmon-polaritons are either ‘propagating’ or ‘localised’, they concern the vast majority of plasmonic applications.

Table 1.5: Overview of the different plasmons.

SPPs are electromagnetic modes sustained at the surface of metals and they are associated with surface charge oscillations with a dual nature: plasmon-photon. They can either be ‘propagating’, or ‘localised’. The difference between propagating surface plasmon-polaritons and localised surface plasmon-polaritons (LSPs) lies in the fact that LSPs occur when the size of the plasmonic material becomes comparable or smaller than the light wavelength. It is the case for small metallic objects, such as nanoparticles or nanostructures resulting from nanoscale surface patterning, and this condition completely changes the nature of the electromagnetic modes [\[43, 44\]](#). The canonical example of the metallic sphere is well-understood from the Mie theory, but it is less trivial for other

⁷A bound state of an electron and an electron hole attracted to each other by the electrostatic Coulomb force.

⁸A quasiparticle composed of a charge carrier coupled to a polarisation field.

configurations, involving multilayers and antennas of complex shapes, due to the lack of analytical solutions [45, 46].

Surface plasmon-polaritons

SPPs are a central part of this topic of research as they are the excited and employed plasmonic modes for surface-enhancing effects. As previously mentioned, these modes occur at metal/dielectric interfaces. Different configurations give rise to these modes, but first we will discuss the standard case of a planar metal/dielectric interface, represented in figure [1.5].

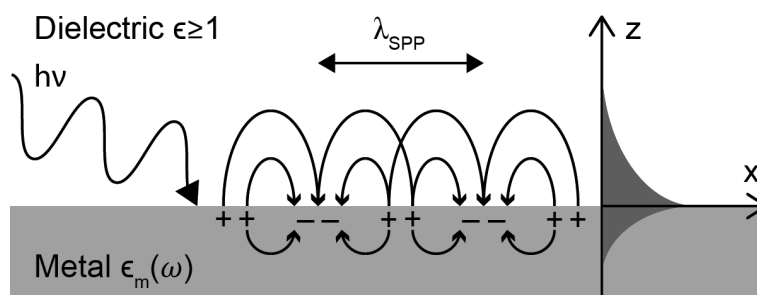


Figure 1.5: Schematic diagram representing SPPs propagating along the metal/dielectric interface, upon excitation by an impinging electromagnetic wave $h\nu$. SPPs are associated with an evanescent field at the interface, exponentially decaying.

From Maxwell equations and the Helmholtz equation, it can be shown that transverse magnetic (TM) solutions lead to the dispersion relation (equation [1.4]) of SPPs propagating at the interface between two half spaces. The dispersion relation is a representation holding much information on the electromagnetic modes permitted within a structure, therefore it depends predominantly on the optical properties of the materials composing the structure, namely, plasmonic materials when talking about plasmonic modes.

$$k_x = k_0 \sqrt{\frac{\epsilon_1 \epsilon_2}{\epsilon_1 + \epsilon_2}} \quad (1.4)$$

With k_x the electromagnetic mode wavevector along the x-axis, *i.e.*, at the metal/dielectric interface, k_0 the light wavevector in free space, ϵ_1 and ϵ_2 the respective permittivity of the metal and the dielectric, which implies $\text{Re}(\epsilon_1) < 0$ and $\text{Re}(\epsilon_2) > 1$ in the classical case. Second, it can be shown that transverse electric (TE) solutions are equal to 0, having for consequence the fact that SPPs only exist under TM-polarised light. Therefore, SPPs are TM-polarised transverse electromagnetic waves, considered as guided modes along the metal/dielectric interface, decaying evanescently both in the metal and the dielectric.

The figure [1.6](a) represents the dispersion relation governed by equation 4 for a simple bilayer system (figure [1.5]). Two different cases are considered, the first case figure [1.6](a)

is a perfect metal/dielectric interface, respectively characterised by $\epsilon_1(\omega)$ and $\epsilon_2 = 1$. In this case, we do not consider any plasma losses, nor background permittivity, so that $\gamma = 0$ and $\epsilon_\infty = 1$. For $\omega > \omega_p$, the wavevector is real so that propagation is allowed, *i.e.*, light travels through the material because the metal does not screen incident light which means that it is dielectric. $\omega_{sp} < \omega < \omega_p$ is a frequency gap, known as the quasibound region, within which the wavevector is purely imaginary, prohibiting any propagation. ω_{sp} is the surface plasmon frequency at higher wavevectors ($\omega_{sp} = \omega_p/\sqrt{2}$). Finally, $\omega < \omega_{sp}$ is the frequency range of interest for which the wavevector is real, although the material is metallic and therefore it should screen any incident light and cancel its electric field. Still, electromagnetic modes are permitted and they correspond to SPPs at large wavevectors and Sommerfeld-Zenneck waves at smaller wavevectors, near the light line [47].

The second case (figure 1.6(b)) presents the case of a real highly-doped semiconductor, with a background permittivity $\epsilon_\infty = 12$ and plasma losses $\gamma \neq 0$ considered. We observe several differences with the first case. First by taking into account plasma losses, the surface plasmon frequency ω_{sp} is not anymore an asymptote and SPPs approach now a maximum at a finite wavevector. Second, the quasibound region $\omega_{sp} < \omega < \omega_p$ is now allowed. Third, the frequency gap of the quasibound region is much narrower when considering the background permittivity. These differences highlight how ‘real’ vs ‘perfect’ cases differ and for a given problem, much care must be taken when assumptions are considered to simplify the problem.

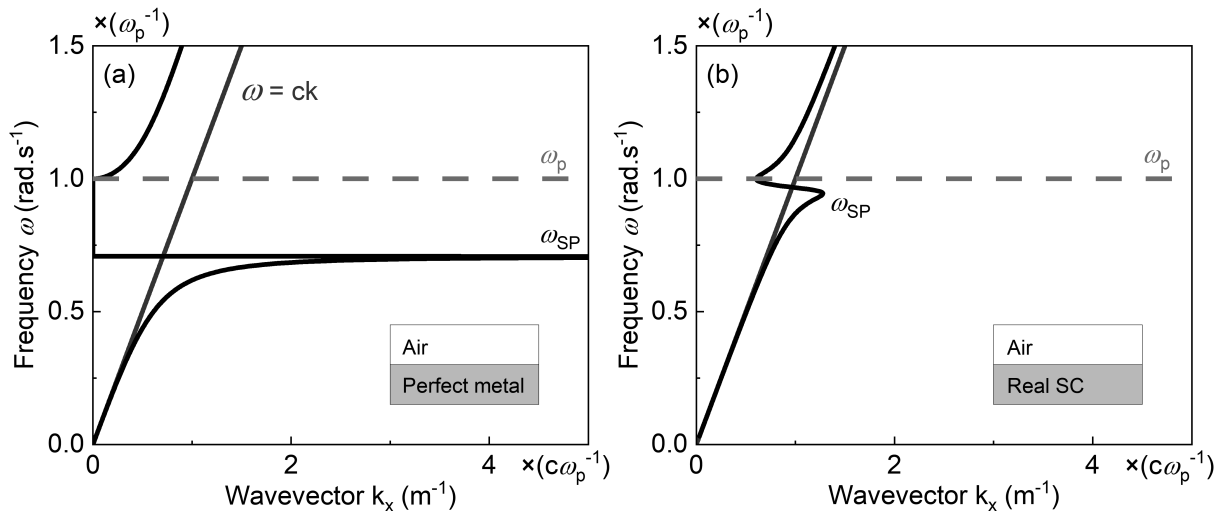


Figure 1.6: Dispersion relations of (a) a perfect metal/insulator interface and (b) a real doped semiconductor/insulator interface. The insets represent a schematic diagram of the considered case. Plasmonic modes occur below the plasma frequency ω_p (red dashed line) and on the right side of the light line $\omega = ck$ (blue line).

Recent developments in plasmonics introduced novel metamaterials, hyperbolic materials, complex stacking of structures, etc. These systems are multi-layered and demand a

more rigorous mathematical treatment that gets, very quickly, increasingly complex and tedious, we will come back to these structures in chapter 3.

Plasmonic materials

In this section, a non-exhaustive review of the different plasmonic materials and their associated frequency of operation is presented. By plasmonic materials, we assume any material with a free charge carrier density. To date, a wide variety of materials have been used from noble metals to materials like ceramics, semiconductors and oxides.

By far, noble metals are historically and practically the most commonly encountered plasmonic materials in the literature with for example gold [48], silver [49], copper [50], and aluminium [51]. The large losses of metals hinder their practical use and is the main reason for the development and research for new plasmonic materials.

III-V semiconductors (SCs) are promising plasmonic materials as (i) they can be coupled to a wide variety of technologies in electronics and optoelectronic devices [52] and are CMOS-compatible, (ii) their plasma frequency can be tuned according to their doping level, and (iii) they have low losses in the mid infrared (MIR) compared to noble metals, which benefit applications like sensing. The diversity of these materials offers various optical bandgaps, which can further be controlled by varying the composition within ternary and quaternary compounds. As plasmonic devices mature, upcoming challenges concern their integration within complex systems, monolithic devices, and photonic integrated circuits; in this regard, III-V SCs are excellent candidates because they are compatible with the silicon industry [53, 54, 55]. We report the employment of GaAs [56, 57], InP [56, 57], InAs [58], InGaAs [59], GaN [60], GaSb [61], InAsSb [62] and InSb [63, 64].

Transparent conducting oxides (TCOs) [65] such as zinc oxide (ZNO) [66], cadmium oxide (CDO) [67], indium-tin oxide (ITO) [68], gallium:zinc oxide (GZO) [69], and aluminium:zinc oxide (AZO) [70] are alternative near-infrared (NIR) plasmonic materials. Besides, a vast diversity of different oxides: ternary [71], perovskite [72] and non-stoichiometric [73, 74] have been reported. Finally, the demonstration of plasmons in graphene [75], with the significant attention it benefited [76], led to the development of 2D plasmonic materials [53, 77] or 2D electron gas within semiconductor heterostructures.

It is important to know that beside the development and research for novel plasmonic materials, an alternative approach is to work around the disadvantages of noble metals in order to decrease their optical losses or reduce their carrier concentration [53]. By introducing non-metallic elements into a metal lattice, one creates intermetallic or metallic compounds [78]. A vast amount of research has been produced in this direction, leading to the development of silicides [79], germanides [80], ceramics [81], noble-transition

metals [82] and noble-alkali compounds [83]. While optical losses still remain high due to interband transitions, silicides, germanides and metal nitrides [84] are of interest thanks to their CMOS compatibility and standard fabrication processes.

Figure 1.7 shows some of the most employed plasmonic materials represented as the free carrier density function of the plasma frequency on the electromagnetic spectrum. It is clear that a higher carrier density is associated to a greater plasma frequency, in agreement with equation 1.3, which imposes a constraint on the operating frequency of the material. In that respect, tunable materials in terms of plasmonic response, *i.e.*, plasma frequency, are very attractive compared to noble metals with unchanging carrier density. The ability to dope a material by introducing impurities, and consequently, additional charges, allows to address various spectral regions of the electromagnetic spectrum, and therefore different applications. It becomes possible to exceed the intrinsic limit imposed by the material original properties. Doping is a passive way to tune the plasmonics response, remark that various means permit a dynamic tuning: electrically, thermally, optically, and magnetically [85].

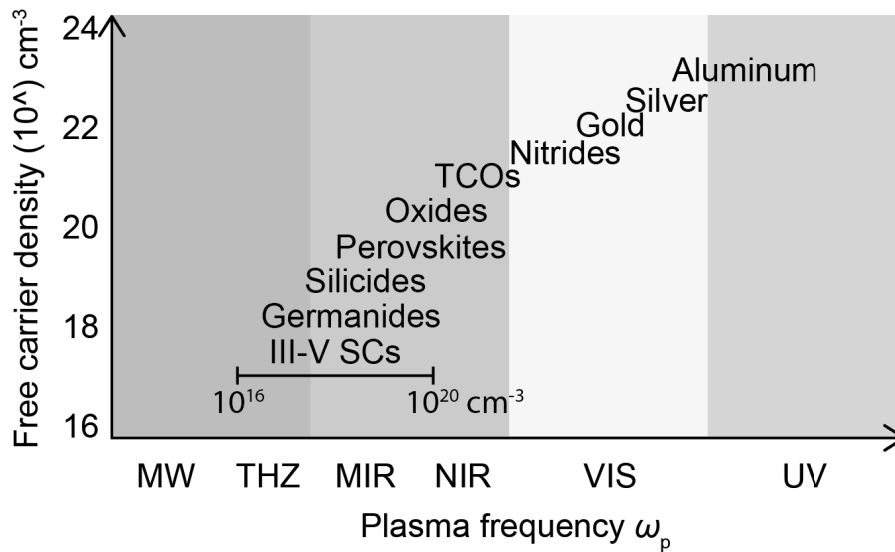


Figure 1.7: Diagram representing the operating frequency of various plasmonic materials characterised by their free carrier density (plasma frequency), as a function of the electromagnetic spectrum.

The choice of a plasmonic material depends on various important parameters such as the frequency imposed by the application, the sensitivity to losses, the need for possible integration, and finally the laboratory facilities available: growth and fabrication techniques. The perfect plasmonic material does not exist. It is a combination of different features that should be taken into consideration when evaluating the trade-off imposed by the desired applications. As the plasmonic material is the first half for the design of

plasmonic devices, picking the right material should also consider the other half: the light coupling method and its associated needs in term of fabrication and implementation.

Plasmonic antennas and the plasmonic resonance

SPPs can be excited in various ways. Indeed, incident light, as it is, cannot couple to the free electrons at the metal surface, this can be appreciated on figure [1.6](#) by the fact that SPP modes lie on the right side of the light line (blue), therefore, even if the light frequency matches that of the SPP, the mismatch in wavevector hinders the light-plasmon coupling. To overcome that, several techniques have been developed to impart the missing momentum, including:

- Total internal reflection generating an evanescent wave with a larger momentum that can be used to excite SPP modes. This method is known as the Otto configuration [\[86, 87\]](#) (figure [1.8\(a\)](#)).
- The Kretschmann configuration was developed based on the same principle but it is easier to implement [\[88, 89\]](#) (figure [1.8\(b\)](#)).
- Highly focused optical beams [\[90\]](#). This technique takes advantage of the high numerical aperture of the objectives, immersed in oil and brought into contact with the metal/dielectric interface, ensuring phase matching and SPPs excitation.
- Near-field excitation allows for local excitation, as opposed to macroscopic excitation of other methods, by the mean of a probe tip with a small aperture size, allowing excitation of SPPs [\[91\]](#).
- Surface roughness or patterning [\[92\]](#) (figure [1.8\(c\)](#)). This method gives a wavevector ‘kick’ to the impinging photons so that their in-plane momentum matches that of surface plasmons, this way photons can transfer their energy to surface plasmons and SPPs arise.

Surface patterning, for practical and scientific interests, became one of the most employed coupling techniques [\[93, 94\]](#). With the development and improvement of fabrication techniques, this method gives additional degrees of freedom over the control of the plasmonic response of the system, as not only the angle of incidence, the wavelength of the incoming light, the thickness of the system layers and the dielectric constant of the materials, influence the plasmonic response. One can now play on the surface geometry in terms of shape and size [\[93\]](#). A variety of plasmonic antennas are presented in figure [1.9](#).

We now introduce the concept of plasmonic resonance which occurs when the light wavevector and frequency match those of SPPs. The coupling is associated with an efficient energy transfer from the light to the plasmonic mode, having a significant impact on the system optical response. This phenomenon is known as the surface plasmon resonance

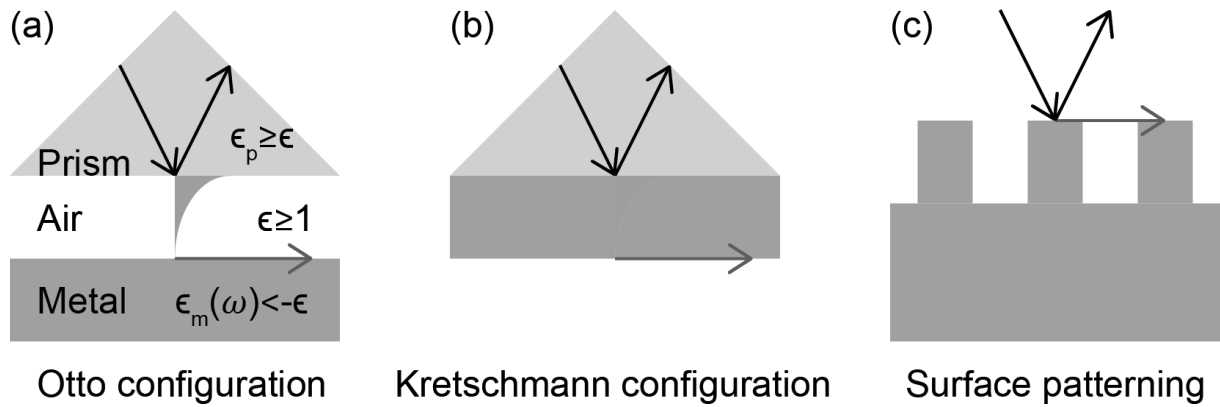


Figure 1.8: Three different light-plasma coupling techniques: Otto and Kretschmann configurations and surface patterning, respectively (a), (b) and (c). Black, blue and red respectively represent the incident light, the evanescent wave and the SPP wave.

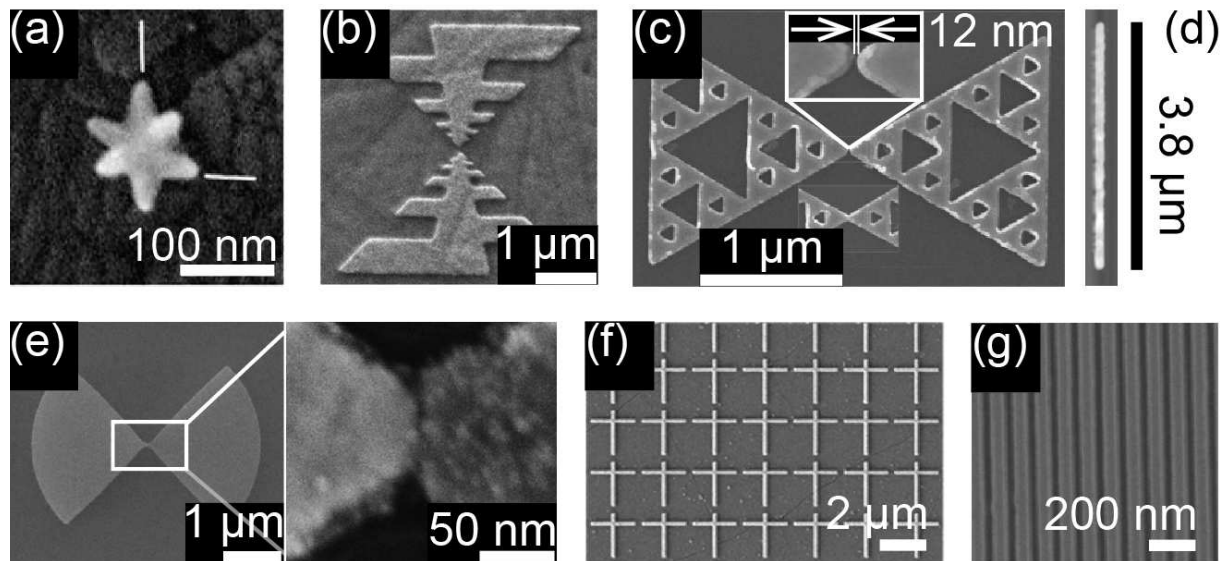


Figure 1.9: Microscopy images of different plasmonic antennas from the literature. An important diversity of antennas shape and size flourished over the years with the development and improvement of fabrication techniques. (a) Nanostar plasmonic antennas [95], (b) multifrequency gold optical antenna [96], (c) Sierpinski triangle for fractal plasmonics [97], (d) gold rod nanoantenna for single antenna plasmonic applications [98], (e) nanogap bowtie gold antenna for SEIRA [99], (f) dual-band perfect absorber for multi-spectral SEIRA [100], and (g) graphene nanoribbons for SEIRA [101].

(SPR). The denomination SPR is sometimes used under different meanings, either as the resonance itself, or as a refractive index sensing technique based on the ‘SPR effect’, *i.e.*, the variation of the refractive index and its influence on the SPR of the system. One should distinguish the SPR from propagating plasmon-polaritons and from LSPs, for the latter, it is named localised surface plasmon resonance (LSPR).

In our study, we will focus on LSPs and their resonance LSPR. The LSPR depends notably on the optical properties of the metal and dielectrics composing the interface, but also, as previously mentioned the shape and size of the surface structure. In the end, the choice of the coupling method also affects the nature of the plasmonic resonance, and depending on the application, one might be preferred [102]. This is the case for spectroscopy enhanced by the surface as the LSPR is associated to a strongly localised and confined enhanced electromagnetic field, widely exploited in the sensing of molecules [103, 44].

Next to SPR-based plasmonic devices, the most encountered plasmonic devices for spectroscopy are based on the LSPR [44], and consequently, a great deal of research has been carried out to understand, optimise and develop highly-efficient surface patterning, also known as nanostructures or simply plasmonic antennas. The main ideas to keep in mind when designing plasmonic antennas are (i) efficient coupling to light, (ii) resonance(s) according to the application, and (iii) highly-enhanced electric field. These conditions are respectively dependent on (i) the set-up and the overlapping between the light spot and the active plasmonic area, (ii) predominantly the size of the antenna, and (iii) the shape of the antenna. Indeed, it has been demonstrated that the LSPR frequency depends on the antenna length (figure 1.10(a-c)), second, rectangular antennas, and overall 2D plasmonic antennas, can display two distinct plasmonic resonances according to the antenna side that is being excited, as it is the case for antennas in figures 1.9(b) and (f). Finally, the shape of a plasmonic antenna has drastic influence over the strength of the enhanced electromagnetic field (figure 1.10(d-f)). The lightning rod effect demonstrates that sharp apexes are associated with a greater spatial confinement and a stronger electromagnetic field [104], as observed in figure 1.10(e,f).

We now understand that upon designing a plasmonic system with an optical response in the infrared, for the sensing of molecules in liquid and gas phase, many different parameters are to be considered. This set of parameters participate in the spectral and spatial response of the sensor, respectively corresponding to the LSPR and the enhanced electromagnetic field.

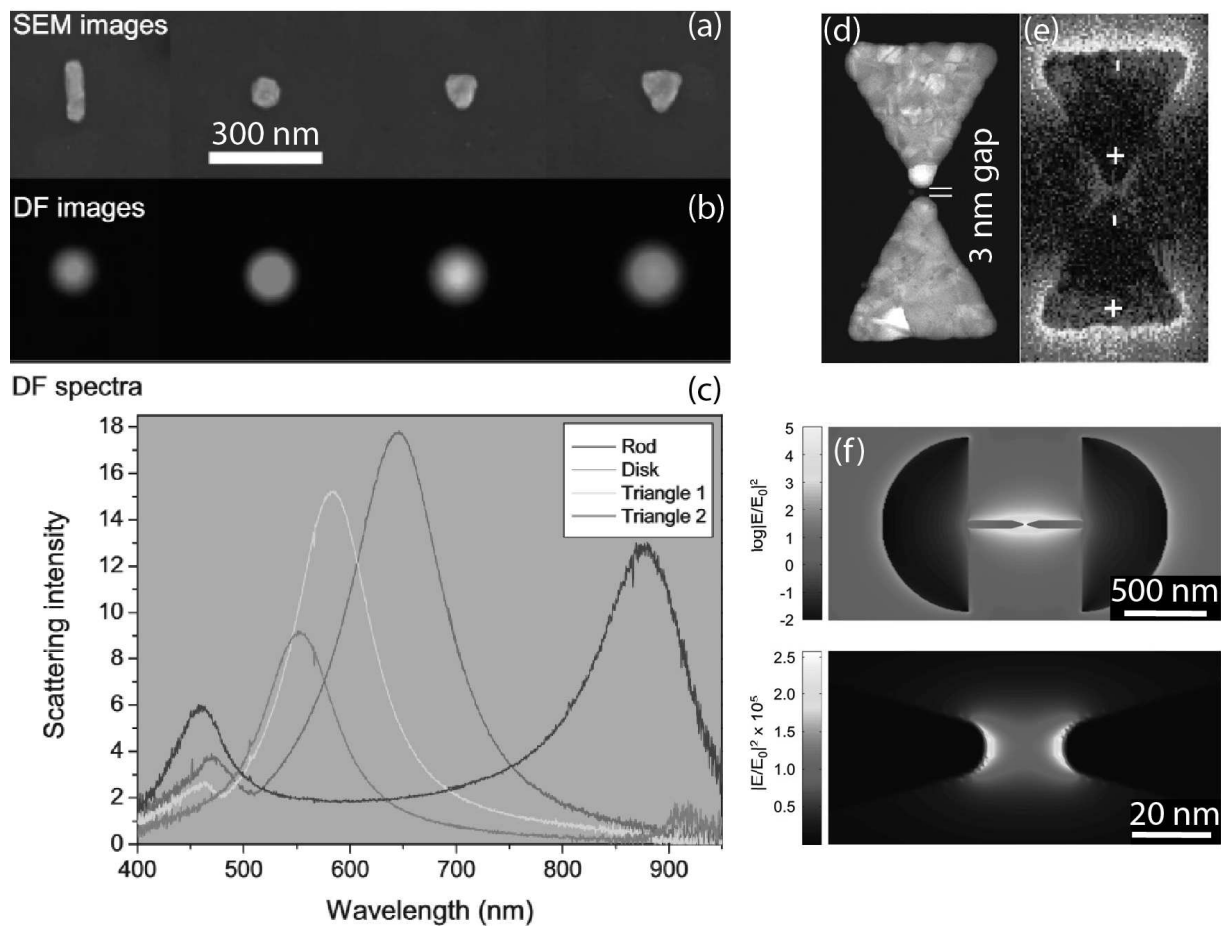


Figure 1.10: (a) Scanning electron image, (b) dark-field image, and (c) dark-field spectra of several gold nanoparticles made by electron-beam lithography. From left to right the shapes are, a rod, a disc, and two triangles of different size [105]. Plasmon coupling of two nanoprisms with sub-3 nm gap: (d) high-angle annular dark field scanning transmission electron microscopy (e) experimental electron energy loss spectroscopy (EELS) map [106]. (f) Typical finite-difference time-domain electromagnetic simulation showing SEIRA enhancement from the electric field maps of a fan-shape gold nanoantenna [107].

1.2.2 Surface-enhanced infrared absorption

Molecular vibrational modes

Molecules are composed of atoms, themselves composed of nuclei and electrons. This system is characterised by multiple energy levels at different scales: electronic levels, vibrational levels and rotational levels. These energy levels are quantised and consequently have discrete energies of the same order as UV/visible, MIR and THz, respectively. Working in the MIR implies that the most encountered transitions from molecules will correspond to their vibrational levels. These levels are associated to the motion of nuclei of the molecule and the so-called vibrations can be understood with a simple harmonic resonator model within which two masses are linked by a spring, respectively two nuclei and the covalent bond. By shining light with energy equal to the difference between two energy levels, absorption may occur (according to the selection rules) and the molecule is said to be excited.

It is important to know that there are plenty of different light-matter interactions but as far as this research is concerned, absorption is of most interest because it is this interaction that we propose to enhance. When excited, a molecule may display various motions known as vibrational modes. For example, valence modes are characterised by a stretching of the spring length (either in a symmetric or asymmetric way), while deformation modes are associated with angle variations of the covalent bond (wagging, twisting, scissoring and rocking). Macroscopically, as a molecule absorbs, light gets attenuated according to the molar absorption coefficient of the molecule ε , its concentration C , and the path length L : it is the Beer-Lambert-Bouguer relation (equation [1.5](#)).

$$A = \varepsilon LC \tag{1.5}$$

Light attenuation A is the main signature in practice, hence, when talking about enhanced infrared absorption, it implies strengthening the light signature as light interacts with a medium through its vibrational energy levels [\[108\]](#). In chapter [2](#), we will address in detail Fourier-transform IR (FTIR) spectroscopy and vibrational modes of molecules. Still, we can observe in figure [1.11](#) the absorption of sarin and DMMP, as a function of the wavenumber, or wavelength, around 1000 cm^{-1} , or $10 \text{ }\mu\text{m}$, respectively. The red dashed line is a fit of Sarin absorption data extracted from the literature [\[109\]](#), and the blue line is the measured absorption of DMMP. We observe that both molecules share their main absorption line in the same spectral range close to $10 \text{ }\mu\text{m}$ [\[110, 109, 111\]](#), which is expected for two molecules with similar chemical structures. This also shows that DMMP is a suitable molecule to be a spectral simulant for sarin.

Surface-enhanced infrared absorption, or SEIRA, is a complex combination of light, molecular vibrations and plasma oscillations, all at resonances. The next section addresses

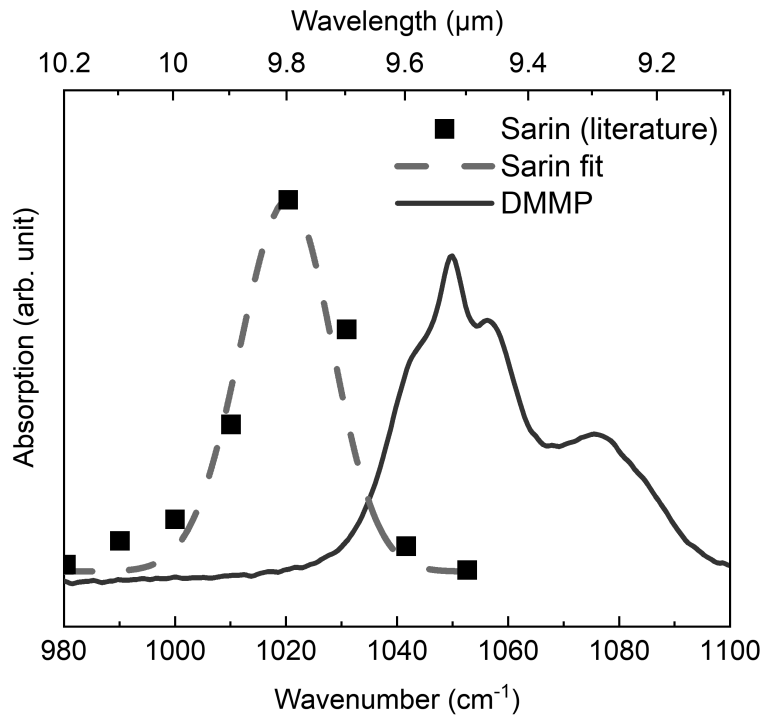


Figure 1.11: Infrared absorption spectra of sarin and DMMP. Sarin data are extracted from the literature [109].

how molecules and plasma interact to produce this enhanced light signature which is the trademark of SEIRA.

Plasmon-molecules interactions

Surface-enhanced Raman scattering (SERS) is a technique that benefited from a lot of attention since its discovery [112]. Although Raman and infrared are the two faces of the vibrational coin, research on the complementary surface-enhanced infrared absorption, now known as SEIRA, was studied at a latter stage. The first report of SEIRA was by Hartstein *et al.* in 1980 [113]. Soon after, numerous works followed and it was soon clear that the enhancement from SEIRA was orders of magnitude below that of SERS. Still, the average cross-section of infrared absorption is about nine orders of magnitude higher than the corresponding Raman, which means that in practice, even small enhancement would lead to interesting results [114].

SEIRA refers to multiple means to enhance the infrared absorption as matter can exhibit different resonances depending on their nature. This is the reason why literature on SEIRA splits into two categories: plasmon-assisted SEIRA, based on the collective oscillations of free charges in matter, and phonon-assisted SEIRA, based on lattice vibrations. Basically, these two branches exploit the electric field associated to the motion of dipoles in matter at resonance. Therefore, as SEIRA can be produced with both metals

and dielectrics, it rapidly developed [115, 116].

The enhancement of SEIRA is a combination of electromagnetic and chemical contributions [117, 94]. The chemical contribution refers to the variations observed on a molecule infrared vibrational signal in terms of frequency and shape, resulting from molecule-plasma interactions [118, 119]. The electromagnetic contribution is attributed to enhanced optical fields and, correspondingly, augmented absorption intensities from plasmons or phonons [114]. Note that such electric field enhancements, not only benefited infrared absorption, but also many other effects and technologies including: fluorescence [120], lithography [121], solar cells [122], and photocatalysis [123].

In practice, SEIRA is associated with two interactions between plasmons and organic molecules: refractive index-dependent plasmonic resonance and plasmon-molecule resonances coupling. In the first case, molecules do not exhibit electronic absorption and the respective resonances of the molecule and the plasma are far apart. Still, we know that plasmons arise at metal/dielectric interface, and its nature (and therefore resonance) depends on the optical properties of both of these media. As molecules adsorb at the surface of the metal, the effective refractive index of the surrounding environment changes, and the plasmon ‘feels’ this variation, and as a consequence, the oscillation of charges will have its restoring force reduced with the increased number of polarisation charges, themselves increasing the screening of the oscillator Coulombic force [124]. This is the principle of SPR-based devices and these devices are sensitive to the variation of the environment refractive index, resulting in a red-shift of the plasmonic resonance [125]. This effect can be appreciated in figure 1.12(a).

In the second case, the plasmonic resonance and a molecule absorption coincide and coupling occurs. From Kramers-Kronig relations, we know that absorption is associated with a strong variation of the refractive index, therefore the first effect explained above also takes place. Besides, the coupling results in a hybridisation of states into a complex system formed by energy transfer between molecules and plasmons. This mixed system has spectral properties drastically different from its two separate constituents. SEIRA originates from this coupling [124], amongst many other applications based on molecule-plasmon interactions such as lasing [126, 127], energy transfer [128] or amplified SPR-based sensors [129]. The second effect, associated to SEIRA, can be appreciated in figure 1.12(b).

SEIRA-based gas sensing: state of the art

Gas sensing using plasmonics has been demonstrated many times [132], yet most of these techniques lack selectivity because they exploit the SPR effect or plasmon-enhanced effects that require a selectivity strategy, *e.g.*, surface chemistry, or fine data analysis and

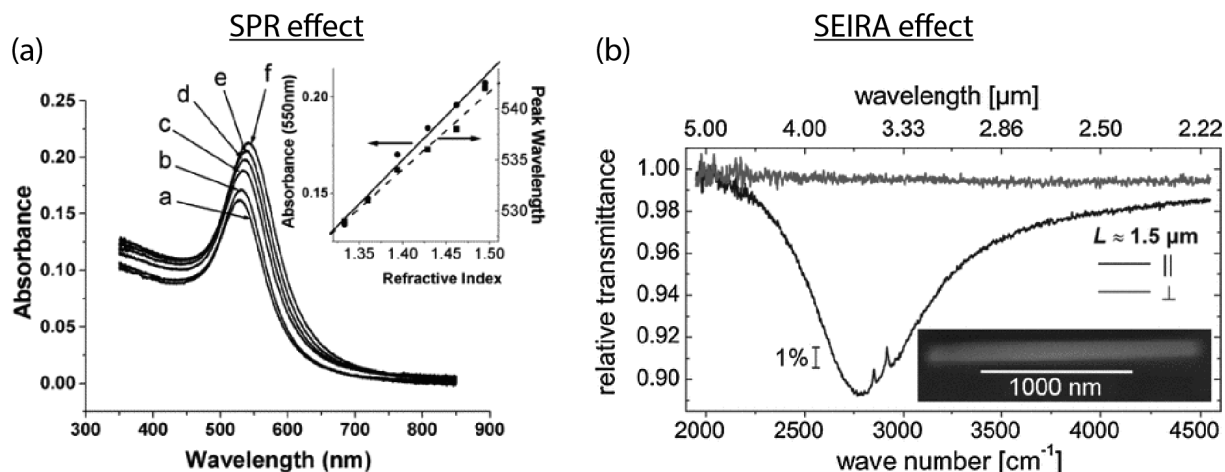


Figure 1.12: (a) SPR effect: Absorbance spectra of a monolayer of immobilized gold colloids on glass in the following: a. water ($n = 1.33$); b. ethanol ($n = 1.36$); c. 3:1 (v/v) ethanol-toluene ($n = 1.39$); d. 1:1 (v/v) ethanol-toluene ($n = 1.429$); e. 1:3 (v/v) ethanol-toluene ($n = 1.462$); f. toluene ($n = 1.495$). The inset shows the dependence of the absorbance maximum as well as the absorbance at 500 nm on the refractive index of the surrounding medium [130]. (b) SEIRA effect: Relative IR transmittance in the spectral region of the fundamental resonance of a gold nanowire, with a monolayer grafted onto, for both polarisations. The inset is a scanning electron micrograph of the plasmonic antenna [131].

treatment [44]. However, SEIRA is intrinsically selective as it targets a molecule characteristic vibrational modes, and therefore, it generates certain interests especially for such specialised application like sensing of CWAs. Efficient SEIRA is dominated by two principles: resonances tuning and spatial overlap between the enhanced electromagnetic field and molecules, which explain the high volume of research produced on these two aspects, through antenna designs [93, 133] and bulk optimisation [133], that respectively led to exotic antenna design (fractals [134], nano-gaps antennas [133, 107], etc.) and metamaterials (metal-insulator-metal structures [107], hyperbolic materials [135], perfect absorbers [136], etc.).

While SEIRA has been successfully employed multiple times for the sensing of liquid at low concentrations [137], its use for the detection of molecules in gas phase is relatively new and little works have been conducted. We report the sensing of ‘simple’ molecules: CH_4 [4], CO_2 [4, 138, 139, 140, 141], SF_6 [142], SO_2 [143], NO_2 [143], N_2O [143], and NO [143].

From the table [1.6], summarising to the best of our knowledge SEIRA-based gas sensing, note that the LOD of gas phase detection based on SEIRA are higher compared to mature technologies, and second, most of these concern ‘light’ molecules, which are quite different from ‘complex’ molecules, including CWAs and their simulant. SEIRA has not been applied to detect more complex molecules characterised by (i) the presence of dif-

ferent functional groups, which may interact differently depending on the composition of the plasmonic material, and (ii) high molar mass in gas phase. As for example, DMMP or sarin can be modified after adsorption on metal oxides. As far as CWAs are concerned, we report only one study for the SEIRA-based detection of a simulant sprayed on a plasmonic platform [30]. In this context, the work carried out in this thesis is, to the best of our knowledge, completely new and innovative.

Detected species	Surface-enhancing material	Response time (s)	Sensitivity	Surface-molecules interaction
CO ₂	Gold	35	400 ppm	MOF
CO ₂	Graphene	60	390 ppm	Polyethylenimine (PEI)
CO ₂	Boron nitride	120	390 ppm	PEI
CO ₂	Silicon	120	20 ppm	PEI
CO ₂	Gold	N/A	52 ppm	MOF
CH ₄	Gold	60	400 ppm	MOF
SO ₂ , NO ₂ , N ₂ O and NO	Graphene	60	800 zmol.µm ²	High physisorption

Table 1.6: Review of gas sensing performed by SEIRA-based sensors.

1.3 Part three: ϵ -near-zero media

1.3.1 Origins

Optoelectronics combined with the mature micro-electronics industry led to the development of optical devices such as photodiodes, photomultipliers, integrated optical circuits, laser diodes, quantum cascade lasers, communications, etc. These devices exploit light-matter interactions within semiconductors and amongst the great diversity of parameters that are studied to further improve these devices (permeability, carrier mobility, carrier lifetime, etc.), the refractive index of a medium is one of the most important. This parameter describes how an electromagnetic wave propagates within the considered medium. The refractive index \tilde{n} is a complex quantity as when light passes through a medium, some will be absorbed, as described by the Beer-Lambert-Bouguer law, from equation [1.5]

$$\tilde{n} = n + i\kappa \quad (1.6)$$

With n , the real part, representing the refractive index and is associated to the phase velocity of light in the medium, while the imaginary part κ is the extinction coefficient and indicates the attenuation of light through the medium. It can be shown that n and κ are also linked to the permittivity ϵ of the medium as follows:

$$\epsilon_1 = n^2 - \kappa^2 \quad \epsilon_2 = 2n\kappa \quad (1.7)$$

With ϵ_1 and ϵ_2 respectively the real and imaginary part of the permittivity. Additionally, we know from the dielectric function (equation [1.2]) and the plasma frequency (equation [1.3]) that ϵ relates to ω_p which itself is a function of the free carrier density N . It therefore comes to light, that if one wants to develop a material with the ability to interact and control light through the refractive index of the material, one option is to play on the free carrier density and take advantage of the fact that ϵ is itself a function of the frequency ω .

Light-matter interactions govern the efficiency of optical systems. Yet, several effects, such as non-linear phenomena or absorption in the infrared from molecules, have weak light-matter interactions yield. It therefore requires complex experimental setups or long interactions lengths through bulky materials structures which are incompatible with integration and scale up. In this framework, plasmonics stands as one of the main avenue studied as its ability to confine light at the nanoscale can be used to increase light-matter interactions [144]. Consequently, modern developments have been drawn towards novel architectures (2D materials [145], perfect absorbers [100, 136], metal-insulator-metal structures [45, 100], cavities [146, 147], and waveguides), antenna designs (gap plasmons, ring resonators [147, 148]) and bulk metamaterials [148, 149] (hyperbolic materials [135, 150],

quantum stacking, highly-nonlinear materials [146]) to further investigate this issue. In this framework, epsilon (ϵ)-near-zero (ENZ) materials rose as a promising technology and in the following sections, we dive in its principles, materials and applications.

1.3.2 Principles

From equations [1.7], the relation between the refractive index of the materials and the permittivity can be also expressed in the following way:

$$n = \sqrt{\epsilon\mu} \quad (1.8)$$

And considering that the magnetic response is small ($\mu = 1$), we directly understand that ENZ implies that the refractive index of the material tends towards small values as well. A medium with a near-zero refractive index doesn't imply that light travels faster than in vacuum, but that its phase velocity is distorted in such a way that literature refers to it as a 'stretched' wavelength phenomenon. This means that the relation between frequency and wavelength in the medium is weakened and this can be exploited for advanced light control and manipulation.

Another aspect of ENZ materials touches the electromagnetic fields associated to such media. Indeed, taking a look at the continuity relations at interfaces, the electric field magnitude will significantly increase with respect to adjacent media (defined by ϵ_a and E_a , the permittivity and the electric field, respectively):

$$E_{\text{ENZ}} = \frac{\epsilon_a E_a}{\epsilon_{\text{ENZ}}} \quad (1.9)$$

It should be mentioned that μ -near-zero media also exist [151], and because both the permittivity and the permeability are function of the frequency, a material may display μ -near-zero and ENZ effects at different frequencies. Engineered media can display both effects at the same frequency, and are defined as ϵ - μ -near-zero media [152]. In practice, one should not forget that losses are an intrinsic part of ENZ materials and it is one of the great limitations as to why although ϵ tends to vanishingly small values, the losses still remain large. Therefore, one understands that designing a perfect ENZ material implies a material with small losses, a negligible magnetic response, at the operating frequency. Finally, for some applications such as waveguiding, impedance Z ^[9] is a major component as it governs the transmission. From the relation $Z = \sqrt{\mu/\epsilon}$, the impedance can be tuned with the permittivity and greatly increased within ENZ media. In the next section, we will review the various ways to obtain ENZ regime.

⁹Characterises the ease with which light is transmitted from a first medium to a second, it is related to the difference between the indices of refraction.

1.3.3 ENZ-supporting materials

Currently, we report five different ways to achieve an ENZ behaviour: (i) the free carriers oscillations, *i.e.*, bulk plasmon at the plasma frequency, (ii) effective media by photonic multilayers [153, 154], (iii) Dirac cone in the centre of the Brillouin zone, corresponding to the Γ point in photonic crystals [155], (iv) at the cut-off frequency of hollow waveguides [156], and (v) phonon frequencies [157]. Overall, all polaritons-based systems display an ENZ point. In our study, only the first method is of interest.

Indeed, we can deduct from the Lorentz-Drude model (equations [1.2], [1.3]) that the collective movements of free carriers result in ENZ at the plasma frequency. For this reason, plasmonic materials are intimately linked to ENZ effects as both have the same origin, hence, most of the plasmonics materials listed before have found applications through their ENZ regime. Commonly used plasmonic-based ENZ materials are TCOs (AZO [158], ITO [159], GZO [160], ICO [161], FCO [162]) and III-V semiconductors (InSb [163], InAs [164]). These materials are more often employed because they can be doped and their plasma frequency can be thus tuned to the operating frequency. Indeed, there is a difference between the plasmonic resonance and the ENZ effect, that are respectively adjustable by the antenna shape and size, and the doping level of the material, which is the reason why noble metals are less often employed as ENZ materials. Additionally, noble metals suffer from important optical losses to find practical use in ENZ-related applications.

Figure [1.13] represents ENZ materials from the literature, as function of their losses represented by the imaginary part of the permittivity, over the electromagnetic spectrum (from the deep-ultraviolet to the microwaves). We observe that around the wavelength of 10 μm , doped semiconductors (such as InAs, InAsSb, InSb and Si) are mostly used. Lines connecting points, representing a material, highlight their tunability over a significant frequency range in the infrared region, and they display less losses than some of their counter-parts in the visible. They are particularly adapted to be used to probe the fingerprint of molecules, making them a promising candidate for gas phase detection of DMMP.

1.3.4 ENZ-associated phenomena

In this section, we non-exhaustively review some important applications that were achieved with ENZ photonics. These applications demonstrate phenomena that highlight the promising technology that ENZ represents.

Perhaps the most famous application of ENZ materials is waveguiding as it was predicted in 2006 that the electric field and the power flow of an electromagnetic wave

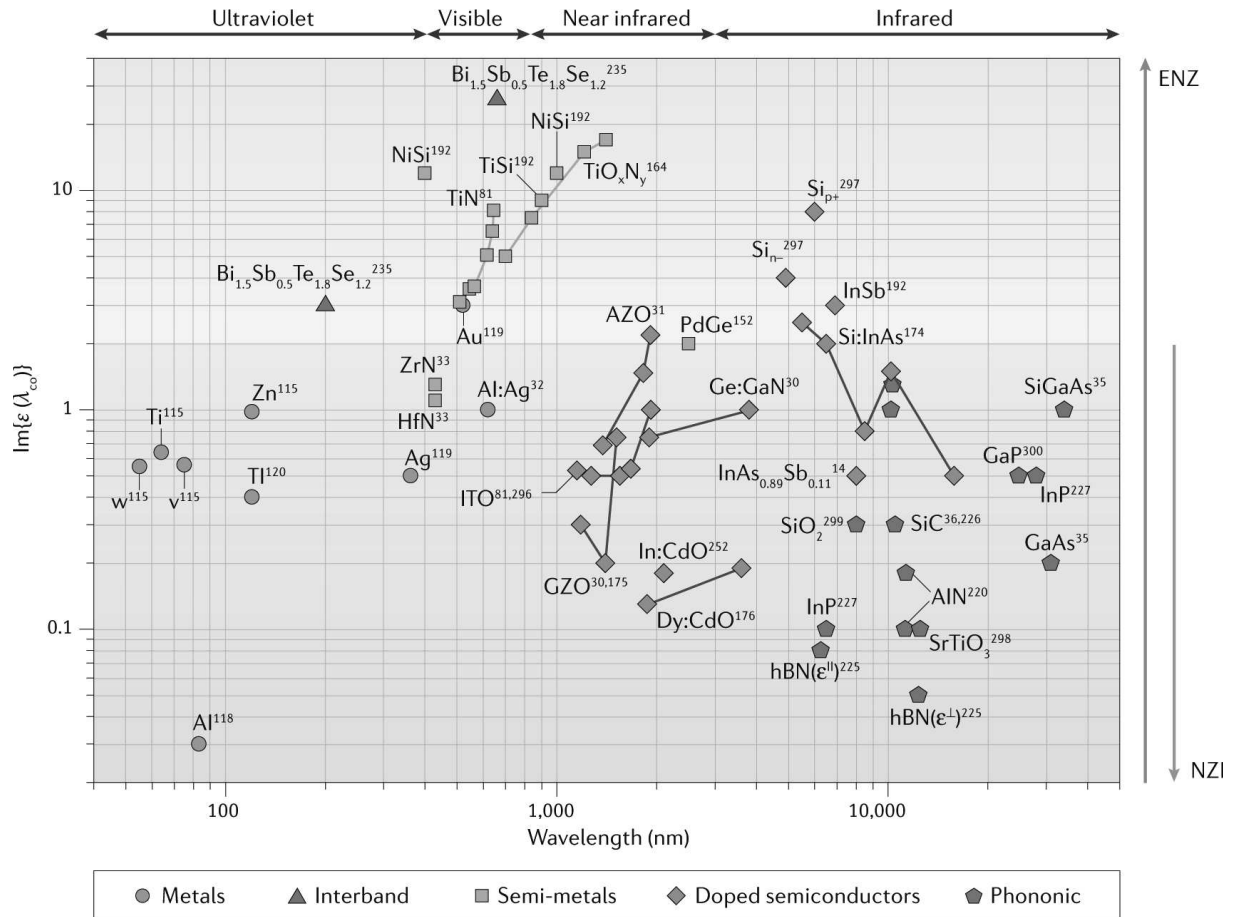


Figure 1.13: The value of the imaginary permittivity ϵ is plotted at the crossover wavelength (λ_{co}) at which the real permittivity is zero. Materials with an imaginary permittivity smaller than 2 at the crossover wavelength exhibit near-zero-index (NZI) properties. The lines connect the different measured values of $\text{Im}(\epsilon)$ for a given statically tunable material and illustrate their variability. Borrowed from [165].

within an ENZ waveguide would be almost totally conserved with a near perfect transmission [166], and this, whatever the shape of the waveguide [167]. It would be experimentally demonstrated two years later by two independent teams, a week apart [168, 169]. This near-perfect transmission phenomenon was later intensively studied and it was found that its origin lies in a near-constant phase of the travelling wave.

This stationary phase phenomenon gave rise to numerous applications such as directive emission, the second most important application of ENZ materials [170]. Indeed, from Fresnel's formula, it can be shown that the angle of refraction at the boundary is a function of both permittivity and the angle of incidence of the ENZ region, leading to a directive emission. The second consequence is that the radiation phase pattern of the radiation source can be tailored [171]. In the same vein, as previously mentioned, strong field discontinuities and enhancements have been observed [172, 173], which would greatly benefit applications including antenna design, enhanced superradiance¹⁰ [174], and, in theory, spectroscopy.

ENZ photonics also attracted important attention as it represents a solution to the two main challenges in the way of nonlinear optics: phase mismatch and weak light-matter interactions [175]. Indeed, the former is not an issue anymore as the phase is constant within ENZ region and the latter greatly benefit from (1) the strong confinement associated with the light-trapping ability of the ENZ material, leading to an increased input energy as it is concentrated within a small region, and (2) the 'slow-light' effect as the group velocity vanishes which implies a close-to-infinity interaction time in theory [176].

Finally, we look into two effects that are interesting in plasmonics: the geometry independence of the plasmonic response and the resonance pinning. The first one was briefly mentioned above as ENZ waveguides present a near-perfect transmission, independently from the waveguide shape. This effect was identified for various experiments and under different conditions [167, 177]. It appears that ENZ media are associated with a near-perfect dispersive behaviour, this means that the optical properties of the bulk materials dominate over other parameters such as the geometry of the system that would initially have drastic influence over the system's response. This is an interesting feature in plasmonics as many applications make use of plasmonic nano-antennas and lowering the dependence between the system's response and the plasmonic nano-antenna supposes that it would be a lot more tolerant to fabrication defects and fabrication errors would become insignificant.

Second, it is well-known in plasmonics that the shape and size of the antenna influence the plasmonic resonance. By suppressing this relation, it has been demonstrated that the

¹⁰Enhanced emission based on collective effects arising when quantum sources are placed sufficiently close to each other.

plasmonic resonance mainly depends on the material properties in ENZ regime, having for consequence a plasmonic resonance pinning [178, 179, 180]. This resonance pinning may facilitate various applications for which matching the plasmonic resonance to another resonance (such as vibrational modes in spectroscopy) in order to achieve coupling is required.

Besides, ENZ has been employed for the design of optical isolators [181], all-optical and electro-optical switches [182, 183] modulators [184, 185], perfect absorbers [186], communications [187], amongst many others [188, 189, 175, 177].

In direct relation with the thesis work, ENZ media were applied in sensing applications with waveguides sensors [190], refractive index sensors based on metasurfaces [190, 191, 192, 193, 194, 195, 196, 197, 198]. ENZ were theoretically studied as enhancing media for SEIRA [199, 200]. Very little work has been experimentally produced to showcase the potential of ENZ for sensing applications [201] with a fundamental work from Folland *et al.* using phonon-based ENZ effects in an effective MIM waveguide structure for SEIRA and strong coupling between the absorbing molecules in the vicinity and phonon-polariton vibrations. They experimented their structure with the volatile organic compound cyclohexane, paving the way for gas sensing by ENZ-enhanced spectroscopy [202]. A second paper by Ma *et al.* paves the way to understand the strong coupling between vibrational modes of organic molecules (in this case, PMMA) and metallic antennas [201], showing that the ‘very strong coupling’ regime between molecules and plasmon is associated to a mode splitting and anti-crossing dispersion.

Although ENZ materials have not been largely employed for SEIRA, we believe that the combination of multiple ENZ-based effects, namely, the plasmonic resonance pinning and the enhanced electromagnetic field, may significantly benefit SEIRA both practically and qualitatively. Indeed, as most SEIRA strategies rely on surface chemistry, ENZ materials bring interesting features free of the characteristic downsides of surface chemistry: stabilization, reuse, reproducibility, and preparation.

Conclusion

In this first chapter, we introduced the reader to the field of plasmonics and its application for the enhanced-absorption of organophosphorus compounds. A review of the literature about OPs detection shows that there is still room for improvement in terms of selectivity, sensitivity, response time and miniaturisation. To these ends, plasmonics appears as a promising sensing technique through the SEIRA effect, based on LSPR and its associated highly-enhanced electric field. In this framework, highly doped III-V SCs are particularly interesting as their operating frequency can be adjusted to the fingerprint of CWAs molecules in the MIR. Finally, we discussed various technologies such as bulk material and

antenna design, as well as, surface chemistries to further improve the performance of a plasmonic-based sensor. Especially, ϵ -near-zero media were addressed as a strategy to further improve the sensitivity and selectivity, without the disadvantages of functionalisation strategies. The next chapter deals with the sensor conception, growth and fabrication. Electromagnetic simulations alongside fabrication and optical characterisations are also presented.

Chapter 2

Conception, fabrication and characterisations

Introduction

This second chapter is dedicated to the entire process in order to obtain plasmonic samples that will be used for the study of ENZ effects and spectroscopy of CWAs in gas phase. The whole process is covered from the very beginning, starting with the establishment of the expectations and the preliminary electromagnetic simulations performed. The physical fabrication of the samples and its numerous control characterisations, with first the crystalline growth and second the fabrication of the plasmonic antennas, are realised and showed. After that, the optical characterisations of the fabricated samples will be carried out in order to validate the conception and fabrication steps. This chapter ends with a checklist of requirements the samples must fulfill to be used in practical applications such as spectroscopy.

2.1 Conception

2.1.1 The plasmonic structure

In this first section, we introduce the reader to the plasmonic structure designed in this thesis work for both the study of ENZ effects and spectroscopy experiments. MIM structures are well-known for their ability to enhance light-matter interactions by trapping light within the insulating layer sandwiched between two metallic layers, as developed in chapter [1](#). In practice this results in two phenomena that have been reported: (1) a perfect absorber behaviour [\[136\]](#) and (2) a SPP trapped at the antenna interfaces, with a magnetic field pinned in the insulator layer, known as gap plasmon [\[203, 204\]](#). The specificity of this work lies in the nature of the spacer layer. While MIM structures and ENZ layers have been employed for a variety of applications, we propose to combine both of these concepts into a metal-ENZ-metal structure. This concept is based on the fact that ENZ

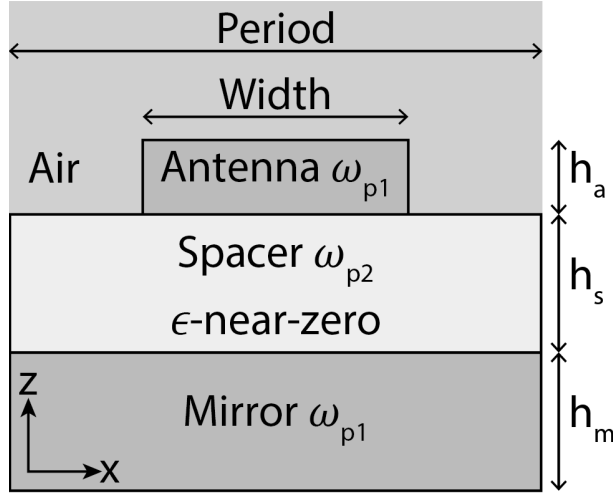


Figure 2.1: Schematic diagram of the metal-insulator-metal structure.

layers are not metallic so that this design conserves the advantages of the MIM structure, while benefiting from the ENZ layer assets. The ENZ behaviour is obtained by doping the layer to the point that its plasma frequency reaches the operating frequency which is around $10 \mu\text{m}$ in our case, close to the absorption of the simulant of sarin: DMMP. Still, we tried other doping levels for the study of ENZ phenomena, and we will discuss these results in chapter 3.

Figure 2.1 displays the desired structure to be grown and processed. This structure is composed of a spacer layer of plasma frequency ω_{p2} sandwiched between two layers of plasma frequency ω_{p1} , well-known as metal-insulator-metal structure. Throughout this work, various designs have been tested in terms of antenna width, period, spacer layer thickness (h_s) and spacer layer doping ω_{p2} . The common points of all the structure evaluated are as follows:

- The top layer is about 100 nm thick (h_a) and it is this layer that will be nanostructured into plasmonic antennas.
- The bottom layer is a thick layer of $1 \mu\text{m}$ (h_m) acting as a mirror layer for IR light to perform reflectance measurements.
- The top and bottom layers are as highly doped as semiconductors can be, which is about $5 \times 10^{19} \text{ cm}^{-3}$ in the case of InAsSb:Si (see section 2.2.1 for further detail), so that the plasma frequency ω_{p1} corresponds to a plasma wavelength $\approx 5 \mu\text{m}$. This way, the material is metallic for the MIR and its plasmonic nature can be exploited.
- The spacer layer is always less doped than its surrounding layers so that $\omega_{p2} < \omega_{p1}$.

2.1.2 Electromagnetic simulations

Modern physics is intimately linked with the development of novel numerical methods and computer improvements. The ability to simulate a structure in order to predetermine its physical response has tremendously benefited the development of complex structures that previously relied on trial-and-errors and empirical laws. Electromagnetism is one of the most well-established physical theory and thus, electromagnetic (EM) simulations became a field of research itself, and are generally considered indispensable for the design of sub-wavelength nanoscale optical devices including plasmonics [205]. The most commonly used EM simulation methods are: (i) finite difference time domain (FDTD) [206], (ii) finite element method (FEM) [207] and (iii) rigorous coupled-wave analysis (RCWA) [208].

In this work, both FDTD and RCWA will be performed with the software Lumerical FDTD solver and RETICOLO (open source Matlab code) [209], respectively. The design of the bulk structure and antenna parameters were performed with RCWA. The open-source code RETICOLO allows to design 1D and 2D systems and simulate their optical response in terms of reflectivity and transmission. This method is easy to use and faster than other methods, but its precision is directly related to the computation time. FDTD was employed to cross-confirm some RCWA results, including the simulation of organic molecules, plus it has the advantage to always converge in the right conditions, which explains why it is a state of the art computational method for electromagnetism. Still, differences always persist between simulations and experiments, and these will be discussed in both chapters 3 and 4.

The figure 2.2 shows an example of a reflectance simulation of 1 μm width nanoribbons plasmonic antenna, with a period of 2 μm , and a 500 nm thick spacer layer doped at $1 \times 10^{19} \text{ cm}^{-3}$ so that its plasma frequency ω_{p2} corresponds to a plasma wavelength of $\approx 10 \mu\text{m}$. We observe that the simulation ranges from 400 up to 5000 cm^{-1} , which is the detector operating range. Second, we observe two peaks: (1) the plasmonic resonance LSPR around 1050 cm^{-1} and second the quarter-wavelength resonance associated to the Fabry-Perot cavity of the MIM structure around 1400 cm^{-1} . Finally, the LSPR is associated to a reflectance close to zero, and due to the fact that there is no transmission thanks to the mirror layer, it means that the absorption is maximised and therefore confirm that such structure behave as a perfect absorber. The inset focuses on the LSPR range for three different width of nanoribbons: 0.5, 1.0 and 1.5 μm . We can appreciate the well-known dependence between the LSPR frequency and the antenna size. As the nanoribbons width increases, the LSPR red-shifts towards higher wavelength or smaller frequencies.

EM simulations can also evaluate the intensity of the electromagnetic field at each point of space of the designed structure, which can then be turned into EM maps. Fig-

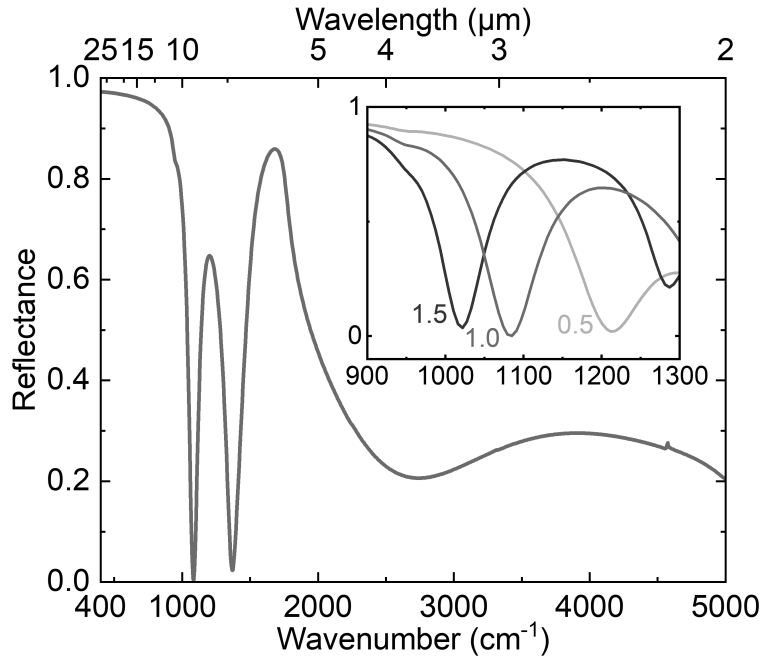


Figure 2.2: Reflectance simulations performed by RCWA of a 1 μm width nanoribbons plasmonic antenna, with a period of 2 μm , and a 500 nm thick spacer layer doped at $1 \times 10^{19} \text{ cm}^{-3}$. The inset represents reflectance, focused in the LSPR range, for three different nanoribbons width: 0.5, 1.0 and 1.5 μm , respectively green, red and blue.

ure [2.3](#) represents the computed and normalised (a) electric field map, and (b) magnetic field map, of a plasmonic nanoribbon antenna along the x-direction, at plasmonic resonance frequency (LSPR $\approx 9.5 \mu\text{m}$). We observe in the (a) map the electric field enhancement on each side of the plasmonic antenna, along the ribbon length, expected at LSPR. In the second map (b), we observe that the magnetic field is mainly confined within the spacer layer, dielectric at the LSPR frequency, in accordance with the expected gap plasmon behaviour associated with the MIM structure.

To conclude, these EM simulations demonstrate how powerful of a tool modern numerical simulations are for evaluating both the near-field and far-field optical responses of a plasmonic device, respectively by simulating its reflectance and the EM field it is associated with. This last point is of special importance as we know that plasmonic devices, by confining light, will enhance the EM field associated to the SPPs, especially in the case of subwavelength antennas such as nanoribbons. In practice, the structure design is optimised for both of these features by determining bulk parameters (materials, thicknesses, and doping levels), as well as antenna parameters (shape, dimensions and period), preceding the physical fabrication of the simulated samples that starts off with the growth.

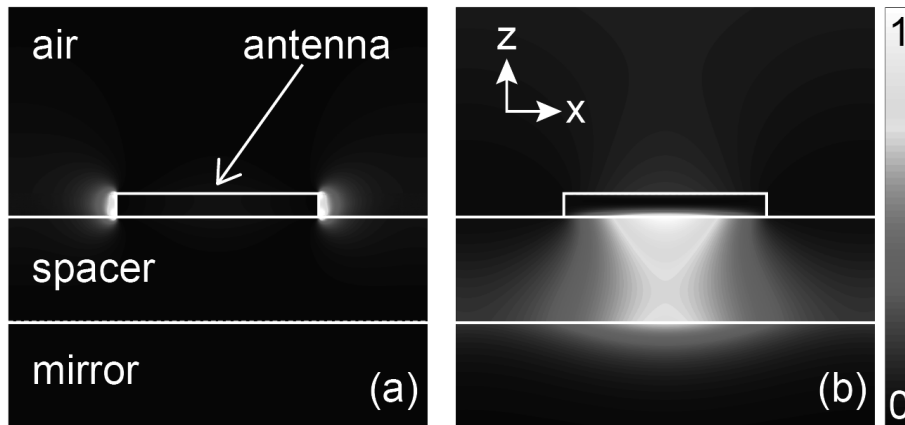


Figure 2.3: Normalised (a) electric field $|E/E_0|^2$ and (b) magnetic field $|H/H_0|^2$ of a ≈ 1 μm -wide ribbon plasmonic antenna, at $\lambda \approx 9.5$ μm , calculated along the x axis by RCWA simulation.

2.2 Samples growth

2.2.1 Molecular-beam epitaxy

The physical fabrication process starts off with the crystalline growth of the samples. The growth of III-V semiconductors (SCs) consists in the formation of crystalline layers, known as epitaxy, on top of a wafer, also called substrate, that is a thin slice of semiconductor that serves as the first building block in the fabrication chain. The growth of crystalline structures on top of the substrate is highly dependent on the state of the surface, as a consequence, surface preparation in epitaxy is, in itself, a domain of research. The substrate is crucial in crystalline growth as it acts as a lattice template for the grown structures, which means that its lattice constant, typically around 6.1 \AA for InAs, GaSb and AlSb, imposes its lattice over the structure grown on top. The growth of structures with different lattice parameters is a highly active topic of research as it leverages technological limitations intrinsic to epitaxy, allowing the development of novel optoelectronic devices and their integration onto photonic integrated circuits with daily-life applications. There exist different techniques for epitaxial growth of III-V SCs: vapor phase or liquid phase epitaxial growth and molecular beam epitaxy (MBE). MBE is a technique specialised in the growth of extremely thin layers with a control at the atomic scale and a high crystal quality [210]. This technique requires ultra-high vacuum (10^{-10} Torr) in order to achieve the highest purity possible of the grown films, by increasing the mean free path of atoms as they reach the wafer. Figure [2.4] presents a photograph of one of the two MBEs used to grow the samples during this work.

Despite InAs and GaSb having a similar lattice constant, respectively of 6.06 and 6.10 \AA , this relatively small difference $\sim 0.6\%$ actually is enough to hamper the growth of InAs over GaSb as the critical thickness of around 80 nm, imposed by the lattice constants dif-

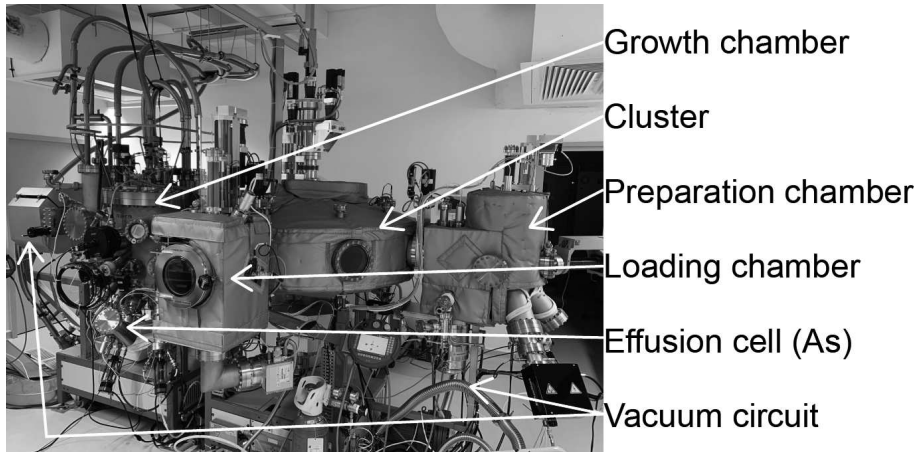


Figure 2.4: Photograph of the molecular beam epitaxy system RIBER C412 model at the Institute of Electronics and Systems of the University of Montpellier.

ference, is smaller than the layers to-be grown. Past this critical thickness, the crystalline structure relaxes and breaks, leading to a great variety of crystalline defects that may introduce additional optical and plasma losses [211, 212]. To solve this problem, the digital alloying technique was used to grow InAsSb rather than InAs, onto GaSb substrates [212]. A digital alloy is a compound whose composition is controlled through numerical pulsing of elements, this means, in the case of InAsSb, that the layers were grown the same way InAs would be grown (typically with a V-III growth rate ratio of ~ 1.5), but antimony is introduced by opening and closing the antimony cell shutter at a certain frequency. This pulsation allows to send a certain amount of antimony, function of the frequency numerically imposed on the shutter. As a consequence, Sb will be introduced and take the place of As within the lattice, and thus will modify the effective lattice constant of the ternary alloy. $\text{InAs}_{0.91}\text{Sb}_{0.09}$ is lattice-matched to the GaSb substrate, while keeping the ability to be doped like InAs. The growth rate is about 1 \AA per second.

Doping is perhaps the most important feature of the semiconductor industry, responsible for the exponential growth it had over the past 50 years. Doping corresponds to the ability to introduce other atoms, *i.e.*, impurities, within the lattice of an intrinsic semiconductor for the purpose of modulating its electrical, optical and structural properties. It is known that silicon atoms act as electron donor within InAs, meaning that it provides additional charges so that InAs:Si has more free electrons than InAs. Considering 10^{23} cm^{-3} atoms, InAs can be doped up to $6 \times 10^{19} \text{ cm}^{-3}$ using silicon, before reaching the solubility limit. InAsSb can also be doped to such high levels. To clarify, one should note confuse antimony and silicon respective purpose, the former is introduced to modify and adapt the lattice constant to that of the GaSb substrate, while the latter is used to dope the structure and tune its optical properties. Once the growth is performed, the structure must be verified and validated before the fabrication process can continue.

2.2.2 Growth characterisations

Surface characterisation

Surface characterisations of the samples after growth are performed using two main microscopy techniques: (i) optical microscopy and (ii) atomic force microscopy (AFM). Usually, a first visual check with the eyes can indicate problems during the growth. For example, the sample surface may look cloudy, or it may look like a white layer is on top, indicating a large number of surface defects or that the solubility limit has been exceeded. Optical microscopy will confirm if these assumptions are verified or not, and we assume that if no surface defects can be observed with a $\times 100$ objective, then the sample is characterised by AFM, which is a more dedicated technique for surface analysis.

The figure [2.5\(a\)](#) shows a standard $10 \times 10 \mu\text{m}^2$ AFM image of InAsSb:Si grown onto GaSb. The software Gwyddion can provide numerous information about the image and in particular, the average roughness (from the root mean square), which is $\sim 200 \text{ pm}$, or 2 \AA , for this case. This value is close to the atoms size composing the samples and therefore it confirms that the growth InAsSb onto GaSb is successful as little to no surface defects are introduced. To clarify, surface defects also refer to deep defects that reach the surface as the growth proceeds, so absence of these surface defects imply that the interface between GaSb and InAsSb is as optimal as possible. In contrast, figure [2.5\(b\)](#) shows the result of GaSb grown on GaAs, resulting in pyramidal defects on the surface due to the lattice mismatch causing a roughness of $\sim 1.4 \text{ nm}$.

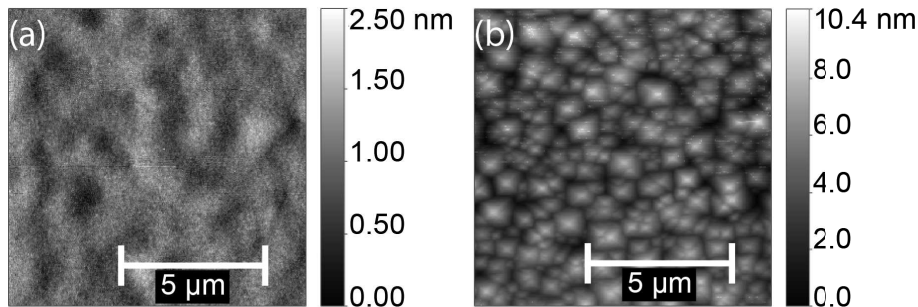


Figure 2.5: Atomic force microscopy images ($10 \times 10 \mu\text{m}^2$) of (a) InAsSb:Si digital alloy grown on GaSb and (b) GaSb grown on GaAs.

Crystalline characterisation

To further verify the crystalline quality of the samples, high-resolution X-ray diffraction (HRXRD) is employed. It provides information about the crystalline state, the lattice constants and the thicknesses of the grown structures. This technique is especially important to calibrate the amount of antimony necessary to correctly match the lattice of InAsSb to the one of GaSb. Figure [2.6](#) displays three different HRXRD spectra. The

first case (a) shows a slightly mismatched InAsSb grown on GaSb. We observe that the GaSb substrate and InAsSb digital alloy peaks are slightly separated, the latter is on the right meaning that the material is in tension and not enough Sb has been introduced in the lattice to perfectly match that of GaSb. As opposed to the second case (b), for which they are confounded implying that InAsSb is perfectly matched to GaSb. Finally the third case (c) highlights the difference when InAsSb is grown on to a GaAs substrate, we observe that the digital alloy and the substrate peaks are completely separated, which is expected with a 7.2% lattice mismatch between the two materials. A growth for this last case may imply the use of a buffer layer, which is a layer grown in-between the substrate and the active layer to (i) ‘bridge’ the lattices of two different materials and (ii) to bury possible defects that may appear at interfaces [211, 212]. Finally, we observe two satellite peaks on each side of the graphs, corresponding to a period within the grown structure. This period is associated to the digital alloy as the pulsing of antimony actually result in sequence of InAs/InAsSb, similar to a superlattice, allowing to retrieve with precision the thickness of the grown layer, contrariwise to the growth of bulk materials.

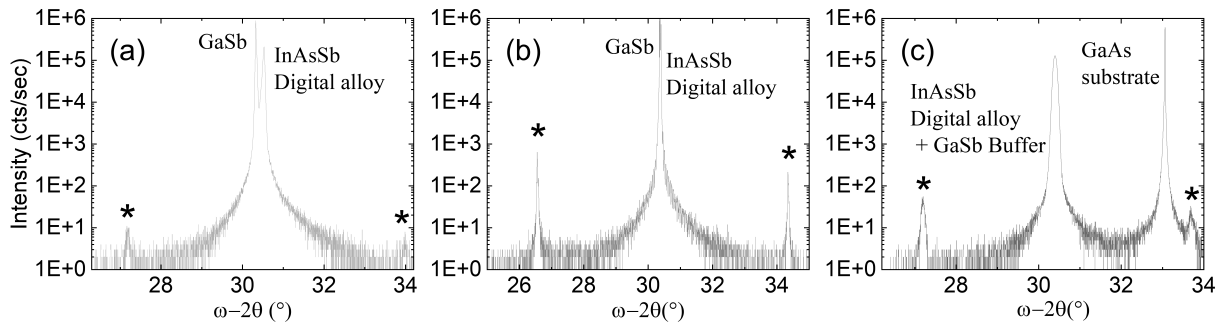


Figure 2.6: High resolution X-ray diffraction spectra of (a) a slightly mismatched InAsSb on GaSb, (b) a perfectly matched InAsSb on GaSb and (c) InAsSb on GaAs. Stars highlight satellite peaks associated to the period of the InAs/InAsSb digital alloy.

Doping characterisation

The plasmonic behaviour of III-V SCs is brought by the ability to dope them and introduce a sufficient amount of free carriers to obtain a high density of electrons, *i.e.*, a plasma. To obtain a plasmonic behaviour in the MIR, the III-V semiconductor must be highly-doped with free carriers having a small effective mass. Hole doping (or p-doping) is possible and would lead to a plasma of holes rather than electrons, but holes are much heavier than electrons and therefore their large effective mass significantly lowers the plasma frequency far below MIR. On the other hand, electrons are much lighter, and especially in InAs, for which the electron effective mass is around $0.023m_0$ (as opposed to holes for which the effective mass is $0.41m_0$), also highlighting the great mobility of free electrons in InAs because losses γ are inversely proportional to the mobility. Both silicon and germanium act as donors in InAs, but as silicon is a smaller atom, its solubility limit is about an

order of magnitude higher than germanium, making it suitable for high doping levels. Only InSb can be as highly-doped as InAs, but its lattice constant is much higher than its 6.1 Å counterparts, which is why it is less employed within heterostructures.

Doping levels can be measured in different ways with Hall effect by far the most employed in the silicon industry [213], despite charge accumulation effects leading to errors in the estimation, especially in InAs [214, 215, 216]. Doping levels can also be measured optically, by probing the Brewster mode occurring at the plasma frequency [217]. This technique consists in a light beam sent with a 60° angle at the surface of highly-doped SCs so that upon reflection, a leaky mode within the bulk of the material probes its free carrier density which will translate into absorption on the reflectance spectrum.

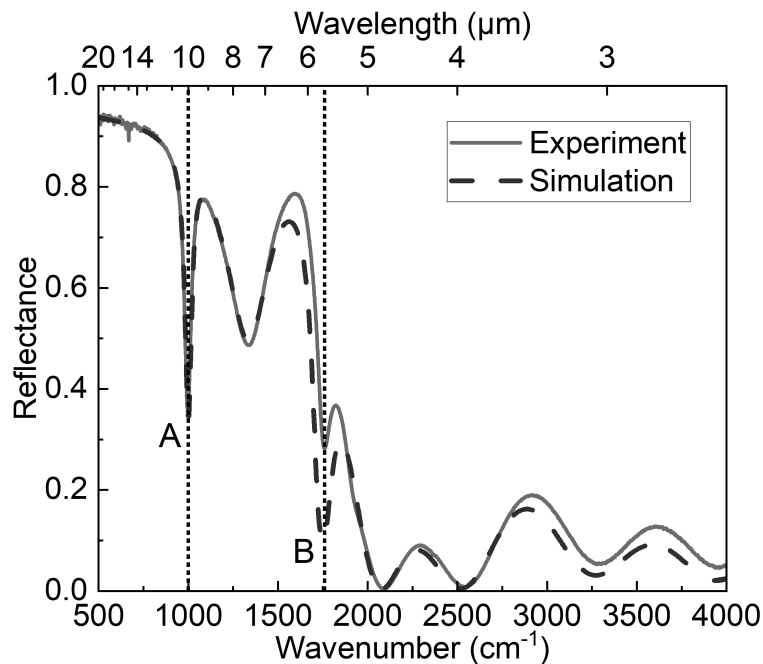


Figure 2.7: Experimental Brewster measurement (full line) and simulation (dashed line). A and B peaks respectively correspond to the plasma wavelengths of the spacer layer, and the highly doped layers, *i.e.*, metal layers. Their respective doping levels are evaluated at 4×10^{19} and 1×10^{19} cm⁻³.

Figure 2.7 shows a Brewster measurement obtained using FTIR. First, we observe that the experiment and the simulation match, which cross-confirms the following conclusions. In this spectrum, we observe various peaks, notably the A and B peaks, that respectively correspond to the spacer and ‘metal’ layers of the sample. From the plasma frequency relation [1.3], we can retrieve the carrier concentration, *i.e.*, doping level, needed to obtain a plasma wavelength at 10 μm, which is around 1×10^{19} cm⁻³ donors, this corresponds to the peak A. As for peak B, it corresponds to the doping level of the metallic layers, around 4×10^{19} cm⁻³, close to the maximum possible in practice, as expected by EM simulations. The peak in-between, as well as the oscillations at higher frequency, are

Fabry-Perot resonances associated to the spacer, acting as a cavity. The simulation, in figure [2.7](#), is performed using transfer-matrix method, next section discusses it. Further information about the Brewster measurement can be found in annex [A](#).

Losses characterisation

The simulation performed with the transfer-matrix method on Matlab allows us to fit various parameters and cross-confirm experimental measurements. From HRXRD, we can extract the exact thicknesses of each layers, besides the fact that MBE allows a nm-scale control of these layers. In addition, from Brewster measures, we retrieve the exact doping level of each layers. As a result, the only unknown parameter according to equation [1.3](#), is the plasma losses γ . Therefore, it is possible to use this parameter to fit and extract the losses for each doping level. For example, the losses are estimated around $1.5 \times 10^{13} \text{ s}^{-1}$ for high doping level of $4 \times 10^{19} \text{ cm}^{-3}$, while it is estimated around $8 \times 10^{12} \text{ s}^{-1}$ for $1 \times 10^{19} \text{ cm}^{-3}$. Losses are negligible for undoped layers. In the end, the plasma losses can be estimated from the plasma frequency with equation [2.1](#) which serves as a good approximation:

$$\gamma \approx \frac{\omega_p}{20} \quad (2.1)$$

It should be noted that this fitting parameter both influence the frequency of the peak, but also its full-width at half-maximum (FWHM). We observed that for InAsSb grown on GaAs, despite the strong lattice mismatch that induced crystalline defects, we did not identify any significant broadening of the peaks on Brewster measurements nor simulations, implying that the plasma oscillations might not be as sensitive as thought to crystalline defects. Confirming this assumption would require further investigations. Once the grown sample satisfies the requirements in terms of quality, thicknesses, doping level and plasma losses, it is ready to undergo further fabrication steps constituting the process of patterning the surface into plasmonic nanoantennas.

2.3 Fabrication

2.3.1 The nano-patterning process: step-by-step

The cleaning procedure

We present here a step-by-step procedure for the fabrication of plasmonic nanoantennas. First, we define the cleaning step as follows, the samples are cleaned using acetone, isopropanol (IPA) and deionised (DI) water. Acetone is primarily used to remove organic remnants and contaminants from the sample surface, but as it evaporates, it may leave

redeposits and stains, which is why IPA follows up to clean all non-polar contaminants left. DI water finishes the cleaning step by washing out the remaining residues. This 3-steps cleaning procedure will be referred as cleaning in the manuscript. Cleaning is perhaps the most important step of the fabrication procedure as the state of the surface entirely conditions the quality of the next steps including lithographies and etchings. This procedure takes about 10 minutes.

The patterning procedure

The patterning of surface into nanostructures like plasmonic nanoantennas is based on two main steps which are the patterning of a mask at the surface, followed by an etching to imprint the design from the mask to the sample surface. The mask can be either a hard mask, made of SiO_2 or Si_3N_4 for example, or a resist. The choice of the type of mask depends on if it can withstand the etching step and for how long. Hard mask can support much stronger etchings like high-power dry etchings but require an additional step to pattern the hard mask itself with a resist. Resists are polymers commonly used in the semiconductor industry because they are sensitive either to light or electrons, and respectively photolithography and electron-beam lithography (EBL) are employed to print the desired design on the resist. Figure 2.8 displays the equipment of (a) photolithography and (b) EBL [218]. Once lithography has been performed, the development of the resist using a chemical called developer allows to selectively remove either the exposed or unexposed resist, depending on its nature as a positive or a negative resist, respectively. The remaining resist can be used as a soft mask for the etching step [219]. The patterning by EBL can be relatively long depending on the pattern dimensions, in our case it would take a night up to one full day.

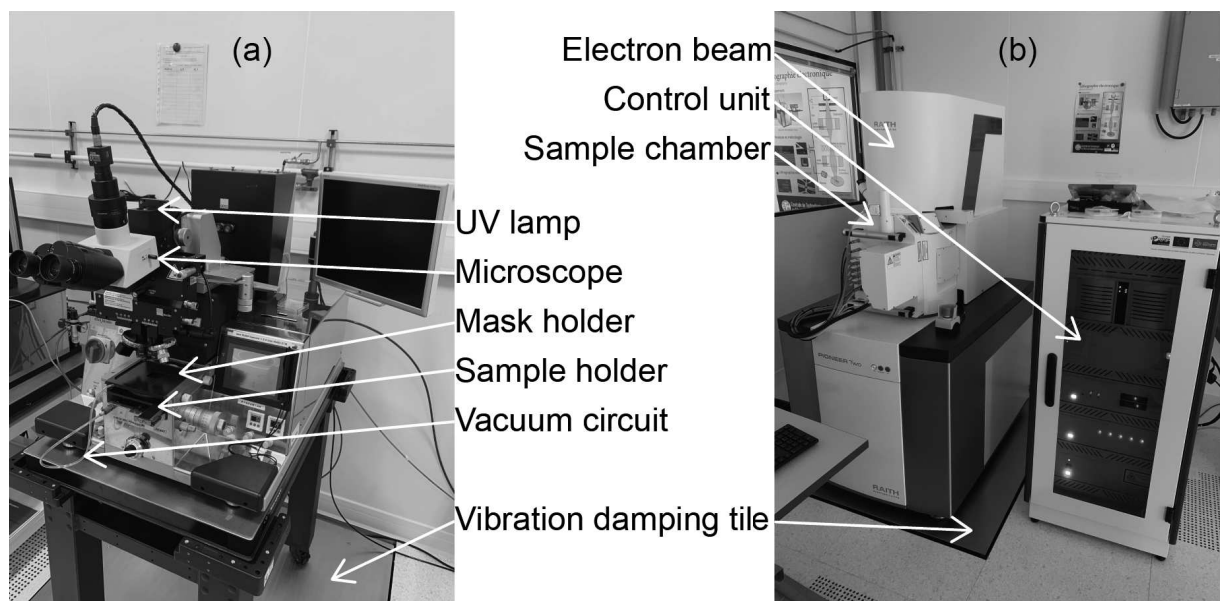


Figure 2.8: Photographs of (a) photolithography and (b) EBL systems.

The etching step

The second step of the patterning is the etching. If one needs a hard mask for the etching of the sample surface, then a preliminary etch of the hard mask below the resist is needed. If not, then the developed resist serves as mask and the etching of the III-V SCs takes place. Etching can be performed in two different ways: wet or dry etching, sometimes a combination of both. Wet etching relies on the use of acids such as: citric, nitric or hydrofluoric (HF) acids, that are commonly used, usually diluted with DI water or hydrogen peroxide (H_2O_2). Dry etching is performed using techniques such as inductively coupled-plasma (ICP) for reactive ion etching (RIE), well-known as ICP-RIE. This technique is based on ionisation of a gas with ions then being attracted towards the wafer so they react with the surface and etch it. Afterwards, the sample is cleaned to remove the remaining resist, or it is etched another time to remove the hard mask. The samples used in this thesis work were fabricated with the following standard fabrication procedure:

1. cleaning procedure,
2. deposition of a ≈ 200 nm thin layer of AZ2020:AZEBR (100v:80v) resist by spin-coating (6000 round-per-minute for 30 s) and 1 min 110 °C baking,
3. patterning by EBL (10 kV),
4. 1 min 110 °C baking,
5. resist development for ≈ 30 s with AZ726 MIF,
6. dry-etching using a 50 W Argon plasma for 5 min,
7. cleaning procedure.

The fabrication steps for the patterning of nanoribbon antennas are summarised in figure [2.9](#).

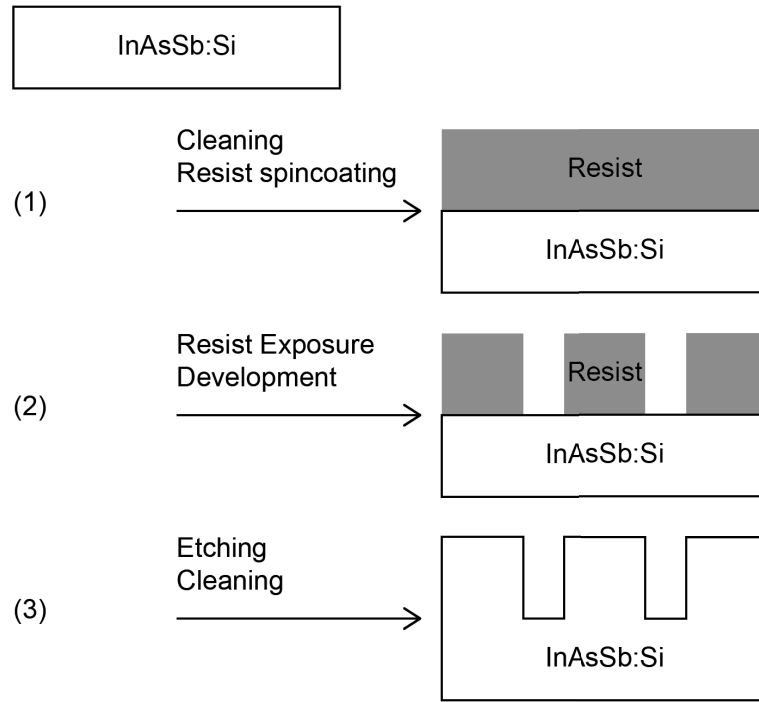


Figure 2.9: Scheme of the fabrication process in three main steps.

2.3.2 Fabrication characterisations

When the surface structuration into plasmonic antennas is finished, several characterisations are performed to verify the state of the surface, dimensions and overall quality of the antennas. The first one is scanning electron microscopy (SEM), to see the state of the whole surface as well as the dimensions and sides of the antennas. This technique uses an electron beam to scan the sample surface and upon electron-surface atoms interaction, secondary electrons are emitted and detected. Secondary electrons generally have low energies on the order of 50 eV, which require a strong vacuum as well as several multipliers in order to increase their energy, so they can be efficiently turned into an electrical signal for 2D intensity display. With modern equipments and in perfect conditions, the resolution of SEM can be as low as few nm. Figure 2.10(a) shows a SEM image of nanoribbon-shape plasmonic antennas.

The second technique is AFM. This technique is specialised to observe the sample surface at close view, with a better resolution than SEM, as observed by the scale of figure 2.5. This largely employed technique in research is known for its nm resolution about 1000 times better than the optical diffraction limit. AFM consists of a cantilever with a sharp tip acting as a probe when brought into proximity of the sample surface, upon which forces between the tip and the sample lead to a deflection of the cantilever according to Hooke's law. This deflection is typically measured optically with a laser pointing at the back of the tip, which is then transduced as an electric signal for image reconstruction, as

represented in figure 2.10(c). Finally optical microscope may also be used to observe the state of the surface (figure 2.10(b)), which may show large scale defects or stains, having a detrimental impact on the sample response.

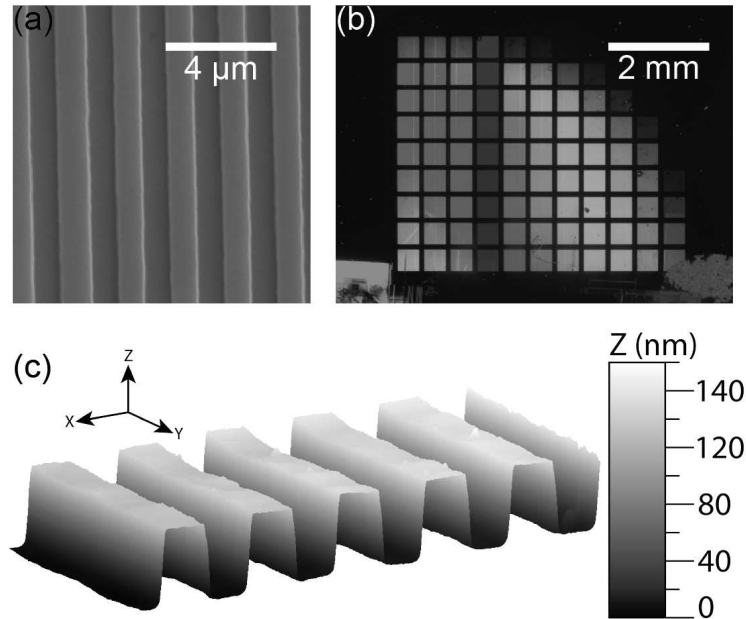


Figure 2.10: Fabrication characterisations: (a) SEM image of nanoribbon shape plasmonic antennas, (b) optical microscopy image of the processed sample, each square is a $500 \times 500 \mu\text{m}^2$ region with each nanoribbons of different width, and (c) 3D reconstruction image obtained by AFM. The structure is a spacer layer of 500 nm thickness (doped $1 \times 10^{19} \text{cm}^{-3}$) sandwiched between two highly doped layers ($4 \times 10^{19} \text{cm}^{-3}$) of 1 μm and 110 nm thicknesses, respectively at the bottom and at the top.

2.4 Optical characterisations

At last the samples are processed into plasmonic nanoantennas and in this section, we develop their optical characterisation by first introducing the Fourier-transform infrared spectroscopy technique, well-known as FTIR. Then we will discuss the optical response of the plasmonic samples and how to make sure that they perform as expected.

2.4.1 Fourier-transform infrared spectroscopy

We previously introduced the notions of infrared radiation and light-plasma coupling and interactions. Now, the instrumentation and technology of FTIR is discussed as it is the main characterisation tool used during this work. FTIR spectroscopy traces back the absorption spectrum of an analyte, therefore the objective is to obtain a spectrum of high quality, which depends on different factors in terms of instrumentation and metrology.

FTIR is composed of a light source that emits in the spectral domain of interest, a wavelength selection mechanism, and a detector.

The light source is usually a broadband source obtained by incandescence as a solid is heated at high temperature. Solids used can be ceramics, or ‘globar’ for glowing-bar made of silicon carbide emitting from 8000 down to 50 cm^{-1} depending on the cooling method. The globar source is the one used in our experiments. On the other end of the beam path, a detector is characterised by its sensitivity, spectral domain, and quantum efficiency. The sensitivity is the smallest signal that can be measured by the detector, corresponding to the amount of light equal to the intrinsic noise. The quantum efficiency is the ratio of induced current over incident flux. A good detector is characterised by a low-level signal sensitivity and a high quantum efficiency, over the whole spectral domain. Still, noise is inevitable and is made of two components: (i) the detection noise associated to random variations of flux during the measure, and (ii) the dark noise which correspond to the signal produced by the detector in absence of light.

Several detector technologies exist such as the thermal detector DTGS (deuterated triglycide sulfate) that converts heat into an electric signal upon exposition, this detector works at ambient temperature but has a limited sensitivity. SCs alloy mercury cadmium telluride (MCT) are widely employed as IR detectors, known for their high sensitivity. This quantum detector is based on the absorption of light which excites the electrons of the SCs from the valence band to the conduction band. In the conduction band, the electrons can be collected and turned into an electric current proportional to the IR intensity. This detector requires nitrogen cooling in order to maintain a difference in carriers population between the valence and conduction bands, which conditions the signal-to-noise ratio (SNR).

The core mechanism of a FTIR spectrometer is based on the Michelson interferometer, by far the most encountered setup in modern FTIRs. The Michelson interferometer is based on interferences of a splitted beam as a function of a moving mirror, the resulting interferogram corresponds to the signal intensity as a function of the displacement of the moving mirror. To obtain a spectrum, one must then perform the Fourier transform (FT) operation of the interferogram, according to the Wiener-Khinchin theorem that states: ‘The FT of an autocorrelated function (in our case corresponding to the interferogram) has a spectral decomposition by the power spectrum’. Typically in practice, this operation is performed a first time on a reference, then on the analyte or sample and the ratio between the two spectra gives information on the sample only, getting rid of the background holding the environmental response as well as the source fluctuations. Figure [2.11](#) shows a photograph of the Hyperion 3000 FTIR coupled to a Schwarzschild-objective microscope.

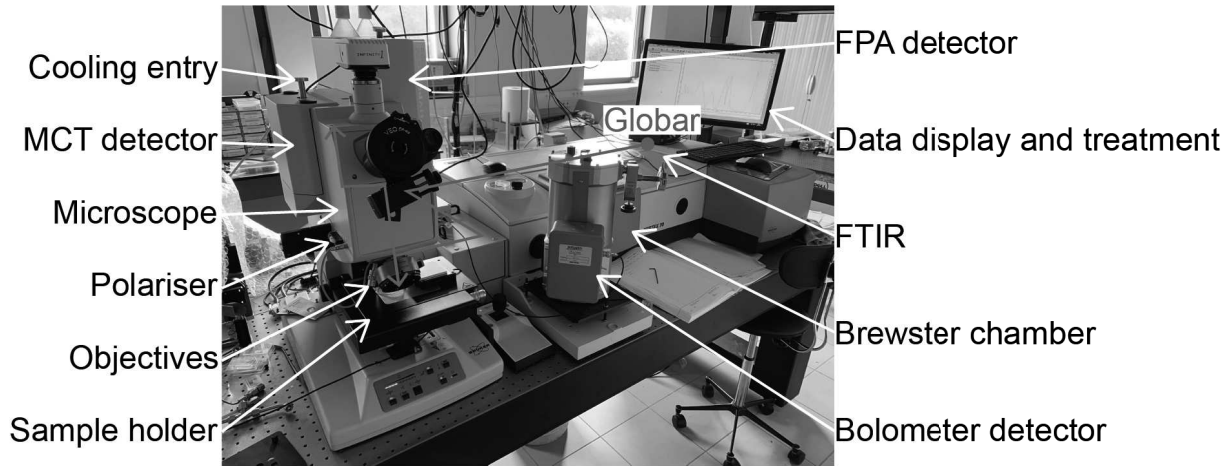


Figure 2.11: Photograph of the Hyperion 3000 FTIR used for optical characterisation of plasmonic samples and spectroscopy experiments. The IR beam path coming from the global source is highlighted as a red arrow.

2.4.2 Validation of the plasmonic samples

We discuss here the typical spectra obtained from the plasmonic samples and identify the markers indicating that the sample plays its role as expected. First we take a look at a reference spectrum, as example, in figure [2.12](#). This spectrum was acquired on plasmonic antennas shaped into nanoribbons of $\sim 1 \mu\text{m}$ width with a period of $2 \mu\text{m}$, averaged over 100 acquisitions of 1 cm^{-1} resolution, with TM-polarised light (nanoribbons long axis perpendicular to the incidence plane), from 400 up to 5000 cm^{-1} . This spectrum is single spectrum, which means it has not been divided yet by the background. From left to right, we observe several signatures:

- at 670 cm^{-1} , the peak corresponds to absorption of environmental CO_2 (deformation mode),
- close to 1000 cm^{-1} , we observe a sharp peak corresponding to the LSPR associated to the plasmonic antennas,
- around 1500 cm^{-1} , a large dip corresponds to the quarter-wavelength resonance associated with the Fabry-Perot cavity of the MIM structure,
- multiple absorption from environmental water (deformation mode) are observed from 1350 to 2000 cm^{-1} ,
- dual peaks at 2350 cm^{-1} correspond to valence mode of the CO_2 absorption,
- valence mode of water absorption are roughly located between 3500 and 4000 cm^{-1} ,
- finally, the oscillations observed from 2000 cm^{-1} up to end are Fabry-Perot resonances of higher-order from the MIM structure.

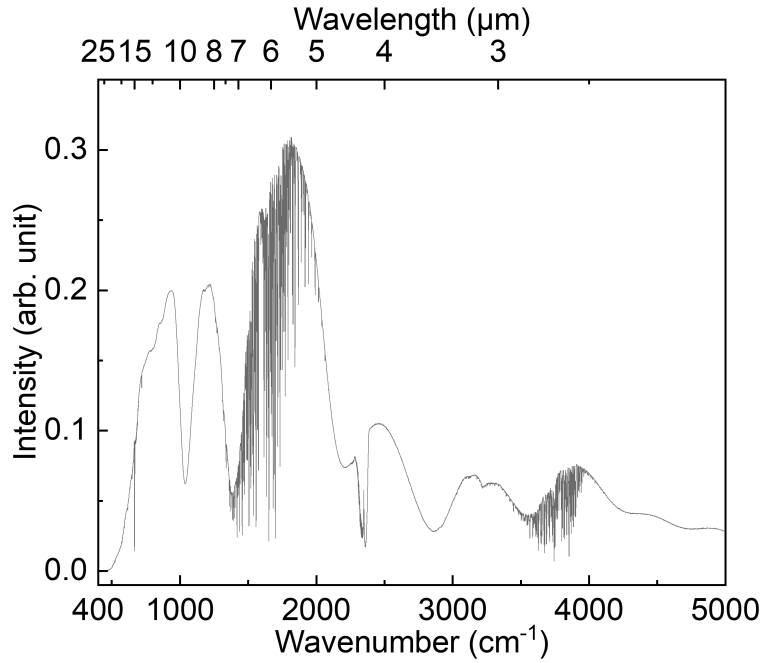


Figure 2.12: Single spectrum of the reflected light by a surface of $\sim 1 \mu\text{m}$ wide nanoribbons plasmonic antennas.

Subtracting the background, *i.e.*, removing the environmental influence, leads to the reflectance spectrum in figure [2.13](#). We observe that the spectrum is free from the spectral signatures of the environment such as CO_2 and water, therefore the spectrum corresponds to the optical response coming from the plasmonic sample only. The markers such as the LSPR and the resonances coming from the Fabry-Perot cavity are much clearer. We can divide the spectrum in three main regions according to the plasma frequencies ω_{p1} and ω_{p2} of the metallic layers (antennas and bottom mirror layer) and the spacer layer composing the MIM structure, respectively.

1. Frequencies below ω_{p2} , so that $\omega < \omega_{p2}$, corresponding to the dark grey region, show a reflectance close to unity in agreement with the fact that frequencies below the plasma frequencies are completely reflected as the light electric field is screened by the free carriers of the material. All the layers of the MIM structure behave as metal.
2. In the light grey region, at frequencies $\omega_{p2} > \omega > \omega_{p1}$, the spacer layer does not cancel anymore incident light and therefore it acts as a dielectric, while the top and bottom layers remain metallic. This spectral range correspond to the MIM behaviour of the structure, which means it is the range within which the structure behave as intended and indeed, we do observe the LSPR in this light grey region.
3. Finally, the white region, at frequencies $\omega > \omega_{p1}$, implies that light oscillates faster than the plasma of the layers composing the structure and it is not canceled anymore. In this range, the structure is completely dielectric, which is corroborated by the fact that the reflectance drops close to zero in the Fabry-Perot resonances minima.

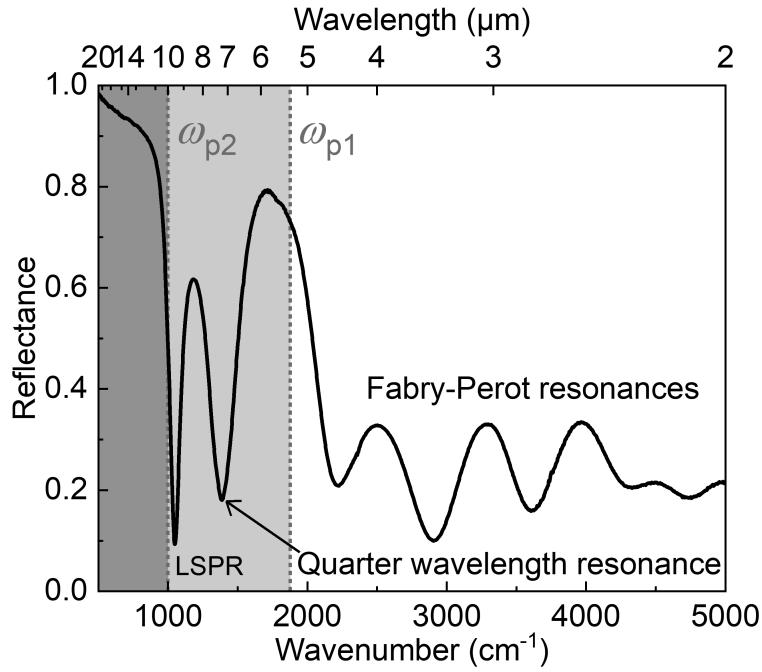


Figure 2.13: Reflectance spectrum from $\sim 1 \mu\text{m}$ wide nanoribbons plasmonic antennas.

Conclusion

This second chapter focused on the conception, design, growth, fabrication and characterisations of the plasmonic samples. This thorough process allows to understand and control the entire manufacturing chain from the very beginning: commercially bought wafers and electromagnetic simulations, to the end: sample characterisations and validation for applications. In the end, the accordance of electromagnetic simulations (figure 2.2) with experimental reflectance measurements (figure 2.13) demonstrates (1) the validity of RCWA-based EM simulations and the physical and material parameters chosen, (2) the high quality of MBE growth, (3) the feasibility and controllability of the fabrication process by EBL and dry etching, and (4) the expected performance of the designed plasmonic sample, ready to be used for practical applications. Every experimental steps are characterised and corroborated by EM simulations. Once the samples have been fabricated, they will be studied in detail. ENZ materials and the associated plasmonic effects are presented in the next chapter, before moving on to the final application: the detection by spectroscopy of CWAs in gas phase.

Chapter 3

Study of plasmonic ϵ -near-zero effects in the infrared with III-V semiconductors

Introduction

The third chapter focuses on the design, fabrication and characterisation of ENZ structures and their associated plasmonic effects. The following study about ENZ materials based on III-V SCs plasmonics is important to demonstrate how this class of materials can be employed for tailoring the optical response of ENZ-based plasmonic devices for sensing applications such as spectroscopy of OPs in gas phase. The first part introduces the design of three ENZ samples. Then their optical characterisations are presented, and we introduce how an ENZ-based MIM structure behaves in terms of its optical response. This rather long introduction is necessary before discussing more complex phenomena associated to the ENZ nature of the structure: the LSPR pinning and the dispersive nature of the ENZ materials, respectively the third and fourth part.

First, we will address the LSPR pinning with a thorough study of both the antenna width and the spacer doping level, *i.e.*, various ENZ regimes, over the optical response of plasmonic antennas. Afterwards, we demonstrate that this pinning phenomenon is spectrally localised and not as ‘radical’ as reported in the literature. Second, we will discuss the dispersive nature of ENZ media by studying their effective refractive index and the phase at reflection associated to the antennas. Experimental results are corroborated by RCWA and FDTD simulations, respectively for the optical response and the dispersion relation of this novel III-V SCs-based M-ENZ-M architecture. We demonstrate that it serves as a promising vehicle for the study of plasmon-ENZ effects as it can be astutely engineered to the desired application, such as spectroscopy, as it will be presented in chapter 4.

3.1 Presentation of the samples

As a reminder, ENZ refers to a spectral range within which a material, or a structure, displays a minimum for the real part of its permittivity, theoretically close to zero. First, from equation [1.2], we know that the permittivity is a function of the plasma frequency, which is why, one mean to obtain the ENZ behaviour of the structure, is to operate close to the plasma frequency of the material composing the structure. Second, from equation [1.3], we know that the plasma frequency is related to the free carrier density N , a parameter that we can control via doping. As a consequence, we studied three different samples, distinguishable by their plasma frequency ω_p (the term plasma frequency is used as a generic term to express both the plasma pulsation or the plasma wavenumber) and their spacer doping level N_s . Figure [3.1] shows the structure of the three studied samples.

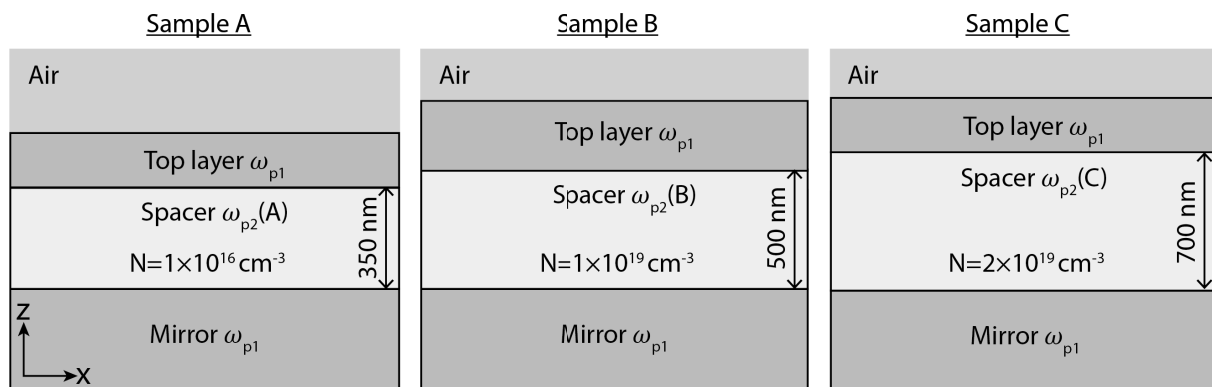


Figure 3.1: Schematic diagrams of the three studied M-ENZ-M samples. The grey layers are highly-doped SCs with $N \approx 4 \times 10^{19} \text{ cm}^{-3}$. The yellow layer of each sample is the ENZ-active layer, with different doping levels associated to three different ENZ regime frequency. The samples A, B and C are respectively doped 1×10^{16} (nid), 1×10^{19} , and $4 \times 10^{19} \text{ cm}^{-3}$.

The structure is based on a MIM design, with the particularity that the insulator layer (represented in yellow) is doped so that it has an ENZ regime at different spectral ranges. In our case, the insulator layer is referred as the spacer layer, characterised by a plasma frequency noted ω_{p2} , while the metallic layers are characterised by a plasma frequency ω_{p1} . The three ENZ layers studied are doped non-intentionally doped (nid), corresponding to $1 \times 10^{16} \text{ cm}^{-3}$, and intentionally doped at $1 \times 10^{19} \text{ cm}^{-3}$, and $2 \times 10^{19} \text{ cm}^{-3}$ respectively for samples A, B, and C. The metallic layers are composed of highly-doped InAsSb:Si ($N \approx 4 \times 10^{19} \text{ cm}^{-3}$) with a plasma wavelength of $\lambda \approx 5 \text{ }\mu\text{m}$, corresponding to a plasma frequency of $\omega_{p1} \approx 3.5 \times 10^{14} \text{ rad.s}^{-1}$. For all samples, $\omega_{p1} > \omega_{p2}$ to ensure a MIM behaviour at frequencies $\omega_{p1} > \omega > \omega_{p2}$. The table [3.1] sums up the material parameters composing the samples.

The three insulating ENZ layers have doping levels that correspond to three different ENZ regime, close to their plasma frequency, which can be calculated from the Lorentz-

Drude model. Figure 3.2 shows the real part of the permittivity ϵ expressed as a function of the wavelength (μm) and the wavenumber (cm^{-1}), for three different doping levels: $1 \times 10^{16} \text{ cm}^{-3}$ (nid), $1 \times 10^{19} \text{ cm}^{-3}$, and $2 \times 10^{19} \text{ cm}^{-3}$. Their corresponding ENZ regime occurs as the lines cross the ENZ dashed red line, *i.e.*, the real part of the permittivity approaches zero. Samples A, B, and C respective ENZ regime occurs around 130, 10, and 7.7 μm (corresponding to 77, 1000, and 1300 cm^{-1} , respectively).

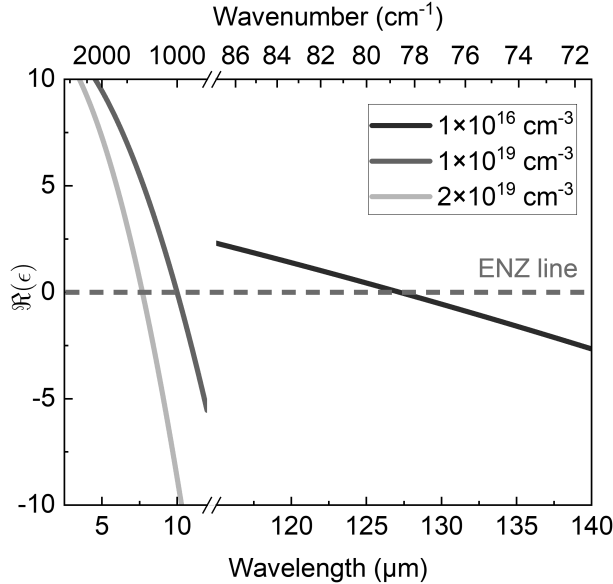


Figure 3.2: Real part of the permittivity ϵ expressed as a function of the wavelength (μm) and the wavenumber (cm^{-1}) for three different doping levels: 1×10^{16} (nid), 1×10^{19} , and $2 \times 10^{19} \text{ cm}^{-3}$. The dashed red line highlights the wavelength at which the real part of the permittivity crosses zero; it is the ENZ line. The permittivity ϵ is calculated with the Lorentz-Drude model. Be careful of the horizontal axis break.

After careful numerical design of the samples using the Lorentz-Drude model and RCWA simulations, the three samples were grown and a wide range of plasmonic nanoantennas, shaped into nanoribbons, were fabricated by EBL in a clean room. The growth and fabrication were evaluated as described in the previous chapter to ensure that the samples are as expected, such that their optical response should be similar to numerical simulations. Figure 3.3 shows an optical microscopy image of each sample, highlighting the large number of different regions, each composed of nanoribbons with different widths. The problematic addressed is as follows: we study the influence of an ENZ layer within a MIM structure, over the optical response of plasmonic nanoantennas. From the literature review in chapter 1, we expect that various well-known plasmonic effects shall be influenced by the presence of a layer with a vanishingly small permittivity. The next section dives into the optical characterisations of each samples, that will serve as the groundwork for the study of these plasmon-ENZ phenomena.

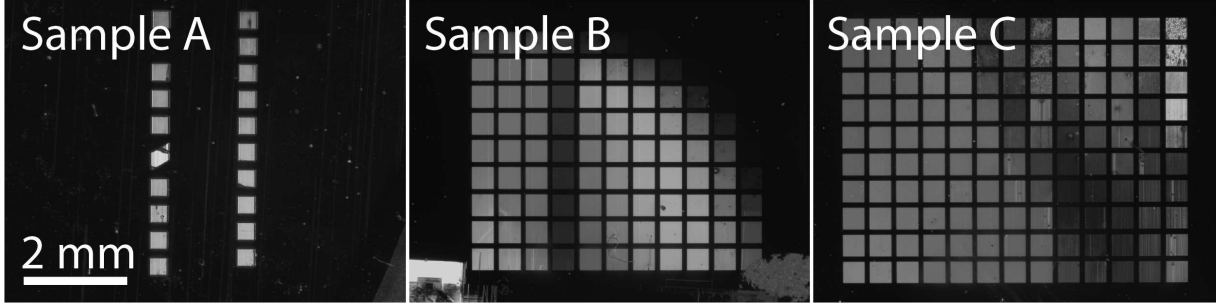


Figure 3.3: Optical microscopy images of ENZ samples A, B, and C. Each square correspond to a different combination of a defined size and dose applied to the electron beam current during the writing process of the lithography, resulting in various nanoribbon antenna widths.

3.2 Optical characterisation

3.2.1 Bulk material characterisation

The first optical characterisation performed on each sample is done on the wafer right after the growth in order to verify their doping level by Brewster measurements. Figure 3.4 shows the Brewster measurements probing the free carrier concentration and therefore can be used to retrieve the doping level of each sample. We observe a peak corresponding to the highly-doped layers (ω_{p1}), and we also observe for samples B and C, a peak corresponding to the doped insulating spacer layer (ω_{p2}) acting as the ENZ layer. Additionally, the plasma damping rates γ were extracted with a home-made code based on transfer-matrix formalism.

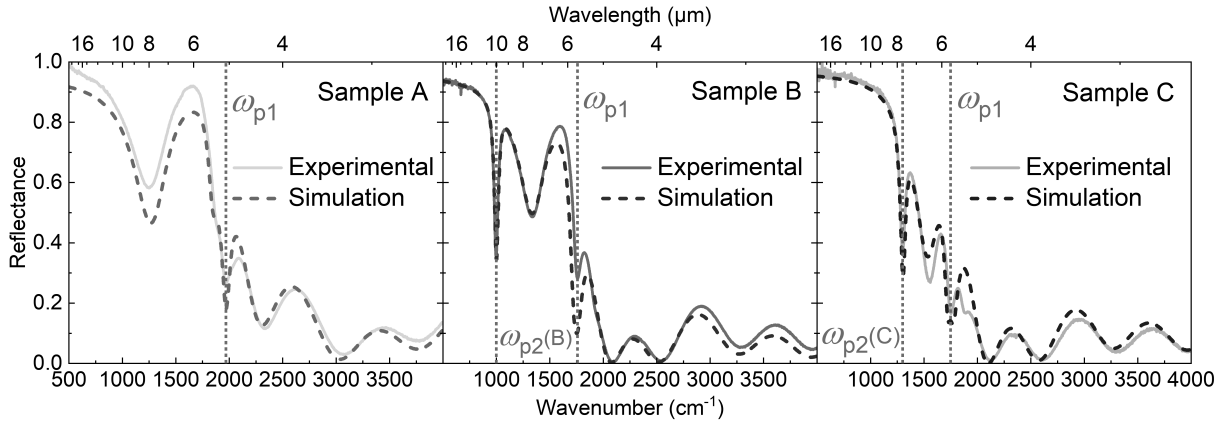


Figure 3.4: Optical reflectance measurements of the Brewster mode for all three ENZ samples. Simulations are performed using transfer-matrix method on Matlab.

For sample A, since the spacer layer is n-doped, so that its plasma wavelength is far in the THz ($\lambda_p = 130 \mu\text{m}$), we do not observe the peak corresponding to the free carrier collective absorption (at ω_{p2}) of this layer. Contrarily to samples B and C, this ω_{p2} peak

is observed at 10 and 7.7 μm , respectively. This demonstrates that the doping level of the experimental ENZ layers perfectly match the expected values established during the design of the structures. The layer thicknesses were all measured by HRXRD. The informations regarding the materials, thicknesses, doping levels and their associated plasma frequencies, for the three different ENZ structures are summarised in table [3.1](#). It is important to keep in mind that $\omega_{p1} > \omega_{p2}$ so that the structure behave as a MIM structure as intended, between ω_{p1} and ω_{p2} .

	Sample A	Sample B	Sample C
Top layer	InAsSb:Si	InAsSb:Si	InAsSb:Si
N_a (cm^{-3})	6×10^{19}	5×10^{19}	4.5×10^{19}
ω_{p1} (rad.s^{-1})	3.7×10^{14}	3.5×10^{14}	3.3×10^{14}
γ_1 (rad.s^{-1})	1.5×10^{13}	1.3×10^{13}	1.2×10^{13}
Spacer layer	GaSb	InAsSb:Si	InAsSb:Si
N_s (cm^{-3})	1×10^{16} (nid)	1×10^{19}	2×10^{19}
ω_{p2} (rad.s^{-1})	1.5×10^{13}	1.9×10^{14}	2.4×10^{14}
γ_2 (rad.s^{-1})	1×10^{12}	8×10^{12}	1×10^{13}
Mirror layer	InAsSb:Si	InAsSb:Si	InAsSb:Si
N_a (cm^{-3})	6×10^{19}	5×10^{19}	4.5×10^{19}
ω_{p1} (rad.s^{-1})	3.7×10^{14}	3.5×10^{14}	3.3×10^{14}
γ_1 (rad.s^{-1})	1.5×10^{13}	1.3×10^{13}	1.2×10^{13}
Substrate	GaSb	GaAs	GaSb

Table 3.1: Materials parameters. nid stands for non-intentionnaly doped, which is around $\approx 1 \times 10^{16} \text{ cm}^{-3}$. N_a and N_s respectively correspond to the doping level of the metallic layers and spacer layers. ω_p are plasma frequencies and their associated losses γ .

3.2.2 Processed samples characterisation

After the bulk optical characterisation the parameters of grown samples were validated, fabrication of plasmonic nanoantennas was performed and the table [3.2](#) sums up the different geometrical parameters of each ENZ samples, with the defined nanoribbons width range.

	h_a (nm)	h_s (nm)	Period (μm)	Widths (μm)
Sample A	100	375	0.8	[0.21-0.46]
Sample B	110	500	2.0	[0.22-1.43]
Sample C	100	700	2.0	[0.29-1.75]

Table 3.2: Measured geometrical parameters of ENZ samples. h_a and h_s refer to the thickness of the antennas (top layer) and the spacer ENZ layer, respectively. The width column refers to the range $[w_1-w_2]$ of nanoribbons size from the smallest w_1 to the largest w_2 with numerous width in between.

According to Tables [3.1](#) and [3.2](#), the antennas period, the spacer thickness as well as the substrate are different for each samples. We hereby address these differences and their potential impact on the samples response. Regarding sample B, the GaAs substrate theoretically introduces more crystalline defects (due to a lattice mismatch of $\approx 7\%$ at InAs/GaAs interface), resulting into stronger plasma losses γ . However, in practice, by optically probing the Brewster mode, we did not identify any significant loss increase through broadening of the Brewster mode peak (figure [3.4](#)), meaning that the substrate material does not significantly impacts the optical response of the structure. Second, the antennas period (800 nm for sample A, compared to 2 μm for samples B and C) slightly changes the antennas duty-cycle and, therefore, the structure effective refractive index which itself impacts the LSPR frequency [[220](#), [221](#)]. Third, the spacer thickness has direct consequences on the quarter-wavelength resonance, which has been found to influence the LSPR frequency through strong coupling phenomenon [[222](#)]. Although having an influence on the LSPR, these differences do not hinder the understanding of the chapter problematic, which is about the ENZ-based insulator within a MIM structure, and its influence on the plasmonic response.

The second optical characterisation is performed after the fabrication process in order to study the optical response of the processed samples by FTIR spectroscopy. The figure [3.5](#) displays a standard FTIR reflectance measurement of the optical response, as a function of the wavenumber, from 500 up to 5000 cm^{-1} , respectively 20 down to 2 μm . The whole structure is metallic at frequencies lower than ω_{p2} (dark grey region), the spacer layer then becomes dielectric while the top and bottom layers remain metallic at frequencies between ω_{p2} and ω_{p1} (light grey region), and finally, at frequencies greater than ω_{p1} the whole structure becomes dielectric (white region). We observe that the LSPR, not to be confused with the quarter wavelength resonance ($\lambda/4$), occurs within the light grey region, between the two plasma frequencies $[\omega_{p2} - \omega_{p1}]$, corresponding to the frequency range within which the structure behaves as a MIM structure. Furthermore, the LSPR corresponds to a near perfect absorption, which is expected for such a structure.

In the end, from Brewster measurements (figure [3.4](#)), we confirmed the doping levels of the layers composing the ENZ-based MIM structure for all three samples, corroborated by transfer-matrix method EM simulations. Following that, FTIR spectroscopy measurements (figure [3.5](#)) confirmed that the samples operate as expected with a perfect absorption and a LSPR occurring when the structure behaves as a MIM. The next two sections concern the study of the ENZ spacer layer over the optical response of the plasmonic samples and how it challenges our certitudes about well-known plasmonic effects.

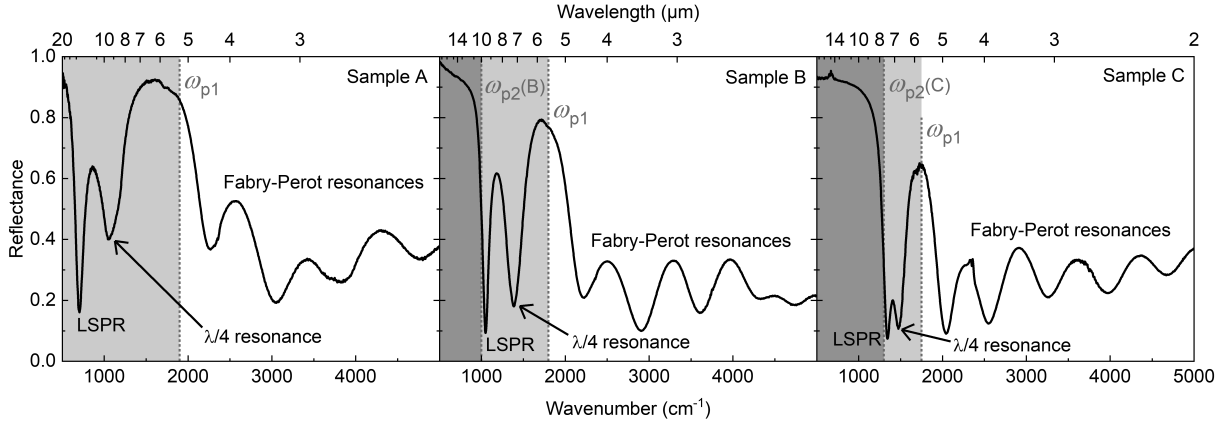


Figure 3.5: Typical reflectance measurements obtained by FTIR spectroscopy samples A, B and C. The whole structure is metallic in the dark grey region, while it is dielectric in the white region. Within the light grey region, the top and bottom layers are metallic, while the spacer layer is dielectric. The white/light grey and light grey/dark grey interfaces correspond to the materials plasma frequencies, respectively, ω_{p1} and ω_{p2} , highlighted as red dotted lines.

3.3 The plasmonic resonance pinning phenomenon

3.3.1 Experimental results

Study of the ENZ layer doping level

First, we study the influence of the spacer layer doping level N_s on the optical response of the structure. Figure 3.6 shows the experimental (full lines) and simulated (dashed lines) optical responses of 500 nm-width nanoantennas for all three samples. We observe that the numerical electromagnetic simulations performed by RCWA (with parameters from tables 3.2, 3.1) match the experimental results. The LSPR frequencies are different for each sample; for samples A, B and C, the LSPR is at 640, 1240 and 1400 cm^{-1} , corresponding to spacer layer doping levels of 1×10^{16} , 1×10^{19} and $2 \times 10^{19} \text{ cm}^{-3}$, respectively. Thus, the LSPR frequency increases as the doping level of the material, on which the antennas are fabricated, increases. This is in accordance with the fact that since plasmonic modes arise at metal/dielectric interface, its properties depend on the nature (*i.e.*, the permittivity) of the materials composing the interface. Therefore as the three ENZ layers have different indices, the LSPR is directly affected by it. Not only doping gives an additional degree of freedom over the plasma frequency of the plasmonic material, but it also brings the ability to adjust the optical properties of the insulator supporting the plasmonic mode. It therefore becomes obvious that it is possible to engineer both the metal and the insulator optical properties, made of doped III-V SCs, to the desired application, from the THz, up to the MIR.

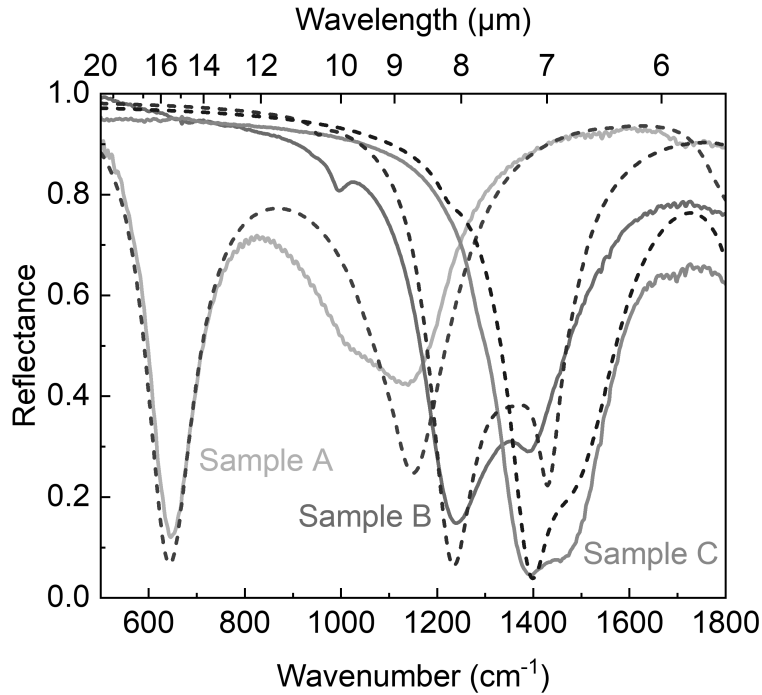


Figure 3.6: Reflectance spectra of 500 nm width nanoantennas for all three samples. The spectral range focuses on the LSPR. Full lines are experimental and dashed lines are RCWA numerical simulations. The LSPR red-shifts as the spacer layer doping level decreases: green: $1 \times 10^{16} \text{ cm}^{-3}$ (nid), red: $1 \times 10^{19} \text{ cm}^{-3}$, blue: $2 \times 10^{19} \text{ cm}^{-3}$.

Study of the plasmonic nanoribbons

Second, we study the influence of the nanoantenna width on the optical response of the structure. Figure 3.7 displays the FTIR measurements of the optical responses of various antenna widths. We observe the characteristic red-shift of the LSPR (from blue to yellow curves) as the antenna width increases (represented by the black arrow). We observe that as the antenna width increases, the associated LSPR slows down when we reach the plasma frequency ω_{p2} of samples B and C, *i.e.*, near the ENZ regime, of the spacer layer below the nanoantennas. This phenomenon is not observed for sample A because its spacer layer is non-intentionally doped, thus its free carrier concentration lies around $1 \times 10^{16} \text{ cm}^{-3}$, corresponding to a plasma frequency in the THz region according to equation 1.3; therefore the probed infrared spectral region is too far from its spacer ENZ regime to observe the LSPR pinning. One must keep in mind that fabricated antennas width, on samples B and C, range from 200 nm up to nearly 2 μm , as opposed to sample A for which antennas of width greater than $\approx 600 \text{ nm}$ have LSPR frequencies out of the MCT detector limit ($\approx 500 \text{ cm}^{-1}$ or 20 μm). We conclude that the optical response of the structures, not only depends on the nanoantenna width, but is also strongly dependent on the nature of the layer below the nanoantennas.

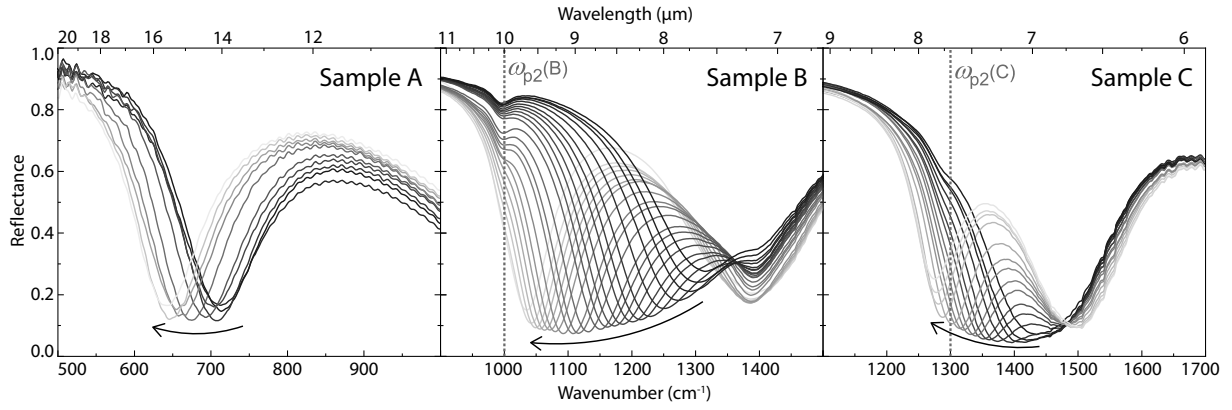


Figure 3.7: Experimental reflectance spectra with increasing nanoantennas widths (from blue to yellow) of samples A, B and C. The black arrows highlight the spectral red-shift of the LSPR as the nanoantennas width increases (cf. Table 3.2).

ENZ layer influence over the size-resonance relation

Finally, we evaluate the red-shift observed in Figure 3.7, as a function of the spacer layer doping level influence, observed in Figure 3.6. Figure 3.8 shows the relation between the LSPR frequency (and wavelength) as a function of the antenna width for each sample. Experimental results are corroborated by numerical simulations performed by RCWA. We observe that as the antenna width increases, the LSPR frequency decreases (*i.e.*, the wavelength increases: red-shift). The striking result is that for samples B and C, the red-shift is much slower than it is for sample A. Indeed, a width variation of 400 nm results in a redshift of around ≈ 250 , ≈ 100 and ≈ 50 cm^{-1} for samples A, B and C, respectively. This “slow-down” of the red-shift accentuates for samples B and C as the LSPR frequency reaches the plasma frequency of their respective spacer layer, $\omega_{p2}(\text{B}) \equiv 1000$ cm^{-1} and $\omega_{p2}(\text{C}) \equiv 1300$ cm^{-1} . As the spacer layer doping level increases and gets closer to the plasma frequency ω_{p1} of the metal layers composing the MIM, the LSPR gets pinned within an increasingly narrower spectral range, defined as $[\omega_{p2} - \omega_{p1}]$.

In sum, close to the plasma frequency, *i.e.*, in the ENZ regime, the LSPR frequency becomes nearly independent on the geometrical properties of the structures (Table 2), and conversely, the LSPR frequency becomes nearly dependent only on the material bulk properties of the structure (Table 1), themselves governed by the doping levels of the different layers. This results implies that within the ENZ regime, a structure will have its optical response dominated by the dispersive behaviour (material dispersion), rather than by the geometry of the structure. Employing III-V semiconductors allowed us to clearly highlight this LSPR pinning phenomenon, and it demonstrates how this class of materials is particularly interesting to study ENZ-based plasmonic phenomena in the IR.

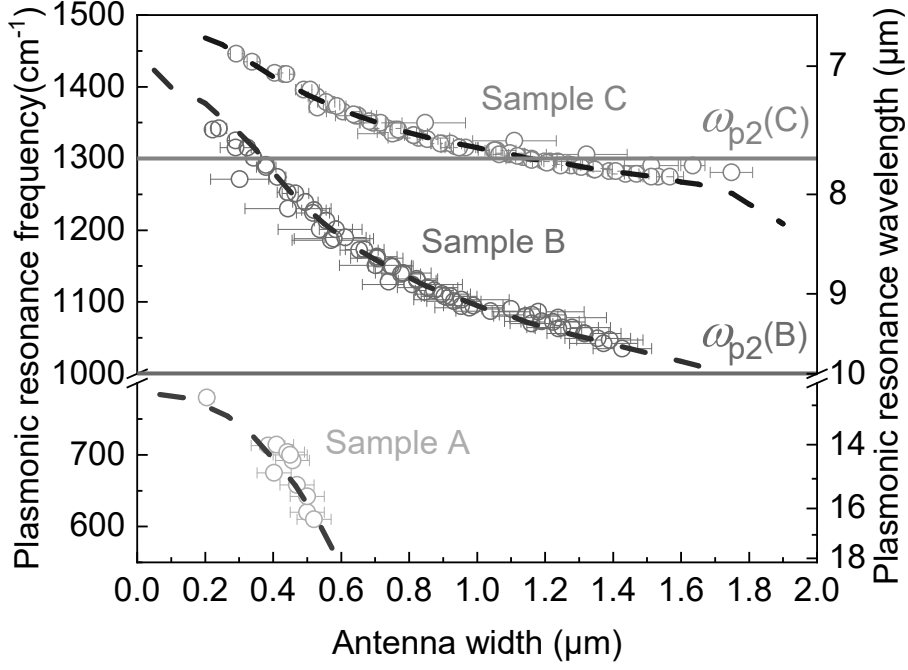


Figure 3.8: LSPR frequencies function of the nanoantennas width. Circles are experimental results, error bars are measured standard deviation of the nanoantennas width, dashed lines are RCWA numerical simulations and full lines are plasma frequencies (*i.e.* ENZ lines) of samples B and C, respectively at 1000 cm^{-1} and 1300 cm^{-1} .

3.3.2 Theoretical results

Solving the dispersion relation

The chosen approach to further understand physics fundamentals behind the LSPR pinning and its associated dispersive feature was to determine the dispersion relation of the ENZ-based MIM structure. The dispersion relation is an interesting representation as it provides light wavevector, along a direction, as a function of its frequency, and consequently, how the whole considered photonic structure influences and interacts with light, which is the important point behind the exponential development of novel photonic structures these past 20 years.

The dispersion relation of a four layers structure made of: air/InAsSb:Si (n++)/InAsSb:Si (n)/InAsSb:Si(n++), similar to the air-M-ENZ-M system depicted in figure [3.1](#), can expressed be as follows:

$$e^{2k_3d_3} = \frac{\left(\frac{k_1}{\epsilon_1} + \frac{k_2}{\epsilon_2}\right)\left(\frac{k_2}{\epsilon_2} - \frac{k_3}{\epsilon_3}\right)\left(\frac{k_4}{\epsilon_4} - \frac{k_3}{\epsilon_3}\right)e^{2k_2d_2} - \left(\frac{k_2}{\epsilon_2} - \frac{k_1}{\epsilon_1}\right)\left(\frac{k_2}{\epsilon_2} + \frac{k_3}{\epsilon_3}\right)\left(\frac{k_4}{\epsilon_4} - \frac{k_3}{\epsilon_3}\right)}{\left(\frac{k_1}{\epsilon_1} + \frac{k_2}{\epsilon_2}\right)\left(\frac{k_2}{\epsilon_2} + \frac{k_3}{\epsilon_3}\right)\left(\frac{k_4}{\epsilon_4} + \frac{k_3}{\epsilon_3}\right)e^{2k_2d_2} - \left(\frac{k_2}{\epsilon_2} - \frac{k_1}{\epsilon_1}\right)\left(\frac{k_2}{\epsilon_2} - \frac{k_3}{\epsilon_3}\right)\left(\frac{k_4}{\epsilon_4} + \frac{k_3}{\epsilon_3}\right)} \quad (3.1)$$

With each of the aforementioned layers, respectively considered as a medium. Each medium is characterised by d_i the thickness of the layer, ϵ_i the permittivity of the medium, and k_i the wavevector within the medium, expressed as follows:

$$k_i = \sqrt{\epsilon_i \left(\frac{\omega}{c}\right)^2 - k_x^2} \quad (3.2)$$

The dispersion relation of a two layers structure is easily solved as it has analytical solutions, which is not the case for structure with > 2 layers. Three layers structure have been studied in the past and analytical approximations have been found. Structures with multiple layers of the same materials, such as a superlattice, have also found analytical solutions since Economou [45]. However, structures of ≥ 4 layers of different materials have a dispersion relation that finds little to none (depending on the materials) simplifications, leading to equation [3.1] for our case. This type of equation is known as a transcendental equation, of the form $x = \exp(-x)$, meaning that it is not possible, with classical algebra, to isolate the variable under study. In our case with equation [3.1], it is not possible to express the wavevector along the interface k_x , as a function of the frequency ω , so that no analytical solutions exist. Solving this type of equation falls in the domain of complex analysis.

The original method implemented in order to solve this equation was to numerically observe the shape of the equation by scanning the real and imaginary parts of the wavevector, along the frequency. Representing the equation in the complex plane $\{\text{Re}(k_x); \text{Im}(k_x)\}$ allows one to visually identify the solutions of the equation in the form of poles and/or zeros, depending on how the equation is coded. Figure [3.9] shows a 3D and 2D representation, respectively (a) and (b) of a transcendental dispersion relation equation for a three layers structure. We observe that solutions of such equation are in the form of minima, corresponding to descending peaks or black spots, *i.e.*, zeros.

The second step is, after identifying the solutions, to track them along the complex plane, and as a function of the frequency. There are several peak-finding methods already implemented in software such as gradient-based methods. Other more advanced methods include Newton's and Muller's methods, and image processing methods. We opted for the robust and well-known Newton's method which is a numerical analysis method based on a root-finding algorithm. Long story short, we faced numerous problems of all kinds including: (i) spurious solutions, (ii) multiple solutions with different starting points (which are necessary to initiate the algorithm), (iii) large order of magnitudes, (iv) large difference between the real and imaginary parts of a solution, (v) solution screening, (vi) numerical resolution limitations, (vii) computation time, (viii) shape deviation of the equation background, (ix) large gaps between the solutions' order of magnitude (x) different signs of solutions (poles or zeros), and (xi) numerical aliasing and harmonics. Despite the failure of this method, it is important to understand that diving into this problem proved to be

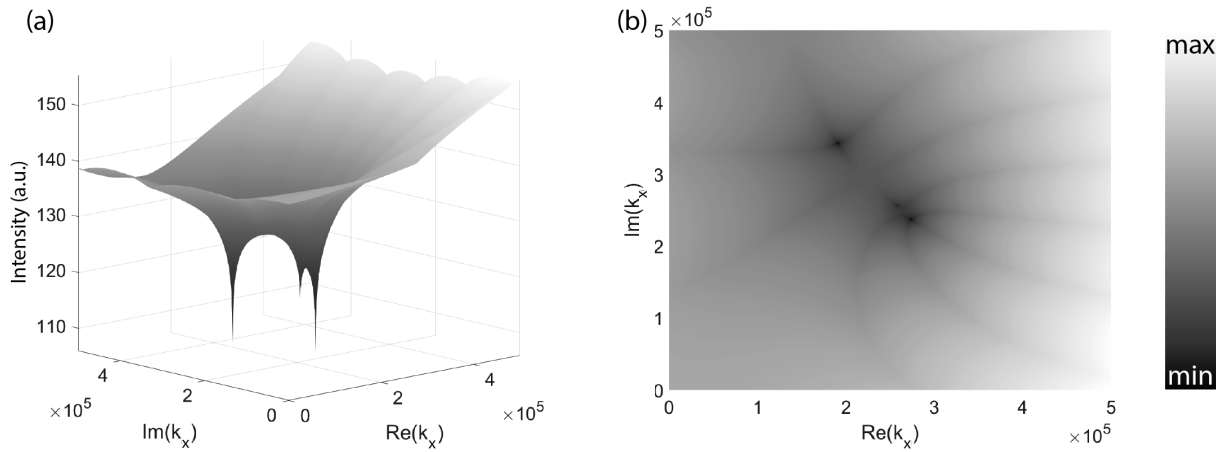


Figure 3.9: (a) 3D and (b) 2D representations of dispersion relation equation for a three layers photonic structure (air/InAsSb:Si (n++)/InAsSb:Si (n+)). Grey scale represents the intensity of the calculus (arb. unit)

crucial in terms of understanding about the problem we wished to solve. The next section shows how we approached the problem using FDTD simulations. Further information regarding the dispersion relation can be found in annex [B](#).

Numerical calculus of the photonic bandstructure

The alternative method is to employ finite-difference time-domain (FDTD) simulations. It allows to calculate the dispersion relation for the stacking considered in figure [3.1](#). The model used can be employed to calculate the bandstructure of any photonic devices. The FDTD software randomly implements multiple broadband dipoles that will excite all possible modes of the system. The wavevector k_x is specified by the Bloch boundary conditions while perfectly matched layer conditions are applied in all other directions. At frequencies where a mode (*i.e.*, a band) exists, the fields will propagate which means that an electromagnetic mode, such as SPPs, is supported. Conversely to other frequencies for which the fields do not propagate and disappear by destructive interference, this way we are able to discriminate between those two outcomes.

Figure [3.10](#) shows a screenshot from FDTD Lumerical software of the bandstructure calculator model. It might be difficult to obtain a result that can be exploited because many parameters impact the calculations. For example, the number of random dipoles and monitors, as well as their wavevector range, is important in terms of precision and calculation time. Also, losses are a major drawback because they significantly broaden the resonances such that the FDTD peak-finder algorithm is parasitised. Finally, the antenna periodicity was not taken into account because increasing the spatial dimensions of the FDTD simulation area, will decrease the wavevector range simulated in an inversely proportional manner. This results in bandstructure aliasing and hinders the interpretation

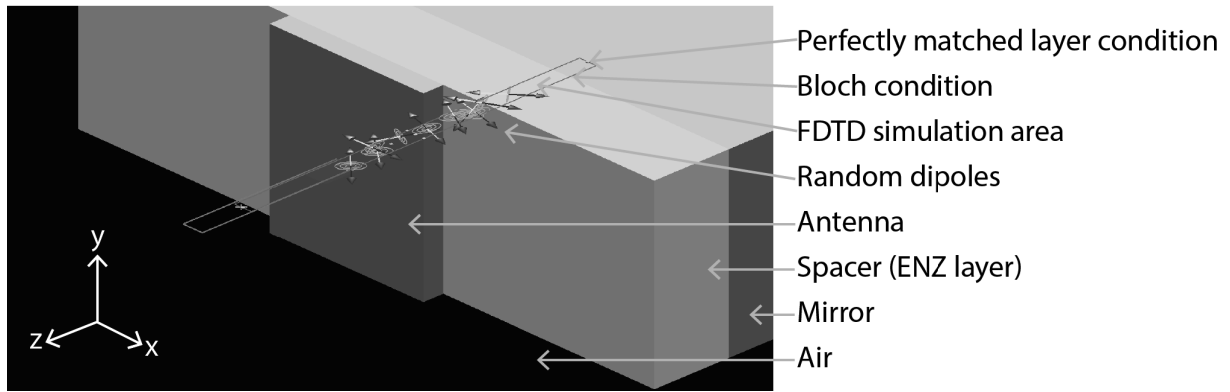


Figure 3.10: Screenshot from FDTD Lumerical software of the bandstructure calculator model displaying 10 randomly placed dipoles.

of the dispersion relation. For these reasons, we calculated the dispersion relation of the bulk structure, without taking into account the plasma losses and the antenna periodicity.

Figure 3.11 shows the dispersion relation of each sample, representing the light frequency ω (rad.s^{-1}), as a function of its wavevector k_x , expressed in m^{-1} , along the x direction. Coloured full lines correspond to solutions of the dispersion relation, associated with the propagation of electromagnetic modes, namely, plasmons. Since plasmons are surface waves propagating along an interface, they are considered as guided modes and their wavevector is often referred to as the propagation constant β in the literature.

We observe that experimental results lay on the upper part of the solution, confined in the frequency range $[\omega_{p2} - \omega_{p1}]$. The calculated solutions are characterised by a maximum: Asymptote 1, and a minimum: Asymptote 2. The Asymptote 1 is the well-established surface plasmons frequency $\omega_{sp} = \omega_{p1}/\sqrt{2}$. On the contrary, the Asymptote 2 is uncommon [223, 224]. Plasmonics commonly involves a metal/dielectric interface with the dielectric being air, while in this case, the dielectric is a doped semiconductor that behaves as an insulator at frequencies greater than ω_{p2} . We observe that the solution for a standard MIM structure (Figure 3.11 sample A) does not display the Asymptote 2; the latter arises as the doping level of the insulator of the MIM increases (Figure 3.11 samples B and C).

Two important conclusions can be drawn from this comparison between experimental and theoretical results. First, we observe that as the solution line approaches the plasma frequency of the insulator ω_{p2} , its slope flattens down having for consequence a slow down in the relation linking light frequency to its wavevector. This bending results from the fact that the real part of the permittivity of the spacer vanishes until it theoretically reaches zero at ω_{p2} .

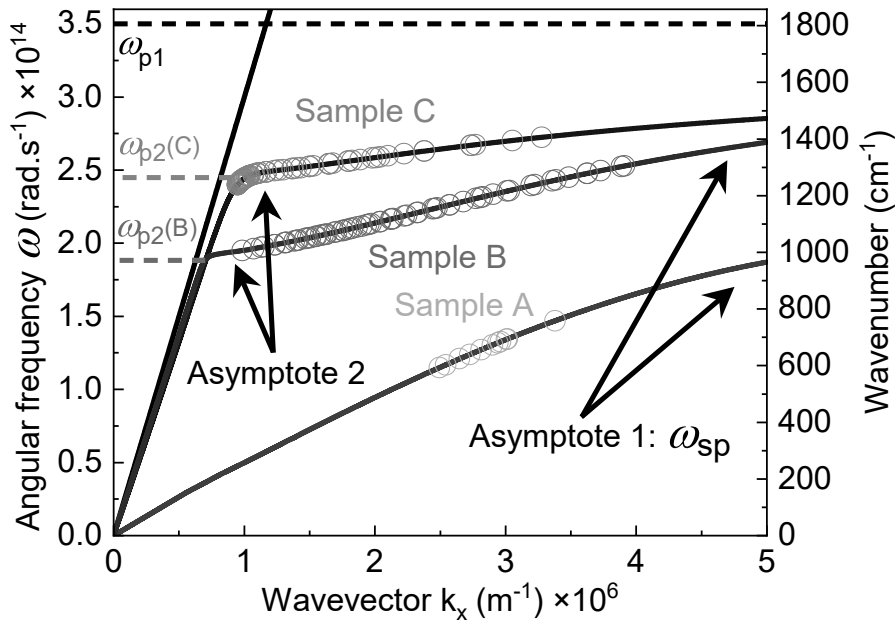


Figure 3.11: Dispersion relations expressed as the light frequency ω function of its wavevector along the x direction k_x . The stacking considered for the calculus is displayed in figure [3.1]. Dashed lines are plasma frequencies of the heavily-doped InAsSb layers ω_{p1} and doped InAsSb spacer ω_{p2} of both samples B and C. The black line correspond to the light line in air. Circles correspond to experimental LSPR frequencies.

Hence, the ϵ -near-zero behaviour of the spacer layer, as the working frequency approaches the plasma frequency ω_{p2} , is responsible for the LSPR pinning observed experimentally, represented by the Asymptote 2.

Second, since the excited plasmonic mode is associated to the MIM structure, one can play on the optical properties of both the metal and the insulator, in particular, as mentioned in the introduction, the dielectric permittivities $\epsilon(\omega)$ through their plasma frequencies ω_p . Therefore, having the ability to tune this parameter end up being a powerful asset of III-V semiconductors over other plasmonic materials traditionally employed. Since III-V semiconductors can be doped up to 10^{20} free carriers per cm^3 , their plasma frequency can be adjusted to the desired working range of any applications, from the THz up to the MIR, with great precision.

Beyond the plasmonic resonance pinning

We would like to draw reader's attention on the fact that, contrarily to the claim that it is not possible to move the LSPR beyond the pinning frequency, as long as an insulator exists within the considered system, e.g, air, then the SPP propagation persists at the new metal/dielectric interface. This finding can be appreciated for sample C, as observed in Figure [3.8]. Experimental results display LSPR frequencies beyond the plasma frequency of ω_{p2} . Consequently, we observe that part of the experimental results lay below the

plasma frequency of sample C on the dispersion relation solution of Figure 3.11. This implies that the nature of the plasmon has changed, i.e, the plasmon is not supported at the same interface as it was in the frequency range $[\omega_{p2} - \omega_{p1}]$.

Figure 3.12 displays the normalized electric field maps for sample C nanoantennas of 400, 800 nm and 1.2 μm width, respectively a), b) and c), at their respective LSPR frequency: 1432, 1344 and 1290 cm^{-1} . We observe that the smallest antenna, resonating at higher frequency, displays a maximum electric field at the antenna/spacer interface. As the width of the nanoantenna increases, the electric field migrates from the lower spacer/antenna interface to the antenna/air top interface, corroborating that the metal/dielectric interface supporting the plasmon changes when the LSPR frequency passes through a material transition, in this case, the plasma frequency. Figure 3.12 d) and e), respectively show the normalized magnetic field maps for the 400 nm and 1.2 μm wide antennas. We observe that the magnetic field is mainly confined within the spacer layer when it is dielectric, as one would expect for a MIM structure, as opposed to when the spacer becomes metallic at frequencies inferior to $\omega_{p2}(\text{C})$, then the magnetic field is pushed back in the air and the structure does not behave as a MIM anymore. These simulations confirm the experimental results and further evidence that III-V semiconductors and their associated fabrication techniques pave the way for a greater control of a plasmonic system optical response. It comes to light that this feature would greatly benefit and facilitate the tailoring of the plasmonic resonance to the absorption lines of molecules for the sensing by SEIRA.

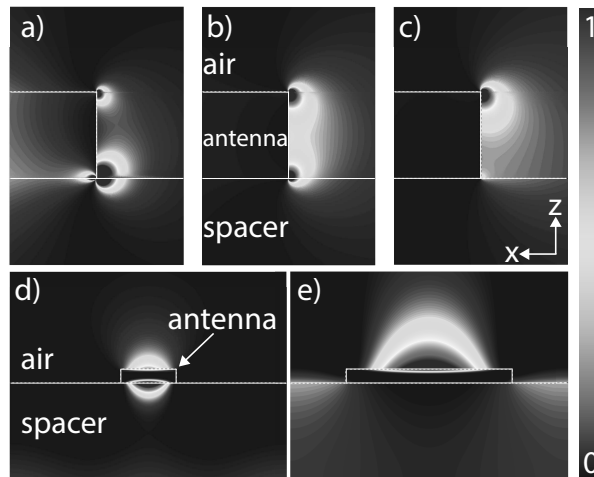


Figure 3.12: Normalized electric field maps $|E_x/E_0|^2$ for nanoantennas of 400 nm (a), 800 nm (b) and 1.2 μm (c) widths, at their respective LSPR frequencies 1432, 1344 and 1290 cm^{-1} . Normalized magnetic field maps $|H_y/H_0|^2$ for nanoantennas of 400 nm (d) and 1.2 μm (e), at their respective LSPR frequencies. Colorbar highlights the fields amplitude (arb. unit). Simulations performed by RCWA with sample C materials and geometrical parameters.

3.4 The dispersive behaviour associated to ENZ media

3.4.1 The effective index theory

We confirmed that the experimental results correspond to the dispersion relation solution by calculating the mode effective refractive index, with Equation [3.3] [203, 178], both theoretically from the solutions of Figure [3.11], and experimentally from the data gathered from Figure [3.8].

$$n_{\text{eff}} = \frac{ck_x}{\omega} = \frac{\lambda_{\text{LSPR}}}{2L} \left(m - \frac{\phi_r}{\pi} \right) \quad (3.3)$$

With c the light speed, k_x the wavevector along the interface, ω the angular frequency, $m = 1, 2, \dots$ the resonance order, λ_{LSPR} the plasmonic resonance wavelength, L the antenna length, and ϕ_r the phase of the modal reflection. We are interested in the fundamental resonance $m = 1$ and consider that the plasmonic antennas behave as classical half-wavelength antennas to fulfill the resonance condition, considering a modal reflection phase ϕ_r taking into account SPP reflections within the antennas.

Figure [3.13] represents the effective refractive index calculated from equation [3.3], expressed as a function of the wavelength and the angular frequency ω . We observe that the effective refractive index of the plasmon mode decreases drastically until plasma frequencies, as opposed to the surface plasmons frequency ω_{sp} at higher wavevector k_x , for which it is known that the effective refractive index increases.

3.4.2 The near-constant phase

The variation of the phase ϕ_r associated to the antenna length becomes marginal as the antenna resonance enters the ENZ regime, as depicted by the increasing density of experimental points within the ENZ cone shown in figure [3.14], meaning that the phase is nearly constant close to the plasma frequency [178].

These results are in agreement with what was reported in the literature as both a near-constant phase and a minimum effective refractive index have been reported and studied. Still, when it comes to determine the effective refractive index of the plasmon mode, the dispersion relation proved to be critical. Indeed, traditionally used effective refractive index models are inadequate for imperfect metal and insulator [220, 221]. Therefore, solving the dispersion relation of a photonic structure is a more rigorous approach when dealing with non-perfect metal (working near its plasma frequency) and non-perfect insulator (varying refractive index), for which very few approximations can be defined [225].

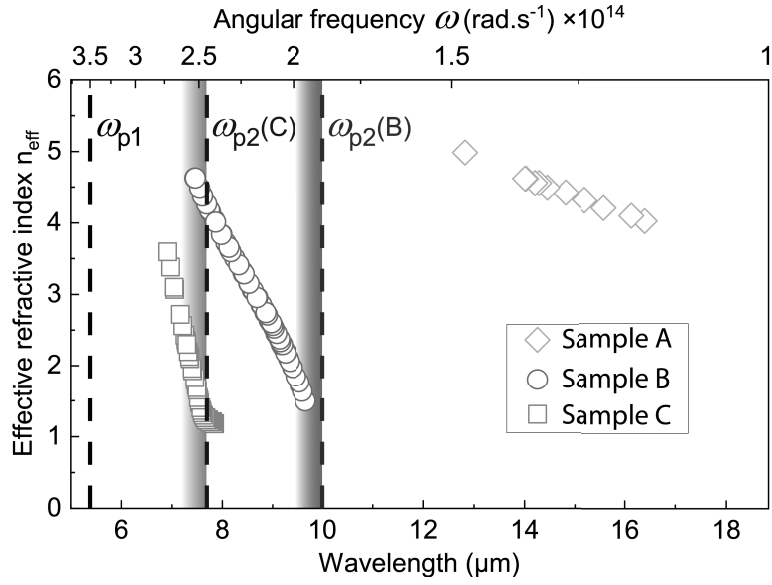


Figure 3.13: Effective refractive index n_{eff} , as function of the wavelength and the angular frequency ω for all three samples. Dashed lines correspond to plasma frequencies of samples B and C. Colored gradients highlight the shrink of the real part of the permittivity of samples B and C respective spacer layer, from $\epsilon = 1$ until it reaches zero $\epsilon = 0$ at their respective plasma frequencies.

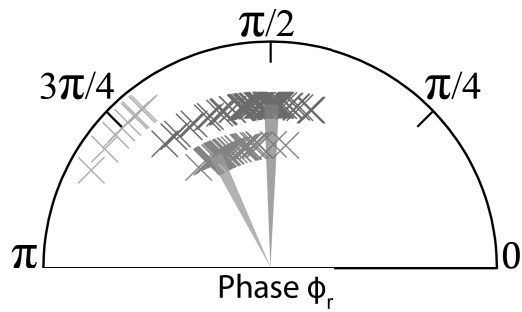


Figure 3.14: Calculated modal reflection phase ϕ_r , with ENZ regimes ($1 > \text{Re}(\epsilon) > 0$) of samples B and C depicted as cones. Green, red and blue data respectively correspond to sample A, B and C.

Between previously published works and the work presented here, the difference lies in the chosen plasmonic and ENZ materials. Previously studied plasmon-ENZ effects are supported by an ENZ medium with plasmonic antennas fabricated on top. The ENZ medium can either be tuned through its plasma frequency, which is the case for TCOs, or it is not tunable (phonon-based); but in both cases, the ENZ regime still remain far away from the LSPR of commonly used plasmonic noble metals. We demonstrated that III-V SCs are exceptional in this regard as the same material, InAsSb in this case, can be grown in differently doped layers monolithically, while having their optical properties in the same spectral region according to the doping levels of both the ENZ and plasmonic layers.

3.4.3 The enhanced electromagnetic field

Knowingly, the final aspect left to be unveiled, for the application of M-ENZ-M structures to spectroscopy, concerns the impact of the ENZ layer on the enhanced EM field associated to the LSPR. As a result of the importance of this feature for the sensing application, it is crucial to further understand how the field fans out in-between the nanoribbons in order to probe the molecules in the environment. We calculate the field with RCWA simulations for both a standard MIM structure, and a M-ENZ-M structure (ENZ regime at 10 μm), respectively corresponding to sample A and B. Figure 3.15 represents the computed enhanced EM field $|E_x/E_0|^2$ for the MIM and the M-ENZ-M structure, respectively (a) and (b). The width of the nanoribbons is such that the LSPR occurs in the MIR, corresponding to 400 nm for the MIM structure and 1.5 μm for the M-ENZ-M structure. The period of the simulations are 800 nm and 1.9 μm respectively so there is a 400 nm gap in-between the nanoribbons, where molecules pass and are being sensed by the enhanced EM field. The maximum field intensity is about one order of magnitude higher for the MIM structure compared to the M-ENZ-M structure. This is not due to the ENZ layer, but is a result of the fact that in order to attain the ENZ regime, larger antennas have to be fabricated such that their corresponding LSPR frequencies are getting closer to the ENZ point of the spacer layer. Wider antennas are less efficient in terms of light-trapping and therefore EM field confinement because their dimensions are not as subwavelength as smaller antennas. The positive compensation is that in respect to equation 1.9, the enhanced EM field associated to the structure plasmonic resonance will be enhanced within the media surrounding the ENZ material and it will diffuse, as observed in figure 3.15(b).

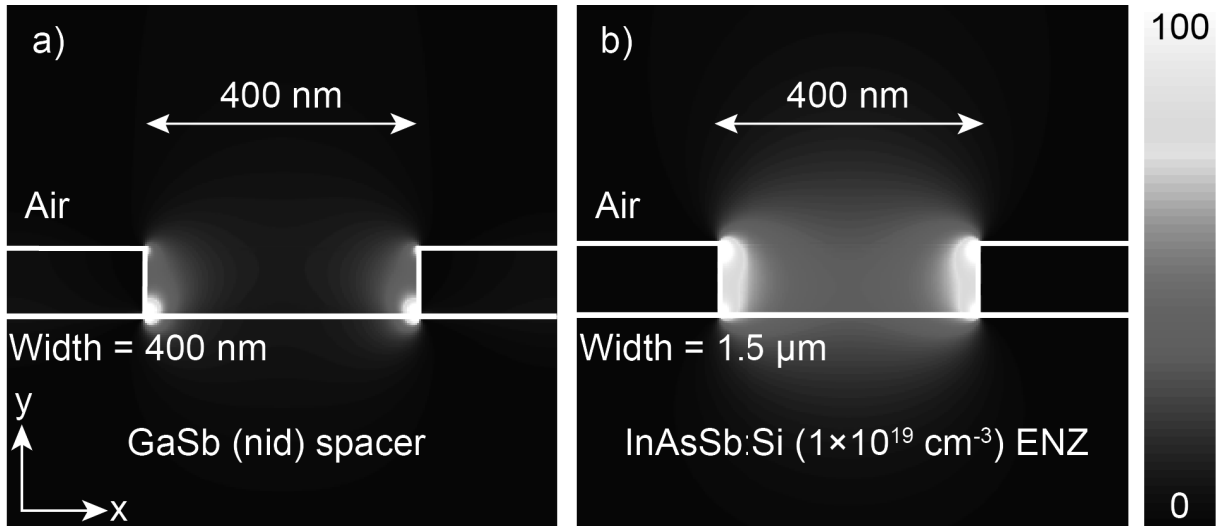


Figure 3.15: Enhanced electromagnetic $|E_x/E_0|^2$ field along x direction for (a) a standard MIM structure (sample A), and (b) an M-ENZ-M structure (sample B), at their respective LSPR wavelength λ_{LSPR} of 13 and 10 μm .

The main idea behind using an ENZ-based structure for sensing application is particularly adapted to gas sensing. By definition, a gas is a medium where all molecules diffuse and occupy the space they are part of, in that sense we consider it as a 3D medium. However, plasmonics and especially SPPs are modes that occur at interfaces and are therefore considered as a 2D system. This mismatch in terms of dimensions is a major drawback as it appears that SPPs are not so well adapted for the sensing of molecules in gas or vapor phase. In order to address this issue, the utilisation of ENZ-based plasmonic structure permits to alter the enhanced EM field from a 2D system towards a 3D solution. The standard description of the enhanced EM field is well-known as hot-spots, *i.e.*, extremely small volume of space where the field is highly confined and enhanced, and these can be considered as a 1D system for plasmonic metallic particles or a 2D system for nanoribbons fabricated into the MIM structure (figure 3.15(a)). Conversely, the M-ENZ-M structure is associated to an enhanced EM field that diffuses much more in the environment, such as air, in a way that the field acquires a 3D nature, making it perfectly suited to spectroscopy applications of molecules in gas or vapor phase, in theory (figure 3.15(b)). Still, the trade-off between this ENZ-based feature and the intensity of the EM field has to be carefully considered, notably depending on the interactions between the molecules and the sensor, when designing a plasmonic detector.

Conclusion

In conclusion, we have demonstrated that III-V semiconductor plasmonics is suitable to study the optical response of ENZ-based systems. They are associated to many practical advantages including: 1) cutting-edge growth and nano-fabrication techniques, *e.g.*

respectively, molecular beam epitaxy and electron-beam lithography, 2) benefit from the mature semiconductor industry for their integration onto photonic integrated circuits and their compatibility with CMOS technology, and 3) high and precise doping level in order to tune their ENZ spectral range. By means of these methods, we fabricated MIM structures, with a doped insulator in order to adjust its plasma frequency, i.e, ENZ regime, to various spectral range. We demonstrate that such structure displays a tunable ENZ regime from the THz up to the MIR, depending on the insulator doping level, with a plasmonic resonance tunable according to the nanoantennas dimensions. We studied the optical response of this system for three different insulator doping levels: $1 \times 10^{16} \text{ cm}^{-3}$, $1 \times 10^{19} \text{ cm}^{-3}$ and $2 \times 10^{19} \text{ cm}^{-3}$, and for various nanoantennas widths, from $\approx 200 \text{ nm}$ up to $\approx 1.8 \text{ }\mu\text{m}$. RCWA electromagnetic simulations confirmed experimental results and also attest, consequently, the high quality of growth and fabrication techniques.

We have determined the dispersion relation of our structures with FDTD simulations, which proved to be a more rigorous approach as compared to commonly used effective refractive index models, inadequate for non-perfect metal and insulator. We provide evidence that the resonance pinning originates from a material transition, in our case, the plasma frequency. Indeed, because we studied various insulator doping levels, associated to various plasma frequencies, we highlighted the resonance pinning under various circumstances and thus, we bring additional insights for the understanding of this pinning phenomenon. As long as an insulator exists within the system, a metal-insulator interface exists and it can support SPP modes, therefore, it explains why we experimentally observed the LSPR persisting at frequencies smaller than the plasma frequency, meaning that the pinning is spectrally localized and associated with the material transition. The underlying consequence of the LSPR pinning is the great tolerance to fabrication defects thanks to the geometry-independent behaviour; a noteworthy asset as modern nanophotonics increasingly relies on expensive and sophisticated fabrication technologies. In the same vein, an optical response essentially dominated by the dispersive behaviour takes advantage of the highly reliable and reproducible growth from molecular beam epitaxy.

To summarise, the metal-ENZ-metal structure proves to be an excellent vehicle to study and take advantage of ENZ phenomena such as the plasmonic resonance pinning, the near constant phase and the dispersive nature of ENZ materials. Great agreement between experimental results, RCWA simulations and theoretical results based on FDTD, demonstrates how III-V semiconductors, such as InAsSb and GaSb, can be employed to engineer the infrared optical response and the enhanced EM field of plasmonic nanostructures for various applications, such as spectroscopy, that will be presented in the next chapter.

Chapter 4

Gas sensing of organophosphorous compounds

Introduction

In this chapter, we discuss the results of OPs gas sensing experiments. First, we introduce the experimental prerequisites, namely, the experimental setup and the plasmonic sample used, before presenting the experimental results. The experimental results consist in two different studies addressing fundamental features of a sensor: sensitivity, selectivity, response time and repeatability. The first study presents the optical response of the plasmonic sensor exposed to different concentrations of DMMP. The second study presents the ability of the sensor to discriminate between DMMP and other molecules, in this case, methane and benzene; as well as its response in a humid environment. Following these results, we will discuss the various interactions that may occur between the InAsSb surface of the plasmonic sensor and DMMP molecules. This investigation includes several characterisations: IR, Raman, and X-ray photoelectron (XPS) spectroscopies, seeking to retrieve physicochemical information about DMMP interactions with the plasmonic substrate made of III-V SCs. Finally, from the previous results, we perform a series of electromagnetic numerical simulations based on two methods: FDTD and RCWA. These simulations are realised in order to corroborate experimental results presented in the second section.

4.1 Experiment prerequisites

4.1.1 Experimental setup

We first present the experimental setup used for the sensing experiments. Figure [4.16](#) represents a schematic diagram of the experimental setup that was installed next to the FTIR spectrometer. It is composed of two main elements: the gas generation system and

the detection cell. The gas generation is obtained by bubbling a solution of 97% pure DMMP contained in a stainless steel container known as bubbler. The bubbler has a gas inlet immersed in the liquid DMMP. An inert carrier gas, in our case dry N_2 , is sent into the solution in order to generate vapors of DMMP by the formation and growth of bubbles within the liquid, releasing a certain amount of DMMP. The N_2 :DMMP then draws up to the gas cell made of stainless steel and a ZnSe window transparent to IR light, aligned with the microscope. The flows are controlled using mass flowmeters. The plasmonic chip is placed inside the gas cell, next to a mirror of the same material for reference measurements. The outlet allows to perform gas sensing experiments in open-circuit configuration.

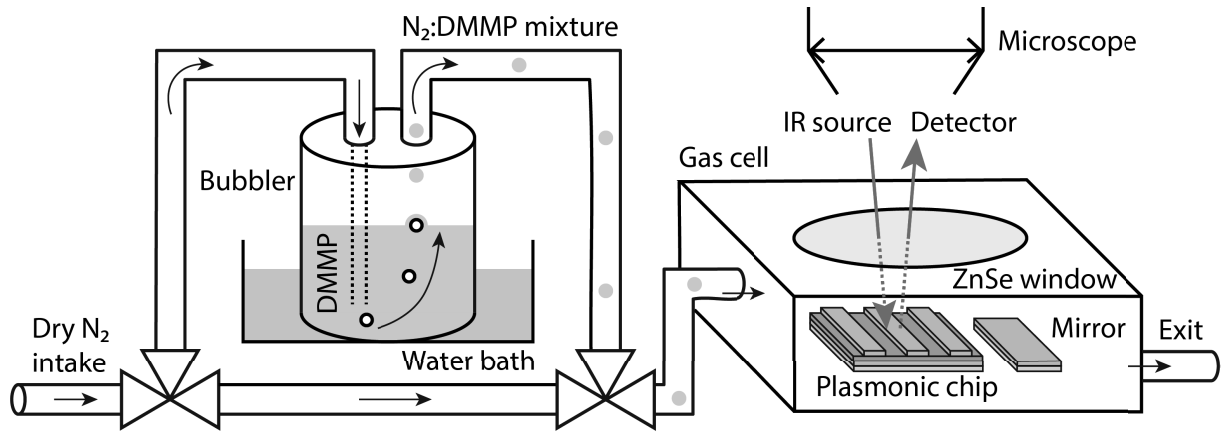


Figure 4.1: Experimental setup for detection of DMMP in gas phase.

The concentration of DMMP generated from the bubbling system depends on the temperature of the DMMP solution within the bubbler, itself immersed in a water bath to adjust and control the temperature with a precision on the order of 0.1 °C. The relation between the concentration and the temperature is given by Antoine equation [4.1](#) [226]:

$$\ln \left(\frac{P}{P^0} \right) = A - \frac{B}{C + T} \quad (4.1)$$

Where P^0 is the gas system ambient pressure, A , B , and C are empirical coefficients taken from the literature [227], and T is the temperature in kelvins, such that A , B , and C are respectively equal to 22.319, 4340 and -51.7, and $T = 278$ K, corresponding to 15 °C. The generated DMMP concentration C is 210 ppm as follows:

$$C = \exp \left(22.319 - \frac{4340}{-51.7 + 278.15} \right) \frac{1}{P^0} = 210 \text{ ppm}$$

The water bath temperature can be adjusted from 1 °C (water-limited) up to dew point of DMMP, related to the vapor pressure of the system (DMMP-limited). For this reason, we do not heat up the water bath above 15 °C to avoid saturation and condensation of DMMP within the system. This would result in the formation of liquid deposits at the surface of both the sensor and the ZnSe IR windows, as well as within the gas cell, which

could in turn disrupt the intended concentration. This temperature range correspond to a DMMP concentration range from about 150 ppm up to 500 ppm, that will be used in practice to expose the plasmonic sample, described in the next section.

4.1.2 The plasmonic sample

The plasmonic transducer that will serve for the sensing of DMMP was determined following the study discussed in chapter 3. The structure is shown in figure 4.2 and will be referred as sample S for spectroscopy. The structure is grown on a 4" GaAs wafer substrate, starting off with a 1 μm thick InAsSb:Si layer, highly n-doped $4 \times 10^{19} \text{ cm}^{-3}$ such that this layer is metallic to MIR light until $\approx 5 \mu\text{m}$. This layer cancels transmission through the sample such that reflectance measurements can be performed and absorption events can easily be retrieved from them, according to equation 4.2:

$$A + R + T = 1 \quad (4.2)$$

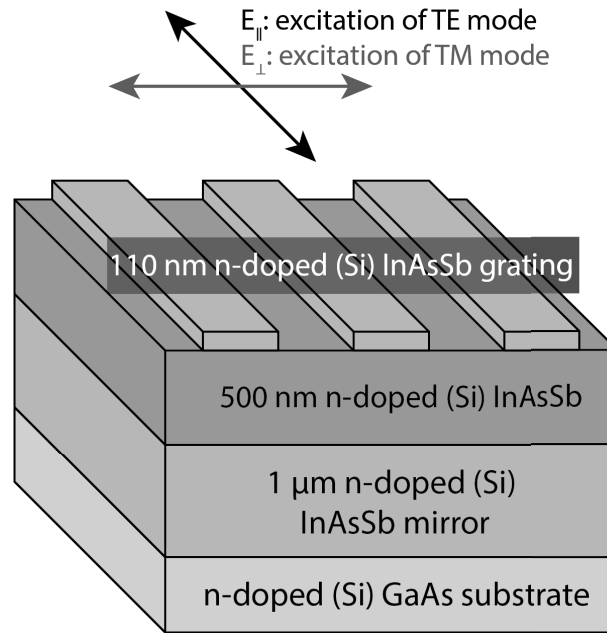


Figure 4.2: Sample S structure: the plasmonic-based MIM sensor.

With A , R , and T , respectively corresponding to the absorption, reflection and transmission. Following this layer is a 500 nm thick layer of InAsSb:Si, doped at $1 \times 10^{19} \text{ cm}^{-3}$ such that its plasma frequency is at 10 μm . This spacer layer acts as an ENZ medium and will benefit our sensing experiments as it was previously reported in chapter 3. Finally, a top layer, thin of 110 nm of highly-doped ($4 \times 10^{19} \text{ cm}^{-3}$) is grown and is intended to be nanostructured into ribbon shape plasmonic nanoantennas. This structure is a MIM structure, acting as a perfect absorber, coupled to an ENZ layer in order to favour spectroscopy experiments.

The advantage of ribbon shape antennas is that it is convenient to discriminate between the plasmonic optical response from the bare optical response of the sample, thanks to light polarisation. As shown by the arrows on top of figure 4.2, incident light polarised such that its electric field is parallel (E_{\parallel}) to the ribbon will not couple to the surface plasmon mode, because the electric field does not ‘see’ antennas, but a plane surface, equivalent to TE-polarised light. Conversely, incident light polarised such that its electric field is perpendicular (E_{\perp}) to the ribbons is equivalent to TM-polarised light because its electric field component ‘sees’ the break in symmetry and it can couple to the SPs mode by wavevector matching, giving rise to SPPs. With ribbon antennas shaped at the nanoscale the arising plasmonic mode is localised, therefore named LSPs and their associated LSPR.

After the structure was grown and verified, as described by the procedure in chapter 2, the plasmonic antennas fabrication was performed. Figure 4.3 shows different characterisations after the fabrication process with (a) an optical microscopy image highlighting different areas with different nanoribbon widths, (b) a SEM image to verify the dimensions of the antennas, and (c) AFM to check on the dimensions and the quality of the surface after the etching. The white rectangle includes three selected areas that will be used for spectroscopy experiments because their optical response matches the absorption modes of DMMP, as we will see in the next section. The nanoribbons period is $1.9 \mu\text{m}$ and their height is about $120 \pm 8 \text{ nm}$. The width of the nanoribbons, within each of these $400 \times 400 \mu\text{m}^2$, are, from bottom to top, 1.16 ± 0.13 , 0.97 ± 0.15 and $0.84 \pm 0.15 \mu\text{m}$. They will be referred in the next sections by these dimensions.

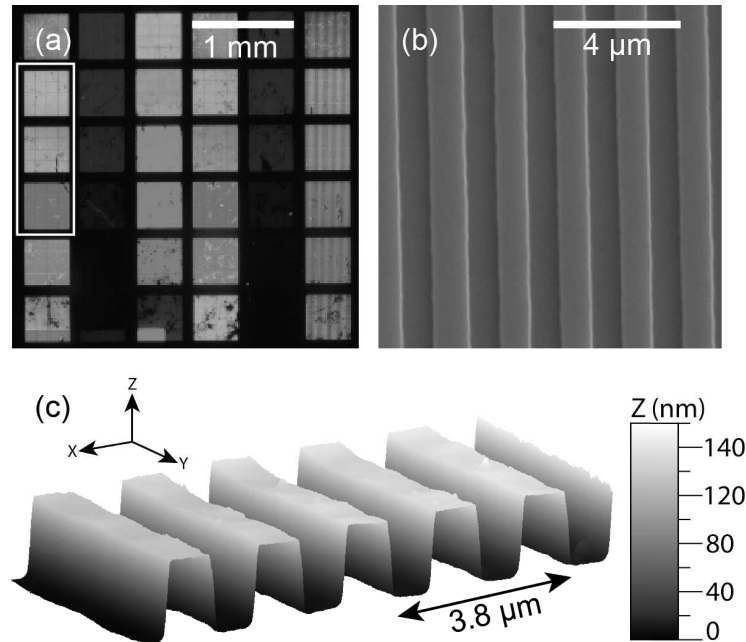


Figure 4.3: Sample S characterisations: (a) optical microscopy image, highlighting different areas with different nanoribbon widths, (b) SEM image, and (c) 3D reconstruction image from AFM. The white rectangle points out the three areas that will be used for sensing experiments: 1.16 , 0.97 and $0.84 \mu\text{m}$.

4.2 Experimental results

4.2.1 Optical characterisations

Infrared absorption of DMMP

The sensing experiments starts off with the detection of DMMP without the plasmonic device. The figure [4.4] shows in (a) a standard reflectance measurement obtained from the experimental setup installed, with a concentration $C = 320$ ppm ($T = 10$ °C). We observe various spectral events including the absorption of environmental water and CO_2 , as well as, the absorption of DMMP, whose fingerprint is mainly located in the range: $700\text{-}1400$ cm^{-1} , shown in (b) [228, 229]. The (b) panel highlights DMMP fingerprint and its various characteristic vibrational modes including stretching ν and bending δ , both can be symmetric: s, or antisymmetric: a, and rocking ρ . The main absorption line at 1050 cm^{-1} or 9.5 μm corresponds to the P–O–C bond (or simply POC), and because it is the most pronounced, as well as characteristic of the phosphorous atom, we focus our interest on this absorption line in this study.

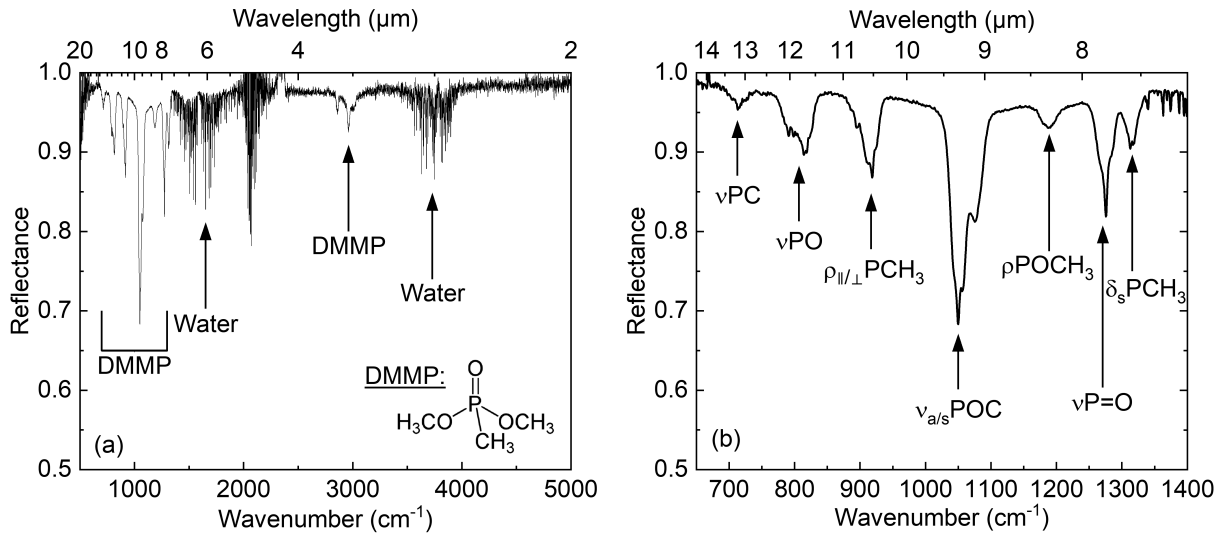


Figure 4.4: Infrared reflectance spectra translating the absorption from DMMP and environmental interferents: water and CO_2 . (a) Broadband FTIR spectrum, and (b) spectrum focused on the optical response from DMMP absorption around 10 μm .

These spectra attest for the presence of DMMP within the system and confirm that (1) the bubbler operates properly, (2) the gas system works as intended, and (3) the ZnSe window indeed allows IR light to pass through. We thus perform sensing experiments with our plasmonic device.

The optical plasmonic response

We verify that sample S fabrication was correctly done by performing optical characterisation of each fabricated areas by FTIR. Ultimately, three areas were selected as previously

mentioned, corresponding to nanoribbons of width: 1.16, 0.97 and 0.84 μm . Figure 4.5 displays (a) the reflectance coming from the DMMP and (b) the optical response of those three sizes of plasmonic antenna. The (b) panel shows the optical response for both polarisations. We observe that for a light polarised perpendicularly E_{\perp} with respect to nanoribbons, a sharp peak occurs around 1100 cm^{-1} , it is the LSPR; while for E_{\parallel} no resonance occurs, as expected. In addition, we observe at 1400 cm^{-1} the quarter-wavelength resonance associated to the Fabry-Perot structure within the MIM. We can appreciate the red-shift of the LSPR as the ribbon width increases. In addition, the LSPR goes down to nearly zero demonstrating the perfect absorber behaviour of the structure. Finally, the three selected areas display their LSPR at around the same frequency of the POC bound, a fundamental condition for SEIRA. The LSPR of the 0.84, 0.97, and 1.16 μm plasmonic nanoribbons are respectively at 1118, 1090, and 1056 cm^{-1} , with an average FWHM of $\approx 130 \text{ cm}^{-1}$, such that DMMP POC absorption line and the LSPR spectrally overlap as intended. The sensitivity study that follows, first addresses the calibration of the concentration generated with the bubbler system, before presenting the sensing results of the plasmonic chip exposed to different concentrations of DMMP.

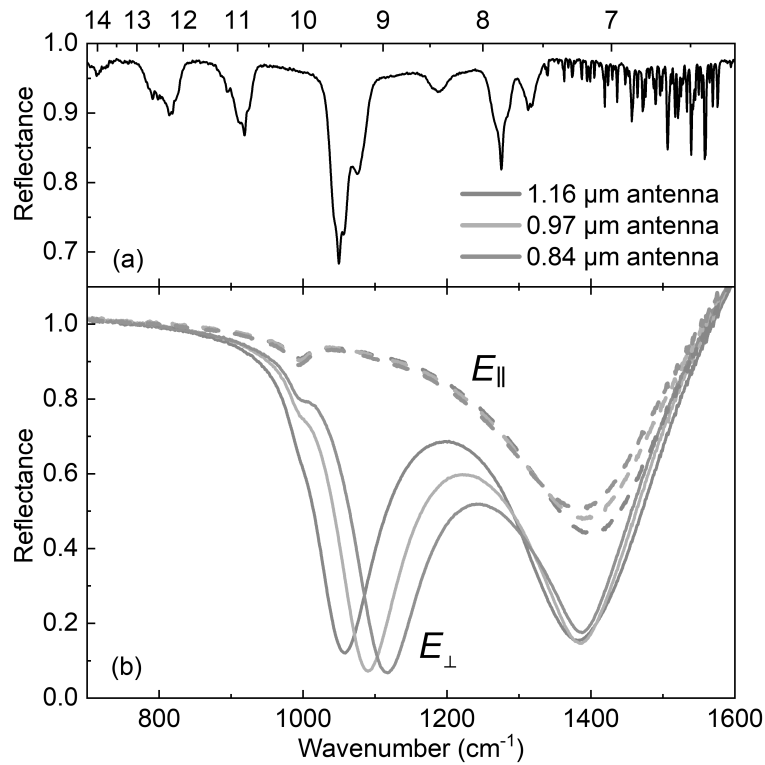


Figure 4.5: (a) Reflectance highlighting the absorption of DMMP in the MIR. (b) Optical response for three sizes of plasmonic nanoribbons, for both polarisation.

4.2.2 Sensitivity study

Concentrations setting

As part of the sensitivity study, we need to control the amount of DMMP sent into the gas cell to make sure the sample is exposed to the desired concentration. From Antoine equation [4.1], we know that the concentration is related to the temperature, controlled with a water bath. Figure [4.6] shows the spectroscopy results of different concentrations ranging from 230 to 440 ppm, corresponding to water bath temperature: 6, 8, 10, 12, and 14 °C, on the absorption signature of DMMP. The inset highlights DMMP main absorption line at 1050 cm^{-1} , associated with the POC bond. In accordance with Antoine's equation [4.1], as the temperature increases, the concentration increases, and consequently the absorption increases, *i.e.*, the reflectance decreases.

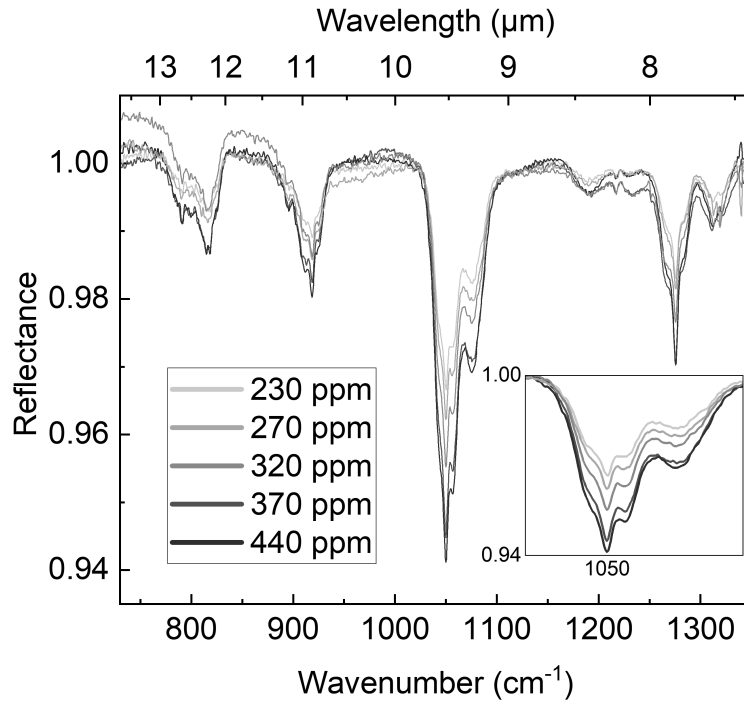


Figure 4.6: Reflectance of DMMP in the MIR as a function of the DMMP concentration. The inset highlights DMMP main absorption line at 1050 cm^{-1} , associated with the POC bond.

A second experiment, performed to further understand how the gas generation operates, is a temporal measurement. By tracking the intensity of the main absorption line of DMMP at 1050 cm^{-1} , we understand the dynamics of DMMP as it fills up the system. The figure [4.7] shows this result for four different concentrations: 100, 210, 320, and 500 ppm. The first one is obtained by diluting (1:1,v:v) the generation of 210 ppm with an additional dry N_2 intake, while the three others concentrations correspond to a water bath temperature T of 5, 10, and 15 °C, respectively. As DMMP fills up the fluidic system, the peak is increasingly pronounced and reflection diminishes, *i.e.*, absorption increases.

Three conclusions can be drawn: (1) as the temperature increases, the concentration increases, in accordance with Antoine's equation [4.1], (2) the reflection intensity decreases as the concentration increases, in accordance with equation [4.2], and finally (3) it takes a long time for the system to stabilise at a given value which means that adsorption might take place in the path of the IR beam.

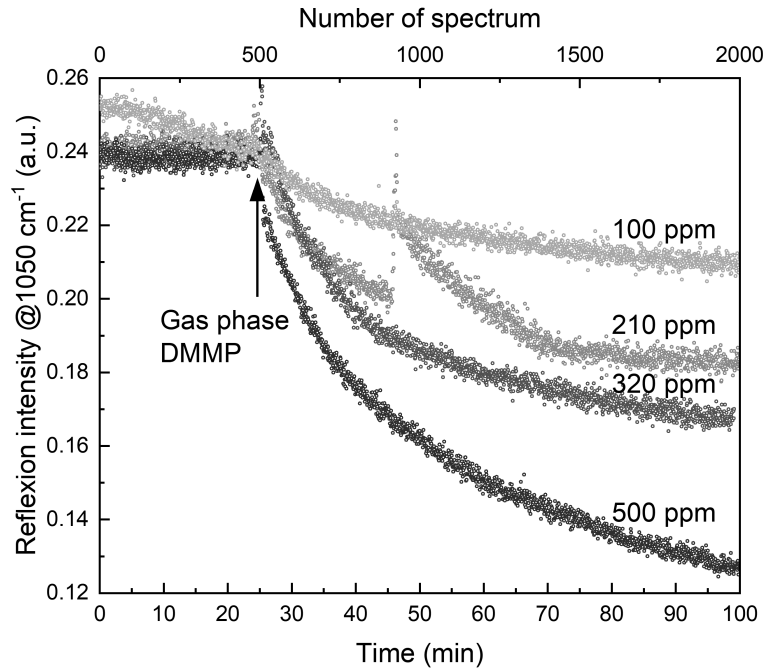


Figure 4.7: Intensity of DMMP main absorption line at 1050 cm^{-1} over time. Four different concentrations are tested: 210, 320, and 500 ppm by varying the water bath temperature, and 100 ppm from a (1:1,v:v) dilution of 210 ppm. The spike at ~ 50 min for 210 ppm corresponds to refilling of the MCT detector with liquid nitrogen, disrupting its sensitivity for some time.

For this latter reason, sensing experiments are performed only after the system has stabilised, which takes approximately an hour, such that the reflection intensity slope has flatten down. Furthermore, a mirror of InAsSb:Si has been placed in the gas cell next to sample S, such that it was exposed to the same conditions, and it will serve for reference measurements. Extreme care has been taken in terms of metrology to eliminate the background influence and avoid misinterpretations of the sensing results. All measurements are normalised by the optical response of this InAsSb:Si reference mirror, eliminating the response coming from adsorption on the ZnSe window, as well as, direct absorption coming from DMMP. As a reminder, we are not interested in the direct absorption of DMMP, but its enhanced absorption thanks to SEIRA, and discriminating both responses is of crucial importance to determinate if the plasmonic device works as intended. At last, we can move on to the sample final application: the enhanced detection of organophosphorous compounds, and in this case, the sarin simulant DMMP.

Sensing experiments

The first sensing experiment consists in exposing the plasmonic sensor to 210 ppm of DMMP vapors. As a reminder, we recall that a proof of enhanced absorption, *i.e.*, SEIRA, comes in the form of spectral signatures such as red-shift coming from the SPR effect and also signal shape variation such as Fano resonances. In practice, we first do a reference measurement on the InAsSb mirror, then we obtain the optical response of the aforementioned 3 areas, only then we send the vapors of DMMP and after stabilisation of the system which takes approximately an hour (see figure 4.7), we repeat the same procedure. In the end, to put it simply, we are looking for signal variations within the LSPR by comparing it before and after exposure to the gas. Figure 4.8 shows in the optical infrared response, focused in the region holding both the LSPR and the absorption lines of DMMP, for both polarisation (a) E_{\perp} , and (b) E_{\parallel} , before (full lines), and after exposure to DMMP (dotted lines). At first sight, we do not observe any significant spectral variations, therefore we cannot conclude if SEIRA was achieved.

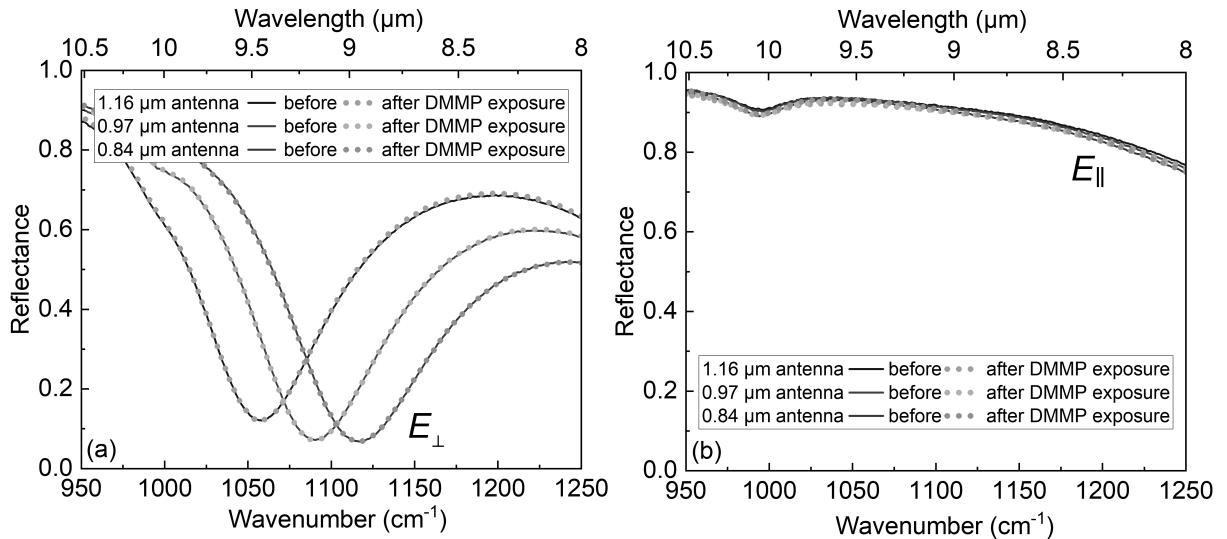


Figure 4.8: Reflectance measurements of three antenna widths: 1.16, 0.97 and 0.84 μm , before (full lines) and after (point lines) exposure to 210 ppm of DMMP vapors, under (a) E_{\perp} , and (b) E_{\parallel} polarisations. Background realised on InAsSb mirror.

To bring to light fine spectral signatures, we calculate the differential reflectance of each area using the following formula:

$$\frac{S_{\text{DMMP}} - S_{\text{ref}}}{S_{\text{ref}}} \times 100 \quad (4.3)$$

With S_{DMMP} and S_{ref} the reflectances after and before DMMP exposure, respectively. Figure 4.9(a) displays the result of this operation. First, we observe that the differential reflectance for a E_{\parallel} light is flat for all three sizes of antenna. Second, the differential reflectance for E_{\perp} light reveals variations. These variations, although quite noisy, are

only attributed to a plasmonic-enhanced sensing because it only occurs when the LSPR is excited. The (b) panel displays the same signals, but slightly smoothed using a moving average over 7 points, such that the noise level flattens down completely. The resulting signal variations only occurs within the LSPR of each plasmonic antennas, and they are on the order of 2, 3, and 3% for the 1.16, 0.97, and 0.84 μm width antennas, respectively.

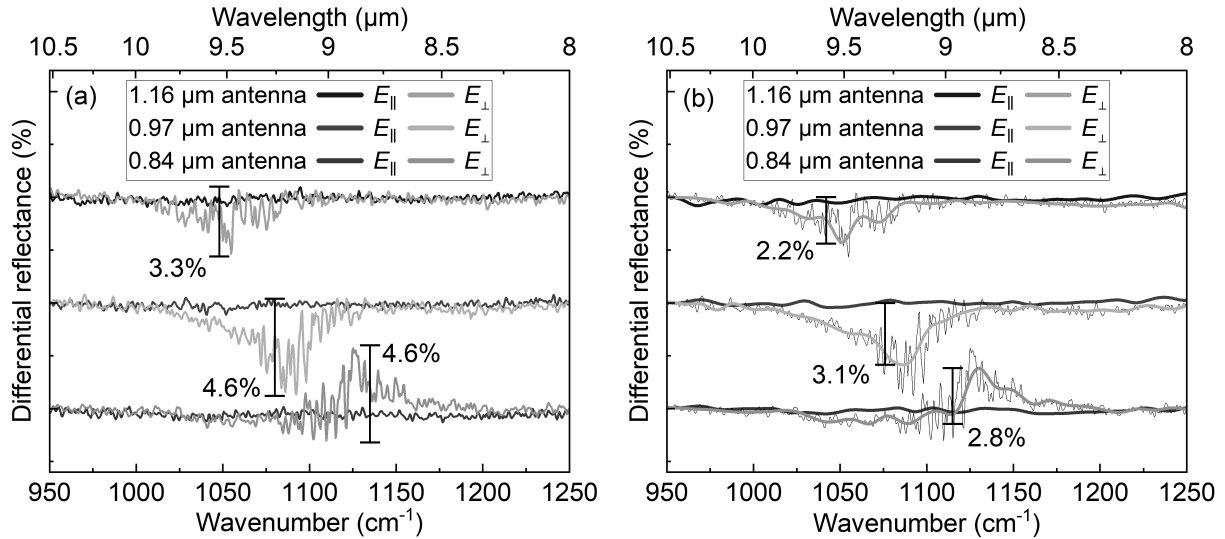


Figure 4.9: Differential reflectance expressed in % for 1.16, 0.97, and 0.84 μm antenna sizes for both polarisations, (a) without, and (b) with smoothing.

After each experiments, the gas cell was abundantly rinsed and the sample was cleaned according to the cleaning procedure detailed in Chapter 2. The exact same experiment was repeated for three different concentrations: 100, 320, and 500 ppm. Figure 4.10 shows the sensing result as differential reflectance. We observe that, contrarily, to our expectations, the differential reflectance sensing signal is about the same for all concentrations. Furthermore, we observe that the shape of the signal is also similar throughout the four experiments: 1.16 and 0.94 μm antennas have a negative differential reflectance while the smallest antennas 0.84 μm wide have a positive differential reflectance.

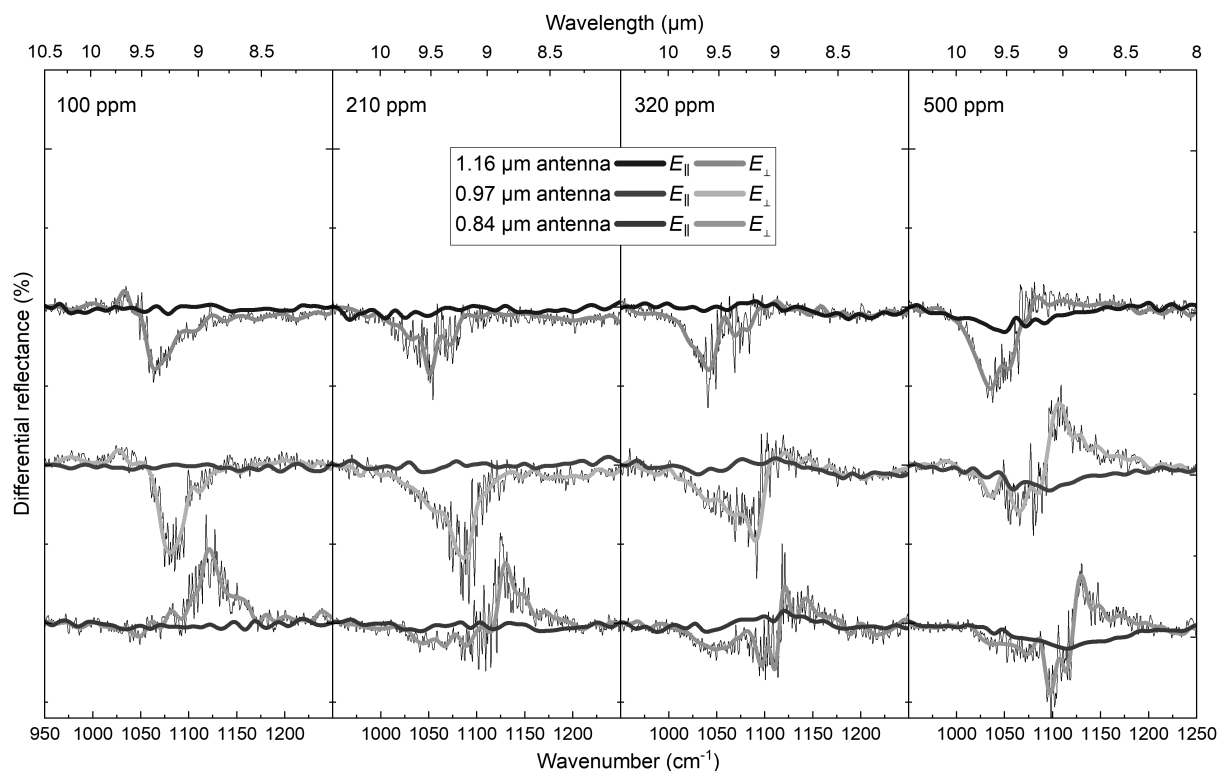


Figure 4.10: Differential reflectance (%) for different concentrations of DMMP mixed with N_2 . Signals are acquired for the three antenna widths under two different polarisations: E_{\perp} and E_{\parallel} . A smoothing as well as a y-shift of 5% between each antenna response is introduced for clarity. Black lines are bare spectra in perpendicular polarization (E_{\perp}).

The sensitivity study is summed up on the histogram in figure [4.11](#) which shows the sensing signal, averaged over the three sizes of antennas and over the number of times the experiment was conducted, as a function of the concentration of DMMP vapors to which the plasmonic sensor was exposed. The error bars are calculated standard deviations. It appears that despite the clear fact that the detector is sensitive to the exposure of DMMP, its response does not scale nor changes significantly according to the concentration.

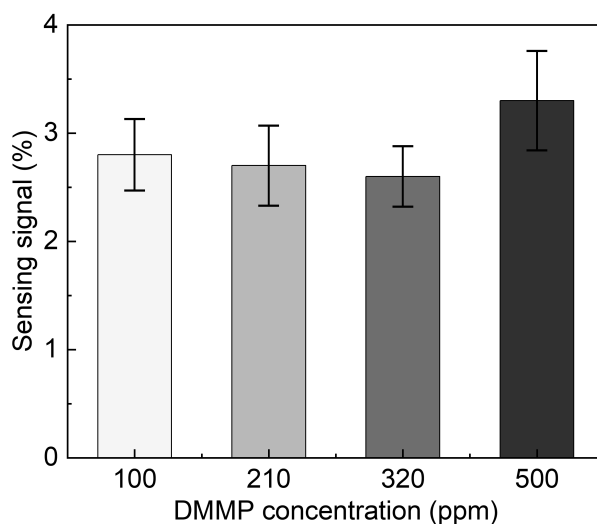


Figure 4.11: Histogram summing up the average sensing results of the three plasmonic regions studied. The sensing signal corresponds to the average differential reflectance signal variation (%) as a function of the DMMP concentration. Error bars correspond to measured standard deviation.

We demonstrated the feasibility of a plasmonic sensor for the gas phase detection of OPs, such as DMMP, giving rise to a signal variation in the order of 3%. The experiment was highly reproducible with a sensing signal similar in terms of frequency, shape and amplitude in each 12 measures, highlighting the reusability of the sensor. Still, we cannot conclude on the limit of detection of the plasmonic sensor. The sensor response, resulting from the plasmon-molecule interactions at resonance frequency, depends on the spatial overlap between the enhanced EM field associated to the LSPR and DMMP molecules. Non-linearity in the sensor response implies that in all four experiments, and for the three studied areas, this enhanced EM field ‘sees’ the same amount of molecules regardless of the DMMP concentration. We therefore make the hypothesis that the sensor surface is saturated with a DMMP layer. We will come back to this assumption after the selectivity study that follows. This selectivity study is performed in order to demonstrate that the sensor is dedicated to the detection of DMMP only.

4.2.3 Selectivity study

We experienced the selectivity of the plasmonic sensor in three different conditions: two interferences were selected, namely, benzene and methane, and finally the response was also evaluated in a humid environment, in this case, within 50% of relative humidity (RH). Interferences are molecules that can parasitize the response of the sensor, either hindering its sensitivity to the desired molecule, resulting in false negatives, or by reacting with the sensor resulting in false positives.

Benzene

The first interferent tested is benzene, a volatile organic compound (VOC) that holds great interest in the sensor community [230]. Additionally, pollutants like benzene are often used to evaluate a sensor response to its chemical structure, which is aromatic in the case of benzene. These reasons justify why we test the plasmonic sensor with it. Practically speaking, the setup does not change except that a 200 ppm benzene bottle was connected to the system. As for the metrology, we perform the exact same spectra acquisition procedure to compare experiments in the best possible way. Figure 4.12(a) shows a reflectance spectrum of 200 ppm of benzene, measured on an InAsSb mirror, after stabilisation. The red arrows attest for the presence of benzene and we proceed to the sensing experiment. Figure 4.12(b) displays the resulting differential reflectance for a E_{\perp} polarised light and for the same three areas that were employed in DMMP sensing. We do not observe any significant signal variation, which is a proof that the plasmonic device is not sensitive to benzene.

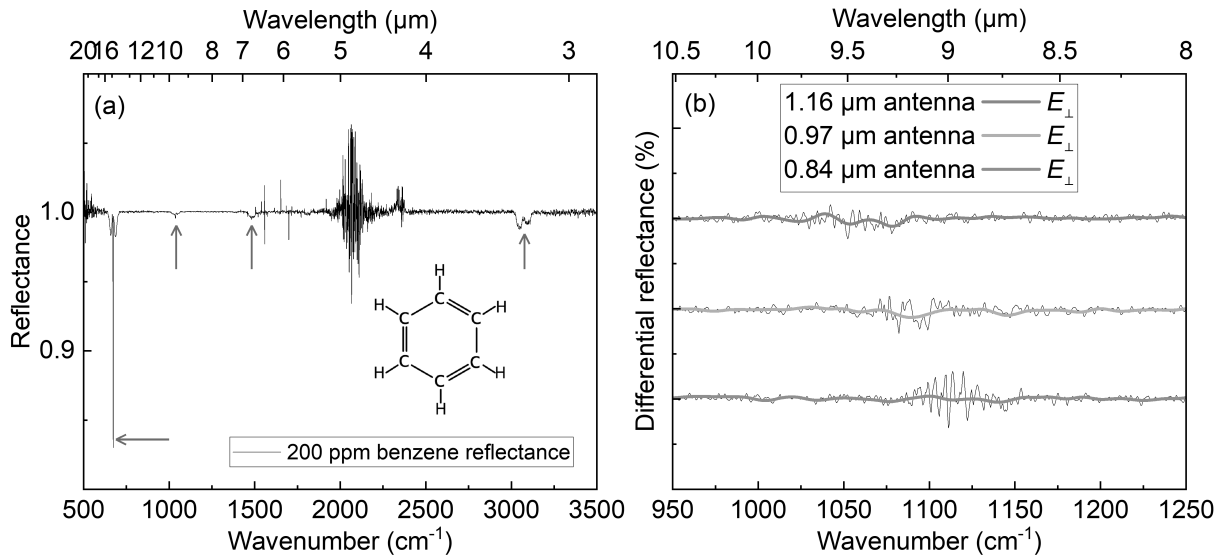


Figure 4.12: (a) Reflectance spectrum of 200 ppm of benzene, measured on an InAsSb mirror. Red arrows highlight absorption lines corresponding to the vibrational modes of benzene. (b) Differential reflectance (%) for three different antenna widths (1.16 μm , 0.97 μm and 0.84 μm) exposed to 200 ppm of benzene. A y-shift of 5% is introduced for clarity. A smoothing is applied to the spectra for clarity. Black lines are bare spectra.

Methane

The second experiment is done with the second interferent: methane, also a VOC [231, 232]. This time, the sensor is exposed to a higher concentration: 50,000 ppm. The absorption spectrum can be appreciated in figure 4.13(a). The same experiment is performed on the plasmonic sample and the results are shown in figure 4.13(b). Alike benzene, the sensor does not show any significant signal variations in the differential reflectance signal,

after methane exposure.

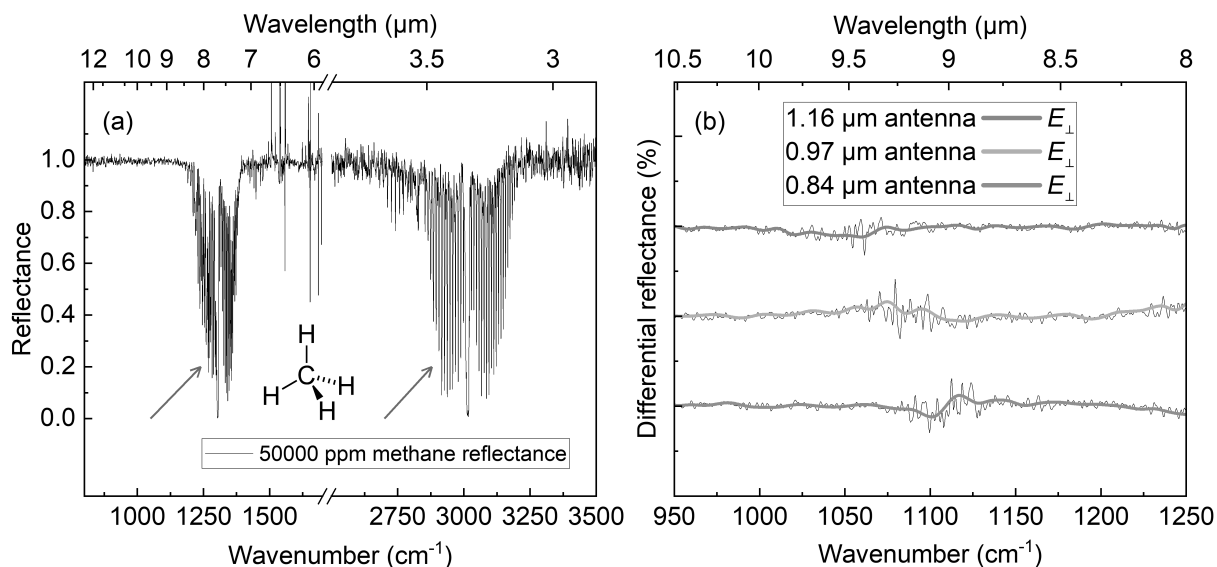


Figure 4.13: (a) Reflectance spectrum for 50,000 ppm of methane, measured on an InAsSb mirror. Red arrows highlight absorption lines corresponding to the vibrational modes of methane. (b) Differential reflectances (%) for three different antenna widths (1.16 μm , 0.97 μm and 0.84 μm), exposed to 50,000 ppm of methane. A y-shift of 5% is introduced for clarity. A smoothing is applied to the spectra for clarity. Black lines are bare spectra.

Humidity

The humidity test required to elaborate an alternative system, with a second bubbler containing water. Both bubbler have N_2 as carrier gas and the same flow was applied to both paths. This would result in a N_2 :DMMP: H_2O mixture with a DMMP concentration divided by 2, resulting in 100 ppm of DMMP and a relative humidity of 50% in volume. The humidity experimental setup is shown in figure 4.14.

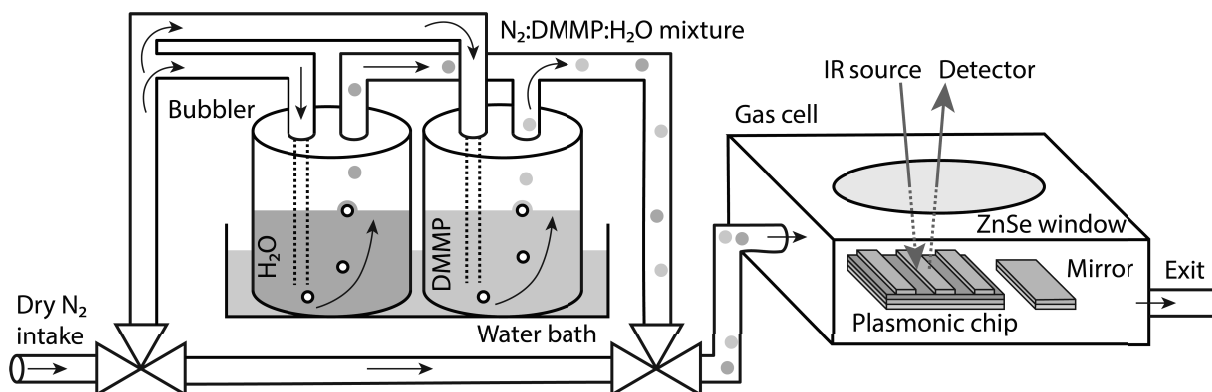


Figure 4.14: Experimental setup for detection of DMMP in gas phase, adapted to introduce humidity.

As for the interferent experiments, the same experiment procedure was performed. It was performed three times and at different periods of time to evaluate the reproducibility of the sensor and the reliability of the results. The three tests are displayed in figure 4.15. We observe that the differential reflectance shows sensing signal in the order of 2%, similar in frequency and shape to the results previously presented in the sensitivity study. Nonetheless, the sensing signal is slightly inferior in presence of water. The work of Bermudez is particularly interesting in this case: he studied the effect of humidity on the interaction of DMMP vapor with surfaces of SiO_2 , Al_2O_3 , and $\text{AlO}(\text{OH})$ by ATR-IR spectroscopy [233]. He demonstrates that strongly interacting molecular species followed by a liquid-like DMMP layer occur after exposure to $\text{DMMP}:\text{H}_2\text{O}$. The strong interaction involves $\text{M}-\text{H}\cdots\text{O}=\text{P}$ bonds and/or $\text{HO}-\text{H}\cdots\text{O}=\text{P}$ bonds to preadsorbed molecular H_2O . Finally, he concludes that DMMP does not appear to penetrate the liquid-like layer of water and H_2O does not seem to displace DMMP molecules that have adsorbed onto the preadsorbed water layer. These results comfort our result in the sense that water does not hinder DMMP adsorption, but its presence competes with DMMP molecules as they adsorb onto the oxide surface [234], which implies that either less DMMP has bound to the sensor surface, either it has bound farther away from the surface, thus lowering the amount of molecules detected and the sensing signal ensuing.

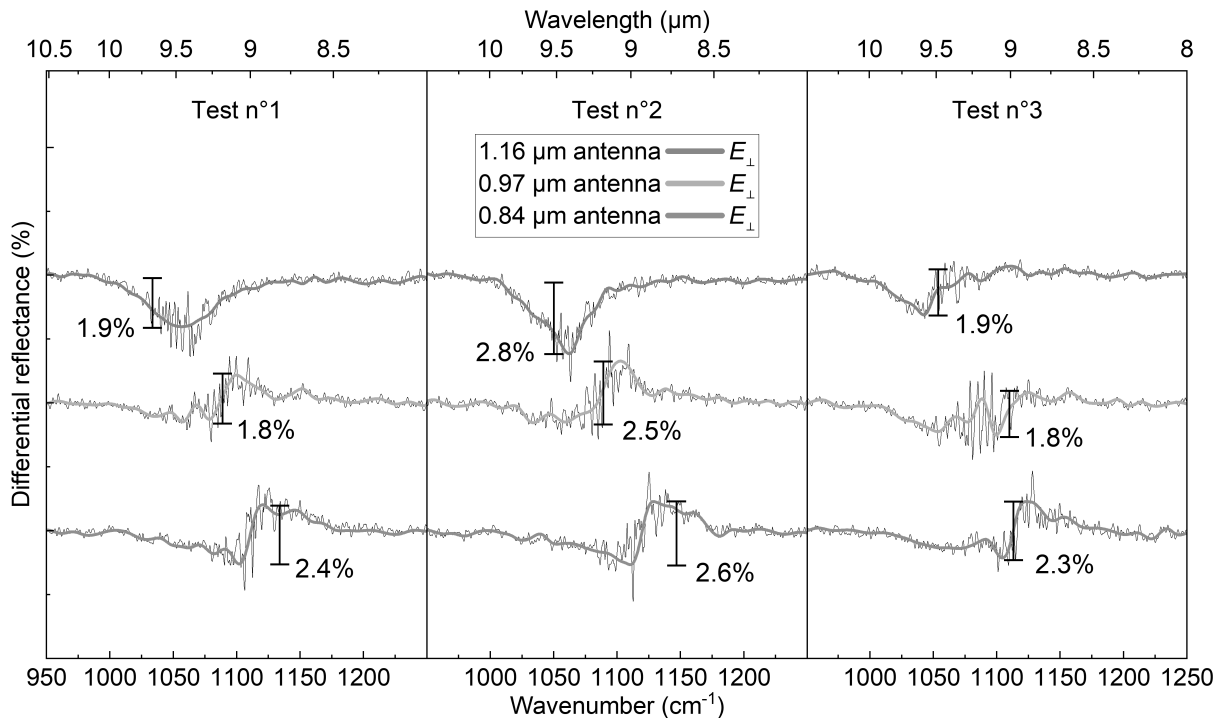


Figure 4.15: Differential reflectances (%) for the three antenna widths (1.16 μm , 0.97 μm and 0.84 μm), under perpendicular polarization regarding nano-ribbons (E_{\perp}), exposed to 100 ppm of DMMP with 50% RH. The experiment was performed three times for reproducibility (each panel). A smoothing is applied to the spectra for clarity. Black lines are bare spectra.

This concludes the selectivity study that consisted in testing the plasmonic device in different conditions than those the sensor was designed for. We demonstrated that the plasmonic sensor was not sensitive to benzene and methane, two commonly encountered VOCs in the environment. Furthermore, we obtained positive sensing results when the sensor was exposed to 100 ppm of DMMP with 50% RH. These results show that the sensor is selective towards DMMP, even in a humid environment. The results of the sensitivity and selectivity studied are summed up in figure 4.16, which further highlights the various features of this plasmonic sensor: sensitivity down to 100 ppm, non-linearity with the concentration, selective towards DMMP, insensitive to VOCs such as methane and benzene, and humidity-tolerant. In addition, the sensor showed great reproducibility throughout all these experiments.

This III-V SCs SEIRA prototype is the first of its kind and we achieved decent levels of detection similar to the works of Huang *et al.* and Wang *et al.*, who respectively investigate a new hydrogen-bond acidic siloxane polymer coupled to a QCM sensor [235], and a resistivity sensor functionalised with single-walled carbon nanotubes [236], and attained ≈ 100 ppm of LOD for both of them. This shows that our plasmonic sensor compares well in terms of sensitivity with analogous studies and it benefits from great selectivity both in terms of sensitivity regarding interferences and characteristic signatures of DMMP in the IR.

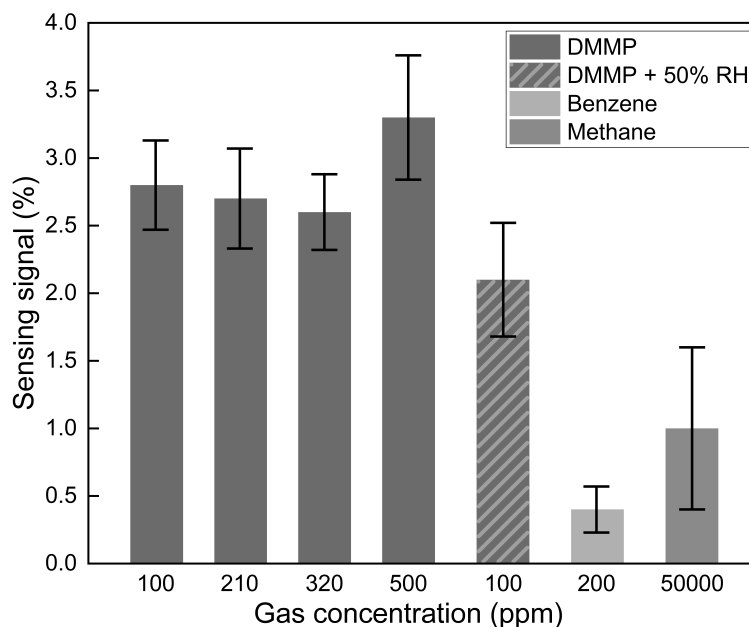


Figure 4.16: Histogram summing up selectivity and sensitivity results of the plasmonic sensor. Sensing signal corresponding to the differential reflectance signal variation (%) in function of each gas and their respective concentration tested. The sensing signal is the average response of all antenna sizes and the number of times the experience was repeated. Error bars correspond to standard deviation.

4.3 Oxide-DMMP interactions

We previously hinted that there must be some sort of interaction between the semiconductor surface and DMMP molecules, resulting in a layer adsorbed at the surface that would saturate the sensing signal. Figure 4.17 illustrates this hypothesis: DMMP molecules may interact with surface or with its native oxide to form a monolayer of DMMP, estimated to be 5 Å thick, approximately the size of the molecule [237]. This assumption is corroborated by the fact that sensing experiments are performed after the system has stabilised over enough time so that potential interactions may occur. This section focuses on the study of these interactions and how it may affect the DMMP molecules, and their consequences for sensing applications.

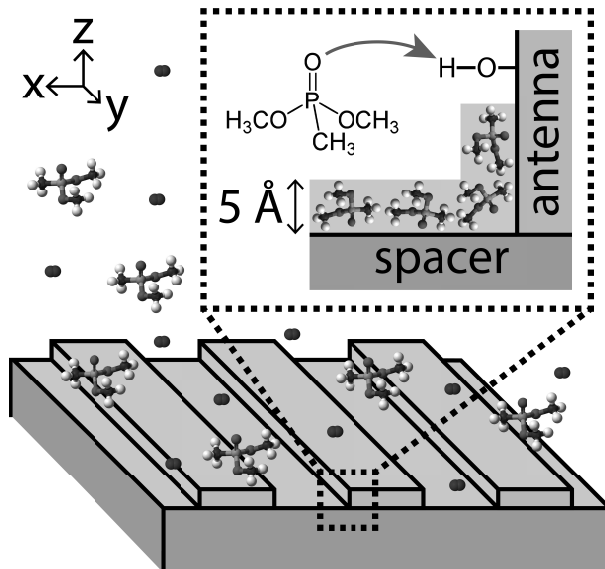


Figure 4.17: Schematic representation of the adsorption process between DMMP and InAsSb native oxide. Under DMMP:N₂ flux, DMMP molecules can interact, either with -OH oxide bond or directly to the SC surface, mainly via its P=O double bond. The inset represents this interaction resulting in a 5 Å DMMP monolayer at the surface.

It was reported in the literature that the DMMP molecules have affinity towards metals such as Pt [238], Ni [239], Mo [240], and Pd [239], as well as an important diversity of metal oxides including V₂O₅ [241], PdO [242], Zr(OH) [243], Y₂O₃ [244, 26], CuO [245, 246, 26], WO₃ [237, 26], TiO₂ [247], Al₂O₃ [248], Fe₂O₃ [249], CeO₂ [250], SiO₂ [251], MoO₂ [252], MoO₃ [253], MnO [254], La₂O₃ [255], ZnO [256, 246], MgO [255], SnO₂ [257, 258, 26], Ag₂O [246], Co₃O₄ [259], LiNi_{0.5}Mn_{1.5}O₄ [260], Ga₂O₃, as well as, Sb₂O₃ [258] and In₂O₃ [261, 26]. The two last are of paramount interest in our study. Most of these papers assess that DMMP interacts with native oxide through different mechanisms such as: bonding between the electron-rich phosphoryl group P=O with surface hydroxyl sites (figure 4.17) or coordinative unsaturated atoms sites, *i.e.*, Lewis acids, van der Waals interaction, H-bonding as well as Brønsted acid coordination [246, 262, 255].

Upon adsorption, chemical reorganisations of the molecular structure may occur, having consequences on its properties including absorption [255]. Accordingly, we investigate the potential interactions between our sensor surface with DMMP by drying a DMMP droplet of 0.1 μL under N_2 flow on a InAsSb mirror, and by performing (1) infrared reflectance, (2) Raman, (3) XPS measurements to learn further informations on the state of DMMP molecules at the InAsSb surface.

4.3.1 Infrared spectroscopy

To evaluate if DMMP molecules interact with the InAsSb:Si surface, we let dry under N_2 flow a droplet of DMMP at the surface on an InAsSb mirror. Figure 4.18 represents the absorption coefficient κ retrieved from FTIR spectra for both DMMP in gas phase (red line), and dried on InAsSb (blue line), using equation 4.4.

$$\kappa = \frac{\log\left(\frac{I_0}{I}\right) \lambda}{4\pi t} \quad (4.4)$$

With I_0 the background measure, I the measure on the dried DMMP droplet, λ the wavelength and t the average thickness of the deposition at the surface, determined using a profilometer. It is clear that the spectra are very different, which comforts the idea that molecules of DMMP undergo chemical restructuring upon adsorption onto the SC surface. This finding is of particular importance because efficient SEIRA relies on frequency match between the LSPR and the absorption lines of molecules. In this regard, determining the absorption modes of adsorbed DMMP is crucial as these are the modes that will interact with the EM field, associated to the SPP wave, at resonances. This spectrum, associated to the adsorption of DMMP onto InAsSb oxide surface, adds up to similar results obtained on an extensive diversity of metal oxides reported in the literature [244, 247, 251]. The main peak values are compared to the literature in table 4.1 and further discussions about surface chemistry are addressed in following section 4.3.4.

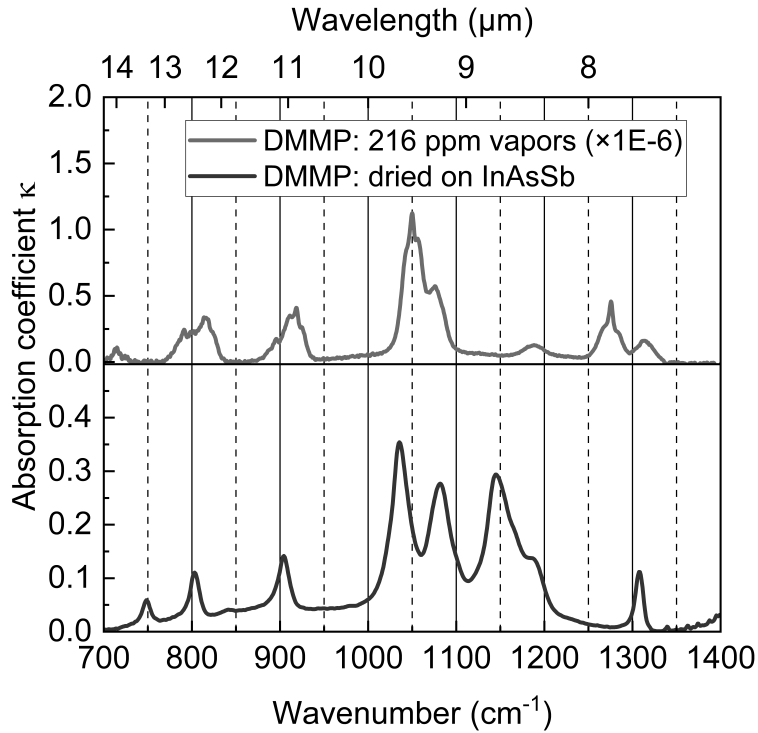


Figure 4.18: Absorption coefficients κ of vapor phase DMMP (red line) and dried DMMP on InAsSb:Si under N_2 flux (blue line).

4.3.2 Raman spectroscopy

The second experiment performed is Raman spectroscopy. Figure 4.19 shows the Raman response from (a) liquid DMMP, and (b) dried DMMP onto InAsSb. The spectra differ drastically in terms of amplitude as well as shape. It is difficult to draw conclusions from this experiment except that DMMP persists at the surface of our samples, even weeks after the deposition, and second, its chemical structure is different from liquid DMMP, which indicates that surface chemistry occurred upon binding. The work of Templeton *et al.*, based on Raman spectroscopy, exhaustively explores how DMMP adsorbs to aluminum oxide and they conclude that DMMP adsorbs molecularly, producing ‘saturation coverage’, from Lewis base/Lewis acid complex between DMMP and the surface hydroxyl [248]. This adsorption leads to various chemical reorganisation including cleavage of a P–O bond with the methoxy fragment likely to remain at the surface. These conclusions are corroborated by our Raman measurements, showing strong differences between the different forms of DMMP [248]. Similar studies have been conducted on silver [263, 264, 265], titanium [266], and graphene [267] oxides. The main peak values are compared to the literature in table 4.1 and further discussions about surface chemistry are addressed in following section 4.3.4.

Chemical bond	Pure DMMP (literature)	Pure DMMP (this work)	Adsorbed DMMP
$\nu_a(\text{CH}_3)\text{P}$	2998/3014	2999	3006
$\nu_a(\text{CH}_3)\text{O}$	2958/2962	3022	2963
$\nu_s(\text{CH}_3)\text{P}$	2924	2928	2933
$\nu_s(\text{CH}_3)\text{O}$	2859	2852/2957	2860
$\delta_a(\text{CH}_3)\text{O}$	1467	1454/1466	1458/1466
$\delta_s(\text{CH}_3)\text{P}$	1421	1421	
$\delta_s(\text{CH}_3)\text{O}$	1319	1313	1315
$\delta_a(\text{CH}_3)\text{P}$	1314		1315
$\nu(\text{P}=\text{O})\text{P}$	1275	1240	1276
$\rho_s(\text{CH}_3)\text{OP}$	1190	1186	1188
$\nu_a(\text{C}-\text{O})\text{P}$	1070		1076
$\nu_s(\text{C}-\text{O})\text{P}$	1049	1058	1051
$\rho(\text{CH}_3)\text{P}$	914	896	919
$\nu(\text{C}-\text{O})\text{P}$	816	820	816
$\nu(\text{PC})$		705/714	714

Table 4.1: Main peaks data of DMMP from this work and literature, for IR [244, 247, 251] (red) and Raman [248] (green) spectroscopies. Values expressed as wavenumbers in cm^{-1} .

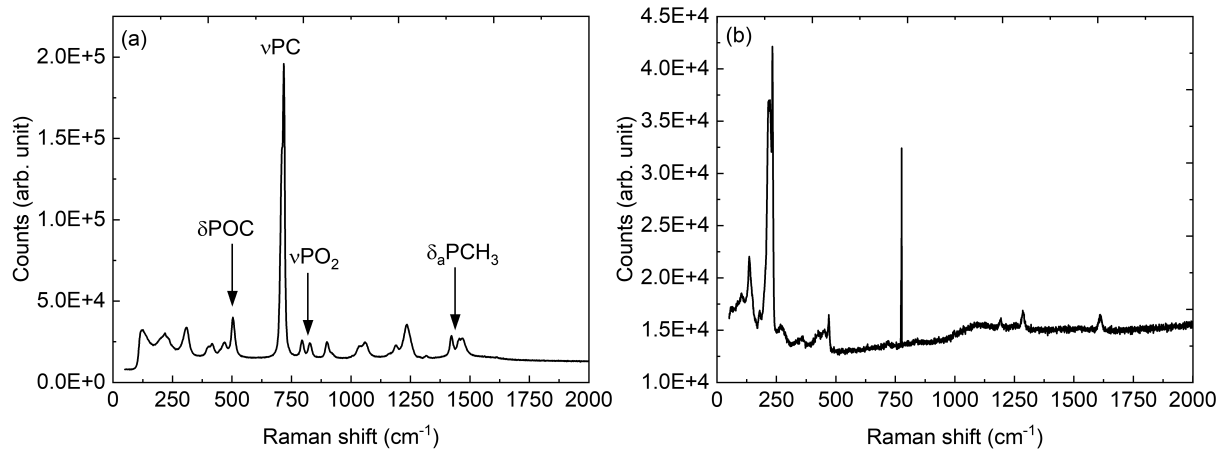


Figure 4.19: Raman spectra of the (a) liquid DMMP, and (b) dried DMMP, on the InAsSb:Si surface. Differences between the two spectra demonstrate interactions between the SC surface and DMMP molecules.

4.3.3 X-ray photoelectron spectroscopy

The third experiment performed is XPS. This method is especially suited in our case as this technique specialises in surface analysis at the atomic scale, and it is able to both qualify and quantify the atomic composition of a surface over few angstroms in depth. Figure 4.20(a) represents the XPS spectrum obtained from InAsSb:Si bare surface. This measurement is interesting as it highlights the different oxides found at the surface: antimony, indium and arsenic oxides, respectively Sb_2O_x ($x = 3, 4, 5$), In_2O_3 , and As_2O_3 . This confirms that the native oxide composed of different oxides is present and it can interact

with any molecules deposited at the surface. When the surface is exposed to DMMP, the obtained XPS spectrum displays the phosphorous peaks (figure 4.20(d)), which attests that DMMP binds to the surface and persists weeks after exposure, if not cleaned. The P2p peak is at 133.5 eV, in accordance with the literature [268]. It is not possible to compare the P2p results of the spincoated and droplet of DMMP because the measurements were mistakenly normalised by the position of this peak, rather than carbon.

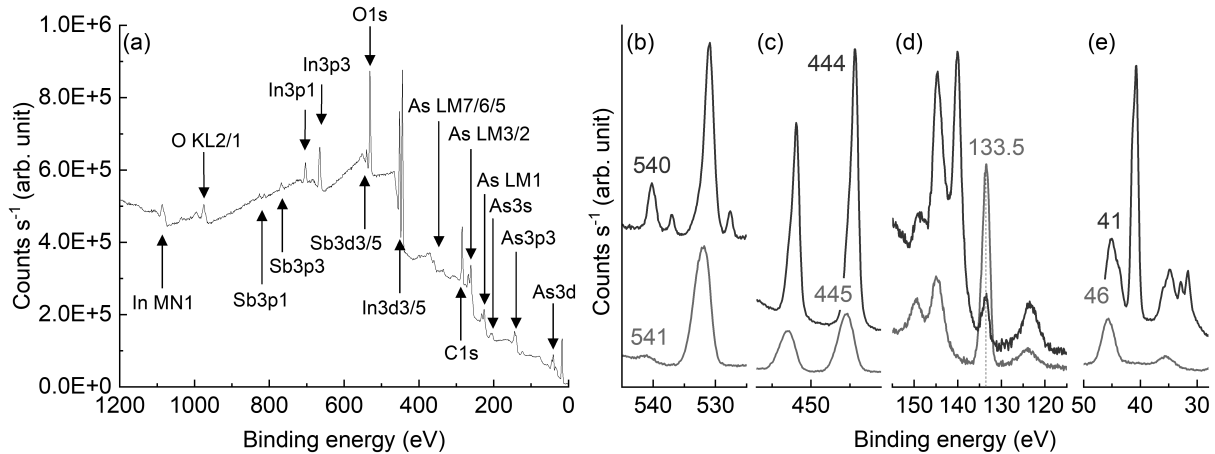


Figure 4.20: XPS spectra of (a) the bare InAsSb:Si surface (reference) highlighting the diversity of oxides at the surface. (b), (c), (d), and (e) focuses on Sb3d3, In3d, P2p, and As3d, respectively: dried spincoated (blue lines) and large droplet (green lines) of DMMP on InAsSb surface demonstrating the presence and persistence of DMMP molecules at the surface.

Still, we observe that the binding energy of antimony Sb3d3 (b), indium In3d (c), and arsenic As3d (e) are slightly shifted to lower energies for the measurement performed on spincoated DMMP, *i.e.*, the photoelectrons have more information from the oxide layer. As3d, C1s, In3d, O1s, and Sb3d3, respectively shift from 46, 286, 445, 532, and 541 to 41, 285, 444, 531, and 540. This small shift of 1 eV is a proof that the native oxide/DMMP interface is not of the same chemical nature in both samples. We notice that the shift associated to arsenide is more pronounced with a difference of 5 eV, with the large differences observed the (e) panel, this could translate into surface reorganisation bringing to play As atoms and its oxide As_2O_3 in particular. This finding adds up to numerous studies reporting DMMP and its interactions with oxides of copper [269], zirconium [270, 271], tungsten [272], molybdenum [273], aluminum [274], lithium [260], and titanium [275].

4.3.4 Surface chemistry discussion

This series of experiments aimed at identifying the potential interactions between the InAsSb surface and DMMP molecules, through the native oxide of the sample, bears several conclusions. First, we expected from the literature review that DMMP might interact with the surface by adsorption and would undergo chemical reorganisation. Second, from

XPS measurements, we conclude that indeed, DMMP adsorbs and persists at the surface after several weeks; plus binding energy differences were found between a thin layer of DMMP and a large amount deposited on top of InAsSb surfaces, hinting at different chemical natures of the DMMP/native oxide interface. Third, we have performed Raman spectroscopy which shows that DMMP adsorbed is drastically different from its liquid form in terms of chemical structure. Finally, infrared spectroscopy holds the most information as it directly impacts our understanding of the sensing experiments previously performed. Indeed, the absorption coefficients of DMMP in gas phase and dried on our sample surface differed in such a way that their respective optical responses are different.

All these results support the assumption that DMMP interacts, binds, adsorbs, and changes, upon contact with InAsSb surfaces. Amongst the various paths DMMP can bind at the surface, represented in figure [4.21](#), adsorption through hydrolysis of oxide $-OH$ group into a dissociated DMMP (path [4.21\(c\)](#)) is one of the most plausible as it involves dissociation of the $P=O$ bond, according to the IR study, into a stable covalent system involving delocalised electrons and arsenic atoms, according to the XPS measures. It is important to keep in mind that these conclusions remain at the stage of hypothesis and should be taken with a grain of salt. In order to further evaluate the profound nature of these interactions, an in-depth study of potential chemical processes needs to be carried out, most likely involving simulations including density functional theory and experiments such as temperature-programmed desorption. These shall provide additional information about the binding energies and how DMMP changes over time as it dries on a surface, and therefore which adsorption mechanism is the most likely to take place.

Still, in the end, the binding of DMMP molecules, with a size of 5 \AA on the InAsSb surface, results in the formation of a 5 \AA thick monomolecular layer, after saturation. The next section deals with electromagnetic numerical simulations that will at last shed some light on the problematic of DMMP saturating the plasmonic detector, responsible for saturation of the sensing signal.

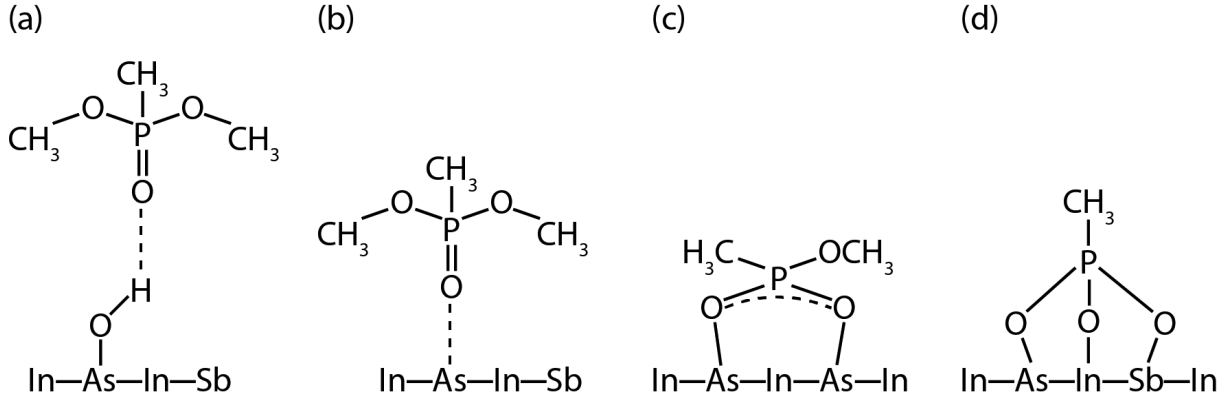


Figure 4.21: Proposed scheme of (a) molecular DMMP adsorbed at a Brønsted acid (hydroxyl) site, (b) molecular DMMP adsorbed at Lewis acid site, (c) dissociated DMMP adsorbed following hydrolysis, and (d) DMMP reorganised into methylphosphonate following methoxy groups desorption.

4.4 Numerical simulation results

4.4.1 Kramers-Kronig relations

In order to perform numerical simulations to evaluate the impact of a 5 Å thick monomolecular layer of DMMP on top of the plasmonic antennas, it is required to know its optical properties, namely the refractive index n , and the absorption coefficient κ , which together form the complex refractive index \tilde{n} of a medium. From experimental measurements, we have already retrieved the absorption coefficient κ of DMMP, both in gas and dried phases. The Kramers-Kronig relations are well-known mathematical relations that connect the real and imaginary parts of any complex function, such as the complex refractive index. In this case, it comes in handy to compute the real part of the complex index \tilde{n} : the refractive index n , from the imaginary part which is the absorption coefficient κ . Equation [4.5] gives the formula to retrieve the refractive index n from the absorption coefficient κ :

$$n(\omega) = n_\infty + \frac{2}{\pi} \int_{\omega_{min}}^{\omega_{max}} \left(\frac{\Omega \cdot \kappa(\Omega)}{\omega^2 - \Omega^2} \right) d\Omega \quad (4.5)$$

With ω the frequency range in $\text{rad}\cdot\text{s}^{-1}$, n_∞ the refractive index at high frequencies, Ω the frequency at discrete values of experimental κ , and $d\Omega$ the frequency step respective to the experimental resolution of κ . Doing so, we finally retrieve the dried DMMP complex refractive index $\tilde{n} = n + i\kappa$. Figure [4.22] shows the real and imaginary parts of the complex refractive index \tilde{n} , respectively the refractive index n and the absorption coefficient κ , for DMMP in pure phase (dotted lines) and dried on InAsSb (full lines). Just as we did in figure [4.18], we appreciate the differences in terms of optical properties between the two states of DMMP. The gas phase, equivalent to the literature, is very much different from the dried state of DMMP, especially around 10 μm , proof of interactions between the SC

surface and DMMP molecules. This result would prove to be crucial when performing electromagnetic simulations, as these differences can be responsible for the drastic spectral variations when we consider a molecular layer as thin as 5 Å. Simply put, the results from numerical simulations are highly dependent on the optical properties of the medium on top of the plasmonic nanoribbons.

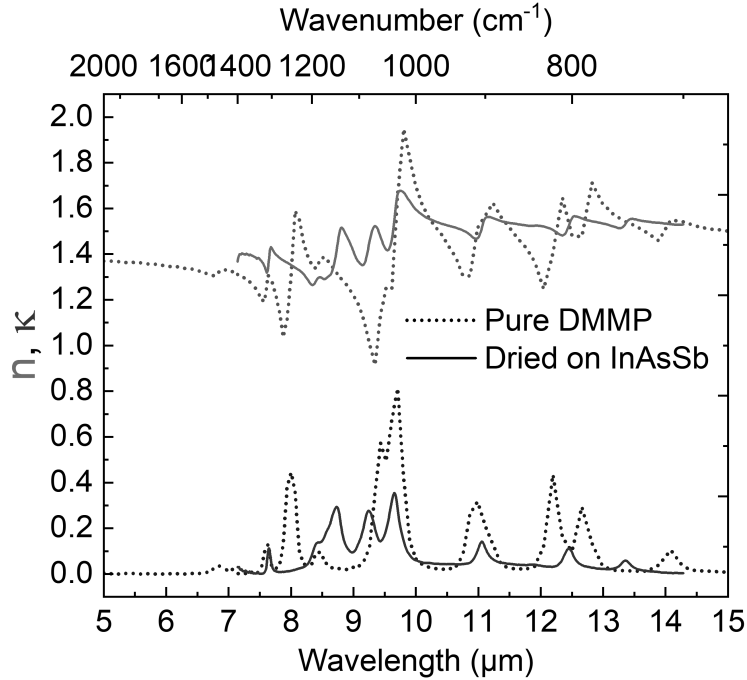


Figure 4.22: Refractive index n and absorption coefficient κ of DMMP in pure phase (dotted lines) and dried on InAsSb:Si (full lines). The refractive index n is calculated from the experimental absorption coefficient κ with Kramers-Kronig relations.

4.4.2 FDTD simulations

We evaluate the impact of a theoretical 5 Å thick DMMP layer on the sensor response by performing FDTD simulations. Figure 4.23 shows how these simulations are performed in practice. The optical parameters of each layers have been double checked with precautions and we make use of the optical properties of dried DMMP onto InAsSb from figure 4.22 to estimate its impact on the optical response of the plasmonic device. Note that a layer as thin as 5 Å required a numerical mesh grid of 50 pm, which considerably increased the computational time of the electromagnetic simulations. The results of these simulations, for all three antenna sizes previously studied: 0.84, 0.97, and 1.16 μm wide nanoribbons, are shown in figure 4.24. Before addressing the results, we discuss a second numerical simulation method employed, in the next section.

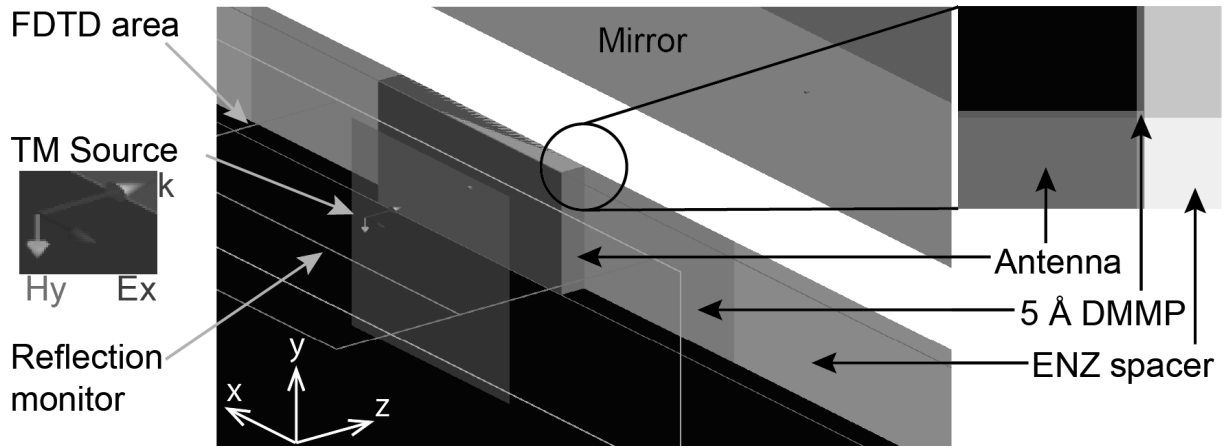


Figure 4.23: Screenshot of FDTD simulation software Lumerical. FDTD was performed to simulate the presence of a 5 Å thick monolayer of DMMP adsorbed on the surface of the plasmonic sensor.

4.4.3 RCWA simulations

We also performed RCWA simulations to confirm and cross-check the results obtained by FDTD to make sure that they were not the result of a numerical error in the form of interferences, a convergence problem, or an aberration of some sort. RCWA simulations are much faster than FDTD simulations, and this allowed us to perform simulations of plasmonic antennas with higher precision. Indeed, where FDTD simulations account for perfect plasmonic antennas, RCWA can take into account size inhomogeneity which are closer to the reality after the fabrication process. We determined each antenna size variations using SEM and AFM characterisations as follows: $1.16 \pm 0.13 \mu\text{m}$, $0.97 \pm 0.15 \mu\text{m}$, and $0.84 \pm 0.15 \mu\text{m}$ antennas. This width inhomogeneity of the fabricated plasmonic nanoribbons has for consequence a substantial broadening of the LSPR, as compared to perfect antennas in FDTD, whose LSPR are much narrower. Figure 4.24 shows the differential reflectance (%), as a function of the wavenumber (cm^{-1}) and the wavelength (μm), for each antennas (1.16, 0.97, and 0.84 μm), under TM-polarised light (E_{\perp}), of experimental measurements, FDTD simulations and RCWA simulations. We observe that simulations match experimental results in terms of amplitude, shape, and frequency. RCWA simulations, by taking into account fabrication defects, are even closer to experimental results. Further practical information regarding the gas sensing simulations can be found in annex C.

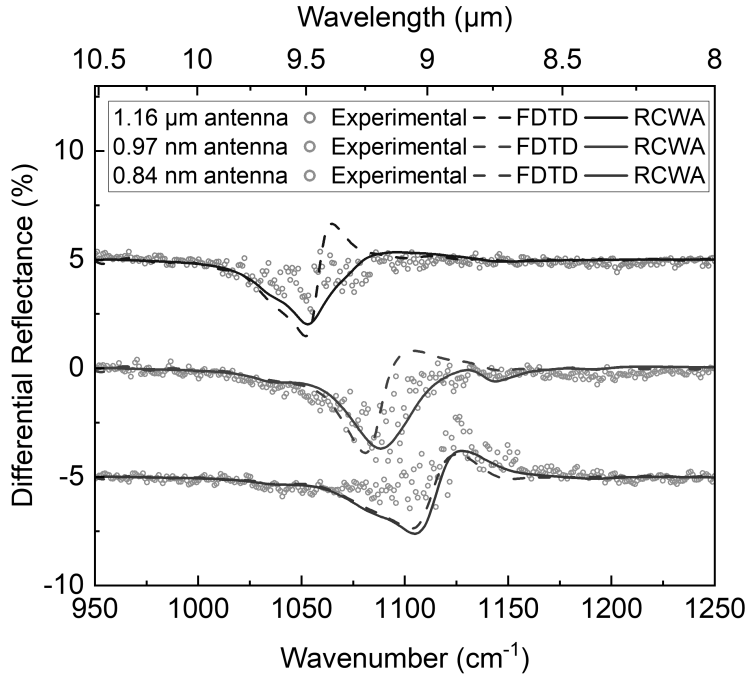


Figure 4.24: Differential reflectances (E_{\perp}): experimental measurements, FDTD simulations and RCWA-corrected simulations. Y-offset of 5% between each antennas is introduced for clarity. Space between two minor ticks corresponds to 2.5%.

The shape of the differential reflectance takes into account the coupling of DMMP molecular vibrations with the LSPR, *i.e.*, it depends on how the plasmonic resonance and the absorption lines overlap spectrally. RCWA simulations are faster and allow many antenna sizes to be simulated. We average the differential reflectance obtained for each antennas part of its size distribution. The resulting RCWA-corrected differential reflectances match experimental results. Much like the Fano resonance [276], the phase variations are strongly correlated to the spectral overlap between the two resonances, although in our case the weak coupling occurs between two continuums of states meaning that FWHMs of both the plasmonic and the molecule resonances are of the same order of magnitude. As a result, both determining the absorption spectrum of DMMP probed by the enhanced EM field, and the consideration of the antennas inhomogeneity in the simulation proved to be essential to confirm experimental results.

Conclusion

We have developed a rapid response gas sensor based on SEIRA mechanism supported by III-V semiconductor metal-like InAsSb:Si nanoribbon antennas for the detection of complex molecules such as CWAs with a detection signal of around 3% in the case of DMMP. Experimental results obtained by IR spectroscopy are confirmed by FDTD and RCWA simulations. The response of a SEIRA-based plasmonic sensor strongly depends

on the coupling strength, function of spatial and spectral overlaps, and we improved it by employing an epsilon-near-zero layer. Exploiting the surface native oxide of our sensor, we detect an extremely thin monolayer of DMMP (5 Å) without any need for functionalisation. InAsSb native oxide has the ability to interact and bind DMMP molecules to bring them in the vicinity of plasmonic nano-antennas, enhancing their absorption and increasing the sensitivity of the sensor. The sensor features selectivity towards DMMP compared to volatile organic compounds benzene and methane, plus it is water tolerant with an identical sensing signal of 2% at 50% relative humidity.

General conclusion and perspectives

In conclusion, we have demonstrated the applicability of III-V semiconductors, in particular InAsSb and GaSb, in both plasmonic-based sensing applications and the study of ENZ-plasmon phenomena. They are associated with many practical advantages including cutting-edge growth and nano-fabrication techniques, *e.g.* respectively, molecular beam epitaxy and electron-beam lithography. They benefit from the mature semiconductor industry for their integration onto photonic integrated circuits and they are compatible with CMOS technologies.

We fabricated metal-insulator-metal structures, with a doped insulator in order to adjust its plasma frequency, *i.e.*, ENZ regime to various spectral range. Such structure displays a tunable ENZ regime from the THz up to the MIR, depending on the insulator doping level, with a plasmonic resonance tunable according to the nanoantennas dimensions. We studied the optical response of three different ENZ samples according to the insulator doping level (1×10^{16} , 1×10^{19} , and 2×10^{19} cm⁻³) and nanoantennas width (from 200 nm up to 1.8 μ m). We have determined the dispersion relation of this metal-ENZ-metal structure using FDTD simulations, which proved to be a more rigorous approach as compared to effective refractive index models found in the literature, that are inadequate for non-perfect metal and insulator. We provide evidence that the resonance pinning phenomenon originates from a material transition, which is the plasma frequency in our case. Furthermore, we demonstrate that as long as an insulator exists within the plasmonic system, a metal-insulator interface exists and it may sustain SPP modes beyond the material transition frequency. The underlying consequence of the LSPR pinning is the great tolerance to fabrication defects associated to the geometry-independent behaviour; a noteworthy asset as modern photonics increasingly relies on expensive and sophisticated fabrication technologies. Additionally, we discussed the nature of various ENZ-based effects including the near-constant phase and the enhanced EM field. This study demonstrates the engineering of III-V SCs into M-ENZ-M architecture and it paves the way for applications such as the sensing of OPs in vapor phase.

The fabricated samples were then employed in gas sensing experiments of the sarin simulant: DMMP, based on surface-enhanced IR absorption. The experimental setup was built from scratch and implemented with a FTIR spectrometer. Experimental results

show a sensing signal of $\approx 3\%$ with a minimum concentration detected of 100 ppm. The sensor response is independent of the DMMP concentration in the range 100-500 ppm, resulting in a signal saturation associated with the formation of a 5 Å thick monomolecular layer of DMMP that has bound to the surface native oxide through different chemical mechanisms. From IR, Raman, and X-ray photoelectron spectroscopies, we further studied the possible interactions that may be responsible for this chemical reaction occurring at the surface, and finally we provide different models of the most plausible assumptions. The reactivity of InAsSb native oxide proved to be an asset with the ability to directly interact with DMMP, without any need for surface chemistry such as functionalisation, therefore binding and bringing DMMP in the vicinity of plasmonic nanoantennas. Consequently, the anchored DMMP molecules have their absorption enhanced, demonstrating that this innate specific interaction between the DMMP molecules and InAsSb surfaces participates in the improvement of the sensor selectivity and sensitivity. The designed, fabricated, and tested sensor is relatively rapid (response time ≈ 5 min), selective towards DMMP because it is directly related to its fingerprint, it is humidity-tolerant (tested up to 50% RH), and VOCs: benzene and methane were not detected meaning they won't interfere. Experimental results were confirmed by FDTD and RCWA simulations.

Taking a step back, although we have simulated, fabricated and tested positively a novel plasmonic sensor, several requirements are yet to be attained for its applicability in field conditions. First of all, the sensor requires a source and a detector, to this end, it is dependent on a FTIR which is quite bulky. A particular concern should then be given towards integration and miniaturisation of the system into a compact solution. The plasmonic sample itself is rather small, in the order of mm^2 , and thanks to its CMOS compatibility, it is easy to imagine an integrated, monolithic and compact device with the source and the detector on both ends. In that regard, an ambitious solution would be to integrate the sensor into a plasmonic waveguide coupled to a quantum cascade laser that acts both as source and detector (QCL-QCD system) depending on the polarisation applied to it.

Second, because the sample sensing signal is not linear with the gas concentration, it was not possible to retrieve a limit of detection, making it difficult to compare to already existing technologies. We propose two experiments that should be performed in order to further characterise the sensor performance. First, the detector should be tested at even lower concentrations (ppb level), which would confirm that no matter the amount of molecules the sensor is exposed to, it will interact with the molecules and bind them to form a monolayer on top of the sensor. If this assumption is confirmed, then the sensor sensitivity is theoretically extremely low, but then its performance is mainly limited by the time necessary to form this monolayer onto the sensor surface. Consequently, measurements over time should be performed to evaluate the sensor signal rather than only

after the system stabilisation, but this implies that DMMP molecules would only interact with the sensor when it is sent into the gas cell.

The experimental setup was recently improved by replacing the stainless steel fluidic system with stainless steel treated with a layer of inert silica preventing the compounds traveling in to react with the stainless steel, especially regarding sulphur, mercury, and phosphorous compounds. Second, the ZnSe infrared windows was substituted with a II-VI polycrystalline CVD diamond window characterised by ‘exceptional chemical resistance’. These modifications aim to reduce the interactions that might take place between DMMP molecules and the experimental setup, in order to reduce the stabilisation time and in such a way that only the plasmonic sensor is able to interact with DMMP molecules.

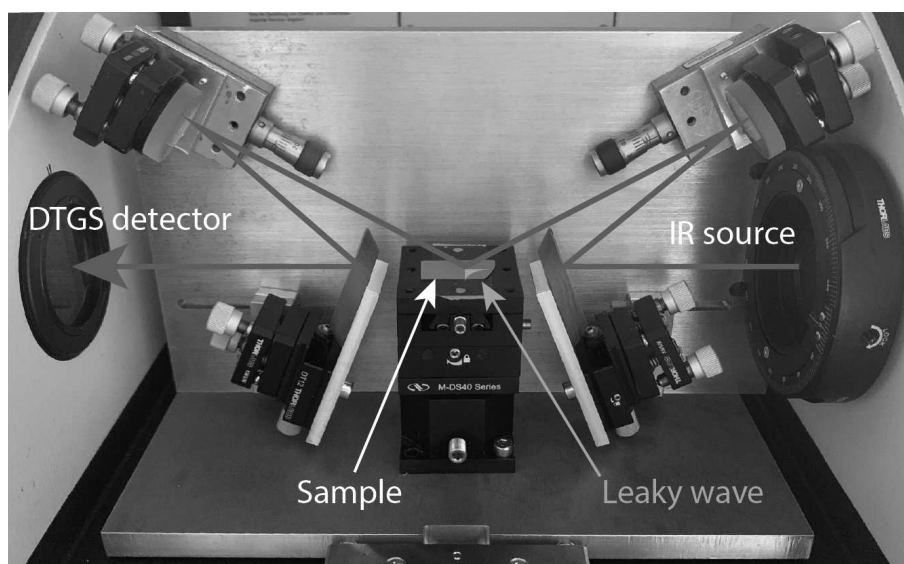
Third, this unique and naturally occurring interaction between the native oxide and DMMP molecules undermine the functionality of the diffused enhanced EM field associated to the ENZ material. Considering the trade-off between ENZ effects and the intensity of the enhanced EM field, we now believe that the intensity of the enhanced EM field should prevail over its spatial distribution. In the case of DMMP, it is now clear that the sensing signal accounts for the surface interactions, which means that the modifications happening at the surface dominate over the rest in the optical response of the system. In that regard, highly-enhanced hot-spots should be favourable compared to a less-enhanced 3D EM field. Besides, molecules in gas phase are characterised by a very low molar absorption coefficient such that even a significant spatial overlap between molecules and the enhanced EM field may not be sufficient to detect them. Still, this first attempt was successful and a thorough study should be conducted to compare standard MIM and M-ENZ-M structures for the sensing of DMMP in vapor phase.

Ultimately, if the system is integrated and the sample features are fully known such that all doubts regarding the limit of detection, selectivity and response time, have been allayed, the sample could be tested in field conditions. Upon which, both the sensitivity and selectivity might need improvements with the employment of different antenna design exploiting lightning rod effects, and the engineering of metamaterials and/or 2D antennas to attain multiresonance, further improving both of these features, especially by targeting the characteristic P–F chemical bond of sarin.

Annexes

A. Brewster experiments

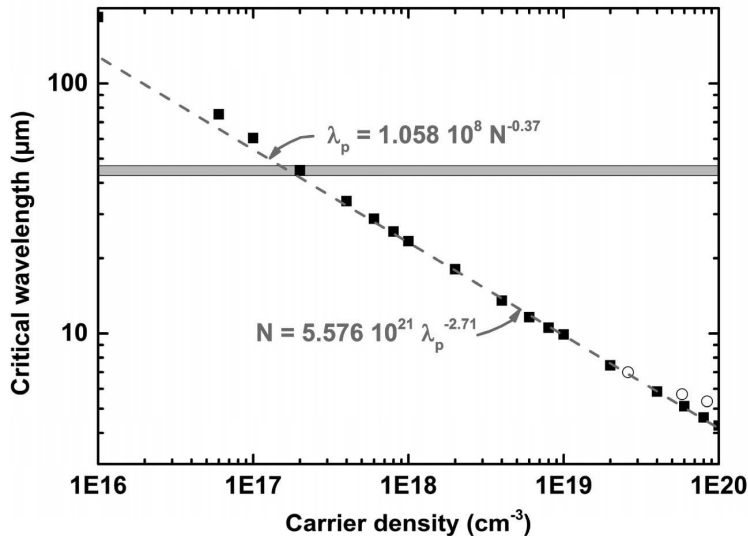
The Brewster simulations are performed using a home-made code based on the transfer-matrix method which consists in solving the Maxwell's equations for an electromagnetic wave propagating in a multi-layered structure by considering the continuity equations at each interface. The code takes as entries the indexes of each layer calculated by the Lorentz-Drude model as well as their thickness. If one knows the electric field at the beginning of a layer, the field on the other side of the layer can be expressed with a simple matrix operation. Therefore a structure composed of multiple layers consists in a system of matrices that can be summed up in a system matrix as the product of each layer matrices. The reflectance and transmittance can then be retrieved from the system transfer matrix. Afterwards, the simulations are compared to the experimental results obtained from the Brewster configuration presented in the figure below.



Photograph of the experimental Brewster mode measurement setup.

Then, the free carrier density is deduced from the Brewster measurements by extracting the dip associated to the free carrier absorption at the critical wavelength. The figure below represents the critical wavelength (plasma frequency) versus the free carrier density in InAs (dark square) with experimental values (open circles). The red dashed line

corresponds to the empirical power law which was used to retrieve the doping level in our samples.



Critical wavelength, λ_p , versus the carrier density in the case of InAs (dark square). The red dashed line corresponds to the power law extracted. The grey part of the figure corresponds to the Reststrahlen band due to optical phonon. The open symbols correspond to experimental values. From [217].

B. Dispersion relation calculi

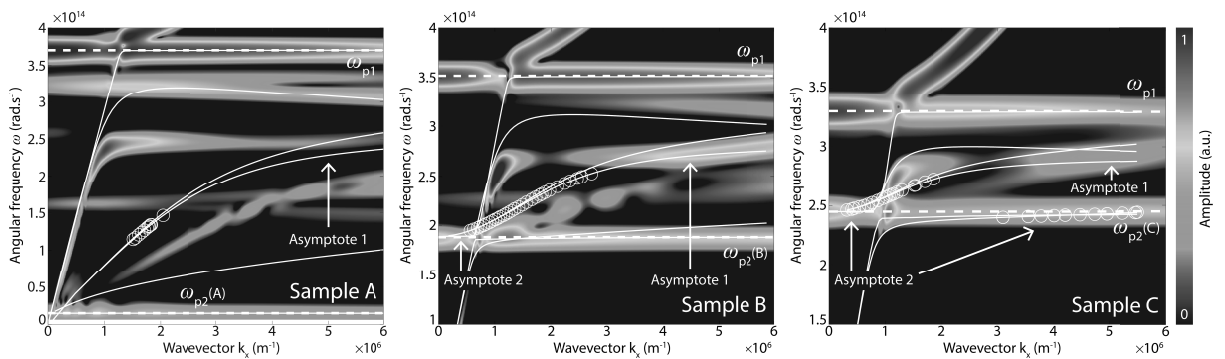
The dispersion relation of a multilayer system is important because this kind of system cannot be considered as single interfaces separately. The reason for that is that when layers have a thickness smaller than the decay length of SPPs propagating at each interfaces, then SPPs interact with each other and couple, giving rise to coupled modes. This can be the case in our 4-layers structure, hence we want to elucidate the general properties of coupled SPPs by solving the dispersion relation of the photonic structure. From Maxwell's equations, it can be shown that each medium, *i.e.* layer, composing the system is characterised three fields components H_y , E_x , and E_z , in the case of TM modes. The requirement of continuity of H_y and E_x , with the relation $k_i^2 = k_x^2 - k_0^2 \epsilon_i$, results in the implicit expression for the dispersion relation linking k_x and ω via:

$$e^{2k_3 d_3} = \frac{\left(\frac{k_1}{\epsilon_1} + \frac{k_2}{\epsilon_2}\right)\left(\frac{k_2}{\epsilon_2} - \frac{k_3}{\epsilon_3}\right)\left(\frac{k_4}{\epsilon_4} - \frac{k_3}{\epsilon_3}\right)e^{2k_2 d_2} - \left(\frac{k_2}{\epsilon_2} - \frac{k_1}{\epsilon_1}\right)\left(\frac{k_2}{\epsilon_2} + \frac{k_3}{\epsilon_3}\right)\left(\frac{k_4}{\epsilon_4} - \frac{k_3}{\epsilon_3}\right)}{\left(\frac{k_1}{\epsilon_1} + \frac{k_2}{\epsilon_2}\right)\left(\frac{k_2}{\epsilon_2} + \frac{k_3}{\epsilon_3}\right)\left(\frac{k_4}{\epsilon_4} + \frac{k_3}{\epsilon_3}\right)e^{2k_2 d_2} - \left(\frac{k_2}{\epsilon_2} - \frac{k_1}{\epsilon_1}\right)\left(\frac{k_2}{\epsilon_2} - \frac{k_3}{\epsilon_3}\right)\left(\frac{k_4}{\epsilon_4} + \frac{k_3}{\epsilon_3}\right)}$$

As stated in the manuscript, finding the solutions of this equation requires advanced peak-finding methods. While FDTD simulations were performed to solve this issue, we present here another method that we employed to corroborate the results obtained by FDTD. This method is based on the simple `fsolve` Matlab function that solves a system of nonlinear equations. The problem is that the dispersion relation of a 4-layers struc-

ture is transcendental, and the fsolve function is not suited for such equation. In a way, fsolve works by dichotomy, so it requires a purely real or imaginary function in order to find the solutions. With this in mind, we first decided to divide the problem in three different systems, each composed of three layers: air/InAsSb:Si(n++)/InAsSb:Si(n+), air/InAsSb:Si(n+)/InAsSb:Si(n++), and InAsSb:Si(n++)/InAsSb:Si(n+)/InAsSb:Si(n++). These systems respectively correspond to: air/antenna/ENZ, air/ENZ/mirror, and antenna/ENZ/mirror. Because the dispersion relation of a 3-layers system is much simpler, one can break it down in such a way that every time to wavevector becomes complex, it can be artificially turned into a real number again. This way, the dispersion relation remains purely real for all wavevectors k_x and the function fsolve can solve it. The downside of this solution is that the results obtained at larger wavevector, *i.e.*, when the wavevector imaginary part is significant, are distorted and do not perfectly account for the reality.

Additionally, we would like to comment that FDTD simulations performed in this manuscript did not take losses into account. The reason for that is that losses significantly broaden the solutions, *i.e.* singularities (poles and zeros), of the dispersion relation, making it extremely difficult to either retrieve the solution lines or even to interpret the amplitude maps obtained with the losses. The figure below shows the dispersion relation maps obtained by FDTD considering the full 4-layers stacking of our plasmonic structure, with on top (white lines) the solution lines obtained with the aforementioned method relying on the fsolve Matlab function. The white circles are experimental LSPR frequencies. It therefore comes to light as to why we opted to simulate the plasmonic structure without considering the losses, as the interpretation of the 2D dispersion relation with the losses is nearly impossible. Still, the white lines obtained with the home-made method serve as a guide to the eye and demonstrate that FDTD is a suitable method for determining the dispersion relation of a plasmonic structure. The asymptote 2 highlights the LSPR pinning.



Dispersion relations of the photonic structure: air/InAsSb:Si(n++)/InAsSb:Si(n+)/InAsSb:Si(n++) for each sample. The amplitude refers to the intensity of the singularities of the dispersion relation. White lines: dispersion relation solutions obtained with the home-made code based on Matlab fsolve function. White empty circles: experimental LSPR frequencies of each sample.

C. Gas sensing simulations

Gas sensing simulations were performed either with FDTD or with RCWA. FDTD simulations were first performed because in the right conditions, FDTD always converges and the result is reliable. To evaluate using FDTD the impact of a 5 Å thick DMMP monolayer at the top of the plasmonic sensor, we designed the structure in terms of thickness and the antennas are characterised by their width. The optical properties of each layer is given as entry in the software. The antenna periodicity is taken into account by the simulation area with anti-symmetric boundary conditions. Perfectly matched layer boundary conditions were used in other directions. The mesh of the structure was set as auto non-uniform in order to reduce numerical dispersion, with a mesh maximal mesh accuracy of type ‘conformal variant 0’. As for the 5 Å layer, a 50 pm mesh was applied in order to correctly compute the interfaces and properly consider its optical response in the system reflectance. The simulation time was set at 10,000 fs with a auto shutoff min of 10^{-6} . In these conditions, each simulation would take several hours in average.

The computational time would prevent us to perform a large amount of EM simulations required to take into account the antenna inhomogeneity observed in practice. To solve this issue and calculate a greater amount of antenna size, we used RCWA. The RCWA open-source RETICOLO code running on Matlab is especially well-suited for this application. Just as FDTD, one can design its photonic structure, based on the optical properties of each layer and their thickness. It performs in an analogous way to the matrix-transfer method in 1D such that it solves the Maxwell’s equation by ensuring fields continuity at each interface. Additionally, this code is normalised by the wavelength dimension which greatly reduces the orders of magnitude in the calculi and therefore significantly speeds up the computational time. We performed identical simulations in order to evaluate the optical response of the 5 Å thick DMMP layer. Simulations were performed with a TM-polarised normal incidence light. The main source of errors when using this method is that one cannot know if the result has converged. To address this issue, one can play on the Fourier harmonics number, which is proportional to the accuracy of the simulation as well as its computational time. This number was set to 1000 for our simulations after making sure that the results were identical to those obtained by FDTD. In the end, the simulation time was around ~ 30 minutes, which would allow us to perform plentiful antenna width simulations and average their reflectance response in order to assess the inhomogeneity impact over the reflectance.

Communication of the scientific results

2023

P. Fehlen, J. Guise, G. Thomas, F. Gonzalez-Posada, P. Loren, L. Cerutti, J-B. Rodriguez, D. Spitzer, T. Taliercio, Engineering the infrared optical response of plasmonic structures with ϵ -near-zero III-V semiconductors. Under review in *Advanced Optical Materials*.

P. Fehlen, J. Guise, G. Thomas, F. Gonzalez-Posada, P. Loren, L. Cerutti, J-B. Rodriguez, D. Spitzer, T. Taliercio, Engineering the optical response of plasmonic structures with ϵ -near-zero III-V semiconductors. Poster presentation. Surface Plasmon Photonics (SPP10) conference, May 21-26, 2023, Rice University, Houston, TX, USA.

P. Fehlen, G. Thomas, F. Gonzalez-Posada, J. Guise, F. Rusconi, L. Cerutti, T. Taliercio, D. Spitzer, Gas sensing of organophosphorous compounds with III-V semiconductor plasmonics, *Sensors and Actuators B: Chemical*, Volume 376, Part B, 2023, 132987, ISSN 0925-4005.

P. Fehlen, G. Thomas, F. Gonzalez Posada, J. Guise, F. Rusconi, L. Cerutti, T. Taliercio, D. Spitzer, "III-V semiconductor plasmonics for gas sensing of organophosphorous compounds," *Proc. SPIE PC12430, Quantum Sensing and Nano Electronics and Photonics XIX*, PC1243017 (17 March 2023); <https://doi.org/10.1117/12.2649983>

J. Guise, S. Blin, H. Ratovo, M. Thual, P. Fehlen, F. Gonzalez Posada, J-B. Rodriguez, L. Cerutti, T. Taliercio, Simultaneous terahertz characterization technique for low doping and carrier lifetime measurements in indium arsenide. Under review in *Journal of Applied Physics*.

2022

N. Aubergier, P. Loren, J. Guise, F. Barho, P. Fehlen, M. Najem, F. Gonzalez-Posada-Flores, S. Blin, L. Cerutti, R. Smaali, E. Centeno, T. Taliercio, "Quantum plasmonics and hyperbolic material for biosensing," *Proc. SPIE 12009, Quantum Sensing and Nano Electronics and Photonics XVIII*, 120090E (5 March 2022); <https://doi.org/10.1117/12.2615652>

P. Loren, P. Fehlen, J. Guise, F. Barho, M. Najem, F. Gonzalez-Posada-Flores, S. Blin, L. Cerutti, R. Smaali, E. Centeno, T. Taliercio, "Semiconductor plasmonics and metamaterials for IR applications," *Proc. SPIE 12002, Oxide-based Materials and Devices XIII*, 1200202 (5 March 2022); <https://doi.org/10.1117/12.2612190>

2021

P. Fehlen, G. Thomas, F. Gonzales-Posada, T. Taliercio, D. Spitzer. Surface-enhanced infrared spectroscopy for selective and sensitive detection of organophosphorous compounds. *Sensors* 2021, 20-22 octobre 2021, Milan (Italie), Oct 2021, Milan, Italy. hal-03623983

P. Fehlen, G. Thomas, F. Gonzalez-Posada, T. Taliercio, D. Spitzer. Selective and sensitive detection of organophosphorous compounds using surface-enhanced spectroscopy in the mid-infrared. 15th International Conference on Mid-Infrared optoelectronic Materials and Devices (MIOMD) (virtuel), 01-03 septembre 2021, Sep 2021, Virtuel, France. hal-03623979

Bibliography

- [1] Gerard J. Fitzgerald. Chemical warfare and medical response during world war i. *American Journal of Public Health*, 98(4):611–625, 2008. PMID: 18356568.
- [2] Zoraida P. Aguilar Eden Joy Pacsial-Ong. Chemical warfare agent detection: a review of current trends and future perspective. *FBS*, 5(2):516–543, 2013.
- [3] Looking back helps us look forward. <https://www.opcw.org/about-us/history>. Accessed: 2023-07-11.
- [4] Hong Zhou, Xindan Hui, Dongxiao Li, Donglin Hu, Xin Chen, Xianming He, Lingxiao Gao, He Huang, Chengkuo Lee, and Xiaojing Mu. Metal–organic framework–surface-enhanced infrared absorption platform enables simultaneous on-chip sensing of greenhouse gases. *Advanced Science*, 7(20):2001173, 2020.
- [5] Frederick R Sidell and Jonathan Borak. Chemical warfare agents: Ii. nerve agents. *Annals of Emergency Medicine*, 21(7):865–871, 1992.
- [6] Javed Ali. Chemical weapons and the iran-iraq war: A case study in noncompliance. *The Nonproliferation Review*, 8(1):43–58, 2001.
- [7] Tetsu Okumura, Nobukatsu Takasu, Shinichi Ishimatsu, Shou Miyonoki, Akihiro Mitsuhashi, Keisuke Kumada, Kazutoyo Tanaka, and Shigeaki Hinohara. Report on 640 victims of the tokyo subway sarin attack. *Annals of Emergency Medicine*, 28(2):129–135, 1996.
- [8] Chemical weapons – opcw report on the use of chemical weapons in syria (13 june 2018). <https://www.diplomatie.gouv.fr/en/french-foreign-policy/security-disarmament-and-non-proliferation/news/2018/article/chemical-weapons-opcw-report-on-the-use-of-chemical-weapons-in-syria-13-06-18>. Accessed: 2023-07-11.
- [9] Daniel M. Quinn. Acetylcholinesterase: enzyme structure, reaction dynamics, and virtual transition states. *Chemical Reviews*, 87(5):955–979, 1987.
- [10] Jonathan Newmark. Nerve agents: Pathophysiology and treatment of poisoning. *Seminars in Neurology*, 24(2):185–196, 2004.

- [11] National Research Council et al. Acute exposure guideline levels for selected airborne chemicals: Volume 3. 2003.
- [12] National Research Council et al. *Testing and evaluation of standoff chemical agent detectors*. National Academies Press, 2003.
- [13] Mayank Agrawal, Dorina F. Sava Gallis, Jeffery A. Greathouse, and David S. Sholl. How useful are common simulants of chemical warfare agents at predicting adsorption behavior? *The Journal of Physical Chemistry C*, 122(45):26061–26069, 2018.
- [14] Rodi Sferopoulos. A Review of Chemical Warfare Agent (CWA) Detector Technologies and Commercial-Off-The-Shelf Items. *Australian Government Department of Defence*, page 98, 2009.
- [15] Herbert H. Hill and Greg Simpson. Capabilities and limitations of ion mobility spectrometry for field screening applications. *Field Analytical Chemistry & Technology*, 1(3):119–134, 1997.
- [16] Terri Longworth and Kwok Ong. Domestic preparedness program testing of the cam-chemical agent monitor (type 1) against chemical warfare agents summary report. page 25, 01 2002.
- [17] Y. Sun and K. Y. Ong. *Detection Technologies for Chemical Warfare Agents and Toxic Vapors (1st ed.)*. CRC Press, 2004.
- [18] Terri L. Longworth and Kwok Y. Ong. Domestic preparedness program: Testing of detectors against chemical warfare agents - summary report (uc ap2c portable chemical contamination control monitor collective unit). 2001.
- [19] Marta Lafuente, Sarah De Marchi, Miguel Urbiztondo, Isabel Pastoriza-Santos, Ignacio Pérez-Juste, Jesús Santamaría, Reyes Mallada, and María Pina. Plasmonic mof thin films with raman internal standard for fast and ultrasensitive sers detection of chemical warfare agents in ambient air. *ACS Sensors*, 6(6):2241–2251, 2021. PMID: 34043325.
- [20] Semra Akgönüllü, Yeşeren Saylan, Nilay Bereli, Deniz Türkmen, Handan Yavuz, and Adil Denizli. *Plasmonic Sensors for Detection of Chemical and Biological Warfare Agents*, chapter 4, pages 71–85. John Wiley & Sons, Ltd, 2021.
- [21] Susan M. Daly, Michele Grassi, Devanand K. Shenoy, Franco Ugozzoli, and Enrico Dalcanale. Supramolecular surface plasmon resonance (spr) sensors for organophosphorus vapor detection. *J. Mater. Chem.*, 17:1809–1818, 2007.
- [22] Kun-Lin Yang, Katie Cadwell, and Nicholas L. Abbott. Use of self-assembled monolayers, metal ions and smectic liquid crystals to detect organophosphonates. *Sensors and Actuators B: Chemical*, 104(1):50–56, 2005.

- [23] George B. Sigal, Cynthia Bamdad, Alcide Barberis, Jack Strominger, and George M. Whitesides. A self-assembled monolayer for the binding and study of histidine-tagged proteins by surface plasmon resonance. *Analytical Chemistry*, 68(3):490–497, 1996. PMID: 8712358.
- [24] Ran Yoo, Sungmee Cho, Min-Jung Song, and Wooyoung Lee. Highly sensitive gas sensor based on al-doped zno nanoparticles for detection of dimethyl methylphosphonate as a chemical warfare agent simulant. *Sensors and Actuators B: Chemical*, 221:217–223, 2015.
- [25] A.L. Simonian, T.A. Good, S.-S. Wang, and J.R. Wild. Nanoparticle-based optical biosensors for the direct detection of organophosphate chemical warfare agents and pesticides. *Analytica Chimica Acta*, 534(1):69–77, 2005. Interpretation, Design and Selection of Biomolecular Interactions.
- [26] Alexey A. Tomchenko, Gregory P. Harmer, and Brent T. Marquis. Detection of chemical warfare agents using nanostructured metal oxide sensors. *Sensors and Actuators B: Chemical*, 108(1):41–55, 2005. Proceedings of the Tenth International Meeting on Chemical Sensors.
- [27] Neeraj Kumar, Pukhrambam Dipak, Dinesh Chandra Tiwari, and Radha Tomar. Study and characterization of polyaniline/zeolite-mor nanocomposite and their role in detection of chemical warfare agent simulant-cees. *Chemical Physics Letters*, 755:137766, 2020.
- [28] Seunghyun Jang, Youngdae Koh, Jihoon Kim, and Honglae Sohn. Detection of G-type nerve agent simulants based on a double reflection DBR porous silicon interferometer. *Journal of the Korean Physical Society*, 52(2):212–215, 2008.
- [29] Abolanle S. Adekunle, Jeseelan Pillay, and Kenneth I. Ozoemena. Electrocatalysis of 2-diethylaminoethanethiol at nickel nanoparticle-electrodecorated single-walled carbon nanotube platform: An adsorption-controlled electrode process. *Electroanalysis*, 20(23):2587–2591, 2008.
- [30] Hao Chen, Shiyan Zhang, Kali A. Miller, and Paul V. Braun. Autonomic molecular transport for ultrasensitive surface-enhanced infrared absorption spectroscopy. *ACS Applied Polymer Materials*, 2(9):3929–3935, 2020.
- [31] Yu-Ri Lee, Jun Kim, and Wha-Seung Ahn. Synthesis of metal-organic frameworks: A mini review. *Korean Journal of Chemical Engineering*, 30(9):1667–1680, Sep 2013.
- [32] Yoon Jeong, Kibong Kim, Olga G. Tsay, David A. Atwood, and David G. Churchill. Update 1 of: Destruction and detection of chemical warfare agents. *Chemical Reviews*, 115(24):PR1–PR76, 2015. PMID: 26654832.

- [33] Jyoti Lather, Pooja Bhatt, Anoop Thomas, Thomas W. Ebbesen, and Jino George. Cavity catalysis by cooperative vibrational strong coupling of reactant and solvent molecules. *Angewandte Chemie International Edition*, 58(31):10635–10638, 2019.
- [34] James T. Hugall, Anshuman Singh, and Niek F. van Hulst. Plasmonic cavity coupling. *ACS Photonics*, 5(1):43–53, 2018.
- [35] Yeşeren Saylan, Semra Akgönüllü, and Adil Denizli. Plasmonic sensors for monitoring biological and chemical threat agents. *Biosensors*, 10(10), 2020.
- [36] Yanqiu Song, Jialei Bai, Rong Zhang, Enqi Wu, Jiang Wang, Shuang Li, Baoan Ning, Minglin Wang, Zhixian Gao, and Yuan Peng. Lspr-enhanced photonic crystal allows ultrasensitive and label-free detection of hazardous chemicals. *Sensors and Actuators B: Chemical*, 310:127671, 2020.
- [37] Mrigank Singh Verma and Manabendra Chandra. Nonlinear plasmonic sensing for label-free and selective detection of mercury at picomolar level. *ACS Sensors*, 5(3):645–649, 2020. PMID: 32067451.
- [38] Amirmostafa Amirjani and Davoud Fatmehsari Haghshenas. Ag nanostructures as the surface plasmon resonance (spr)-based sensors: A mechanistic study with an emphasis on heavy metallic ions detection. *Sensors and Actuators B: Chemical*, 273:1768–1779, 2018.
- [39] H. Thenmozhi, M.S. Mani Rajan, and Kawsar Ahmed. D-shaped pcf sensor based on spr for the detection of carcinogenic agents in food and cosmetics. *Optik*, 180:264–270, 2019.
- [40] Vered Heleg-Shabtai, Hagai Sharabi, Amalia Zaltsman, Izhar Ron, and Alexander Pevzner. Surface-enhanced raman spectroscopy (sers) for detection of vx and hd in the gas phase using a hand-held raman spectrometer. *Analyst*, 145:6334–6341, 2020.
- [41] Marta Lafuente, Ismael Pellejero, Víctor Sebastián, Miguel A. Urbiztondo, Reyes Mallada, M. Pilar Pina, and Jesús Santamaría. Highly sensitive sers quantification of organophosphorous chemical warfare agents: A major step towards the real time sensing in the gas phase. *Sensors and Actuators B: Chemical*, 267:457–466, 2018.
- [42] E. Mauriz, A. Calle, L.M. Lechuga, J. Quintana, A. Montoya, and J.J. Manclús. Real-time detection of chlorpyrifos at part per trillion levels in ground, surface and drinking water samples by a portable surface plasmon resonance immunosensor. *Analytica Chimica Acta*, 561(1):40–47, 2006.
- [43] Jacqueline Jatschka, André Dathe, Andrea Csáki, Wolfgang Fritzsche, and Ondrej Stranik. Propagating and localized surface plasmon resonance sensing — a critical

- comparison based on measurements and theory. *Sensing and Bio-Sensing Research*, 7:62–70, 2016.
- [44] Kathryn M. Mayer and Jason H. Hafner. Localized surface plasmon resonance sensors. *Chemical Reviews*, 111(6):3828–3857, 2011. PMID: 21648956.
- [45] E. N. Economou. Surface plasmons in thin films. *Phys. Rev.*, 182:539–554, Jun 1969.
- [46] B. Prade, J. Y. Vinet, and A. Mysyrowicz. Guided optical waves in planar heterostructures with negative dielectric constant. *Phys. Rev. B*, 44:13556–13572, Dec 1991.
- [47] John Polo, Tom Mackay, and Akhlesh Lakhtakia. *Electromagnetic surface waves: a modern perspective*. Newnes, 2013.
- [48] Vincenzo Amendola, Roberto Pilot, Marco Frasconi, Onofrio M Maragò, and Maria Antonia Iatì. Surface plasmon resonance in gold nanoparticles: a review. *Journal of physics. Condensed matter : an Institute of Physics journal*, 29(20):203002, May 2017.
- [49] Matthew Rycenga, Claire M. Cobley, Jie Zeng, Weiyang Li, Christine H. Moran, Qiang Zhang, Dong Qin, and Younan Xia. Controlling the synthesis and assembly of silver nanostructures for plasmonic applications. *Chemical Reviews*, 111(6):3669–3712, 2011. PMID: 21395318.
- [50] Vahagn Mkhitarian, Katia March, Eric Nestor Tseng, Xiaoyan Li, Leonardo Scarcabelli, Luis M. Liz-Marzán, Shih-Yun Chen, Luiz H. G. Tizei, Odile Stéphan, Jenn-Ming Song, Mathieu Kociak, F. Javier García de Abajo, and Alexandre Gloter. Can copper nanostructures sustain high-quality plasmons? *Nano Letters*, 21(6):2444–2452, 2021. PMID: 33651617.
- [51] Mark W. Knight, Nicholas S. King, Lifei Liu, Henry O. Everitt, Peter Nordlander, and Naomi J. Halas. Aluminum for plasmonics. *ACS Nano*, 8(1):834–840, 2014. PMID: 24274662.
- [52] Eric Tournié, Laura Monge Bartolome, Marta Rio Calvo, Zeineb Loghmari, Daniel A. Díaz-Thomas, Roland Teissier, Alexei N. Baranov, Laurent Cerutti, and Jean-Baptiste Rodriguez. Mid-infrared iii–v semiconductor lasers epitaxially grown on si substrates. *Light: Science & Applications*, 11(1):165, Jun 2022.
- [53] Gururaj V. Naik, Vladimir M. Shalaev, and Alexandra Boltasseva. Alternative plasmonic materials: Beyond gold and silver. *Advanced Materials*, 25(24):3264–3294, 2013.

- [54] Yujun Zhong, Shyamala Devi Malagari, Travis Hamilton, and Daniel M. Wasserman. Review of mid-infrared plasmonic materials. *Journal of Nanophotonics*, 9(1):093791, 2015.
- [55] Thierry Taliercio and Paolo Biagioni. Semiconductor infrared plasmonics. *Nanophotonics*, 8(6):949–990, 2019.
- [56] Takayuki Watanabe, Stephane A. Boubanga-Tombet, Yudai Tanimoto, Denis Fateev, Viacheslav Popov, Dominique Coquillat, Wojciech Knap, Yahya M. Meziani, Yuye Wang, Hiroaki Minamide, Hiromasa Ito, and Taiichi Otsuji. Inp- and gaas-based plasmonic high-electron-mobility transistors for room-temperature ultrahigh-sensitive terahertz sensing and imaging. *IEEE Sensors Journal*, 13(1):89–99, 2013.
- [57] M. Cada, D. Blazek, J. Pistora, K. Postava, and P. Siroky. Theoretical and experimental study of plasmonic effects in heavily doped gallium arsenide and indium phosphide. *Opt. Mater. Express*, 5(2):340–352, Feb 2015.
- [58] Junghyun Park, Ju-Hyung Kang, Xiaoge Liu, Scott J. Maddox, Kechao Tang, Paul C. McIntyre, Seth R. Bank, and Mark L. Brongersma. Dynamic thermal emission control with inas-based plasmonic metasurfaces. *Science Advances*, 4(12):eaat3163, 2018.
- [59] H. Saxena, R. E. Peale, and W. R. Buchwald. Tunable two-dimensional plasmon resonances in an InGaAs/InP high electron mobility transistor. *Journal of Applied Physics*, 105(11):113101, 06 2009.
- [60] T. Kozawa, T. Kachi, H. Kano, Y. Taga, M. Hashimoto, N. Koide, and K. Manabe. Raman scattering from LO phonon-plasmon coupled modes in gallium nitride. *Journal of Applied Physics*, 75(2):1098–1101, 01 1994.
- [61] M. A. Omar. Intervalley transfer, plasma frequency, and plasmon-lo-phonon interaction in *n*-type gallium antimonide. *Phys. Rev.*, 186:791–793, Oct 1969.
- [62] Thierry Taliercio, Vilianne NTsame Guilengui, Laurent Cerutti, Jean-Baptiste Rodriguez, Franziska Barho, Maria-José Milla Rodrigo, Fernando Gonzalez-Posada, Eric Tournié, Michael Niehle, and Achim Trampert. Fano-like resonances sustained by si doped inassb plasmonic resonators integrated in gasb matrix. *Opt. Express*, 23(23):29423–29433, Nov 2015.
- [63] Maryam Moridsadat, Saeed Golmohammadi, and Hamed Baghban. Tunable multi-band plasmonic response of indium antimonide touching microrings in the terahertz range. *Appl. Opt.*, 57(16):4368–4375, Jun 2018.
- [64] Qianyi Mu, Fei Fan, Sai Chen, Shitong Xu, Chuanzhong Xiong, Xin Zhang, Xi-anhui Wang, and Shengjiang Chang. Tunable magneto-optical polarization de-

- vice for terahertz waves based on insb and its plasmonic structure. *Photon. Res.*, 7(3):325–331, Mar 2019.
- [65] Viktoriia E. Babicheva, Alexandra Boltasseva, and Andrei V. Lavrinenko. Transparent conducting oxides for electro-optical plasmonic modulators. *Nanophotonics*, 4(2):165–185, 2015.
- [66] Edward Sachet, Mark D. Losego, Joshua Guske, Stefan Franzen, and Jon-Paul Maria. Mid-infrared surface plasmon resonance in zinc oxide semiconductor thin films. *Applied Physics Letters*, 102(5):051111, 02 2013.
- [67] Edward Sachet, Christopher T. Shelton, Joshua S. Harris, Benjamin E. Gaddy, Douglas L. Irving, Stefano Curtarolo, Brian F. Donovan, Patrick E. Hopkins, Peter A. Sharma, Ana Lima Sharma, Jon Ihlefeld, Stefan Franzen, and Jon-Paul Maria. Dysprosium-doped cadmium oxide as a gateway material for mid-infrared plasmonics. *Nature Materials*, 14(4):414–420, Apr 2015.
- [68] Shi Qiang Li, Peijun Guo, Lingxiao Zhang, Wei Zhou, Teri W. Odom, Tamar Seideman, John B. Ketterson, and Robert P. H. Chang. Infrared plasmonics with indium–tin-oxide nanorod arrays. *ACS Nano*, 5(11):9161–9170, 2011. PMID: 22017677.
- [69] Jongbum Kim, Gururaj V. Naik, Alexander V. Gavrilenko, Krishnaveni Dondapati, Vladimir I. Gavrilenko, S. M. Prokes, Orest J. Glembocki, Vladimir M. Shalaev, and Alexandra Boltasseva. Optical properties of gallium-doped zinc oxide—a low-loss plasmonic material: First-principles theory and experiment. *Phys. Rev. X*, 3:041037, Dec 2013.
- [70] A. K. Pradhan, R. M. Mundle, Kevin Santiago, J. R. Skuza, Bo Xiao, K. D. Song, M. Bahoura, Ramez Cheaito, and Patrick E. Hopkins. Extreme tunability in aluminum doped zinc oxide plasmonic materials for near-infrared applications. *Scientific Reports*, 4(1):6415, Sep 2014.
- [71] Xiangchao Meng and Zisheng Zhang. Plasmonic ternary ag–rgo–bi₂moo₆ composites with enhanced visible light-driven photocatalytic activity. *Journal of Catalysis*, 344:616–630, 2016.
- [72] S. C. Kehr, Y. M. Liu, L. W. Martin, P. Yu, M. Gajek, S.-Y. Yang, C.-H. Yang, M. T. Wenzel, R. Jacob, H.-G. von Ribbeck, M. Helm, X. Zhang, L. M. Eng, and R. Ramesh. Near-field examination of perovskite-based superlenses and superlens-enhanced probe-object coupling. *Nature Communications*, 2(1):249, Mar 2011.
- [73] Karthish Manthiram and A. Paul Alivisatos. Tunable localized surface plasmon resonances in tungsten oxide nanocrystals. *Journal of the American Chemical Society*, 134(9):3995–3998, 2012. PMID: 22332881.

- [74] Joseph M. Luther, Prashant K. Jain, Trevor Ewers, and A. Paul Alivisatos. Localized surface plasmon resonances arising from free carriers in doped quantum dots. *Nature Materials*, 10(5):361–366, May 2011.
- [75] A. N. Grigorenko, M. Polini, and K. S. Novoselov. Graphene plasmonics. *Nature Photonics*, 6(11):749–758, Nov 2012.
- [76] F. Javier García de Abajo. Graphene plasmonics: Challenges and opportunities. *ACS Photonics*, 1(3):135–152, 2014.
- [77] Andrei Nemilentsau, Tony Low, and George Hanson. Anisotropic 2d materials for tunable hyperbolic plasmonics. *Phys. Rev. Lett.*, 116:066804, Feb 2016.
- [78] M G Blaber, M D Arnold, and M J Ford. A review of the optical properties of alloys and intermetallics for plasmonics. *Journal of Physics: Condensed Matter*, 22(14):143201, mar 2010.
- [79] Richard Soref, Robert E. Peale, and Walter Buchwald. Longwave plasmonics on doped silicon and silicides. *Opt. Express*, 16(9):6507–6514, Apr 2008.
- [80] Justin W. Cleary, William H. Streyer, Nima Nader, Shiva Vangala, Ivan Avrutsky, Bruce Claflin, Joshua Hendrickson, Daniel Wasserman, Robert E. Peale, Walter Buchwald, and Richard Soref. Platinum germanides for mid- and long-wave infrared plasmonics. *Opt. Express*, 23(3):3316–3326, Feb 2015.
- [81] Mukesh Kumar, Naoto Umezawa, Satoshi Ishii, and Tadaaki Nagao. Examining the performance of refractory conductive ceramics as plasmonic materials: A theoretical approach. *ACS Photonics*, 3(1):43–50, 2016.
- [82] D. A. Bobb, G. Zhu, M. Mayy, A. V. Gavrilenko, P. Mead, V. I. Gavrilenko, and M. A. Noginov. Engineering of low-loss metal for nanoplasmonic and metamaterials applications. *Applied Physics Letters*, 95(15):151102, 10 2009.
- [83] M G Blaber, M D Arnold, and M J Ford. Designing materials for plasmonic systems: the alkali–noble intermetallics. *Journal of Physics: Condensed Matter*, 22(9):095501, feb 2010.
- [84] C. Metaxa, S. Kassavetis, J.F. Pierson, D. Gall, and P. Patsalas. Infrared plasmonics with conductive ternary nitrides. *ACS Applied Materials & Interfaces*, 9(12):10825–10834, 2017. PMID: 28266835.
- [85] Eric Herrmann, Hua Gao, Zhixiang Huang, Sai Rahul Sitaram, Ke Ma, and Xi Wang. Modulators for mid-infrared and terahertz light. *Journal of Applied Physics*, 128(14):140903, 10 2020.

- [86] Andreas Otto. Excitation of nonradiative surface plasma waves in silver by the method of frustrated total reflection. *Zeitschrift für Physik A Hadrons and nuclei*, 216(4):398–410, Aug 1968.
- [87] E. K. Akowuah, T. Gorman, and S. Haxha. Design and optimization of a novel surface plasmon resonance biosensor based on otto configuration. *Opt. Express*, 17(26):23511–23521, Dec 2009.
- [88] E. Kretschmann and H. Raether. Notizen: Radiative decay of non radiative surface plasmons excited by light. *Zeitschrift für Naturforschung A*, 23(12):2135–2136, 1968.
- [89] A. P. Vinogradov, A. V. Dorofeenko, A. A. Pukhov, and A. A. Lisiansky. Exciting surface plasmon polaritons in the kretschmann configuration by a light beam. *Phys. Rev. B*, 97:235407, Jun 2018.
- [90] A. Bouhelier and G. P. Wiederrecht. Excitation of broadband surface plasmon polaritons: Plasmonic continuum spectroscopy. *Phys. Rev. B*, 71:195406, May 2005.
- [91] B. Hecht, H. Bielefeldt, L. Novotny, Y. Inouye, and D. W. Pohl. Local excitation, scattering, and interference of surface plasmons. *Phys. Rev. Lett.*, 77:1889–1892, Aug 1996.
- [92] Eloise Devaux, Thomas W. Ebbesen, Jean-Claude Weeber, and Alain Dereux. Launching and decoupling surface plasmons via micro-gratings. *Applied Physics Letters*, 83(24):4936–4938, 12 2003.
- [93] Vincenzo Giannini, Antonio I. Fernández-Domínguez, Susannah C. Heck, and Stefan A. Maier. Plasmonic nanoantennas: Fundamentals and their use in controlling the radiative properties of nanoemitters. *Chemical Reviews*, 111(6):3888–3912, 2011. PMID: 21434605.
- [94] Frank Neubrech, Christian Huck, Ksenia Weber, Annemarie Pucci, and Harald Giessen. Surface-enhanced infrared spectroscopy using resonant nanoantennas. *Chemical Reviews*, 117(7):5110–5145, 2017. PMID: 28358482.
- [95] Colleen L. Nehl, Hongwei Liao, and Jason H. Hafner. Optical properties of star-shaped gold nanoparticles. *Nano Letters*, 6(4):683–688, 2006. PMID: 16608264.
- [96] Heykel Aouani, Hana Šípová, Mohsen Rahmani, Miguel Navarro-Cia, Kateřina Hegerová, Jiří Homola, Minghui Hong, and Stefan A. Maier. Ultrasensitive broadband probing of molecular vibrational modes with multifrequency optical antennas. *ACS Nano*, 7(1):669–675, 2013. PMID: 23199257.
- [97] Lorenzo Rosa, Kai Sun, and Saulius Juodkazis. Sierpinski fractal plasmonic nanoantennas. *Rapid Research Letters*, 5(5-6):175–177, 2011.

- [98] Lorenzo Rosa, Kai Sun, and Saulius Juodkazis. Sierpinski fractal plasmonic nanoantennas. *physica status solidi (RRL) – Rapid Research Letters*, 5(5-6):175–177, 2011.
- [99] Liangliang Dong, Xiao Yang, Chao Zhang, Benjamin Cerjan, Linan Zhou, Ming Lun Tseng, Yu Zhang, Alessandro Alabastri, Peter Nordlander, and Naomi J. Halas. Nanogapped au antennas for ultrasensitive surface-enhanced infrared absorption spectroscopy. *Nano Letters*, 17(9):5768–5774, 2017. PMID: 28787169.
- [100] Kai Chen, Ronen Adato, and Hatice Altug. Dual-band perfect absorber for multi-spectral plasmon-enhanced infrared spectroscopy. *ACS Nano*, 6(9):7998–8006, 2012. PMID: 22920565.
- [101] Yilei Li, Hugen Yan, Damon B. Farmer, Xiang Meng, Wenjuan Zhu, Richard M. Osgood, Tony F. Heinz, and Phaedon Avouris. Graphene plasmon enhanced vibrational sensing of surface-adsorbed layers. *Nano Letters*, 14(3):1573–1577, 2014. PMID: 24528250.
- [102] Jiri Homola, Ivo Koudela, and Sinclair S. Yee. Surface plasmon resonance sensors based on diffraction gratings and prism couplers: sensitivity comparison. *Sensors and Actuators B: Chemical*, 54(1):16–24, 1999.
- [103] E. Hutter and J. H. Fendler. Exploitation of localized surface plasmon resonance. *Advanced Materials*, 16(19):1685–1706, 2004.
- [104] Miguel Navarro-Cia and Stefan A. Maier. Broad-band near-infrared plasmonic nanoantennas for higher harmonic generation. *ACS Nano*, 6(4):3537–3544, 2012. PMID: 22429069.
- [105] W. A. Murray and W. L. Barnes. Plasmonic materials. *Advanced Materials*, 19(22):3771–3782, 2007.
- [106] Huigao Duan, Antonio I. Fernández-Domínguez, Michel Bosman, Stefan A. Maier, and Joel K. W. Yang. Nanoplasmonics: Classical down to the nanometer scale. *Nano Letters*, 12(3):1683–1689, 2012. PMID: 22313285.
- [107] Lisa V. Brown, Xiao Yang, Ke Zhao, Bob Y. Zheng, Peter Nordlander, and Naomi J. Halas. Fan-shaped gold nanoantennas above reflective substrates for surface-enhanced infrared absorption (seira). *Nano Letters*, 15(2):1272–1280, 2015. PMID: 25565006.
- [108] Michel Dalibart. Spectroscopie dans l’infrarouge. 33(1990):1–2, 2008.
- [109] Michael B. Pushkarsky, Michael E. Webber, Tyson Macdonald, and C. Kumar N. Patel. High-sensitivity, high-selectivity detection of chemical warfare agents. *Applied Physics Letters*, 88(4):044103, 01 2006.

- [110] Steven W. Sharpe, Timothy J. Johnson, Pamela M. Chu, James Kleimeyer, and Brad Rowland. Quantitative infrared spectra of vapor phase chemical agents. In Patrick J. Gardner, editor, *Chemical and Biological Sensing IV*, volume 5085, pages 19 – 27. International Society for Optics and Photonics, SPIE, 2003.
- [111] Xiao Shan, Jack C. Vincent, Sue Kirkpatrick, Maurice D. Walker, Mark R. Sambrook, and David C. Clary. A combined theoretical and experimental study of sarin (gb) decomposition at high temperatures. *The Journal of Physical Chemistry A*, 121(33):6200–6210, 2017. PMID: 28704051.
- [112] M. Fleischmann, P.J. Hendra, and A.J. McQuillan. Raman spectra of pyridine adsorbed at a silver electrode. *Chemical Physics Letters*, 26(2):163–166, 1974.
- [113] A. Hartstein, J. R. Kirtley, and J. C. Tsang. Enhancement of the infrared absorption from molecular monolayers with thin metal overlayers. *Phys. Rev. Lett.*, 45:201–204, Jul 1980.
- [114] Ricardo Aroca and S. Rodriguez-Llorente. Surface-enhanced vibrational spectroscopy. *Journal of Molecular Structure*, 408-409:17–22, 1997. *Molecular Spectroscopy and Molecular Structure 1996*.
- [115] C. F. Eagen. Nature of the enhanced optical absorption of dye-coated ag island films. *Appl. Opt.*, 20(17):3035–3042, Sep 1981.
- [116] Masatoshi Osawa. Dynamic processes in electrochemical reactions studied by surface-enhanced infrared absorption spectroscopy (seiras). *Bulletin of the Chemical Society of Japan*, 70(12):2861–2880, 1997.
- [117] Masatoshi Osawa. *Surface-Enhanced Infrared Absorption*, pages 163–187. Springer Berlin Heidelberg, Berlin, Heidelberg, 2001.
- [118] T. Wadayama, T. Sakurai, S. Ichikawa, and W. Suëtaka. Charge-transfer enhancement in infrared absorption of thiocyanate ions adsorbed on a gold electrode in the kretschmann atr configuration. *Surface Science*, 198(3):L359–L364, 1988.
- [119] Andrey E. Miroshnichenko, Sergej Flach, and Yuri S. Kivshar. Fano resonances in nanoscale structures. *Rev. Mod. Phys.*, 82:2257–2298, Aug 2010.
- [120] Anika Kinkhabwala, Zongfu Yu, Shanhui Fan, Yuri Avlasevich, Klaus Müllen, and W. E. Moerner. Large single-molecule fluorescence enhancements produced by a bowtie nanoantenna. *Nature Photonics*, 3(11):654–657, Nov 2009.
- [121] Kosei Ueno, Saulius Juodkazis, Toshiyuki Shibuya, Yukie Yokota, Vygantas Mizeikis, Keiji Sasaki, and Hiroaki Misawa. Nanoparticle plasmon-assisted two-photon polymerization induced by incoherent excitation source. *Journal of the American Chemical Society*, 130(22):6928–6929, 2008. PMID: 18461929.

- [122] S. Pillai, K. R. Catchpole, T. Trupke, and M. A. Green. Surface plasmon enhanced silicon solar cells. *Journal of Applied Physics*, 101(9):093105, 05 2007.
- [123] Xuming Zhang, Yu Lim Chen, Ru-Shi Liu, and Din Ping Tsai. Plasmonic photocatalysis. *Reports on Progress in Physics*, 76(4):046401, mar 2013.
- [124] Huanjun Chen, Tian Ming, Lei Zhao, Feng Wang, Ling-Dong Sun, Jianfang Wang, and Chun-Hua Yan. Plasmon–molecule interactions. *Nano Today*, 5(5):494–505, 2010.
- [125] Avraham Rasooly, Keith E Herold, and Keith E Herold. *Biosensors and biodetection*. Springer, 2009.
- [126] J. Seidel, S. Grafström, and L. Eng. Stimulated emission of surface plasmons at the interface between a silver film and an optically pumped dye solution. *Phys. Rev. Lett.*, 94:177401, May 2005.
- [127] M. A. Noginov, G. Zhu, M. Mayy, B. A. Ritzo, N. Noginova, and V. A. Podolskiy. Stimulated emission of surface plasmon polaritons. *Phys. Rev. Lett.*, 101:226806, Nov 2008.
- [128] P. Andrew and W. L. Barnes. Energy transfer across a metal film mediated by surface plasmon polaritons. *Science*, 306(5698):1002–1005, 2004.
- [129] Amanda J. Haes, Shengli Zou, Jing Zhao, George C. Schatz, and Richard P. Van Duyne. Localized surface plasmon resonance spectroscopy near molecular resonances. *Journal of the American Chemical Society*, 128(33):10905–10914, 2006. PMID: 16910686.
- [130] Nidhi Nath and Ashutosh Chilkoti. A colorimetric gold nanoparticle sensor to interrogate biomolecular interactions in real time on a surface. *Analytical Chemistry*, 74(3):504–509, 2002. PMID: 11838667.
- [131] Frank Neubrech, Annemarie Pucci, Thomas Walter Cornelius, Shafqat Karim, Aitzol Garcia-Etxarri, and Javier Aizpurua. Resonant plasmonic and vibrational coupling in a tailored nanoantenna for infrared detection. *Phys. Rev. Lett.*, 101:157403, Oct 2008.
- [132] Na Liu, Ming L. Tang, Mario Hentschel, Harald Giessen, and A. Paul Alivisatos. Nanoantenna-enhanced gas sensing in a single tailored nanofocus. *Nature Materials*, 10(8):631–636, Aug 2011.
- [133] Hong Zhou, Dongxiao Li, Xindan Hui, and Xiaojing Mu. Infrared metamaterial for surface-enhanced infrared absorption spectroscopy: pushing the frontier of ultra-sensitive on-chip sensing. *International Journal of Optomechatronics*, 15(1):97–119, 2021.

- [134] Gregory Q. Wallace and François Lagugné-Labarthe. Advancements in fractal plasmonics: structures, optical properties, and applications. *Analyst*, 144:13–30, 2019.
- [135] F. Peragut, L. Cerutti, A. Baranov, J. P. Hugonin, T. Taliercio, Y. De Wilde, and J. J. Greffet. Hyperbolic metamaterials and surface plasmon polaritons. *Optica*, 4(11):1409–1415, Nov 2017.
- [136] Na Liu, Martin Mesch, Thomas Weiss, Mario Hentschel, and Harald Giessen. Infrared perfect absorber and its application as plasmonic sensor. *Nano Letters*, 10(7):2342–2348, 2010. PMID: 20560590.
- [137] Marion Baillieul, Emmanuel Rinnert, Jonathan Lemaitre, Karine Michel, Florent Colas, Loïc Bodiou, Guillaume Demésy, Seyriu Kakuta, Anna Rumyantseva, Gilles Lerondel, Kada Boukerma, Gilles Renversez, Timothée Toury, Joël Charrier, and Virginie Nazabal. Surface functionalization with polymer membrane or seira interface to improve the sensitivity of chalcogenide-based infrared sensors dedicated to the detection of organic molecules. *ACS Omega*, 7(51):47840–47850, 2022.
- [138] Yuhua Chang, Dihan Hasan, Bowei Dong, Jingxuan Wei, Yiming Ma, Guangya Zhou, Kah Wee Ang, and Chengkuo Lee. All-dielectric surface-enhanced infrared absorption-based gas sensor using guided resonance. *ACS Applied Materials & Interfaces*, 10(44):38272–38279, 2018. PMID: 30360088.
- [139] Xinyuan Chong, Yujing Zhang, Erwen Li, Ki-Joong Kim, Paul R. Ohodnicki, Chih-hung Chang, and Alan X. Wang. Surface-enhanced infrared absorption: Pushing the frontier for on-chip gas sensing. *ACS Sensors*, 3(1):230–238, 2018. PMID: 29262684.
- [140] Nestor Jr. Bareza, Bruno Paulillo, Tetiana M. Slipchenko, Marta Autore, Irene Dolado, Song Liu, James H. Edgar, Saül Vélez, Luis Martín-Moreno, Rainer Hillenbrand, and Valerio Pruneri. Phonon-enhanced mid-infrared CO₂ gas sensing using boron nitride nanoresonators. *ACS Photonics*, 9(1):34–42, 2022.
- [141] Nestor Jr. Bareza, Kavitha K. Gopalan, Rose Alani, Bruno Paulillo, and Valerio Pruneri. Mid-infrared gas sensing using graphene plasmons tuned by reversible chemical doping. *ACS Photonics*, 7(4):879–884, 2020.
- [142] Yoshiaki Nishijima, Yuta Adachi, Lorenzo Rosa, and Saulius Juodkazis. Augmented sensitivity of an IR-absorption gas sensor employing a metal hole array. *Opt. Mater. Express*, 3(7):968–976, Jul 2013.
- [143] Hai Hu, Xiaoxia Yang, Xiangdong Guo, Kaveh Khaliji, Sudipta Romen Biswas, F. Javier García de Abajo, Tony Low, Zhipei Sun, and Qing Dai. Gas identification with graphene plasmons. *Nature Communications*, 10(1):1131, Mar 2019.

- [144] Huakang Yu, Yusi Peng, Yong Yang, and Zhi-Yuan Li. Plasmon-enhanced light–matter interactions and applications. *npj Computational Materials*, 5(1):45, Apr 2019.
- [145] Li Tao, Zefeng Chen, Zhiyong Li, Jiaqi Wang, Xin Xu, and Jian-Bin Xu. Enhancing light-matter interaction in 2d materials by optical micro/nano architectures for high-performance optoelectronic devices. *InfoMat*, 3(1):36–60, 2021.
- [146] Kuidong Wang, Ai-Yin Liu, Hui-Hsin Hsiao, Cyriaque Genet, and Thomas Ebbesen. Large optical nonlinearity of dielectric nanocavity-assisted mie resonances strongly coupled to an epsilon-near-zero mode. *Nano Letters*, 22(2):702–709, 2022. PMID: 34994573.
- [147] Alexander Benz, Salvatore Campione, John F. Klem, Michael B. Sinclair, and Igal Brener. Control of strong light–matter coupling using the capacitance of metamaterial nanocavities. *Nano Letters*, 15(3):1959–1966, 2015. PMID: 25625404.
- [148] Young Chul Jun, John Reno, Troy Ribaud, Eric Shaner, Jean-Jacques Greffet, Simon Vassant, Francois Marquier, Mike Sinclair, and Igal Brener. Epsilon-near-zero strong coupling in metamaterial-semiconductor hybrid structures. *Nano Letters*, 13(11):5391–5396, 2013. PMID: 24124754.
- [149] Jun Guan, Jeong-Eun Park, Shikai Deng, Max J. H. Tan, Jingtian Hu, and Teri W. Odom. Light–matter interactions in hybrid material metasurfaces. *Chemical Reviews*, 122(19):15177–15203, 2022. PMID: 35762982.
- [150] Lifeng Li. Improved method for computing of light-matter interaction in multilayer corrugated structures: comment. *J. Opt. Soc. Am. A*, 25(11):2803–2804, Nov 2008.
- [151] Sarawuth Chaimool, Chawalit Rakluea, and Prayoot Akkaraekthalin. Mu-near-zero metasurface for microstrip-fed slot antennas. *Applied Physics A*, 112(3):669–675, Sep 2013.
- [152] Ahmed M. Mahmoud and Nader Engheta. Wave–matter interactions in epsilon-and-mu-near-zero structures. *Nature Communications*, 5(1):5638, Dec 2014.
- [153] Lin Zhao and Hui Xie. A novel optical ϵ -near-zero material realized by multi-layered ag/sic film structures. *Optik*, 183:513–522, 2019.
- [154] Ruben Maas, James Parsons, Nader Engheta, and Albert Polman. Experimental realization of an epsilon-near-zero metamaterial at visible wavelengths. *Nature Photonics*, 7(11):907–912, Nov 2013.
- [155] Xueqin Huang, Yun Lai, Zhi Hong Hang, Huihuo Zheng, and C. T. Chan. Dirac cones induced by accidental degeneracy in photonic crystals and zero-refractive-index materials. *Nature Materials*, 10(8):582–586, Aug 2011.

- [156] Cristian Della Giovampaola and Nader Engheta. Plasmonics without negative dielectrics. *Phys. Rev. B*, 93:195152, May 2016.
- [157] L. Nordin, O. Dominguez, C. M. Roberts, W. Streyer, K. Feng, Z. Fang, V. A. Podolskiy, A. J. Hoffman, and D. Wasserman. Mid-infrared epsilon-near-zero modes in ultra-thin phononic films. *Applied Physics Letters*, 111(9):091105, 08 2017.
- [158] Aleksei Anopchenko, Sudip Gurung, Long Tao, Catherine Arndt, and Ho Wai Howard Lee. Atomic layer deposition of ultra-thin and smooth al-doped zno for zero-index photonics. *Materials Research Express*, 5(1):014012, jan 2018.
- [159] M. Zahirul Alam, Israel De Leon, and Robert W. Boyd. Large optical nonlinearity of indium tin oxide in its epsilon-near-zero region. *Science*, 352(6287):795–797, 2016.
- [160] Kuan-An Chen, Sen Liang, Jun Zheng, Chengcan Han, Yueguang Zhang, Lei Lin, and Hui Ye. Berreman type perfect absorber based on epsilon near zero material gallium doped zinc oxide. *Opt. Mater. Express*, 13(7):1859–1869, Jul 2023.
- [161] Angela Cleri, John Tomko, Kathleen Quiambao-Tomko, Mario V. Imperatore, Yanglin Zhu, J. Ryan Nolen, Joshua Nordlander, Joshua D. Caldwell, Zhiqiang Mao, Noel C. Giebink, Kyle P. Kelley, Evan L. Runnerstrom, Patrick E. Hopkins, and Jon-Paul Maria. Mid-wave to near-ir optoelectronic properties and epsilon-near-zero behavior in indium-doped cadmium oxide. *Phys. Rev. Mater.*, 5:035202, Mar 2021.
- [162] Evan L. Runnerstrom, Kyle P. Kelley, Edward Sachet, Christopher T. Shelton, and Jon-Paul Maria. Epsilon-near-zero modes and surface plasmon resonance in fluorine-doped cadmium oxide thin films. *ACS Photonics*, 4(8):1885–1892, 2017.
- [163] Prasad P. Iyer, Mihir Pendharkar, Chris J. Palmstrøm, and Jon A. Schuller. Ultra-wide thermal free-carrier tuning of dielectric antennas coupled to epsilon-near-zero substrates. *Nature Communications*, 8(1):472, Sep 2017.
- [164] Jae Seung Hwang, Jin Xu, and Aaswath P. Raman. Simultaneous control of spectral and directional emissivity with gradient epsilon-near-zero inas photonic structures, 2022.
- [165] Nathaniel Kinsey, Clayton DeVault, Alexandra Boltasseva, and Vladimir M. Shalaev. Near-zero-index materials for photonics. *Nature Reviews Materials*, 4(12):742–760, Dec 2019.
- [166] Mário Silveirinha and Nader Engheta. Tunneling of electromagnetic energy through subwavelength channels and bends using ϵ -near-zero materials. *Phys. Rev. Lett.*, 97:157403, Oct 2006.
- [167] I. Liberal, A. M. Mahmoud, and N. Engheta. Geometry-invariant resonant cavities. *Nature Communications*, 7(1):10989, Mar 2016.

- [168] Brian Edwards, Andrea Alu, Michael E. Young, Mario Silveirinha, and Nader Engheta. Experimental verification of epsilon-near-zero metamaterial coupling and energy squeezing using a microwave waveguide. *Phys. Rev. Lett.*, 100:033903, Jan 2008.
- [169] Ruopeng Liu, Qiang Cheng, Thomas Hand, Jack J. Mock, Tie Jun Cui, Steven A. Cummer, and David R. Smith. Experimental demonstration of electromagnetic tunneling through an epsilon-near-zero metamaterial at microwave frequencies. *Phys. Rev. Lett.*, 100:023903, Jan 2008.
- [170] Stefan Enoch, Gérard Tayeb, Pierre Sabouroux, Nicolas Guérin, and Patrick Vincent. A metamaterial for directive emission. *Phys. Rev. Lett.*, 89:213902, Nov 2002.
- [171] Andrea Alu, Mario G. Silveirinha, Alessandro Salandrino, and Nader Engheta. Epsilon-near-zero metamaterials and electromagnetic sources: Tailoring the radiation phase pattern. *Phys. Rev. B*, 75:155410, Apr 2007.
- [172] Salvatore Campione, Domenico de Ceglia, Maria Antonietta Vincenti, Michael Scalora, and Filippo Capolino. Electric field enhancement in epsilon-near-zero slabs under tm-polarized oblique incidence. *Phys. Rev. B*, 87:035120, Jan 2013.
- [173] Simon Vassant, Jean-Paul Hugonin, Francois Marquier, and Jean-Jacques Greffet. Berreman mode and epsilon near zero mode. *Opt. Express*, 20(21):23971–23977, Oct 2012.
- [174] Romain Fleury and Andrea Alu. Enhanced superradiance in epsilon-near-zero plasmonic channels. *Phys. Rev. B*, 87:201101, May 2013.
- [175] Orad Reshef, Israel De Leon, M. Zahirul Alam, and Robert W. Boyd. Nonlinear optical effects in epsilon-near-zero media. *Nature Reviews Materials*, 4(8):535–551, Aug 2019.
- [176] A. Ciattoni, C. Rizza, and E. Palange. Extreme nonlinear electrodynamics in metamaterials with very small linear dielectric permittivity. *Phys. Rev. A*, 81:043839, Apr 2010.
- [177] Hao Li, Ziheng Zhou, Yijing He, Wangyu Sun, Yue Li, Inigo Liberal, and Nader Engheta. Geometry-independent antenna based on epsilon-near-zero medium. *Nature Communications*, 13(1):3568, Jun 2022.
- [178] Clayton T. DeVault, Vladimir A. Zenin, Anders Pors, Krishnakali Chaudhuri, Jongbum Kim, Alexandra Boltasseva, Vladimir M. Shalaev, and Sergey I. Bozhevolnyi. Suppression of near-field coupling in plasmonic antennas on epsilon-near-zero substrates. *Optica*, 5(12):1557–1563, Dec 2018.

- [179] Jongbum Kim, Aveek Dutta, Gururaj V. Naik, Alexander J. Giles, Francisco J. Bezares, Chase T. Ellis, Joseph G. Tischler, Ahmed M. Mahmoud, Humeysra Caglayan, Orest J. Glembocki, Alexander V. Kildishev, Joshua D. Caldwell, Alexandra Boltasseva, and Nader Engheta. Role of epsilon-near-zero substrates in the optical response of plasmonic antennas. *Optica*, 3(3):339–346, Mar 2016.
- [180] Mohsin Habib, Daria Briukhanova, Nekhel Das, Bilge Can Yildiz, and Humeysra Caglayan. Controlling the plasmon resonance via epsilon-near-zero multilayer metamaterials. *Nanophotonics*, 9(11):3637–3644, 2020.
- [181] Arthur R. Davoyan, Ahmed M. Mahmoud, and Nader Engheta. Optical isolation with epsilon-near-zero metamaterials. *Opt. Express*, 21(3):3279–3286, Feb 2013.
- [182] Andres D. Neira, Gregory A. Wurtz, and Anatoly V. Zayats. All-optical switching in silicon photonic waveguides with an epsilon-near-zero resonant cavity [invited]. *Photon. Res.*, 6(5):B1–B5, May 2018.
- [183] Ze Tao Xie, Jiaye Wu, H. Y. Fu, and Qian Li. Tunable electro- and all-optical switch based on epsilon-near-zero metasurface. *IEEE Photonics Journal*, 12(4):1–10, 2020.
- [184] Yanhua Sha, Jiaye Wu, Ze Tao Xie, H. Y. Fu, and Qian Li. Comparison study of multi-slot designs in epsilon-near-zero waveguide-based electro-optical modulators. *IEEE Photonics Journal*, 13(3):1–12, 2021.
- [185] Qian Gao, Erwen Li, and Alan X. Wang. Comparative analysis of transparent conductive oxide electro-absorption modulators [invited]. *Opt. Mater. Express*, 8(9):2850–2862, Sep 2018.
- [186] Tae Young Kim, Md. Alamgir Badsha, Junho Yoon, Seon Young Lee, Young Chul Jun, and Chang Kwon Hwangbo. General strategy for broadband coherent perfect absorption and multi-wavelength all-optical switching based on epsilon-near-zero multilayer films. *Scientific Reports*, 6(1):22941, Mar 2016.
- [187] Cheng Zhang, Yuqian Zu, Wen Yang, Shouzhen Jiang, and Jie Liu. Epsilon-near-zero medium for optical switches in ho solid-state laser at 2.06 μm . *Optics & Laser Technology*, 129:106271, 2020.
- [188] Jiaye Wu, Ze Tao Xie, Yanhua Sha, H. Y. Fu, and Qian Li. Epsilon-near-zero photonics: infinite potentials. *Photon. Res.*, 9(8):1616–1644, Aug 2021.
- [189] Xinxiang Niu, Xiaoyong Hu, Saisai Chu, and Qihuang Gong. Epsilon-near-zero photonics: A new platform for integrated devices. *Advanced Optical Materials*, 6(10):1701292, 2018.
- [190] Andrea Alu and Nader Engheta. Dielectric sensing in ϵ -near-zero narrow waveguide channels. *Phys. Rev. B*, 78:045102, Jul 2008.

- [191] Zhenya Meng, Hailin Cao, Run Liu, and Xiaodong Wu. An electrically tunable dual-wavelength refractive index sensor based on a metagrating structure integrating epsilon-near-zero materials. *Sensors*, 20(8), 2020.
- [192] Mina Vafaei, Mahmood Moradi, and Gholam Hossein Bordbar. Highly sensitive refractive index sensing by epsilon near zero metamaterials. *Optik*, 244:167617, 2021.
- [193] Behnoush Ghafari, Mohammad Danaie, and Majid Afsahi. Perfect absorber based on epsilon-near-zero metamaterial as a refractive index sensor. *Sensing and Imaging*, 24(1):15, May 2023.
- [194] Miguel Beruete, Nader Engheta, and Victor Pacheco-Peña. Experimental demonstration of deeply subwavelength dielectric sensing with epsilon-near-zero (ENZ) waveguides. *Applied Physics Letters*, 120(8):081106, 02 2022.
- [195] Abhishek Kumar Jha and M. Jaleel Akhtar. Design of multilayered epsilon-near-zero microwave planar sensor for testing of dispersive materials. *IEEE Transactions on Microwave Theory and Techniques*, 63(8):2418–2426, 2015.
- [196] Zelio Fusco, Mahdiar Taheri, Renheng Bo, Thanh Tran-Phu, Hongjun Chen, Xuyun Guo, Ye Zhu, Takuya Tsuzuki, Thomas P. White, and Antonio Tricoli. Non-periodic epsilon-near-zero metamaterials at visible wavelengths for efficient non-resonant optical sensing. *Nano Letters*, 20(5):3970–3977, 2020. PMID: 32343590.
- [197] V Pacheco-Pena, M Beruete, P Rodríguez-Ulibarri, and N Engheta. On the performance of an enz-based sensor using transmission line theory and effective medium approach. *New Journal of Physics*, 21(4):043056, apr 2019.
- [198] Tianyu Yang, Can Ding, Richard W. Ziolkowski, and Y. Jay Guo. A controllable plasmonic resonance in a sic-loaded single-polarization single-mode photonic crystal fiber enables its application as a compact lwir environmental sensor. *Materials*, 13(18), 2020.
- [199] Rafik Smaali, Antoine Moreau, and Emmanuel Centeno. Epsilon-near-zero surface waves enhance infrared vibrational spectroscopy. *Applied Physics Letters*, 122(26):261701, 06 2023.
- [200] Rafik Smaali, Thierry Taliercio, Antoine Moreau, and Emmanuel Centeno. Reshaping plasmonic resonances using epsilon-near-zero materials for enhanced infrared vibrational spectroscopy. *Applied Physics Letters*, 119(18):183701, 11 2021.
- [201] Penghua Ma, Kaizhen Liu, Guangyan Huang, Youyi Ding, Wei Du, and Tao Wang. Epsilon-near-zero substrate-enabled strong coupling between molecular vibrations and mid-infrared plasmons. *Opt. Lett.*, 47(17):4524–4527, Sep 2022.

- [202] Thomas G. Folland, Guanyu Lu, Autumn Bruncz, J. Ryan Nolen, Marko Tadjer, and Joshua D. Caldwell. Vibrational coupling to epsilon-near-zero waveguide modes. *ACS Photonics*, 7(3):614–621, 2020.
- [203] J. Yang, C. Sauvan, A. Jouanin, S. Collin, J.-L. Pelouard, and P. Lalanne. Ultrasmall metal-insulator-metal nanoresonators: impact of slow-wave effects on the quality factor. *Opt. Express*, 20(15):16880–16891, Jul 2012.
- [204] Sergey I. Bozhevolnyi and Thomas Søndergaard. General properties of slow-plasmon resonant nanostructures: nano-antennas and resonators. *Opt. Express*, 15(17):10869–10877, Aug 2007.
- [205] Amirmostafa Amirjani and S. K. Sadrnezhad. Computational electromagnetics in plasmonic nanostructures. *J. Mater. Chem. C*, 9:9791–9819, 2021.
- [206] Kim Huat Lee, Iftikhar Ahmed, R. Goh, Eng Huat Khoo, Er-Ping Li, and Terence Gih Guang Hung. Implementation of the fdtd method based on lorentz-drude dispersive model on gpu for plasmonics applications. *Progress in Electromagnetics Research-pier*, 116:441–456, 2011.
- [207] Shiquan He, Wei E. I. Sha, Lijun Jiang, Wallace C. H. Choy, Weng Cho Chew, and Zaiping Nie. Finite-element-based generalized impedance boundary condition for modeling plasmonic nanostructures. *IEEE Transactions on Nanotechnology*, 11(2):336–345, 2012.
- [208] Yu Ying, Jiakai Wang, Nan Hu, Ke Xu, Liangliang Sun, and Guangyuan Si. Determination of refractive index using surface plasmon resonance (spr) and rigorous coupled wave analysis (rcwa) with a d-shaped optical fiber and a nano-gold grating. *Instrumentation Science & Technology*, 48(4):376–385, 2020.
- [209] Jean-Paul Hugonin and Philippe Lalanne. Light-in-complex-nanostructures/reticolo: V9, 2021.
- [210] Marian A Herman and Helmut Sitter. *Molecular beam epitaxy: fundamentals and current status*, volume 7. Springer Science & Business Media, 2012.
- [211] Chin-An Chang, C. M. Serrano, L. L. Chang, and L. Esaki. Effect of lattice mismatch on the electron mobilities of InAs grown on GaAs by MBE. *Journal of Vacuum Science and Technology*, 17(2):603–605, 03 1980.
- [212] J. G. Belk, D. W. Pashley, B. A. Joyce, and T. S. Jones. Dislocation displacement field at the surface of inas thin films grown on gaas(110). *Phys. Rev. B*, 58:16194–16201, Dec 1998.

- [213] Ch. Blömers, T. Grap, M. I. Lepsa, J. Moers, St. Trellenkamp, D. Grützmacher, H. Lüth, and Th. Schäpers. Hall effect measurements on InAs nanowires. *Applied Physics Letters*, 101(15):152106, 10 2012.
- [214] L. Ö. Olsson, C. B. M. Andersson, M. C. Håkansson, J. Kanski, L. Ilver, and U. O. Karlsson. Charge accumulation at InAs surfaces. *Phys. Rev. Lett.*, 76:3626–3629, May 1996.
- [215] G. R. Bell, T. S. Jones, and C. F. McConville. Accumulation layer profiles at InAs polar surfaces. *Applied Physics Letters*, 71(25):3688–3690, 12 1997.
- [216] J. R. Weber, A. Janotti, and C. G. Van de Walle. Intrinsic and extrinsic causes of electron accumulation layers on InAs surfaces. *Applied Physics Letters*, 97(19):192106, 11 2010.
- [217] Thierry Taliercio, Vilianne Ntsame Guilengui, Laurent Cerutti, Eric Tournié, and Jean-Jacques Greffet. Brewster “mode” in highly doped semiconductor layers: an all-optical technique to monitor doping concentration. *Opt. Express*, 22(20):24294–24303, Oct 2014.
- [218] G. Barbillon, J.-L. Bijeon, J. Plain, M. Lamy de la Chapelle, P.-M. Adam, and P. Royer. Electron beam lithography designed chemical nanosensors based on localized surface plasmon resonance. *Surface Science*, 601(21):5057–5061, 2007.
- [219] Etienne Herth, Pascal Tilmant, Marc Faucher, Marc François, Christophe Boyaval, Francois Vaurette, Yves Deblacq, Bernard Legrand, and Lionel Buchaillot. Electron beam nanolithography in aznlof 2020. *Microelectronic Engineering*, 87(11):2057–2060, 2010.
- [220] Lukas Novotny. Effective wavelength scaling for optical antennas. *Phys. Rev. Lett.*, 98:266802, Jun 2007.
- [221] F. Neubrech, T. Kolb, R. Lovrincic, G. Fahsold, A. Pucci, J. Aizpurua, T. W. Cornelius, M. E. Toimil-Molares, R. Neumann, and S. Karim. Resonances of individual metal nanowires in the infrared. *Applied Physics Letters*, 89(25), 12 2006. 253104.
- [222] Franziska B. Barho, Fernando Gonzalez-Posada, Laurent Cerutti, and Thierry Taliercio. Heavily doped semiconductor metamaterials for mid-infrared multispectral perfect absorption and thermal emission. *Advanced Optical Materials*, 8(6):1901502, 2020.
- [223] J. A. Dionne, L. A. Sweatlock, H. A. Atwater, and A. Polman. Plasmon slot waveguides: Towards chip-scale propagation with subwavelength-scale localization. *Phys. Rev. B*, 73:035407, Jan 2006.

- [224] Dang Yuan Lei, Alexandre Aubry, Yu Luo, Stefan A. Maier, and John B. Pendry. Plasmonic interaction between overlapping nanowires. *ACS Nano*, 5(1):597–607, 2011. PMID: 21190374.
- [225] Stéphane Collin, Fabrice Pardo, and Jean-Luc Pelouard. Waveguiding in nanoscale metallic apertures. *Opt. Express*, 15(7):4310–4320, Apr 2007.
- [226] George Wm. Thomson. The antoine equation for vapor-pressure data. *Chemical Reviews*, 38(1):1–39, 1946. PMID: 21016992.
- [227] Ann B. Butrow, James H. Buchanan, and David E. Tevault. Vapor pressure of organophosphorus nerve agent simulant compounds. *Journal of Chemical & Engineering Data*, 54(6):1876–1883, 2009.
- [228] Sneha Neupane, Robert Peale, and Subith Vasu. Infrared absorption cross sections of several organo-phosphorous chemical-weapon simulants. *Journal of Molecular Spectroscopy*, 355:59–65, 2019.
- [229] Seokmin Jeon, Igor V. Schweigert, Pehr E. Pehrsson, and Robert B. Balow. Kinetics of dimethyl methylphosphonate adsorption and decomposition on zirconium hydroxide using variable temperature in situ attenuated total reflection infrared spectroscopy. *ACS Applied Materials & Interfaces*, 12(13):14662–14671, 2020. PMID: 32105054.
- [230] Md. Faiyaz Bin Hassan, Sanjida Sultana, M. Ifaz Ahmad Isti, Samiha Nuzhat, Shovasis Kumar Biswas, and Hriteshwar Talukder. Liquid benzene analyte based dual core surface plasmon resonance sensor for chemical sensing. In *2020 11th International Conference on Computing, Communication and Networking Technologies (ICCCNT)*, pages 1–6, 2020.
- [231] Babak Moeinmaleki, Hassan Kaatuzian, and Abdolber Mallah Livani. Design and simulation of a resonance-based plasmonic sensor for mass density sensing of methane and carbon dioxide gases. *Plasmonics*, 18(1):225–240, Feb 2023.
- [232] Satyendra K. Mishra, Sandeep N. Tripathi, Veena Choudhary, and Banshi D. Gupta. Surface plasmon resonance-based fiber optic methane gas sensor utilizing graphene-carbon nanotubes-poly(methyl methacrylate) hybrid nanocomposite. *Plasmonics*, 10(5):1147–1157, Oct 2015.
- [233] V. M. Bermudez. Effect of humidity on the interaction of dimethyl methylphosphonate (dmmp) vapor with sio₂ and al₂o₃ surfaces, studied using infrared attenuated total reflection spectroscopy. *Langmuir*, 26(23):18144–18154, 2010. PMID: 21069963.

- [234] Doron Kaplan, Ido Nir, and Liora Shmueli. Effects of high relative humidity on the dynamic adsorption of dimethyl methylphosphonate (dmmp) on activated carbon. *Carbon*, 44(15):3247–3254, 2006.
- [235] Jia Huang, Yadong Jiang, Xiaosong Du, and Juan Bi. A new siloxane polymer for chemical vapor sensor. *Sensors and Actuators B: Chemical*, 146(1):388–394, 2010.
- [236] Yanyan Wang, Zhihua Zhou, Zhi Yang, Xiaohang Chen, Dong Xu, and Yafei Zhang. Gas sensors based on deposited single-walled carbon nanotube networks for dmmp detection. *Nanotechnology*, 20(34):345502, aug 2009.
- [237] Sofian M. Kanan, Anil Waghe, Bruce L. Jensen, and Carl P. Tripp. Dual wo3 based sensors to selectively detect dmmp in the presence of alcohols. *Talanta*, 72(2):401–407, 2007.
- [238] Michael A. Henderson and J. M. White. Adsorption and decomposition of dimethyl methylphosphonate on platinum(111). *Journal of the American Chemical Society*, 110(21):6939–6947, 1988.
- [239] X Guo, J Yoshinobu, and J T Yates, Jr. Decomposition of an organophosphate compound (dimethyl methylphosphonate) on the ni(111) and pd(111) surfaces. *Journal of Physical Chemistry; (USA)*, 94:17, 8 1990.
- [240] VS Smentkowski, P Hagens, and JT Yates Jr. Study of the catalytic destruction of dimethyl methylphosphonate (dmmp): oxidation over molybdenum (110). *The Journal of Physical Chemistry*, 92(22):6351–6357, 1988.
- [241] Anastasia V. Grigorieva, Aleksey B. Tarasov, Eugene A. Goodilin, Siranuysh M. Badalyan, Marina N. Rumyantseva, Alexander M. Gaskov, Alexander Birkner, and Yuri D. Tretyakov. Sensor properties of vanadium oxide nanotubes. *Mendeleev Communications*, 18(1):6–7, 2008.
- [242] Paulina Powroznik, Lucyna Grzadziel, Wieslaw Jakubik, and Maciej Krzywiecki. Sarin-simulant detection by phthalocyanine/palladium structures: From modeling to real sensor response. *Sensors and Actuators B: Chemical*, 273:771–777, 2018.
- [243] Igor V. Schweigert and Daniel Gunlycke. Hydrolysis of dimethyl methylphosphonate by the cyclic tetramer of zirconium hydroxide. *The Journal of Physical Chemistry A*, 121(40):7690–7696, 2017.
- [244] Wesley O. Gordon, Brian M. Tissue, and John R. Morris. Adsorption and decomposition of dimethyl methylphosphonate on $\gamma\text{-}\text{Al}_2\text{O}_3$ nanoparticles. *The Journal of Physical Chemistry C*, 111(8):3233–3240, 2007.
- [245] Ran Yoo, Somi Yoo, Dongmei Lee, Jeongmin Kim, Sungmee Cho, and Wooyoung Lee. Highly selective detection of dimethyl methylphosphonate (dmmp) using cuo

- nanoparticles /zno flowers heterojunction. *Sensors and Actuators B: Chemical*, 240:1099–1105, 2017.
- [246] Wei-Che Hung, Je-Chuang Wang, and Kuo-Hui Wu. Adsorption and decomposition of dimethyl methylphosphonate (dmmp) on expanded graphite/metal oxides. *Applied Surface Science*, 444:330–335, 2018.
- [247] Camelia N. Rusu and John T. Yates. Adsorption and decomposition of dimethyl methylphosphonate on tio₂. *The Journal of Physical Chemistry B*, 104(51):12292–12298, 2000.
- [248] MK Templeton and WH Weinberg. Adsorption and decomposition of dimethyl methylphosphonate on an aluminum oxide surface. *Journal of the American Chemical Society*, 107(1):97–108, 1985.
- [249] Teweldemedhin M. Tesfai, V. N. Sheinker, and Mark B. Mitchell. Decomposition of dimethyl methylphosphonate (dmmp) on alumina-supported iron oxide. *The Journal of Physical Chemistry B*, 102(38):7299–7302, 1998.
- [250] Tianyu Li, Roman Tsyshevsky, Lucas Algrim, Monica McEntee, Erin M. Durke, Bryan Eichhorn, Christopher Karwacki, Michael R. Zachariah, Maija M. Kuklja, and Efrain E. Rodriguez. Understanding dimethyl methylphosphonate adsorption and decomposition on mesoporous ceo₂. *ACS Applied Materials & Interfaces*, 13(45):54597–54609, 2021.
- [251] Sofian M. Kanan and Carl P. Tripp. An infrared study of adsorbed organophosphonates on silica: a prefiltering strategy for the detection of nerve agents on metal oxide sensors. *Langmuir*, 17(7):2213–2218, 2001.
- [252] Ashley R Head, Roman Tsyshevsky, Lena Trotochaud, Yi Yu, Osman Karshioğlu, Bryan Eichhorn, Maija M Kuklja, and Hendrik Bluhm. Dimethyl methylphosphonate adsorption and decomposition on moo₂ as studied by ambient pressure x-ray photoelectron spectroscopy and DFT calculations. *Journal of Physics: Condensed Matter*, 30(13):134005, mar 2018.
- [253] Ashley R. Head, Roman Tsyshevsky, Lena Trotochaud, Yi Yu, Line Kyhl, Osman Karshioğlu, Maija M. Kuklja, and Hendrik Bluhm. Adsorption of dimethyl methylphosphonate on moo₃: The role of oxygen vacancies. *The Journal of Physical Chemistry C*, 120(51):29077–29088, 2016.
- [254] Scott R. Segal, Steven L. Suib, Xia Tang, and Sunita Satyapal. Photoassisted decomposition of dimethyl methylphosphonate over amorphous manganese oxide catalysts. *Chemistry of Materials*, 11(7):1687–1695, 1999.

- [255] Mark B. Mitchell, V. N. Sheinker, and Eric A. Mintz. Adsorption and decomposition of dimethyl methylphosphonate on metal oxides. *The Journal of Physical Chemistry B*, 101(51):11192–11203, 1997.
- [256] Scott Holdren, Roman Tsyshevsky, Kenan Fears, Jeffrey Owrutsky, Tao Wu, Xizheng Wang, Bryan W. Eichhorn, Maija M. Kuklja, and Michael R. Zachariah. Adsorption and destruction of the g-series nerve agent simulant dimethyl methylphosphonate on zinc oxide. *ACS Catalysis*, 9(2):902–911, 2019.
- [257] Zhimin Yang, Yaqing Zhang, Liang Zhao, Teng Fei, Sen Liu, and Tong Zhang. The synergistic effects of oxygen vacancy engineering and surface gold decoration on commercial SnO_2 for ppb-level dmmp sensing. *Journal of Colloid and Interface Science*, 608:2703–2717, 2022.
- [258] Soo Chool Lee, Ho Yun Choi, Soo Jae Lee, Woo Suk Lee, Jeung Soo Huh, Duk Dong Lee, and Jae Chang Kim. The development of SnO_2 -based recoverable gas sensors for the detection of dmmp. *Sensors and Actuators B: Chemical*, 137(1):239–245, 2009.
- [259] Sivalingam Ramesh, Young-Jun Lee, Sabeur Msolli, Jong-Gyu Kim, Heung Soo Kim, and Joo-Hyung Kim. Synthesis of a Co_3O_4 @ gold/mwnt/polypyrrole hybrid composite for dmmp detection in chemical sensors. *RSC advances*, 7(80):50912–50919, 2017.
- [260] Mengqing Xu, Dongsheng Lu, Arnd Garsuch, and Brett L. Lucht. Improved performance of $\text{LiNi}_{0.5}\text{Mn}_{1.5}\text{O}_4$ cathodes with electrolytes containing dimethylmethylphosphonate (dmmp). *Journal of The Electrochemical Society*, 159(12):A2130, oct 2012.
- [261] Daqi Chen, Kaihuan Zhang, Hui Zhou, Guokang Fan, You Wang, Guang Li, and Ruifen Hu. A wireless-electrodeless quartz crystal microbalance with dissipation dmmp sensor. *Sensors and Actuators B: Chemical*, 261:408–417, 2018.
- [262] Peter Mäkie, Gunnar Westin, Per Persson, and Lars Österlund. Adsorption of trimethyl phosphate on maghemite, hematite, and goethite nanoparticles. *The Journal of Physical Chemistry A*, 115(32):8948–8959, 2011. PMID: 21711003.
- [263] Jean C. S. Costa, Romulo A. Ando, Antônio C. Sant’Ana, and Paola Corio. Surface-enhanced raman spectroscopy studies of organophosphorous model molecules and pesticides. *Phys. Chem. Chem. Phys.*, 14:15645–15651, 2012.
- [264] Nelli Taranenko, Jean-Pierre Alarie, David L. Stokes, and Tuan Vo-Dinh. Surface-enhanced raman detection of nerve agent simulant (dmmp and dimp) vapor on electrochemically prepared silver oxide substrates. *Journal of Raman Spectroscopy*, 27(5):379–384, 1996.

- [265] Fei Yan and Tuan Vo-Dinh. Surface-enhanced raman scattering detection of chemical and biological agents using a portable raman integrated tunable sensor. *Sensors and Actuators B: Chemical*, 121(1):61–66, 2007. Special Issue: 25th Anniversary of Sensors and Actuators B: Chemical.
- [266] Jiří Henych, Václav Štengl, Andreas Mattsson, Jakub Tolasz, and Lars Österlund. Chemical warfare agent simulatant dmmp reactive adsorption on tio₂/graphene oxide composites prepared via titanium peroxo-complex or urea precipitation. *Journal of Hazardous Materials*, 359:482–490, 2018.
- [267] Yanyan Wang, Ming Yang, Weixiao Liu, Lei Dong, Da Chen, and Changsi Peng. Gas sensors based on assembled porous graphene multilayer frameworks for dmmp detection. *Journal of Materials Chemistry C*, 7(30):9248–9256, 2019.
- [268] NIST X ray Photoelectron Spectroscopy Database. Nist standard reference database number 20, national institute of standards and technology. 2023.
- [269] Linjie Wang, Michael Denchy, Nicolas Blando, Lucas Hansen, Ben Bilik, Xin Tang, Zachary Hicks, and Kit H. Bowen. Thermal decomposition of dimethyl methylphosphonate on size-selected clusters: A comparative study between copper metal and cupric oxide clusters. *The Journal of Physical Chemistry C*, 125(21):11348–11358, 2021.
- [270] Michael A. Denchy, Linjie Wang, Nicolas Blando, Lucas Hansen, Benjamin R. Bilik, Xin Tang, Zachary Hicks, Gerd Gantefoer, and Kit H. Bowen. Adsorption and decomposition of dimethyl methylphosphonate on size-selected zirconium oxide trimer clusters. *The Journal of Physical Chemistry C*, 125(43):23688–23698, 2021.
- [271] Michael A. Denchy, Linjie Wang, Benjamin R. Bilik, Lucas Hansen, Sandra Albornoz, Francisco Lizano, and Kit H. Bowen. Effect of a single platinum atom within a small metal oxide cluster: Reaction of dmmp with size-selected pt₁zr₂o₇ supported on hopg. *The Journal of Physical Chemistry A*, 127(13):2895–2901, 2023. PMID: 36951644.
- [272] Xin Tang, Zachary Hicks, Gerd Ganteför, Bryan W. Eichhorn, and Kit H. Bowen. Adsorption and decomposition of dmmp on size-selected (wo₃)₃ clusters. *ChemistrySelect*, 3(13):3718–3721, 2018.
- [273] Xin Tang, Zachary Hicks, Linjie Wang, Gerd Ganteför, Kit H Bowen, Roman Tsyshkevsky, Jianwei Sun, and Maija M Kuklja. Adsorption and decomposition of dimethyl methylphosphonate on size-selected (moo₃)₃ clusters. *Physical Chemistry Chemical Physics*, 20(7):4840–4850, 2018.

- [274] Lixin Cao, Scott R. Segal, Steven L. Suib, Xia Tang, and Sunita Satyapal. Thermocatalytic oxidation of dimethyl methylphosphonate on supported metal oxides. *Journal of Catalysis*, 194(1):61–70, 2000.
- [275] J Zhou, K Varazo, J.E Reddic, M.L Myrick, and D.A. Chen. Decomposition of dimethyl methylphosphonate on tio₂(110): principal component analysis applied to x-ray photoelectron spectroscopy. *Analytica Chimica Acta*, 496(1):289–300, 2003. Looking to the Future of Analytical Chemistry - 2003.
- [276] Andrea Lovera, Benjamin Gallinet, Peter Nordlander, and Olivier J.F. Martin. Mechanisms of fano resonances in coupled plasmonic systems. *ACS Nano*, 7(5):4527–4536, 2013. PMID: 23614396.

Détection sensible et sélective de composés organophosphorés par spectroscopie infrarouge exaltée par effet de surface

Résumé

Les agents chimiques de guerre comme les composés organophosphorés (dont le sarin), sont extrêmement dangereux pour l'humain à de très faibles concentrations. Malgré la convention sur l'interdiction des armes chimiques (1997), leur usage persiste et ce faisant ils représentent une menace importante envers les populations civiles et militaires. Dans ce travail, nous proposons un nouveau capteur plasmonique basé sur l'absorption infrarouge exaltée de surface (SEIRA) à partir de semi-conducteurs III-V. La combinaison de la sensibilité et de la sélectivité exaltées, respectivement par les effets plasmoniques et la spectroscopie des modes vibrationnels caractéristiques dans l'infrarouge, associé à la compatibilité CMOS et l'industrie mature des semi-conducteurs, ouvre de nouvelles perspectives pour la détection de molécules dangereuses. De plus, cette solution innovante implémente un matériau ϵ -near-zero (ENZ), une classe émergente de matériaux pour améliorer l'interaction lumière-matière ainsi que le contrôle sur la réponse optique d'une structure plasmonique. Tirant avantage de la structure reconnue métal-isolant-métal, nous avons conçu un dispositif métal-ENZ-métal pour l'étude des phénomènes basés sur l'ENZ et la détection de composés organophosphorés en phase gazeuse. Ces composants ont été employés pour détecter le méthylphosphonate de diméthyle (DMMP), simulant du sarin. Les capteurs conçus et fabriqués ont montré un temps de réponse de 5 minutes et leur sélectivité fut éprouvée avec du benzène et du méthane. Nous avons démontré la détection de DMMP avec une concentration minimale de 100 ppm. Nous avons identifié que le capteur est sensible à la formation d'une monocouche de 5 Å de DMMP adsorbé en surface du capteur par le biais de son oxyde natif, preuve que le capteur puisse être sensible à de très faibles concentrations.

Abstract

Chemical warfare agents, such as the organophosphorous compounds (sarin), are extremely dangerous molecules towards human at extremely low concentrations. Despite the 1997 Chemical Weapons Convention, their use persists making them an important threat for military and civilian population. In this work, we propose a novel plasmonic sensor based on surface-enhanced infrared absorption (SEIRA) made of III-V semiconductors. The combination of enhanced sensitivity using plasmonic effects, with increased selectivity by probing the molecules characteristic vibration modes in the infrared, associated with the CMOS-compatibility and mature industry of semiconductors, opens new perspectives for the sensing of dangerous molecules. Besides, this innovative solution implements a ϵ -near-zero (ENZ) medium, an emerging class of materials known for their ability to improve light-matter interactions as well as the control over the optical response of a plasmonic structure. Taking advantage of the well-known metal-insulator-metal structure, we designed a metal-ENZ-metal device that will serve as vehicle for the study of ENZ phenomena and the sensing of organophosphorous compounds in gas phase. These devices were tested for the detection of a simulant of the sarin molecule: dimethyl methylphosphonate (DMMP). The designed and fabricated sensors have a 5 min response time and their selectivity was positively experienced with benzene and methane. We demonstrated the sensing of DMMP at concentration as low as 100 ppm. We identified that the sensor was sensitive to a 5 Å-thick monolayer of DMMP that has adsorbed at the surface of our sensor through its native oxide, a proof that the sensor shall be sensitive to much lower concentrations.

Résumé en français

1) Introduction

L'immense pouvoir létal des agents chimiques de guerre (ACG), y compris des composés organophosphorés (COP), même à des concentrations extrêmement faibles, et ce en absence d'odeurs, invisibles et persistants, rend cette catégorie de molécules particulièrement dangereuse car elle échappe à nos sens naturels. Lors de l'inhalation, les effets létaux des agents neurotoxiques apparaissent pour des concentrations aussi faibles que quelques mg.m^{-3} , ce qui correspond à quelques molécules par milliards. En règle générale, ces molécules sont composées d'éléments courants, tels que le carbone, l'azote, l'oxygène, le fluor et le phosphore, avec un poids moléculaire léger d'environ 100 g.mol^{-1} . Ces deux caractéristiques représentent des défis majeurs en termes de sensibilité, de sélectivité et de temps de réponse d'un capteur. La plupart des techniques disponibles dans le commerce consistent en des dispositifs qui souffrent d'inconvénients importants tels que leur volume (chromatographie en phase gazeuse), le manque de sélectivité (capteurs gravimétriques), une faible sensibilité (spectrométrie de mobilité ionique) ou un temps de réponse long (papier colorimétrique). Par conséquent, il y a eu un intérêt croissant ces dernières années pour le développement de techniques innovantes qui surmontent les inconvénients des méthodes susmentionnées. Le développement des dispositifs de détection modernes est intimement liée à la recherche de nouvelles surfaces et de nouveaux matériaux physico-chimiquement réactifs afin d'améliorer les interactions entre les molécules et le capteur. D'une certaine manière, le transducteur et le milieu d'amélioration (physique ou chimique) sont les deux principales composantes sur lesquelles les efforts de la recherche scientifique se concentrent.

Dans ce cadre, la plasmonique apparaît comme un moyen sous-estimé et pourtant prometteur pour la détection des ACG. La plasmonique étudie et exploite les oscillations des porteurs de charge libres de la matière, qui peuvent améliorer la sensibilité d'un dispositif de détection. En particulier, depuis l'article publié en 1980 dans les *Physical Review Letters*, intitulé "Enhancement of the infrared absorption from molecular monolayers with thin metal overlayers" par Hartstein *et al.* [*Phys. Rev. Lett.* **45**, 201 (1980)], il a été démontré que l'absorption des molécules peut être améliorée en exploitant les modes plasmoniques de surface provenant de particules métalliques. L'absorption de molécules est particulièrement intéressante dans l'infrarouge : la région spectrale où les molécules présentent des résonances caractéristiques connues sous le nom de modes vibrationnels. En fin de compte, de nombreuses études ont démontré avec succès l'utilisation de dispositifs basés sur les plasmons pour la détection de molécules par absorption infrarouge améliorée par la surface (SEIRA). Cependant, seule une poignée d'articles a abordé la problématique de la détection de gaz à l'aide de cette technique.

D'autre part, les plateformes de détection modernes sont encore améliorées par la chimie de surface ou la fonctionnalisation. Différentes technologies ont été développées à cet égard, notamment des polymères, des monocouches auto-assemblées, des réseaux métallo-organiques, des oxydes et même des nanoparticules dotées de propriétés plasmoniques. Si elles sont intéressantes en termes de sensibilité et de sélectivité, car elles améliorent les interactions molécule-capteur, ces stratégies présentent un certain nombre de limitations pratiques telles que la réutilisation et la stabilité (temporelle, thermique, etc.). Une deuxième approche pour améliorer les performances d'un capteur consiste à utiliser un milieu qui améliore la réponse du

transducteur. À cet égard, les milieux epsilon proche de zéro (ENZ), sont apparus comme un moyen intéressant d'améliorer les interactions entre la lumière et la matière lorsque la permittivité du milieu atteint zéro. Au milieu des années 2000, cette nouvelle classe de matériaux a suscité un énorme intérêt dans la communauté électromagnétique en raison des effets particuliers associés à un faible indice de réfraction. Néanmoins, leur application à la détection reste marginale par rapport à la conception de guides d'ondes et de métamatériaux.

Dans ce travail de thèse, nous développons un dispositif plasmonique pour la détection des ACG, et plus particulièrement pour la détection du sarin. Le comportement plasmonique est obtenu en utilisant des semi-conducteurs III-V fortement dopés (InAsSb et GaSb) de telle sorte qu'une résonance plasmonique se produit dans l'infrarouge moyen. Le couplage plasmon-molécule est obtenu par chevauchement spectral et spatial. Le chevauchement spectral implique que la résonance plasmonique et les modes de vibration de la molécule sont à la même fréquence. Le chevauchement spatial fait référence à la proximité entre les molécules et le champ électromagnétique exalté, associé aux oscillations des porteurs de charge libres, à la fréquence de résonance plasmonique. La structure de l'échantillon est basée sur une structure métal-ENZ-métal conçue pour améliorer les interactions lumière-matière et renforcer l'absorption infrarouge des molécules CWA. Nous démontrons avec succès l'applicabilité de la plasmonique à base de semi-conducteurs III-V pour les applications de détection dans l'infrarouge et pour l'ingénierie des métamatériaux avec un contrôle amélioré de la réponse plasmonique par l'utilisation d'un milieu ENZ.

2) Fabrication des échantillons

Les structures métal-isolant-métal (MIM) sont bien connues pour leur capacité à améliorer les interactions lumière-matière en piégeant la lumière dans la couche isolante prise en sandwich entre deux couches métalliques. Dans la pratique, cela se traduit par deux phénomènes qui ont été rapportés : (1) un comportement d'absorbeur parfait et (2) un plasmon-polariton de surface (SPP) piégé aux interfaces de l'antenne, avec un champ magnétique coincé dans la couche isolante, connu sous le nom de *gap plasmon*. La spécificité de ce travail réside dans la nature de la couche isolante. Alors que les structures MIM et les couches ENZ ont été utilisées pour une grande variété d'applications, nous proposons de combiner ces deux concepts dans une structure métal-ENZ-métal. Ce concept est basé sur le fait que les couches ENZ ne sont pas métalliques, de sorte qu'elle conserve les avantages de la structure MIM, tout en bénéficiant des atouts de la couche ENZ. Le comportement ENZ est obtenu en dopant la couche de sorte que sa fréquence plasma atteigne la fréquence de fonctionnement du capteur qui est autour de 10 μm dans notre cas, proche de l'absorption du simulant de sarin : méthylphosphonate de diméthyle (DMMP). Nous avons également essayé d'autres niveaux de dopage pour l'étude des phénomènes ENZ. La figure 1 présente la structure métal-ENZ-métal étudiée au travers de trois échantillons fabriqués.

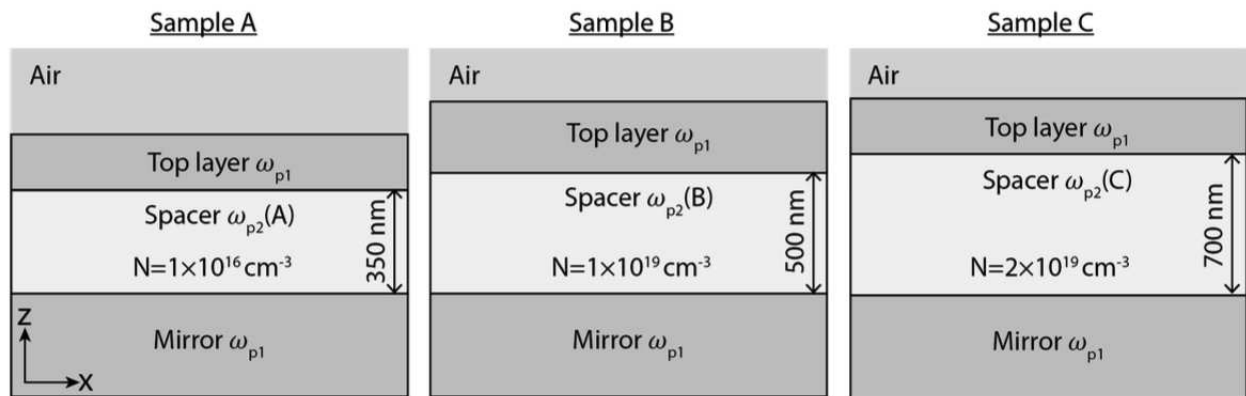


Figure 1. Schémas des trois échantillons métal-ENZ-métal étudiés. Les couches grises sont fortement dopées ($4 \cdot 10^{19} \text{ cm}^{-3}$).

a) Simulations électromagnétiques

La physique moderne est intimement liée au développement de nouvelles méthodes numériques et à l'amélioration des ordinateurs. La capacité de simuler une structure afin de prédéterminer sa réponse physique a énormément profité au développement de structures complexes qui dépendaient auparavant d'essais et d'erreurs et de lois empiriques. L'électromagnétisme est l'une des théories physiques les mieux établies et, par conséquent, les simulations électromagnétiques sont devenues un domaine de recherche à part entière, et sont généralement considérées comme indispensables pour la conception de dispositifs optiques à l'échelle nanométrique sub-longueur d'onde, y compris la plasmonique. Les méthodes de simulation électromagnétique les plus couramment utilisées sont les suivantes : (i) la méthode des différences finies dans le domaine temporel (FDTD), (ii) la méthode des éléments finis (FEM) et (iii) l'analyse rigoureuse des ondes couplées (RCWA).

Dans ce travail, la FDTD et la RCWA seront réalisées avec le logiciel Lumerical FDTD Solver et RETICOLO (code Matlab open source), respectivement. La conception de la structure principale et la détermination des paramètres des antennes ont été réalisées avec la RCWA. Le code libre RETICOLO permet de concevoir des systèmes 1D et 2D et de simuler leur réponse optique en termes de réflectivité et de transmission. Cette méthode est facile à utiliser et plus rapide que d'autres méthodes, mais sa précision est directement liée au temps de calcul. La FDTD a été utilisée pour confirmer certains résultats de la RCWA, y compris la simulation de molécules organiques, et elle a l'avantage de toujours converger dans les bonnes conditions, ce qui explique pourquoi elle est une méthode de calcul de référence pour l'électromagnétisme.

b) Croissance épitaxiale et caractérisations

Le processus de fabrication physique commence par la croissance cristalline des échantillons. La croissance des semi-conducteurs III-V (SC) consiste en la formation de couches cristallines, sur un substrat (*wafers*) de semi-conducteur, premier élément de la chaîne de fabrication. La croissance des structures cristallines sur le substrat dépend fortement de l'état de la surface, de sorte que la préparation de la surface pour l'épitaxie est, en soi, un domaine de recherche. Le substrat est crucial dans la croissance cristalline car il impose sa

maille cristalline aux structures crues, typiquement autour de 6,1 Å pour l'InAs, le GaSb et l'AlSb. La croissance de structures avec une maille cristalline différente est un sujet de recherche très actif pour le développement de nouveaux dispositifs optoélectroniques et leur intégration dans des circuits intégrés photoniques avec des applications quotidiennes.

Les caractérisations de la surface des échantillons après la croissance sont effectuées à l'aide de deux techniques de microscopie : (i) la microscopie optique et (ii) la microscopie à force atomique (AFM). Pour vérifier la qualité cristalline des échantillons, on utilise la diffraction des rayons X à haute résolution (HRXRD). Elle fournit des informations sur l'état cristallin, la maille du réseau et les épaisseurs des structures crues. Cette technique est particulièrement importante pour calibrer la quantité d'antimoine nécessaire pour faire correspondre correctement la maille d'InAsSb à celle du GaSb.

Le comportement plasmonique des semi-conducteurs III-V est obtenu grâce à la capacité de les doper et d'introduire une quantité suffisante de porteurs libres pour obtenir une densité élevée d'électrons, c'est-à-dire un plasma. Pour obtenir un comportement plasmonique dans le MIR, le semi-conducteur III-V doit être fortement dopé avec des porteurs libres ayant une faible masse effective. Le dopage par trous (ou dopage p) est possible et conduirait à un plasma de trous plutôt que d'électrons, mais les trous sont beaucoup plus lourds que les électrons et, par conséquent, leur masse effective élevée abaisse considérablement la fréquence du plasma, bien en deçà du MIR. En revanche, les électrons sont beaucoup plus légers, en particulier dans l'InAs, pour lequel la masse effective des électrons est d'environ $0,023m_0$ (contrairement aux trous pour lesquels la masse effective est de $0,41m_0$), ce qui souligne également la grande mobilité des électrons libres dans l'InAs. Les niveaux de dopage peuvent être mesurés de différentes manières, l'effet Hall étant de loin le plus utilisé dans l'industrie du silicium, bien que les effets d'accumulation de charge entraînent des erreurs dans l'estimation, en particulier dans l'InAs. Les niveaux de dopage peuvent également être mesurés optiquement, en sondant le mode de Brewster se produisant à la fréquence du plasma. Cette technique consiste à envoyer un faisceau lumineux avec un angle de 60° à la surface de SC fortement dopés de sorte que, lors de la réflexion, un mode de fuite correspondant à la densité de porteurs libres peut être excité, ce qui se traduira par une absorption sur le spectre de réflectance.

c) Fabrication

La texturation de la surface en nanostructures telles que des nano-antennes plasmoniques est basée sur deux étapes principales : le design d'un masque à la surface, suivi d'une gravure pour imprimer le motif du masque à la surface de l'échantillon. Le masque peut être soit un masque dur, fait de SiO_2 ou de Si_3N_4 par exemple, soit une résine. Le choix du type de masque dépend de sa capacité à résister à l'étape de la gravure et de sa durée. Les masques durs peuvent supporter des gravures beaucoup plus fortes, comme les gravures sèches, mais nécessitent une étape supplémentaire pour modeler le masque dur lui-même avec une résine. Les résines sont des polymères couramment utilisés dans l'industrie des semi-conducteurs parce qu'ils sont sensibles à la lumière ou aux électrons, et la photolithographie et la lithographie par faisceau d'électrons (LFE) sont employées pour imprimer le motif souhaité sur la résine. Une fois la lithographie effectuée, le développement de la résine à l'aide d'un produit chimique appelé révélateur permet d'enlever sélectivement la résine exposée ou non exposée, selon la nature positive ou négative de la résine. La résine restante peut être utilisée comme masque pour l'étape de gravure. Le design par LFE peut être relativement long en fonction des dimensions du motif ; dans notre cas, cela prend une nuit jusqu'à une journée entière.

La deuxième étape de la structuration est la gravure. Si l'on a besoin d'un masque dur pour la gravure de la surface de l'échantillon, une gravure préliminaire du masque dur sous la résine est nécessaire. Dans le cas contraire, la résine développée sert de masque et la gravure des semi-conducteurs III-V a lieu. La gravure peut être réalisée de deux manières différentes : par voie humide ou par voie sèche, parfois en combinant les deux. La gravure humide repose sur l'utilisation d'acides tels que les acides citrique, nitrique ou fluorhydrique (HF), qui sont couramment utilisés, généralement dilués avec de l'eau déionisée ou du peroxyde d'hydrogène. La gravure à sec est réalisée à l'aide de techniques telles que le plasma à couplage inductif pour la gravure ionique réactive, bien connue sous le nom d'ICP-RIE. Cette technique est basée sur l'ionisation d'un gaz, les ions étant ensuite attirés vers la surface de l'échantillon pour la graver. Les échantillons utilisés dans ce travail de thèse ont été fabriqués selon la procédure de fabrication standard suivante : (1) procédure de nettoyage, (2) dépôt de la résine, (3) design par LFE, (4) recuit, (5) développement, (6) gravure sèche et (7) procédure de nettoyage. La figure 2 montre en (a) une image obtenue par microscopie électronique à balayage, (b) microscopie optique et (c) microscopie à force atomique, d'un échantillon une fois sa fabrication terminée. Enfin le capteur plasmonique est caractérisée optiquement.

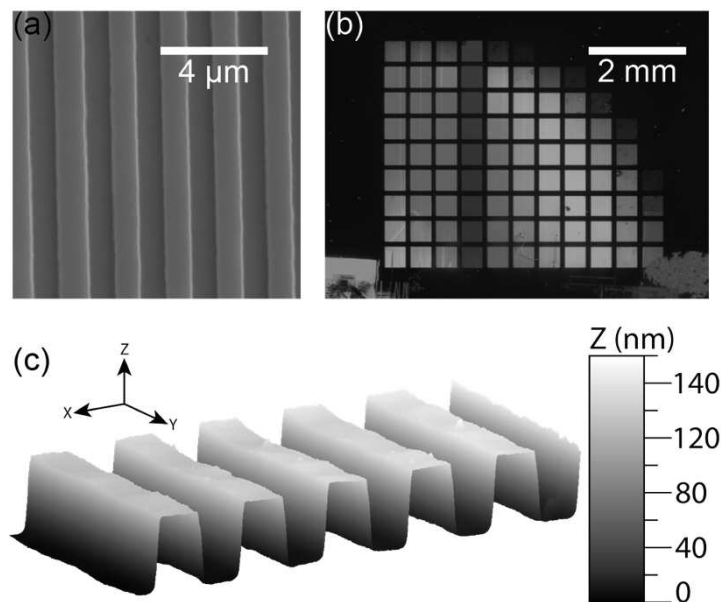


Figure 2. Caractérisations de la fabrication : (a) image MEB des antennes plasmoniques, (b) image optique de l'échantillon fabriqué et (c) reconstruction 3D obtenue par AFM.

Nous allons maintenant aborder l'instrumentation et la technologie de la spectroscopie infrarouge à transformée de Fourier (FTIR), qui est le principal outil de caractérisation utilisé dans le cadre de ce travail. La spectroscopie FTIR retrace le spectre d'absorption d'un analyte, l'objectif est donc d'obtenir un spectre de haute qualité, ce qui dépend de différents facteurs en termes d'instrumentation et de métrologie. Elle se compose d'une source lumineuse qui émet dans le domaine spectral d'intérêt, d'un mécanisme de sélection de la longueur d'onde et d'un détecteur. Le mécanisme de base d'un spectromètre FTIR repose sur l'interféromètre de Michelson, qui est de loin le dispositif le plus utilisé dans les FTIR modernes. L'interféromètre de Michelson est basé sur les interférences d'un faisceau divisé en fonction d'un miroir

mobile, l'interférogramme résultant correspond à l'intensité du signal en fonction du déplacement du miroir mobile. Pour obtenir un spectre, il faut ensuite effectuer la transformée de Fourier (FT) de l'interférogramme. Dans la pratique, cette opération est effectuée une première fois sur une référence, puis sur l'analyte ou l'échantillon, et le rapport entre les deux spectres communique des informations sur l'échantillon uniquement, en éliminant le bruit de fond lié à la réponse de l'environnement ainsi que les fluctuations de la source. La figure 3 présente un spectre de réflectance caractéristique du capteur plasmonique avec une résonance plasmonique (LSPR) obtenue autour de 10 microns. La réponse optique d'un capteur plasmonique est largement dominé par les propriétés optiques des matériaux le composant, ici les fréquences plasma ω_{p1} et ω_{p2} , respectivement les couches fortement dopées et la couche ENZ.

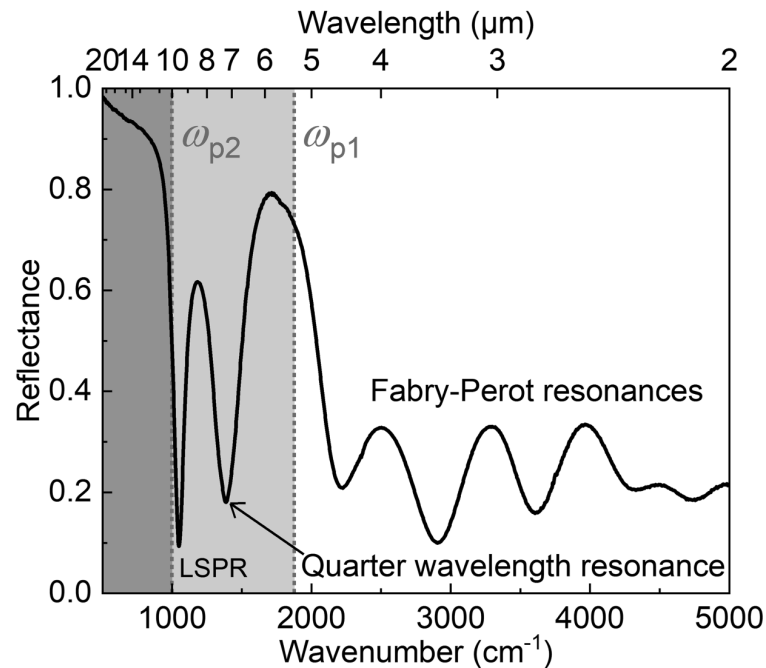


Figure 3. Spectre de réflectance par des nano-rubans plasmoniques d'une largeur de 1 µm.

3) Résultats des expériences

a) Plasmonique et permittivité proche de zéro

Le troisième partie se concentre sur la conception, la fabrication et la caractérisation des structures ENZ et de leurs effets plasmoniques associés. L'étude suivante sur les matériaux ENZ basés sur la plasmonique des SC III-V est importante pour démontrer comment cette classe de matériaux peut être utilisée pour adapter la réponse optique des dispositifs plasmoniques à base d'ENZ pour des applications de détection telles que la spectroscopie des COP en phase gazeuse. La première partie présente la conception de trois échantillons ENZ. Puis sont abordés des phénomènes plus complexes associés à la nature ENZ de la structure : l'épinglage LSPR, la phase constante des antennes plasmoniques sur milieu ENZ et la nature dispersive des matériaux ENZ.

La figure 4 montre la relation entre la fréquence LSPR (et la longueur d'onde) en fonction de la largeur de l'antenne pour chaque échantillon. Les résultats expérimentaux sont corroborés par les simulations numériques réalisées par le RCWA. On observe que lorsque la largeur de l'antenne augmente, la fréquence LSPR diminue (c'est-à-dire que la longueur d'onde augmente : décalage vers le rouge). Le résultat frappant est que pour les échantillons B et C, le décalage vers le rouge est beaucoup plus lent que pour l'échantillon A. En effet, une variation de largeur de 400 nm entraîne un décalage vers le rouge d'environ 250, 100 et 50 cm^{-1} pour les échantillons A, B et C, respectivement. Ce ralentissement du décalage vers le rouge s'accroît pour les échantillons B et C lorsque la fréquence LSPR atteint la fréquence plasma du milieu ENZ respectif, $\omega_{p2}(B)$ à 1000 cm^{-1} et $\omega_{p2}(C)$ à 1300 cm^{-1} . Au fur et à mesure que le niveau de dopage de la couche ENZ augmente et se rapproche de la fréquence plasma ω_{p1} des couches métalliques, la LSPR est coincée dans une gamme spectrale de plus en plus étroite, définie par $[\omega_{p2} - \omega_{p1}]$.

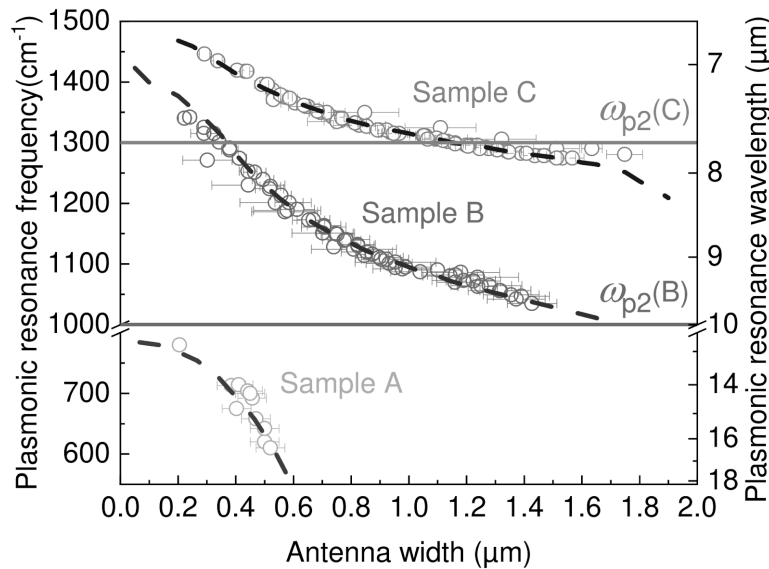


Figure 4. Fréquences de résonance plasmonique selon la largeur du nanoruban et en fonction du dopage de la couche ENZ intermédiaire.

La différence entre les travaux publiés précédemment et ceux présentés ici réside dans le choix des matériaux plasmoniques et ENZ. Les effets hybrides plasmon-ENZ étudiés précédemment sont soutenus par un milieu ENZ sur lequel sont fabriquées des antennes plasmoniques. Le milieu ENZ peut être accordé par sa fréquence plasma, comme c'est le cas pour les TCO, ou il n'est pas accordable (basé sur les phonons) ; mais dans les deux cas, le régime ENZ reste loin de la LSPR des métaux nobles plasmoniques couramment utilisés. Nous avons démontré que les SC III-V sont exceptionnels à cet égard car le même matériau, InAsSb dans ce cas, peut être cru pour des couches dopées différemment et ce de manière monolithique, tout en ayant leurs propriétés optiques dans la même région spectrale en fonction des niveaux de dopage des couches ENZ et plasmoniques.

Concernant le champ électromagnétique exalté, associé à la résonance plasmonique : son intensité maximale est supérieure d'environ un ordre de grandeur pour la structure MIM par rapport à la structure M-ENZ-M. Cela n'est pas dû à la couche ENZ, mais au fait que pour atteindre le régime ENZ, il faut fabriquer des antennes plus grandes, de sorte que leurs fréquences LSPR correspondantes se rapprochent du point

ENZ de la couche isolante. Les antennes plus larges sont moins efficaces en termes de piégeage de la lumière et donc de confinement du champ électromagnétique, car leurs dimensions ne sont pas aussi inférieures à la longueur d'onde que celles des antennes plus petites. La compensation positive est que le champ électromagnétique exalté de la structure sera renforcé dans le milieu environnant, tandis que la structure MIM classique présente des points chauds. En ce sens, le matériau ENZ semble adapté pour des applications en spectroscopie.

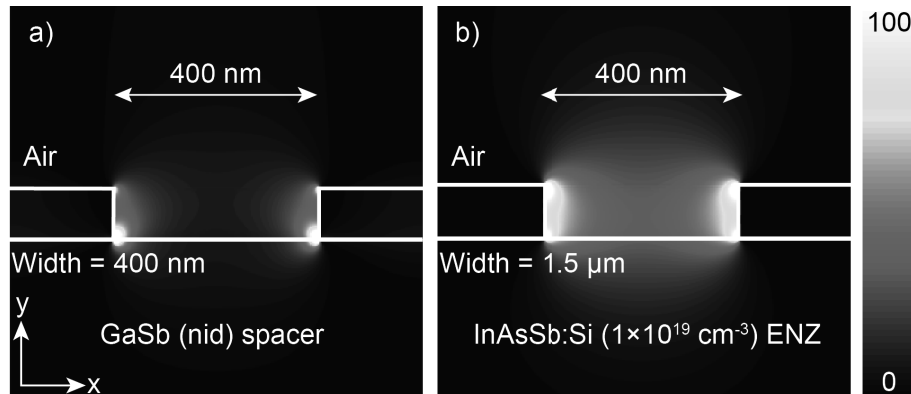


Figure 5. Champ électromagnétique exalté selon x pour (a) une structure MIM standard, et (b) la structure M-ENZ-M, à leur fréquence de résonance plasmonique respective.

L'idée principale qui sous-tend l'utilisation d'une structure basée sur un ENZ pour les applications de détection est que ces derniers sont particulièrement adaptés à la détection de gaz. Par définition, un gaz est un milieu où toutes les molécules occupent l'espace dont elles font partie ; en ce sens, nous le considérons comme un milieu 3D. Cependant, en plasmonique, la plupart des modes, dont les SPP, sont des modes qui se produisent aux interfaces et sont donc considérés comme un système 2D. Cette inadéquation en termes de dimensions est un inconvénient majeur, car il apparaît que les SPP ne sont pas très bien adaptés à la détection de molécules en phase gazeuse. Pour résoudre ce problème, l'utilisation d'une structure plasmonique à base d'ENZ permet de modifier le champ électromagnétique d'un système 2D vers une solution 3D. La description standard du champ électromagnétique amplifié est bien connue sous la forme de points chauds, c'est-à-dire un volume extrêmement petit où le champ est fortement concentré et amplifié, et ceux-ci peuvent être considérés comme un système 1D pour les particules métalliques plasmoniques ou un système 2D pour les nanorubans fabriqués dans la structure MIM (figure 5(a)). Inversement, la structure M-ENZ-M est associée à un champ électromagnétique amélioré qui se diffuse beaucoup plus dans l'environnement de sorte que le champ acquiert une nature 3D, ce qui le rend parfaitement adapté aux applications de spectroscopie des molécules en phase gazeuse, en théorie (figure 5(b)). Néanmoins, le compromis entre cette caractéristique basée sur l'ENZ et l'intensité du champ électromagnétique doit être soigneusement pris en compte, notamment en fonction des interactions entre les molécules et le capteur, lors de la conception d'un capteur plasmonique.

En résumé, la structure métal-ENZ-métal s'avère être un excellent véhicule pour étudier et tirer profit des phénomènes ENZ tels que le pincement de la résonance plasmonique, la phase quasi constante et la nature dispersive des matériaux ENZ. La grande concordance entre les résultats expérimentaux, les simulations RCWA et les résultats théoriques basés sur la FDTD montre comment les semi-conducteurs III-V, tels que

InAsSb et GaSb, peuvent être utilisés pour modifier la réponse optique infrarouge et l'amélioration du champ électromagnétique des nanostructures plasmoniques pour diverses applications, telles que la spectroscopie, qui est présentée dans la partie suivante.

b) Détection d'un composé organophosphoré

Dans cette partie, nous présentons les résultats des expériences de détection de gaz par COP. Les résultats expérimentaux consistent en deux études différentes portant sur les caractéristiques fondamentales d'un capteur : sensibilité, sélectivité, temps de réponse et répétabilité. La première étude présente la réponse optique du capteur plasmonique exposé à différentes concentrations de DMMP. La seconde étude présente la capacité du capteur à discriminer entre le DMMP et d'autres molécules, en l'occurrence le méthane et le benzène, ainsi que sa réponse dans un environnement humide. Après ces résultats, nous discutons des diverses interactions qui peuvent se produire entre la surface InAsSb du capteur plasmonique et les molécules de DMMP. Cette étude comprend plusieurs caractérisations : spectroscopies IR, Raman, et XPS (spectrométrie photoélectronique X), cherchant à récupérer des informations physico-chimiques sur les interactions du DMMP avec le substrat plasmonique constitué de SC III-V. Enfin, à partir des résultats précédents, nous réalisons une série de simulations numériques électromagnétiques basées sur deux méthodes : FDTD et RCWA. Ces simulations sont réalisées afin de corroborer les résultats expérimentaux présentés dans la deuxième section.

Les expériences de détection commencent par la détection du DMMP sans le dispositif plasmonique. La figure 6 montre en (a) une mesure de réflectance standard obtenue à partir du dispositif expérimental installé, avec une concentration de 320 ppm. Nous observons diverses signatures spectrales, notamment l'absorption de l'eau et du CO₂ présents dans l'environnement, ainsi que l'absorption du DMMP, dont l'empreinte se situe principalement dans la plage 700-1400 cm⁻¹, illustrée en (b). Le panneau (b) met en évidence l'empreinte spectrale du DMMP et ses divers modes vibrationnels caractéristiques. La principale raie d'absorption à 1050 cm⁻¹ ou 9,5 μm correspond à la liaison P-O-C, et comme c'est la plus prononcée, ainsi que la plus caractéristique d'un COP, nous concentrons notre intérêt sur cette raie d'absorption dans cette étude.

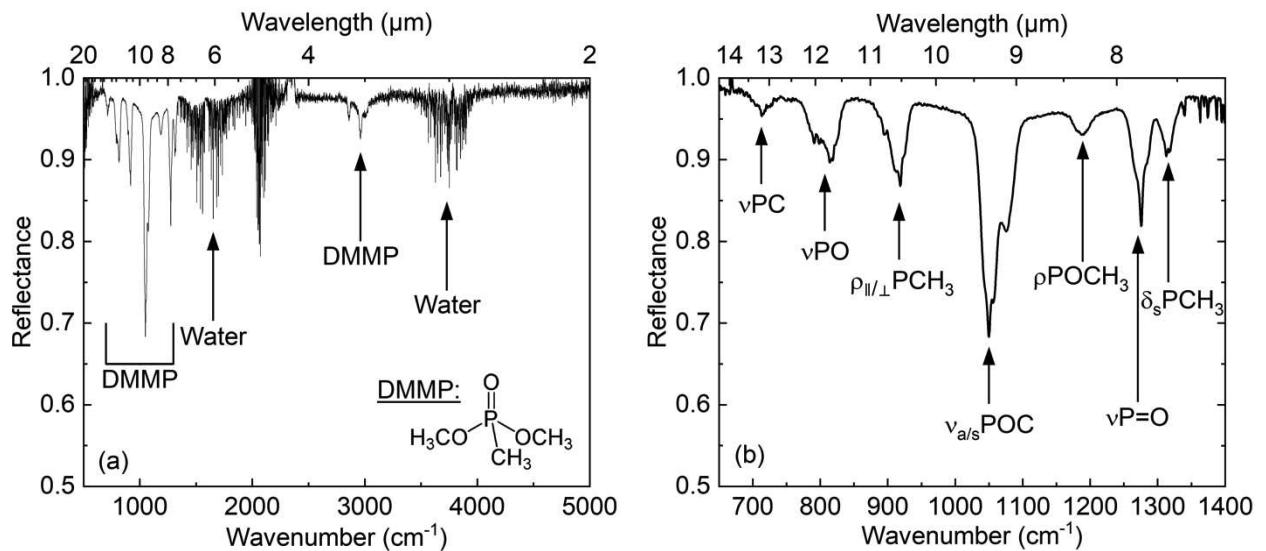


Figure 6. Spectres de réflectance infrarouge traduisant l'absorption du DMMP et de l'environnement : eau et CO_2 . (a) Spectre large gamme et (b) empreinte moléculaire du DMMP autour de 10 μm .

Au travers des différentes expériences, nous avons démontré que le capteur plasmonique n'était pas sensible au benzène et au méthane, deux interférents couramment rencontrés dans l'environnement. En outre, nous avons obtenu des résultats positifs lorsque le capteur a été exposé à 100 ppm de DMMP avec une humidité relative de 50 %. Ces résultats montrent que le capteur est sélectif vis-à-vis du DMMP, même dans un environnement humide. Les résultats de la sensibilité et de la sélectivité étudiées sont résumés dans la figure 7, qui met en évidence les différentes caractéristiques de ce capteur plasmonique : sensibilité jusqu'à 100 ppm, non-linéarité de la réponse avec la concentration, sélectivité vis-à-vis du DMMP, insensibilité aux interférents tels que le méthane et le benzène, et tolérance à l'humidité. Ce prototype de capteur SEIRA à SC III-V est le premier du genre et nous avons atteint des niveaux de détection décents similaires aux travaux de Huang et al. et Wang et al. qui ont respectivement étudié un nouveau polymère siloxane acide à liaison hydrogène couplé à un capteur QCM [Sens. Actuators B: Chem. **146**, 1, 388-394 (2010)], et un capteur de résistivité fonctionnalisé avec des nanotubes de carbone monoparois [Nanotechnology. **20**, 345502 (2009)], et ont atteint une sensibilité à 100 ppm pour les deux. Cela montre que notre capteur plasmonique se compare bien en termes de sensibilité aux études analogues et qu'il bénéficie d'une grande sélectivité, à la fois en termes de sensibilité aux interférents et de signatures caractéristiques du DMMP dans l'IR.

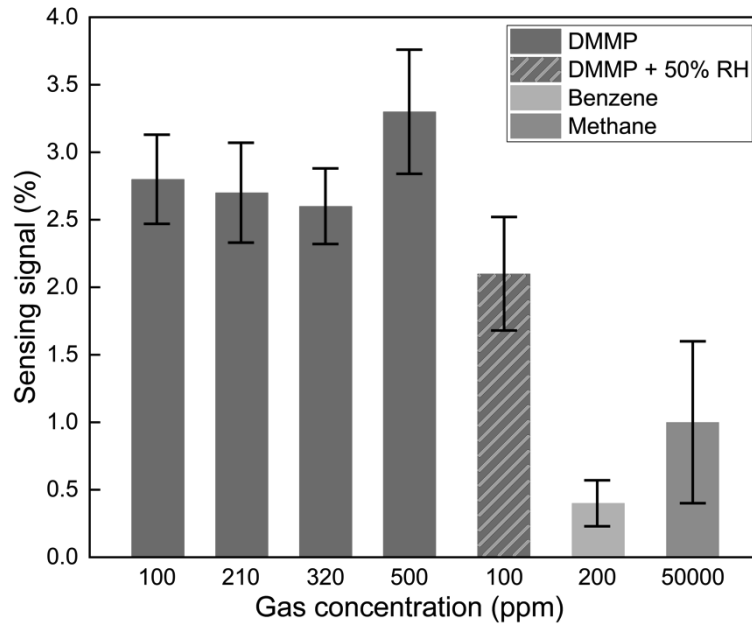


Figure 7. Histogramme résumant les résultats des expériences de sensibilité et de sélectivité du capteur plasmonique.

Nous avons précédemment suggéré qu'il devait y avoir une sorte d'interaction entre la surface des semi-conducteurs et les molécules de DMMP, résultant en une couche adsorbée à la surface qui sature le signal de détection. La figure 8 illustre cette hypothèse : Les molécules de DMMP peuvent interagir avec la surface ou avec son oxyde natif pour former une monocouche de DMMP, dont l'épaisseur est estimée à 5 Å, approximativement la taille de la molécule. Cette hypothèse est corroborée par le fait que les expériences de détection sont réalisées après que le système se soit stabilisé suffisamment longtemps pour que ces interactions potentielles puissent se produire.

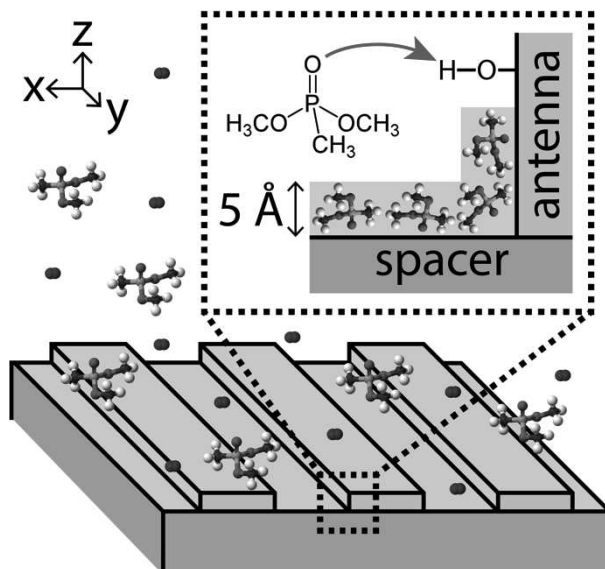


Figure 8. Représentation schématique du processus d'adsorption entre le DMMP et la surface du capteur en InAsSb. Le résultat hypothétique des interactions est la formation d'une monocouche de DMMP de 5 Å.

Lors de l'adsorption, des réorganisations chimiques de la structure moléculaire peuvent se produire, ce qui a des conséquences sur ses propriétés, y compris l'absorption. Par conséquent, nous étudions les interactions potentielles entre la surface de notre capteur et le DMMP en séchant une gouttelette de 0,1 μL sous flux de N_2 sur un miroir en InAsSb, et en effectuant (1) des mesures de réflectance infrarouge, (2) des mesures Raman, (3) des mesures XPS pour obtenir des informations supplémentaires quant à l'état des molécules de DMMP à la surface d'InAsSb. Cette série d'expériences visant à identifier les interactions potentielles entre la surface d'InAsSb et les molécules de DMMP, par l'intermédiaire de l'oxyde natif de l'échantillon, porte plusieurs conclusions. Tout d'abord, nous nous attendions, d'après la littérature, à ce que le DMMP interagisse avec la surface par adsorption et subisse une réorganisation chimique. Deuxièmement, les mesures par XPS nous ont permis de conclure qu'en effet, le DMMP s'adsorbe et persiste à la surface après plusieurs semaines ; de plus, des différences d'énergie de liaison ont été constatées entre une fine couche de DMMP séché et du DMMP pur, ce qui laisse supposer des natures chimiques différentes. Troisièmement, nous avons effectué de la spectroscopie Raman qui montre que le DMMP adsorbé est radicalement différent de sa forme liquide en termes de structure chimique. Enfin, la spectroscopie infrarouge est celle qui contient le plus d'informations car elle a un impact direct sur notre compréhension des expériences de détection réalisées précédemment. En effet, les coefficients d'absorption du DMMP en phase gazeuse et du DMMP séché sur la surface de notre échantillon sont différents de telle sorte que leurs réponses optiques respectives sont différentes. Toujours est-il qu'au final, la fixation de molécules de DMMP, d'une taille de 5 Å sur la surface d'InAsSb, aboutit à la formation d'une couche monomoléculaire de 5 Å d'épaisseur, après saturation. La section suivante traite des simulations numériques électromagnétiques qui permettront enfin de mettre en lumière la problématique de la saturation du détecteur plasmonique par le DMMP, responsable de la saturation du signal de détection.

Afin d'effectuer des simulations numériques pour évaluer l'impact d'une couche monomoléculaire de DMMP de 5 Å d'épaisseur sur les antennes plasmoniques, il est nécessaire de connaître ses propriétés optiques, à savoir l'indice de réfraction n et le coefficient d'absorption κ , qui forment ensemble l'indice de réfraction complexe d'un milieu. Des mesures expérimentales nous ont déjà permis de déterminer le coefficient d'absorption du DMMP, tant en phase gazeuse qu'en phase sèche. Les relations de Kramers-Kronig sont des relations mathématiques bien connues qui relient les parties réelles et imaginaires de toute fonction complexe, telle que l'indice de réfraction complexe. La phase gazeuse est très différente de l'état séché du DMMP, surtout autour de 10 μm , preuve des interactions entre la surface du SC et les molécules de DMMP. Ce résultat s'avère crucial lors des simulations électromagnétiques, car ces différences peuvent être responsables des variations spectrales drastiques lorsque l'on considère une couche moléculaire aussi fine que 5 Å. En d'autres termes, les résultats des simulations numériques dépendent fortement des propriétés optiques du milieu situé au-dessus des nanorubans plasmoniques.

La figure 9 montre la réflectance différentielle (%), en fonction du nombre d'ondes et de la longueur d'onde, pour chaque antenne (1,16, 0,97 et 0,84 μm de largeur), sous une lumière polarisée TM, des mesures expérimentales, des simulations FDTD et des simulations RCWA. Nous observons que les simulations correspondent aux résultats expérimentaux en termes d'amplitude, de forme et de fréquence. Les simulations RCWA, en prenant en compte les défauts de fabrication, sont encore plus proches des résultats expérimentaux.

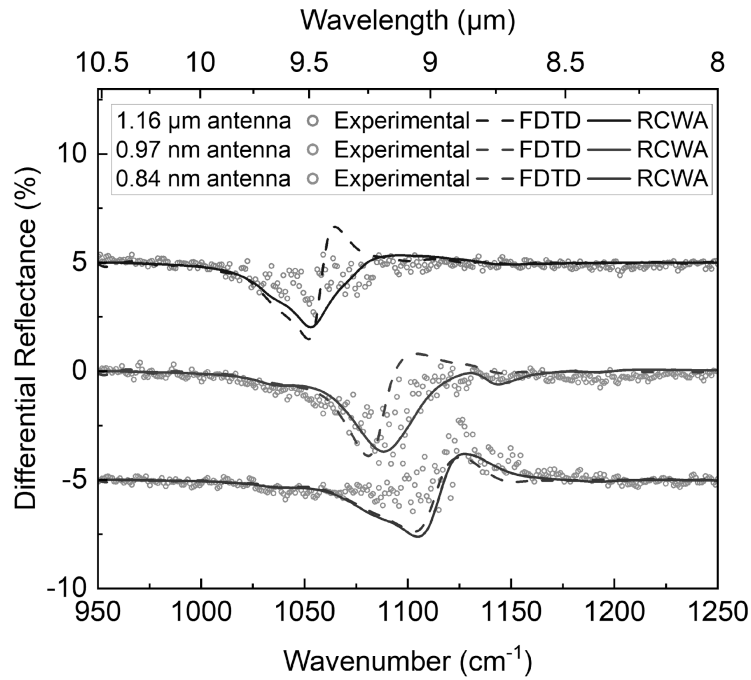


Figure 9. Réflectances différentielles des résultats expérimentaux et des simulations FDTD et RCWA. Un décalage en ordonnée est introduit par soucis de clarté.

La forme de la réflectance différentielle tient compte du couplage des vibrations moléculaires du DMMP avec la LSPR, c'est-à-dire qu'elle dépend de la façon dont la résonance plasmonique et les lignes d'absorption se chevauchent spectralement. Comme pour la résonance de Fano, les variations de phase sont fortement corrélées au chevauchement spectral entre les deux résonances, bien que dans notre cas, le faible couplage se produise entre deux continums d'états, ce qui signifie que les largeurs à mi-hauteur des résonances plasmoniques et des résonances de la molécule sont du même ordre de grandeur. Par conséquent, la détermination du spectre d'absorption du DMMP sondé par le champ magnétique amélioré et la prise en compte de l'inhomogénéité des antennes dans la simulation se sont avérées essentielles pour confirmer les résultats expérimentaux.

Nous avons développé un capteur de gaz à réponse rapide basé sur le mécanisme SEIRA soutenu par des antennes de nanorubans InAsSb:Si pour la détection de molécules complexes telles que les ACG avec un signal de détection d'environ 3 % dans le cas du DMMP. Les résultats expérimentaux obtenus par spectroscopie IR sont confirmés par des simulations FDTD et RCWA. La réponse d'un capteur plasmonique à base de SEIRA dépend fortement de la force de couplage, fonction des recouvrements spatial et spectral, et nous l'avons amélioré en employant une couche ENZ. L'oxyde natif InAsSb a la capacité d'interagir et de lier les molécules de DMMP pour les piéger à proximité des nano-antennes plasmoniques, améliorant ainsi leur absorption et augmentant la sensibilité du capteur. Le capteur se démarque par sa sélectivité vis-à-vis du DMMP par rapport aux composés organiques volatils que sont le benzène et le méthane, ainsi que par sa tolérance en milieu humide, avec un signal de détection identique de 2 % à 50 % d'humidité relative.

4) Conclusion

En conclusion, nous avons démontré l'applicabilité des semi-conducteurs III-V, en particulier l'InAsSb et le GaSb, dans les applications de détection plasmonique et l'étude des phénomènes ENZ-plasmon. Ils sont associés à de nombreux avantages pratiques, notamment des techniques de croissance et de nanofabrication de pointe, telles que l'épitaxie par jets moléculaires et la lithographie à faisceau d'électrons. Ils bénéficient de la maturité de l'industrie des semi-conducteurs pour leur intégration dans les circuits intégrés photoniques et sont compatibles avec les technologies CMOS.

Nous avons fabriqué des structures métal-isolant-métal, avec un isolant dopé afin d'ajuster sa fréquence plasmonique, c'est-à-dire le régime ENZ, à différentes gammes spectrales. Une telle structure présente un régime ENZ accordable du THz jusqu'au MIR, en fonction du niveau de dopage de l'isolant, avec une résonance plasmonique accordable en fonction des dimensions des nano-antennes. Nous avons étudié la réponse optique de trois échantillons ENZ différents en fonction du niveau de dopage de l'isolant (1×10^{16} , 1×10^{19} , et $2 \times 10^{19} \text{ cm}^{-3}$) et de la largeur des nano-antennes (de 200 nm à 1,8 μm). Nous avons déterminé la relation de dispersion de cette structure métal-ENZ-métal à l'aide de simulations FDTD, qui se sont révélées être une approche plus rigoureuse que les modèles d'indice de réfraction effectif trouvés dans la littérature, qui sont inadéquats pour les métaux et isolants imparfaits. Nous prouvons que le phénomène d'épinglage de la résonance provient d'une transition du matériau, qui est la fréquence du plasma dans notre cas. En outre, nous démontrons que tant qu'un isolant existe dans le système plasmonique, une interface métal-isolant persiste et peut soutenir des modes plasmoniques au-delà de la fréquence de transition du matériau. La conséquence sous-jacente de l'épinglage LSPR est la grande tolérance aux défauts de fabrication associée à une caractéristique d'indépendance à la géométrie ; un atout notable car la photonique moderne repose de plus en plus sur des technologies de fabrication coûteuses et sophistiquées. En outre, nous avons discuté de la nature de divers effets basés sur l'ENZ, notamment la phase quasi-constante et le champ électromagnétique amélioré. Cette étude démontre l'ingénierie des SC III-V dans l'architecture M-ENZ-M et ouvre la voie à des applications telles que la détection des COP en phase vapeur.

Les échantillons fabriqués ont ensuite été utilisés dans des expériences de détection de gaz du simulant du sarin : le DMMP, en se basant sur l'absorption IR renforcée par la surface (SEIRA). Les résultats expérimentaux montrent un signal de détection de $\approx 3 \%$ avec une concentration minimale détectée de 100 ppm. La réponse du capteur est indépendante de la concentration de DMMP dans la plage 100-500 ppm, ce qui entraîne une saturation du signal associée à la formation d'une couche monomoléculaire de DMMP de 5 Å d'épaisseur qui s'est liée à l'oxyde natif de la surface par différents mécanismes chimiques. À partir des spectroscopies IR, Raman et de photoélectrons X, nous avons étudié les interactions possibles qui peuvent être responsables de cette réaction chimique se produisant à la surface, et enfin nous présentons différents modèles des hypothèses les plus plausibles. La réactivité de l'oxyde natif InAsSb s'est avérée être un avantage pour sa capacité à interagir directement avec le DMMP, sans recours à une chimie de surface, liant et amenant ainsi le DMMP à proximité des nano-antennes plasmoniques. En conséquence, l'absorption des molécules de DMMP ancrées est améliorée, ce qui démontre que cette interaction spécifique entre les molécules de DMMP et les surfaces d'InAsSb participe à l'amélioration de la sélectivité et de la sensibilité du capteur. Le capteur conçu, fabriqué et testé est relativement rapide (temps de réponse ≈ 5 min), sélectif vis-à-vis du DMMP car il est directement relié à son empreinte spectrale, et il est tolérant à l'humidité (testé

jusqu'à 50% d'humidité relative) ainsi qu'aux interférents comme le benzène et le méthane. Les résultats expérimentaux ont été confirmés par des simulations FDTD et RCWA.

Enfin, si le système est intégré et que les caractéristiques de l'échantillon sont parfaitement connues, de sorte que tous les doutes concernant la limite de détection, la sélectivité et le temps de réponse ont été dissipés, l'échantillon peut être testé dans des conditions de terrain. La sensibilité et la sélectivité peuvent être davantage améliorées par l'utilisation de différentes conceptions d'antennes exploitant les effets de pointe et par l'ingénierie des métamatériaux et/ou des antennes 2D pour obtenir une multi-résonance, ce qui améliorerait encore ces deux caractéristiques, notamment en ciblant la liaison chimique P-F caractéristique du sarin.